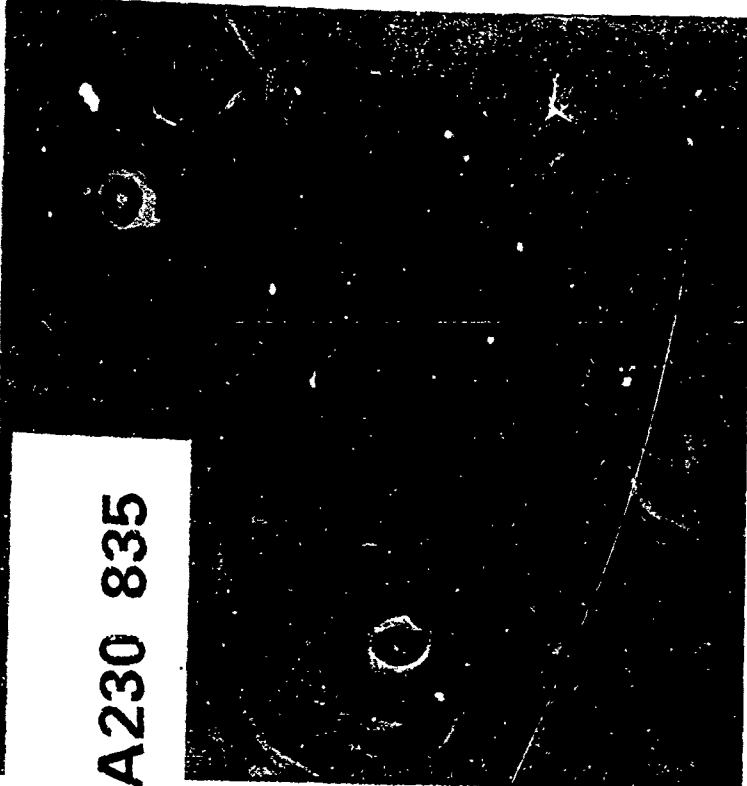


AD-A230 835



DTIC
SELECTED
JAN 16 1991
S D D D

DISTRIBUTION STATEMENT A
Approved for public release
Distribution Unlimited

91 1 187

2000 1000 0000
1

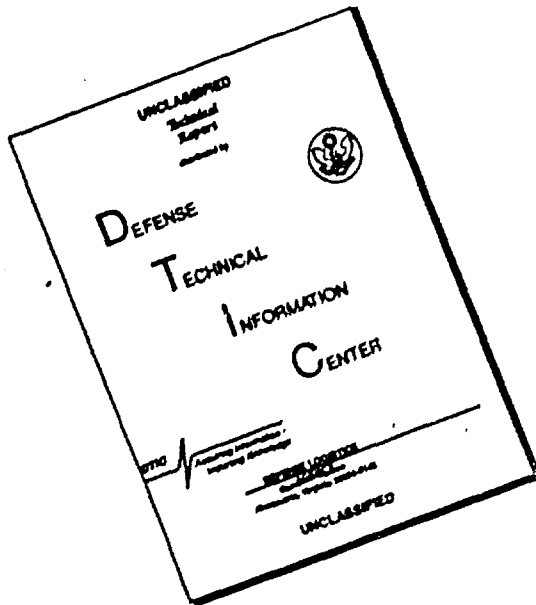
L E S

LARGE EDDY
SIMULATION...
WHERE DO
WE STAND ?

International Workshop
December 19-21, 1990

St. Petersburg Beach Hilton,
St. Petersburg Beach, Florida

DISCLAIMER NOTICE



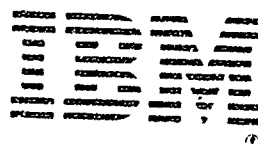
**THIS DOCUMENT IS BEST
QUALITY AVAILABLE. THE COPY
FURNISHED TO DTIC CONTAINED
A SIGNIFICANT NUMBER OF
PAGES WHICH DO NOT
REPRODUCE LEGIBLY.**

ORGANIZING COMMITTEE

J. FERZIGER
B. GALPERIN
K. KUWAHARA
S. ORSZAG
V. YAKHOT
T. ZANG

PRESENTATIONS BY

K. BEDFORD
M. CANE
W. COTTON
J. FERZIGER
P. GIVI
J. HERRING
G. HOLLOWAY
K. HORIUTI
Y. HUSSAINI
C. LEITH
M. LESIEUR
D. LILLY
P. MASON
J. MCWILLIAMS
P. MULLER
P. MOIN
G. KARNIADAKIS
S. ORSZAG
S. RAGAB
U. SCHUMANN
J. SMAGORINSKY
V. YAKHOT
J. WYNGAARD
T. ZANG



SiliconGraphics
Computer Systems



NASA
LANGLEY
RESEARCH
CENTER



The views, opinions and or findings contained in this report are those of the author(s) and should not be construed as an official Dept. of the Army position, policy, or decision, unless so designated by other documentation.

This work relates to Dept. of Navy Grant N00014-90-J-4120 issued by the Office of Naval Research. The United States Government has a royalty-free license throughout the world in all copyrightable material contained herein.

Program for the International Workshop
"Large Eddy Simulation - Where Do We Stand?"
St. Petersburg, FL, December 19 - 21, 1990

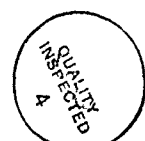
December 19, Morning
General Session
K. Kuwahara, Chairman

1. J. Smagorinsky
Some Historical Remarks on the Use of Non-Linear Viscosities in Geophysical Models.
2. J. Herring
Contribution of Two-Point Closure to Large-Eddy Simulation.
3. A. J. Chorin
Application of Statistical Mechanics to Turbulence Modeling.
4. S. Orszag
Field Theoretic Approach to LES Models.
5. J. H. Ferziger
Models for Use in Large Eddy Simulation.

Accesion For	
NTIS	CRA&I <input checked="" type="checkbox"/>
DIC	TAB <input type="checkbox"/>
Unpublished	<input type="checkbox"/>
Justification	
By _____	
Distribution / _____	
Availability Codes	
Dist	Avail. add/or Special
A-1	

December 19, Afternoon
Compressible, Reacting Flows; Combustion
J. Ferziger, Chairman

1. V. Yakhot
Renormalization Group for LES of Compressible Flows and Premixed Turbulent Combustion.
2. C. K. Madnia and P. Givi
LES and DNS of Reacting Homogeneous Turbulence.
3. C. E. Leith
Stochastic Backscatter in a Subgrid-Scale Model: 3D Compressible Flows.
4. G. Erlebacher and M. Y. Hussaini
DNS and LES of Compressible Turbulence.
5. S. A. Ragab
LES of Compressible Mixing Layers.



December 20, Morning
Incompressible Flows
S. Orszag, Chairman

1. P. Moin
Some Issues in Computation of Turbulent Flows.
2. M. Lesieur, P. Comte, X. Normand, O. Metais and A. Silveira
Spectral Large-Eddy Simulation of Turbulent Shear Flows.
3. K. Horiuti
Anisotropic Representation of Subgridscale Reynolds Stress in LES.
4. G. E. Karniadakis, S. A. Orszag and V. Yakhot
Large-Eddy/RNG Simulation of Flow Over a Backward-Facing Step.
5. T. A. Zang and U. Piomelli
Large-Eddy Simulation of Transitional Flows.

December 20, Afternoon
Atmospheric Sciences
J. Smagorinsky, Chairman

1. J. C. Wyngaard and C.-H. Moeng
LES in Geophysical Turbulence Parameterization.
2. U. Schumann and K. Krettenauer
Numerical Simulation of Turbulent Convection over Wavy Terrain.
3. W. R. Cotton, R. L. Walko, P. J. Flatau and K. R. Costigan
Using RAMS in LES Mode-from Inhomogeneous Surfaces to Cirrus Clouds.
4. D. Lilly
Helicity Revisited - Background and New Developments in an Erratic and Paradoxial Subject.
5. P. J. Mason
Large-Eddy Simulation of the Stably Stratified Atmospheric Boundary Layer.

December 21, Morning
Physical Oceanography
J. Herring, Chairman

1. G. Holloway
Subgridscale Modeling for Large Scale Ocean Circulation.
2. P. Muller
Diapycnal Mixing in the Ocean: a Review.
3. J. C. McWilliams, P. C. Gallacher, C.-H. Moeng and J. C. Wyngaard
Large-Eddy Simulations of Oceanic Boundary Layers.
4. M. A. Cane
Near Surface Mixing and the Oceans' Role in Climate.
5. K. W. Bedford
Conjunctive Filtering Procedures in Surface Water Flow and Transport.

INTERNATIONAL WORKSHOP
on LARGE EDDY SIMULATION
Where Do We Stand?

St. Petersburg, Florida
December 19-21, 1990

**SOME HISTORICAL REMARKS ON THE USE OF
NON-LINEAR VISCOSITIES IN GEOPHYSICAL MODELS**

Joseph Smagorinsky

EXTENDED ABSTRACT

When Phillips did his first extended quasi-geostrophic general circulation numerical integrations in 1956, he encountered large-scale filamentation of the vortex lines reflecting a piling-up of kinetic energy at the smallest resolvable scales. A subsequent analysis by Phillips (1959) revealed this to be the result of a non-linear cascade from large scales which could be stabilized by periodically eliminating all components with wavelengths smaller than 4 times the grid size. Von Neumann suggested that his and Richtmeyer's computational experience with one-dimensional shock waves (1950) indicated the value of a non-linear artificial viscosity. Charney and Phillips (personal communication) successfully adapted a 2-dimensional version of the idea, with viscosity proportional to the magnitude of the lateral deformation in some trial quasi-geostrophic integrations.

Smagorinsky, in the early 1960s (in an unpublished manuscript) set out to rationalize the use of a non-linear viscosity by appealing to modern turbulence theory, as a basis for long integrations with the primitive equations. The idea was to arrive at a formulation of the turbulent transfer in the grid-size scales assuming the 3-dimensional isotropic -5/3 similarity law of Kolmogoroff and Heisenberg was valid. If this were indeed an inertial subrange, then energy at subgrid scales would be removed at the same rate that it was being cascaded from the larger explicitly treated scales, thereby preserving the shape of the spectrum in the vicinity of the smallest resolvable scales.

As has been usual, it was assumed that the formalisms of elasticity theory were a valid analogue, and the requirement of reflective symmetry and of axial symmetry about the vertical axis reduced the problem to one of 12 non-zero

coefficients of which 3 are independent. The further constraint of quasi-hydrostatic equilibrium with the side condition that the energy dissipation be positive-definite reduces the number of arbitrary coefficients in the 5 remaining stress equations to 2.

Bass' (1949) solution of the Kolmogoroff-Heisenberg integral equations in the inertial subrange, taken together with the stress equations, yields expressions for the 2 turbulent viscosities due to horizontal and vertical strains of the horizontal component of the wind. In particular, the horizontal exchange coefficient is proportional to the magnitude of the horizontal deformation, resulting in a non-linear eddy viscosity.

The proportionality is through a characteristic length squared, which was assumed to be proportional to the local grid-size. This then determined the scale at which the flow transitions from being explicitly resolved to being treated statistically at subgrid scales. The non-dimensional proportionality constant was interpreted to be closely related to the Kármán constant. Since that time, Lilly (1967) and Deardorff (1971) related the non-dimensional constant to the Kolmogoroff constant. In particular, Deardorff suggested that the characteristic length is, in turn, proportional to the integral scale of turbulence corresponding to the truncated finite-difference spectrum. That is, in Lilly's words, the corresponding wave number is the largest unambiguously representable on a finite difference mesh. With this, the constants defined by different authors can be related to each other, with only one experimental determination (with the exception of Yakhot and Orszag, 1986) necessary for each characteristic type of flow.

One must come to grips with the fact that the Heisenberg theory is for 3-dimensionally isotropic flow and we, at grid scale, are concerned with quasi-two-dimensional, quasi-static flow, but which has a physically significant third dimensional component. Kraichnan (1971) and others have pointed out that the Heisenberg functional form of the turbulence spectrum can be assumed valid for 2-dimensional turbulence, provided the Kolmogoroff constant is taken to be substantially larger (6.7 instead of 1.4). Also, Deardorff (1985) concluded that flows dominated by mean shear required a larger Kolmogoroff constant (that is the turbulence behaves more 2-dimensionally) than ordinary 3-dimensional turbulence.

Over the past two decades there has been a great move to the use of spectral methods for global atmospheric modeling, and a corresponding move away from the use of non-linear viscosities. On the other hand, oceanographic

application still employ finite difference methods to deal with irregular boundaries. Most recently, however, the promise of parallel computer architecture and the advantages of semi-Lagrangian advective schemes may lure large-scale atmospheric modelers back to finite-difference models and non-linear viscosities.

REFERENCES

- Bass, J., 1949: Sur les bases mathématiques de la théorie de la turbulence d'Heisenberg. C. R. Acad. Sci., Paris, 228 (part 1), p. 228.
- Deardorff, J. W., 1971: On the magnitude of the subgrid scale eddy coefficient. J. Comput. Phys., 7, 120-133.
- Deardorff, J. W., 1985: Sub-grid-scale turbulence modeling. In Issues in Atmospheric and Oceanic Modeling, Part B. Weather Dynamics, Advances in Geophysics (Eds. Barry Saltzman and Syukuro Manabe), 429pp.
- Kraichnan, R. H., 1971: Inertial-range transfer in two- and three-dimensional turbulence. J. Fluid Mech., 47, 525-?.
- Lilly, D. K., 1967: The representation of small-scale turbulence in numerical simulation experiments. Proceedings of the IBM Scientific Symposium on Environmental Sciences. IBM Form No. 320-1951, 195-202.
- Neumann, J. von and R. D. Richtmeyer, 1950: A method for the calculation of hydrodynamic shocks. Jour. Appl. Phys., 21, 232-237
- Phillips, N. A., 1956: The general circulation of the atmosphere: a numerical experiment. Q. J. Roy. Soc., 82, 123-164.
- Phillips, N. A., 1959: An example of non-linear computational instability, In The Atmosphere and the Sea in Motion (Editor B. Bolin), The Rossby Memorial Volume, Rockefeller Institute Press, 509pp.
- Smagorinsky, J., 1962: The formulation of eddy transport processes for the quasi-static inertial subrange of atmospheric motions, unpublished manuscript.

Smagorinsky, J., 1963: General circulation experiments with the primitive equations, I. The basic experiment. Monthly Weather Review, 91, 99-152.

Smagorinsky, J., S. Manabe and J. L. Holloway, 1965: Numerical results from a nine-level general circulation model of the atmosphere. Monthly Weather Review, 93, 727-768.

Yakhot, V. and S. A. Orszag, 1986: Renormalization group analysis of turbulence, I. Basic theory. Jour. Sci. Comp., 1, 3-51.

Contribution of Two-point Closure to Large Eddy Simulations

by J. R. Herring

National Center for Atmospheric Research,* Boulder, Colorado 80307

Abstract

Although LES seems an inevitable tool for high Reynolds number flows, its usual derivation is obscured by the intrinsic unpredictability of turbulent flows. This problem is illustrated by considering the attempt to derive LES via the two-point closure form of the statistical theory of turbulence. In this context, we argue that any precise distinction between large-scale deterministic LES scales and statistically specified "sub-grid scales" is lost after the predictability time, unless the distinction corresponds to a stable statistical symmetry of the problem (see e.g., Fox and Lilly, 1972; Herring, 1979). After describing some simple two-point closure procedures (principally the test field model (TFM), Kraichnan, 1971), we note that such methods may be used to place bounds on LES-computed velocity fields in the sense that the flow's variances computed on a compressed range of scales $[0, k_{LES}]$ are the same as would be computed on the full range of scales, $[0, \infty]$, provided the closure is accurate. This alternate point of view avoids the predictability dilemma noted above, but it also detaches the LES flow from the real flow. We next present—in summary form—current information on the accuracy of statistical theories, principally the TFM and related theories. We note that although for three-dimensional turbulence the accuracy of such a theory seems promising, in two-dimensions the development of isolated compact vortices (McWilliams, 1984) presents a serious and as yet unanswered challenge to two-point closures. As used in LES calculations, such methods are representable as eddy viscosities and conductivities (see e.g., Kraichnan, 1976; Lesieur, 1987), and some results are briefly discussed for isotropic and homogeneous flows drawn in part from Chollet (1983).

The Leonard term (Leonard, 1974; Leonard and Patterson, 1977) that appear because $\overline{\bar{u} \bar{u}} \neq \overline{u \bar{u}}$ (overlines denoting filtering with respect to an as yet arbitrary filter shape) is next considered. We note that the spectral form of two-point closures may be used to evaluate this term in a simple way, and we discuss its importance, particularly at large Reynolds numbers for which DNS methods are difficult.

Next, we consider the effects of relaxing the isotropic constraint and compare how the more general anisotropic formalism differs from the standard Smagorinsky (1963) procedure, in which the eddy viscosity is computed solely in terms of the large-eddy strain. Such a step is necessary in order to discern a possible dependence of eddy coefficients on vorticity as well as strain. We consider—in this connection—the possible role of the second invariant of the strain in characterizing eddy viscosity.

Next we describe the application of these ideas to two-dimensional and quasi-geostrophic turbulence. Here, the characterization of the eddy viscosity (based on two-point closure) is simpler, and we are able to delineate the role of strain and vorticity in the composition of eddy viscosity in a clearer way.

* The National Center for Atmospheric Research is sponsored by the National Science Foundation.

References

- Chollet, J. P., 1983: *Turbulence tridimensionnelle isotrope: modelization statistique des petit échelles et simulation numérique des grandes échelles.* These de doctorat d'Etat, Grenoble.
- Fox, D. G. and Lilly, D. K., 1972: Numerical simulation of turbulent flow, *Rev. Geophys. Space Phys.*, **10**/*1*, 51-72.
- Herring, J. R., 1978: Sub-grid scale modeling, an introduction and overview. In *Turbulent Shear Flow I*, B. E. Launder, F. W. Schmidt, and J. H. Whitelaw, eds., Springer-Verlag, Heidelberg, 347-351.
- Kraichnan, R. H., 1971: An almost-Markovian Galilean-invariant turbulence model. *J. Fluid Mech.*, **47**, 513.
- Kraichnan, R. H., 1976: Eddy viscosity in two- and three-dimensional turbulence. *J. Atmos. Sci.*, **33**, 1521-1536.
- Leonard, A., 1974: On the energy cascade in large-eddy simulation of turbulent fluid flows. *Adv. Geophys.*, **18A**, 273.
- Leonard, A. and Patterson G. S., 1977: Numerical Study of the Energy Loss of Large Eddies in Turbulent Flow Simulation. NCAR-GTP Historical Collection.
- Lesieur, M., 1987: *Turbulence in Fluids*. Martinus and Nijhoff Publishers, Dordrecht, The Netherlands.
- McWilliams, J. C., 1984: The emergence of isolated vortices in turbulent flows. *J. Fluid Mech.*, **148**, 21-43.
- Smagorinsky, J., 1963: General circulation experiments with the primitive equations. *Mon. Wea. Rev.*, **91**, *3*, 99-164.

APPLICATION OF STATISTICAL MECHANICS TO TURBULENCE MODELING
(Extended Abstract)

Alexandre J. Chorin
Department of Mathematics
University of California
Berkeley, CA 94720

Introduction. The goal of large eddy simulation in turbulence theory is the replacement of descriptions of turbulent flow that contain many unknowns to be computed by descriptions with fewer unknowns (hopefully, many fewer). Methods for performing such reductions are well known in statistical mechanics, where they are known as renormalization group techniques (with related techniques, such as adiabatic elimination procedures, being used, for example, in the context of Fokker-Planck equations). Our goal here is to discuss the application of a class of real-space renormalization group techniques to a vortical description of incompressible turbulence.

Heuristics. We begin by describing heuristic forms of these renormalization techniques. Suppose the flow is described by a collection of vortex elements (blobs, filaments, or segments). Allow the flow to evolve in time. Vortex lines stretch, and the vortex description becomes ever more expensive. As the vortex lines stretch they fold (this is a consequence of conservation of energy, and a manifestation of the Kosterlitz-Thouless transition mechanism in vortex theory). The support of the vorticity shrinks, and thus tight hairpins must form. It is natural to try to erase tightly wound counterrotating elements in such hairpins, and several algorithms for doing this have been proposed. It has been found in particular that any deviation from the exact self-consistency condition $\operatorname{div} \operatorname{curl} u = 0$ leads to a rapid accumulation of errors, and thus the best hairpin removal should be attached to a vortex

method where the elements are closed filaments (the alternative of nonlocal projected elements is hard to use). The removal is then equivalent to a limit on the curvature of the computational vortices as well as to the erasure of all elements whose scale (as measured by the corresponding radius of curvature) is smaller than a predetermined small parameter h . Numerical examples will be displayed.

The major open questions with this kind of removal algorithms are their theoretical justification and the existence of improvements — for example, hairpin removal leaves the strength (= circulation) of the vortices fixed; one is used in quantum renormalization schemes to the renormalization of the coupling constants (here, the circulation squared). One has to imbed the ad-hoc removal algorithm within a systematic rescaling procedure. The next section will provide such an imbedding.

Equilibrium statistical mechanics of vortex filaments. Consider a collection of vortex filaments in thermal equilibrium (enforced by limiting their stretching). The translation-invariant ensemble of such filaments that has maximum entropy has a Kolmogorov spectrum. The quasi-equilibrium (= statistically steady state) obtained by perturbing such an equilibrium through removal of energy at small scales and stirring at large scales is near equilibrium if the entropy is large. These facts do not contradict the fact that if a collection of vortices is allowed to evolve without viscosity, energy removal at small scales, stirring, or no reconnection, no thermal equilibrium can be reached. These remarks make it plausible that the appropriate renormalization theory for the small scales is an equilibrium theory. Renormalization equations can be set up, based on an expansion in the chemical potential; to first order, they lead to a constant ratio of coupling constant to temperature, i.e. to the hairpin removal algorithm.

References

- A. J. Chorin, "Hairpin removal in vortex interactions", *Jour. Comp. Phys.*, 1990 (in press).
- _____, "Constrained random walks and vortex filaments in turbulence theory", *Comm. Math. Phys.* 132 (1990), 519-536.
- _____, "Vortex equilibria in turbulence and quantum analogues", Report PAM 512 (1990), Mathematics Dept, UC Berkeley.

Field Theoretic Approach to LES Models

Steven A. Orszag

Applied and Computational Mathematics
Princeton University
Princeton, New Jersey 08544-1000

ABSTRACT

In this talk a survey will be given of the basis of large-eddy simulations of turbulent flow. Recent work based on renormalization group ideas that give a rational basis for SGS viscosities will be described. Applications to complex shear flows and compressible turbulence will be given. Finally, an assessment will be given of future prospects of LES in light of complex engineering modeling requirements at high Reynolds numbers.

Models for Use in Large Eddy Simulation

Joel H. Ferziger

Department of Mechanical Engineering,
Stanford University, Stanford, CA

The need to use subgrid scale (SGS) models in large eddy simulation (LES) needs no justification. For relatively simple low Reynolds number flows, the quality of the model is not very important; only a small fraction of the energy resides in the small scales and error in the predicted distribution of the SGS energy or Reynolds stress do no great harm to the overall quality of the simulation. It suffices that the model dissipates the required amount of energy. The Smagorinsky eddy viscosity model is adequate to this task and nothing more is required. This model can be derived by a number of methods--heuristics, spectral theories, renormalization group (RNG) theory, etc.

For more complex or higher Reynolds number flows, model quality becomes more important. Often the spectra at the highest resolved wavenumbers are not well predicted by the Smagorinsky model. A number of suggested improvements have been put forward. For high Reynolds number homogeneous turbulence, eddy viscosities which affect the small scales more strongly than Smagorinsky's (spectral eddy viscosities) have been suggested and applied successfully. The scale similarity model, although originally intended as a substitute for Smagorinsky's model, in fact transfers energy from the smallest resolved scales to larger scales and thereby accomplishes the same effect. Finally, treatment of the SGS by spectral theory has been done successfully, but is costly. An obvious avenue of improvement, using partial differential equations to describe the SGS turbulence has been tried only a few times with limited success.

Users of the Smagorinsky model have been plagued by the need to change the model parameter according to the type of flow; the choice of length scale in highly anisotropic turbulence (which usually implies highly anisotropic grids) has been another issue. These problems appear to be circumvented by a recent suggestion of Germano and coworkers. In this method, the large eddy simulated field is high pass filtered to give the smallest scale field which is treated as a stand-in for the unrepresented fields. From this field, the model parameter can be determined. Direct application of this method was shown by Piomelli et al (see the paper by Moin in this conference) to be unstable; fortunately, it is readily stabilized by introducing averaging. The parameter then self-consistently determined, eliminating the need for reformulation each time the flow is modified. This method appears to have great promise.

Approximate boundary conditions to be used at walls and other boundaries is another critical issue. The most recent advances in this field were made by Piomelli who suggested two modified law-of-the-wall conditions for smooth walls; rough walls can probably be treated in a similar manner. However, there is still a need for conditions that are able to deal with flow separation and reattachment and three dimensionality.

Finally, we recall that 'extra strains' have significant effects on turbulent flows. The question is whether they affect the small scales of the turbulence strongly enough to require modification of the model. Not much is presently known about this issue. It is the author's opinion that phenomena that strongly depend on the behavior of the small scales will need to be accounted for in the model while those whose effects are felt primarily in the large scales can probably be treated with the models described above. Examples of phenomena of the former type are shock waves (and perhaps compressibility in general) and combustion while stratification, rotation and curvature may fall in the latter category.

Renormalization Group for LES of Compressible Flows and Premixed
Turbulent Combustion

Victor Yakhot

Applied and Computational Mathematics
Princeton University
Princeton, New Jersey 08544-1000

ABSTRACT

I will present a systematic derivation of the renormalization group for compressible turbulent flows and turbulent combustion. The method involves elimination of the small-scale velocity fluctuations and derivation of the effective transport coefficients. The most striking effect predicted by the method is the scale-dependence of the effective speed of sound which reduces the effective Mach number. Thus, we believe that only weak eddy shocklets can exist in the three-dimensional isotropic turbulence even at arbitrarily high Mach number. The sub-grid model for premixed flame front is derived and used for LES of the front propagation in turbulent channel flow.

LES and DNS of Reacting Homogeneous Turbulence

by

Cyrus K. Madnia and Peyman Givi
Department of Mechanical and Aerospace Engineering
State University of New York at Buffalo
Buffalo, New York 14260

Long Abstract Submitted for Presentation at the International Workshop
Large Eddy Simulations - Where Do We Stand?

St. Petersburg, Florida
December 19-21, 1990

Abstract

In the review of the recent computational work on turbulent reacting flows Drummond¹, Oran and Boris² and Givi³ indicate the need for further development in both the methodology and the implementation of DNS and LES. The results of previous and ongoing works towards the developments of advanced numerical algorithms for the simulations of reacting turbulent fields have been successful, and we have been using these tools as a means of understanding some of the interesting intricate flow dynamics in reactive systems.

It is now a well-established fact that foreseeable developments of advanced computational facilities, will not be sufficient to relax the restriction of DNS to flows having small to moderate variations of the characteristic length and time scales^{3,4,5}. Hence the boundaries of applicability of DNS are, and will continue to be, somewhat restricted. Nevertheless, within its domain, DNS can be used to enhance our understanding of the physics of chemically reacting turbulent flows by (1) providing specific information concerning the detailed structures of the flow, and (2) providing a quantitative basis for evaluating the performance of turbulence closures. It is now proven that DNS has been an outstanding tool for such studies and, in addition, has provided useful guidelines for future investigations.

LES appear to provide a good alternative to DNS for computing flows having ranges of parameters similar to those encountered in practical systems^{4,5,6}. The approach based on LES has a particular advantage over the Reynolds-averaged procedures in that only the effects of small-scale turbulence motion have to be modelled. Therefore, the construction of accurate "subgrid scale" closures is an important task in its implementation. The extensive experience gained during the past two decades in constructing turbulence models for the Reynolds-averaged equations of turbulent combustion should prove to be quite useful in the development of these closures. A major advantage offered by LES is that, subgrid closure modeling can be substantially simplified by performing computations over grids of different size^{5,6,7}. In this way, the performance of a model on coarse grids can be directly evaluated by comparing its predictions with those obtained on

fine grids. This procedure has been followed in previous works^{5,7} and the simulated results have often produced satisfactory subgrid closures. All the efforts to-date, however, have been toward constructing closures for non-reacting flows.

Our efforts, to date, have been mainly concentrated on using the data obtained by DNS for the purpose of validating models for turbulence modeling and subgrid closure. In both tasks, the basic frame of closure is based on probability density functions (PDF's) of scalar variables. The PDF methods have proven very useful in the analytical treatment of reacting turbulent fields^{8,9}, and it is anticipated that their implementations would be useful for treating the subgrid fluctuations in turbulent reacting flows. In the presentations, we will provide a brief review of our previous findings in using the DNS data for validating PDF methods in turbulent combustion modeling, and we will present the results of some of our ongoing efforts in using PDF methods for the treatment of fluctuations within the subgrid in LES. In both cases, we limit the discussions to the analysis of homogeneous turbulence, since in this case all the complications associated with spatial inhomogeneity are removed. The ideas developed here, however, can be used for the subgrid closure in inhomogeneous flows, such as reacting mixing layers¹⁰, and more complex flows. In this abstract, we limit the discussion to the extent used in LES modeling.

In efforts related to LES, we have used the data base obtained by DNS for a detailed study of the PDF characteristics within the subgrid. This data base is generated by direct simulation of an initially unpremixed homogeneous turbulent flow under the influence of a passive chemical reaction of the type $A + B \rightarrow Products$. As an initial effort, it is assumed that the chemistry is infinitely fast (i.e. Damkohler Number $\rightarrow \infty$); therefore a flame sheet approximation is employed. With this approximation, the transport of an inert scalar quantity is sufficient to portray the statistical behavior of the species field. Simulations are performed for both two- and three-dimensional homogeneous flows for several values of the turbulent Mach number. A spectral-collocation algorithm based on Fourier expansion function⁷ is employed in the numerical simulations. The fluid obeys the Navier-Stokes equations for an ideal gas. Periodic boundary conditions are employed in all directions for both two dimensional and

three dimensional simulations. A 256×256 uniform collocation grids was used for two dimensional calculations. The number of collocation points for the three dimensional simulations was $128 \times 128 \times 128$.

A range of initial fluctuating Mach number was considered to study the effect of compressibility on mixing and chemical reaction. For the purpose of flow visualization, sample two dimensional contour plots of the pressure field are presented in Figs. 1 and 2. Figure 1 represents a typical pressure contour plot for a low compressible case and Fig. 2 corresponds to a high compressible case. An interesting feature displayed in Fig. 1 is the presence of the shocklets. A two dimensional contour plot of species concentration for a high compressible case is shown in Fig. 3. The normalized time corresponding to this case is such that the effect of initial conditions is no longer substantial.

The DNS data base obtained is used to study the behavior of the probability density functions (PDF's) of scalar properties within the subgrid. After the generation of the data base on the fine grid, the results are statistically analyzed within an ensemble of these grids to describe the large scale conduct on the coarse grid. The ratio of the mesh spacings (resolution) provided by the coarse and the fine grids is a measure of the size of the filter which would be used in LES. At initial and intermediate computational times the pdf of inert scalar within the subgrid can be approximated with the class of two-parameter model distributions, and at final times the pdf asymptotically adopts a Gaussian distribution. This had been already surmised in incompressible flow simulations, as previous DNS results^{11,12} had suggested. However, in present simulations this behavior is observed both in incompressible flows and in compressible flows dominated with shocklets. This observation is somewhat useful since it suggests that in subgrid modeling of an inert scalar property, the information on the first two moments of the variable is enough to parametrize the pdf within the subgrid.

With the knowledge gained to date, it is anticipated that the approach based on pdf parametrization based on its first two moments may prove serviceable for turbulent combustion simulations. The approach based on the solution of a transport equation for pdf, however, may not be practical

at this stage. An estimate of computational requirements indicates that the cost associated with LES (a semi-deterministic solution of large scale with a probabilistic description of small scale by solving a pdf transport equation) is of the same order as that of DNS on the fine grids, unless the ratio of the fine to coarse grid is large.

Our ongoing investigation is concerned with investigating the effects of finite Damkohler number, which is most appropriate for pdf modeling, and also on including the influence of the heat release. The statistical analyses are also being done for different flow types and for various filter widths. We are also at the final stages of developing a parametrized PDF model for the closure modeling of unpremixed homogeneous reacting turbulent flows.

Acknowledgements

This work is sponsored by NASA Langley Research Center under Grant NAG-11122, and by Office of Naval Research under Grant N00014-90-J-4013. Computational Resources are provided by NASA LaRC, NAS, and NCSA at the University of Illinois.

References

1. Drummond, J. P., "Supersonic Reacting Internal Flow Fields," chapter in "Numerical Approaches in Combustion Modeling," *AIAA Prog. in Aeron. and Astr.*, eds: E.S. Oran and J.P. Boris, in press, 1990.
2. Oran, E. S. and Boris, J. P., "Numerical Simulations of Reactive Flow," Elsevier Publishing Co., Washington, D. C., 1987.
3. Givi, P., "Model Free Simulations of Turbulent Reactive Flows," *Prog. Energy Comb. Science*, 15, 1, 1989.
4. Reynolds, W. C., "The Potential and Limitations of Direct and Large Eddy Simulations," Position Paper at Whither Turbulence Workshop, Cornell University, Ithaca, New York, March 22-24, 1989.
5. Ferziger, J. H., "Higher-Level Simulations of Turbulent Flows," Stanford University Report No. TF-16, Department of Mechanical Engineering, Stanford University, Stanford, CA., 1981.
6. Schumann, U. and Friedrich, R. (Eds.), "Direct and Large Eddy Simulation of Turbulence," Proceedings of the EUROMECH Colloquium No. 199, Munchen, FRG, Sep. 30-Oct. 2, 1985.

7. Erlebacher, G., Hussaini, M. Y., Speziale, C. G. and Zang, T. A., *NASA CR 178279*, ICASE Report 87-20, NASA Langley Research Center, Hampton, VA., 1987.
8. O'Brien, E. E., "The Probability Density Function (pdf) Approach to Reacting Turbulent Flows," in *Turbulent Reacting Flows*, p. 185, Libby, P. A. and Williams, F. A. (ets.), Springer-Verlag, New York, NY, 1980.
9. Pope, S. B., "PDF Methods for Turbulent Reactive Flows," *Prog. Energy Combust. Sci.*, 11, p. 119 (1985).
10. Givi, P., Madnia, C. K., Steinberger, C. J., Carpenter, M. H. and Drummond, J. P., "Effects of Compressibility and Heat Release in a High Speed Reacting Mixing Layer," submitted to *Combust. Sci. Tech.*, 1990.
11. Givi, P. and McMurtry, P. A., "Nonpremixed Reaction in Homogeneous Turbulence: Direct Numerical Simulations," *AIChE Journal*, 34, No. 6, p. 1039, 1988.
12. Eswaran, V. and Pope, S. B., "Direct Numerical Simulations of Turbulent Mixing of a Passive Scalar," *Phys. Fluids*, 31, p. 506, 1988.

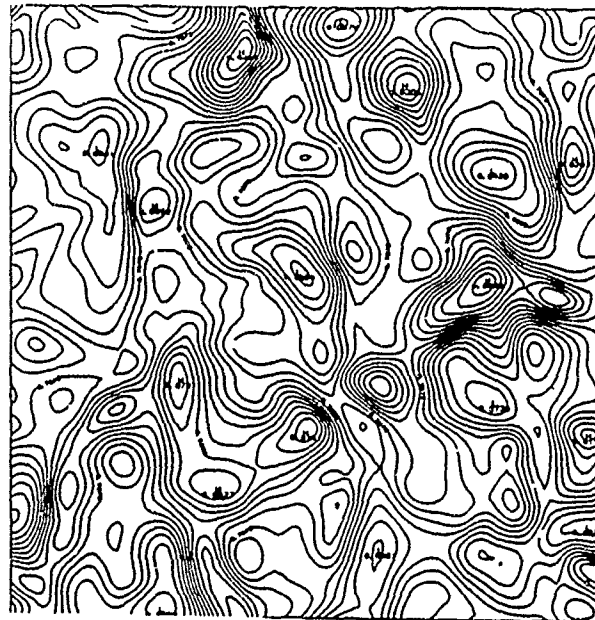


Figure 1. Contour plot of pressure for low compressible case.



Figure 2. Contour plot of pressure for high compressible case.

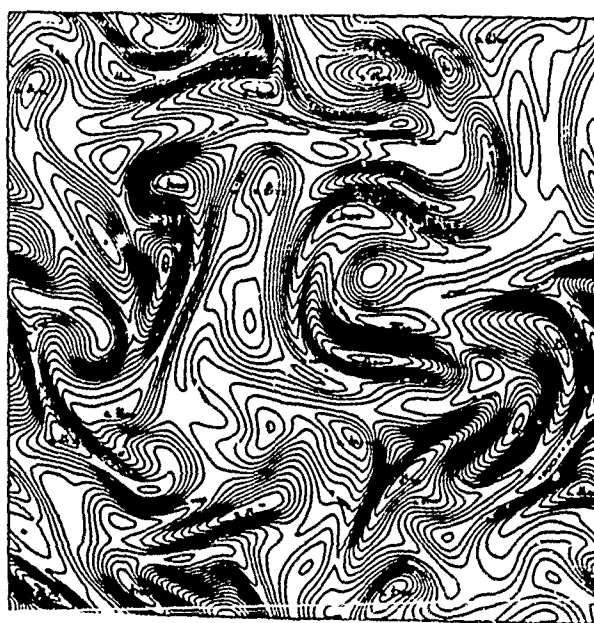


Figure 3. Contour plot of species A concentration for high compressible case.

STOCHASTIC BACKSCATTER IN A SUBGRID-SCALE MODEL: 3D COMPRESSIBLE FLOWS

**C. E. Leith
Lawrence Livermore National Laboratory
Livermore, CA 94550**

ABSTRACT

A subgrid-scale model with stochastic backscatter supplementing the well-known Smagorinsky eddy viscosity is formulated in the context of a three-dimensional (3D) large eddy simulation (LES) of compressible hydrodynamics. This natural extension of earlier work with a 2D LES of a shear mixing layer has been implemented on a BBN TC2000 highly parallel computer. Timing studies show that this relatively new computer architecture is well suited to such a simulation.

Prepared for the International Workshop on Large Eddy Simulation, to be held December 19-21, 1990, in Saint Petersburg, Florida

1. Introduction

The nonlinearity of fluid flow leads typically to the excitation of many interacting scales of motion which, unless strongly damped by viscosity, become chaotic. The resulting turbulent motion has important transport properties which can not be reliably predicted from statistical theories of turbulence in complicated flow configurations of practical interest. Instead one turns to numerical simulation in order to generate realizations of a flow from which average transport properties may be extracted. The Reynolds number measures the importance of nonlinearity compared to linear viscous effects. For the high Reynolds numbers that occur in many applications, the range of excited scales can far exceed the range feasible for direct numerical simulation (DNS) on present or future computers. Observations show, however, that the turbulent transport of interest is carried primarily by the largest scales of motion. This has led to the hope that large eddy simulation (LES) would be adequate for practical use.

In LES, the turbulence problem is reduced to treating, as well as one can, the effect of the unresolved subgrid scales on those explicitly computed. In the earliest models of geophysical fluid flows, which have essentially infinite Reynolds number, it was recognized (Phillips, 1959) that unless some artificially large viscosity was introduced, the natural nonlinear cascade toward small scales would produce nonsensical behavior. The simplest cure is to introduce a linear viscosity large enough that the associated Kolmogorov dissipation scale lies within the resolved range. In practice this has been found to damp unnecessarily the large eddies of interest, and a pragmatic approach has been to use instead a linear hyperviscosity proportional to some high power of the Laplacian and thus more concentrated on the barely resolvable scales. Such linear viscosities suffer from requiring prior knowledge of the turbulent nature of the flow and from being global in nature. They are thus not well suited to inhomogeneous turbulence.

Over a quarter century ago, Smagorinsky (1963) introduced a nonlinear eddy viscosity tied to the grid size and to the estimated local subgrid-scale turbulent kinetic energy production and cascade rate. It had the decided advantage of adjusting itself to provide a local viscosity of the needed strength without prior knowledge of the turbulence. A similar artificial viscosity had been devised by von Neumann and Richtmyer

(1950) to treat shocks in compressible flows. Although a deeper understanding of the problem has led to the development of many subgrid-scale viscosity prescriptions that are much more elaborate, none has been much more successful.

Subgrid-scale viscosity is, of course, designed to account for the mean damping effect of the unresolved eddies on the larger, resolved, scales of motion. But there is another effect that is qualitatively different. Subgrid-scale eddies also induce a random forcing of the large scales through nonlinear interaction. Although such stochastic backscatter has been understood theoretically for some time (Kraichnan, 1976; Leslie and Quarini, 1979) in the context of homogeneous turbulence, there has been little experience with the consequences for LES. One immediate consequence of adding backscatter is that the LES acquires a stochastic nature. An ensemble of simulations is needed to reveal the mean and fluctuating components of the explicitly computed flow. It is unfortunate that the large eddies are not deterministic, but this fact is completely consistent with the chaotic nature of turbulent flows that renders them of limited deterministic predictability (Leith and Kraichnan, 1972) on all scales. A detailed description of a subgrid-scale model that includes both a Smagorinsky viscosity and stochastic backscatter is given in Section 2.

Stochastic backscatter was applied successfully to the plane shear temporal mixing layer (Leith, 1990) induced by Kelvin-Helmholtz instability, but in this case the LES was two-dimensional in spite of the use of a three-dimensional subgrid-scale model. Such an inconsistency is partially justified for the shear mixing layer which is known to generate primarily two-dimensional large eddies. The principle purpose of the present paper is to formulate a consistent three-dimensional LES.

The 3D compressible Eulerian hydrodynamics equations are given in Section 3. They have been implemented with a standard Lax-Wendroff algorithm to run in parallel on up to 50 nodes presently available on the BBN TC2000 parallel computer at LLNL. The whole domain of the calculation is decomposed into subdomains, one for each node. Computation is carried out in parallel for the volume of each subdomain whereas only border information need be communicated in parallel between nodes. The resulting surface to volume ratio benefit reduces the time spent in communication relative to that in arithmetic to satisfactorily low levels for calculations of reasonable size. Details of the Lax-Wendroff

scheme and its parallel implementation are provided in Section 4 for those interested in the use of such relatively new computer architectures.

2. Subgrid-scale model

The most important requirement of a subgrid-scale model is that it have some mechanism to simulate the mean turbulent energy cascade from large scales to small across the resolution scale of the LES hydrodynamics model. If, as is usually assumed, the resolution length scale λ or wavenumber scale $k = 1/\lambda$ lies within the Kolmogorov inertial range with energy cascade rate ϵ whose energy spectrum is given by the well-known law $E(k) = \alpha \epsilon^{2/3} k^{-5/3}$, then there is some hope for universality of behavior and simple dimensional scaling laws can be used to deduce an appropriate eddy viscosity.

The resolution length scale λ of the model is, of coarse, also the length scale of the largest unresolved eddies. Let K be the specific turbulent kinetic energy of the unresolved eddies given by

$$K = \int_{k_*}^{\infty} E(k) dk \approx \epsilon^{2/3} k^{-2/3} \approx \epsilon^{2/3} \lambda^{2/3}. \quad (1)$$

We assume here, for simplicity, that the Reynolds number is infinite and thus that the inertial range extends to indefinitely high wavenumbers k . The symbol \approx means equality to within a dimensionless constant factor.

In simple eddy viscosity models, local turbulence with length scale λ and specific kinetic energy K induces an eddy viscosity with coefficient $\nu_T = C_1 K^{1/2} \lambda \approx K^{1/2} \lambda$. This is the product of an rms eddy velocity and a mixing length multiplied by an adjustable dimensionless coefficient that can not be determined through this kind of dimensional scaling analysis. Similarly, from Eq. (1), the turbulent dissipation rate may be estimated by $\epsilon \approx K^{3/2}/\lambda$.

The explicitly resolved deviatoric strain rate tensor components are given by

$$S_{ij} = v_{i,j} + v_{j,i} - (2/3) v_{k,k} \delta_{ij} \quad (2)$$

where v_i are the resolved velocity vector components with x_j derivatives v_{ij} and δ_{ij} are the Kronecker tensor components. The summation convention applies. For any eddy viscosity coefficient ν_T , the local eddy viscous specific stress tensor components are $\nu_T S_{ij}$, and the local shear production rate of subgrid-scale turbulent energy K is given by the eddy viscous stress work $\nu_T S_{ik} v_{i,k} = \nu_T S^2$, where the local scalar strain rate S is defined such that $S^2 = S_{ij} v_{ij} = (S_{ij} S_{ij})/2$. The local balance condition for K is therefore that $\epsilon = \nu_T S^2$, or $K^{3/2}/\lambda \approx K^{1/2} \lambda S^2$, whence $K \approx (\lambda S)^2$ and $\nu_T \approx \lambda^2 S$. The Smagorinsky eddy viscosity is defined as

$$\nu_T = (C_S \lambda)^2 S \quad (3)$$

where C_S is the traditional Smagorinsky constant.

We next consider the stochastic backscatter which, for isotropic homogeneous turbulence in three dimensions, is known (Kraichnan, 1976) to have a k^4 spectrum to lowest order in wavenumber k . This means that backscatter is concentrated on scales of motion that are only a little larger than the resolvable limit. In a three-dimensional fluid dynamics code, the lowest order effect of stochastic backscatter may be achieved by introducing on the calculational grid an isotropic space- and time-white random acceleration vector potential from which is derived a nondivergent random acceleration term to be added to the momentum equation.

The mean of the random acceleration potential is zero. Its variance is determined by the following dimensional scaling argument. The space derivative of a vector potential ϕ_i [$L^2 T^{-2}$] is an acceleration a_i [$L T^{-2}$] with the dimensions shown. The space-time covariance of ϕ_i is given by

$$\begin{aligned} \Phi_{ik}(x,t;x',t') &= \langle \phi_i(x,t) \phi_k(x',t') \rangle [L^4 T^{-4}] \\ &= \psi(x,t) \delta(x - x') \delta(t - t') \delta_{ik} \end{aligned} \quad (4)$$

The last expression implicitly defines a variance function $\psi(x,t)$ for the assumed isotropic space- and time-white random process. It may be written explicitly as

$$\psi(x,t) = (1/3) \int dt' \int dx' \Phi_{kk}(x,t;x',t') [L^7 T^{-3}] \quad (5)$$

As with eddy viscosity, one now constructs a dimensionally correct expression for $\psi(x,t)$ in terms of the local strain rate $S [T^{-1}]$ and the resolution length scale $\lambda [L]$. To within a dimensionless coefficient, this must then be $\psi(x,t) = S^3 \lambda^7$. In finite difference approximation ϕ_k can only be space- and time-white on resolved scales. In fact, the integral of Eq. (5) for $\psi(x,t)$ becomes, in finite approximation,

$$\psi(x,t) = (1/3) \langle \phi_k \phi_k \rangle \lambda^3 \delta t \quad (6)$$

The dimensionally proper scaling is therefore achieved if the random acceleration potential for each component and at each grid point and time step are chosen independently as

$$\phi_k = C_b (S \delta t)^{3/2} (\lambda / \delta t)^2 g_k [L^2 T^{-2}] \quad (7)$$

where g_k is a unit gaussian random number, i. e., drawn from a population with zero mean and unit variance. All dimensionless coefficients in this derivation are lumped into the single one C_b , which is adjustable but should be of order one.

The procedure just described is based on the implicit assumption that the resolution scale λ is the same as the grid interval, say δx . But random disturbances on the scale δx are so poorly treated by finite difference schemes that it may be better to run a smoothing average filter over the field of ϕ_k 's chosen above so that the filtered field has spatial correlation extending over about $2\delta x$. We may still take $\lambda = \delta x$ and absorb the filter effect into the constant C_b .

3. Compressible hydrodynamics equations

The equations of motion for 3D compressible hydrodynamics are formulated in conservation form as

$$\partial U / \partial t + F_{i,i} = K \quad (8)$$

in terms of the 5-vector of predicted variables

$$\begin{aligned} \mathbf{U} = & \begin{array}{l} \rho \\ \rho v_1 \\ \rho v_2 \\ \rho v_3 \\ \rho e \end{array} \end{aligned} \quad (9)$$

the 5-vector of fluxes

$$\begin{aligned} \mathbf{F}_i = & \begin{array}{l} \rho v_i \\ \rho v_1 v_i - \tau_{1i} + \epsilon_{1ij} \rho \phi_j \\ \rho v_2 v_i - \tau_{2i} + \epsilon_{2ij} \rho \phi_j \\ \rho v_3 v_i - \tau_{3i} + \epsilon_{3ij} \rho \phi_j \\ \rho e v_i - \tau_{ij} v_j + \sigma_i \end{array} \end{aligned} \quad (10)$$

and the 5-vector of sources

$$\begin{aligned} \mathbf{K} = & \begin{array}{l} 0 \\ \rho f_1 \\ \rho f_2 \\ \rho f_3 \\ \rho f_i v_i + \rho q \end{array} \end{aligned} \quad (11)$$

The variables that appear in these equations are density ρ , velocity v_i , total specific energy e , stress tensor τ_{ij} , stochastic backscatter potential ϕ_k of Eq. (7), diffused energy flux σ_k , external specific body force f_k , and external specific energy source q . The total specific energy is made up of internal specific energy i and kinetic energy so that $e = i + u_i u_i / 2$. The summation convention applies, and ϵ_{ijk} is the standard alternating tensor. The stress tensor is made up of an isotropic part involving the gas pressure p assumed to satisfy a γ -law equation of state, $p = (\gamma - 1) \rho i$, and an eddy viscous part so that

$$\tau_{ij} = -\rho \delta_{ij} + \rho v_T S_{ij} \quad (12)$$

where v_T is the Smagorinsky eddy viscosity coefficient given by Eq. (3).

The eddy diffusion coefficient κ_T for internal energy is assumed to be proportional to the eddy viscosity coefficient, thus $\kappa_T = v_T/\text{Pr}$, where Pr is the dimensionless eddy Prandtl number. The eddy flux of internal energy is given by

$$\sigma_k = -\kappa_T i_k \quad (13)$$

Note that in this formulation stochastic backscatter is introduced in Eq. (10) as a random stress. For constant density this reduces to the nondivergent acceleration discussed in Section 2 and in an earlier note (Leith, 1990). The present formulation ensures that stochastic backscatter conserves momentum exactly rather than statistically.

4. Numerical scheme

The finite difference model for the integration of the equations of motion is based on the Lax-Wendroff predictor-corrector scheme. Let U_0 be the old values of U at the beginning of the time step, U_p the predicted values appropriate for a half time step, and U the new values at the end of the step. The three-dimensional domain of the model is divided by a regular Cartesian mesh into a three-dimensional array of cells. The fields U and the fluxes F_i based on them by Eq. (10) are defined as cell-centered quantities. Spatial differences are obtained by differencing neighbor values to east and west for x_1 , to north and south for x_2 , and up and down for the x_3 -direction. In obvious notation the predictor step becomes

$$\begin{aligned} U_p = & (U_0^e + U_0^w + U_0^n + U_0^s + U_0^u + U_0^d)/6 \\ & - (\delta t/4\delta x_1) [F_1(U_0^e) - F_1(U_0^w)] \\ & - (\delta t/4\delta x_2) [F_2(U_0^n) - F_2(U_0^s)] \\ & - (\delta t/4\delta x_3) [F_3(U_0^u) - F_3(U_0^d)] \\ & + (\delta t/2) K(U_0) \end{aligned} \quad (14)$$

and the corrector step

$$\begin{aligned} \mathbf{U} = \mathbf{U}_0 & \\ - (\delta t / 2\delta x_1) [\mathbf{F}_1(\mathbf{U}^e) - \mathbf{F}_1(\mathbf{U}^w)] \\ - (\delta t / 2\delta x_2) [\mathbf{F}_2(\mathbf{U}^n) - \mathbf{F}_2(\mathbf{U}^s)] \\ - (\delta t / 2\delta x_3) [\mathbf{F}_3(\mathbf{U}^u) - \mathbf{F}_3(\mathbf{U}^d)] \\ + (\delta t) \mathbf{K}(\mathbf{U}) \end{aligned} \quad (15)$$

At the end of the time step, an update $\mathbf{U}_0 = \mathbf{U}$ is needed to prepare for the next time step.

As a simple specific example of the parallel implementation of this algorithm, consider the numerical simulation of compressible hydrodynamics in a periodic cube subdivided into $48 \times 48 \times 48 = 110592$ cubical cells. Make a two-dimensional decomposition into $3 \times 3 = 9$ columns each consisting of $16 \times 16 \times 48 = 12288$ cells, and assign each column to one processor node. Owing to the compact nature of the finite difference stencil, each node only needs information from a border layer of cells in each of four neighboring nodes. The cell arrays on each node are expanded to $18 \times 18 \times 50 = 16200$ in order to include such outer border cells. The data for such outer border cells are obtained by an exchange between inner and outer border cells on adjacent nodes. Such data exchanges require internodal communication that is independent of the details of the numerical algorithm as long as it involves an explicit forward time step calculation based at most on a $3 \times 3 \times 3 = 27$ cell stencil.

The calculational time step cycle reduces then to a sequence of arithmetic evaluation sweeps interleaved with communication sweeps all done in parallel. The nature and timing of the sequence in an implementation of this simple example on the BBN TC2000 is shown as follows:

time cycle timing	sec
gaussian	
generate gaussian (18x18x50x3=48600)	3.8
exchange borders (4x18x50x3=10800)	0.1
predictor step	
compute fluxes (16x16x48x5x4=245760)	1.6
exchange borders (4x18x50x5x4=72000)	0.6
advance hydro (16x16x48x5=61440)	1.1
exchange borders (4x18x50x5=18000)	0.2
corrector step	
compute fluxes (245760)	1.6
exchange borders (72000)	0.6
advance hydro (61440)	0.8
exchange borders (18000)	0.2
update	0.1
total	10.7
total exchange	1.7

In parentheses are shown either the number of 64-bit results computed or the number of 64-bit words transmitted. For this calculation the computational speed per node is about one megaflop per second and the communication time is about 9 microseconds per word.

In the time cycle the first step produces a field of random gaussian g_k for which border values are then exchanged with neighbors in order to provide a consistent basis for the generation of the backscatter potentials ϕ_k as part of the flux calculations. The same g_k field is used for both the predictor and corrector step.

The extra price paid for the use of parallel computing is communication which in this example takes about 15% of the total time. For the domain-decomposition message-passing paradigm used here the scaling properties are quite simple. If, for example, we double each dimension of the cube to 96x96x96=884736 cells, and at the same time increase the node array to 6x6x36, so that there are now 16x16x96 cells on each node, both arithmetic time and communication time is doubled, and the ratio remains the same. If, on the other hand, for the larger cube we still use a 3x3x9 array of nodes, then the arithmetic time is increased by

8-fold whereas that for communication only by 4-fold. This reflects the surface to volume ratio benefit enjoyed by communication relative to arithmetic.

5. Outlook

Although the basic LES model has been tested against simple known solutions such as acoustic standing waves, it has not yet been applied to the study of turbulent mixing layers. Before a large investment in computing time is made for such studies, better visualization tools are needed, and this is where the present effort is focussed. Early studies are expected to be of a 3D version of the shear mixing layer calculations made earlier in 2D and of the buoyancy driven mixing layer induced by Rayleigh-Taylor instability. For this latter, an extension of the present subgrid-scale model to account for buoyancy sources of subgrid-scale turbulence will be used.

Acknowledgement

The staff of the LLNL Massively Parallel Computing Initiative provided outstanding support for this effort. Eugene Brooks, as leader of the Initiative, and Tammy Welcome, as developer of the Livermore Message Passing System, were particularly helpful. Paul Amala developed a single node version of the Lax-Wendroff scheme that was the starting point of the parallel version used here. This work was performed under the auspices of the U.S. Department of Energy by the Lawrence Livermore National Laboratory under Contract No. W-7405-ENG-48.

References

- Kraichnan, R. H., 1976: J. Atmos. Sci. **33**, 1521.
- Leslie, D. C. and G. L. Quarini, 1979: J. Fluid Mech. **91**, 65
- Leith, C. E., 1990: Phys. Fluids A **2**, 297.
- Leith, C. E., and R. H. Kraichnan, 1972: J. Atmos. Sci. **29**, 1041
- Philips, N. A., 1959: Rossby Memorial Volume, Rockefeller Institute Press, New York
- von Neumann, J., and R. D. Richtmyer, 1950: J. Appl. Phys. **21**, 232.
- Smagorinsky, J., 1963: Mon. Weather Rev. **91**, 99

Direct Numerical¹ Simulation and Large-Eddy Simulation of Compressible Turbulence.

G. Erlebacher

M.Y. Hussaini

*Institute for Computer Applications in Science and Engineering
NASA Langley Research Center, Hampton, VA 23665*

Extended Abstract for the International Workshop on "Large Eddy Simulations ... Where Do We Stand?" Held at St. Petersburg, Fl., Dec. 19-21, 1990.

Compressible turbulence is currently the subject of increased research in the fluid dynamics community. The experience accumulated over the last several decades in incompressible turbulence now serves as a starting point in the quest for understanding the basic physical mechanisms that differentiate compressible turbulence from its incompressible counterpart. To this end, ideas are freely borrowed from compressible transition research which has come a long way towards classifying the various modes and effects in compressible flows, albeit in the linear regime.

Although still very incomplete, our knowledge of incompressible turbulence was accumulated through a combination of experiments, theory and direct numerical simulation (DNS). Today, researchers are studying compressible turbulent flows using primarily DNS (Passot and Pouquet 1987, Erlebacher and Hussaini 1987, Orszag and Kida 1990, Blaisdell 1990, Lele, Lee and Moin 1990). Whenever possible, some theoretical justification of the results found in the numerical simulations is provided (Erlebacher et al. 1990, Sarkar et al. 1989). Past theoretical work on compressible turbulent flows concentrated mostly on modifications of incompressible scaling laws to include Mach number effects (Zakharov and Sagdeev 1970, Kadomtsev and Petviashvili 1973, Moiseev, Sagdeev, Tur and Yanovskii 1977, and L'vov and Mikhailov 1978). It is unlikely that the near future will bring about experiments detailed enough to confirm or reject some of these theories. However, with the explosion in supercomputer memory and speed, it is possible that DNS may soon provide some clues to spur theoretical research along the right direction.

In his seminal paper on supersonic turbulence, Kovasznay (1957) described the decomposition of compressible turbulence into acoustic, vortical and entropy modes. This interpretation of the eigenmodes of the flow has remained a beacon in the interpretation of results both in compressible turbulence and compressible transition research. The nonlinear interaction between these modes was considered by Chu and Kovasznay (1958). Another way to separate compressible and incompressible effects on the turbulence is to perform a Helmholtz decomposition on the velocity field (Moyal 1952, Passot and Pouquet 1987, Erlebacher et al. 1990, Sarkar et al. 1989, Lele, Yee and Moin 1990). Despite the progress made, much

more work is required before the "incompressible" and "compressible" characteristics of the turbulent flow are fully classified.

Direct numerical simulations have uncovered several regimes of isotropic turbulence which are now under study. An original classification was attempted by Passot and Pouquet (1987) when they uncovered the presence of either weak or strong shocks in the flow depending on the initial conditions. They found that strong shocks are present when the fluctuating Mach number (M_t) is $O(1)$, while weak shocklets can be present even for small M_t . On the other hand, Feiereisen et al. (1981) and Erlebacher et al. (1987) performed DNS of compressible turbulence (with $M_t = 0.5$) which had *almost* incompressible statistical properties. The reason was brought about a couple of years later by Erlebacher et al. (1990) who related the initial conditions of the flow to the characteristically different turbulent regimes. Since then, Kida and Orszag (1990) have considered both forced and unforced isotropic turbulence, and work has begun on homogeneous shear flow turbulence (Sarkar et al. 1990, Blaisdell 1990).

The ultimate objective of understanding turbulence physics (besides academic interest) is to model complex turbulent flows of practical importance with a view to predict certain gross properties of engineering interest. To this end, turbulence models must be developed since the Reynolds numbers of aerodynamic interest are much too high for direct numerical simulations on even today's fastest supercomputers. There are two standard approaches. The first approach replaces the Navier-Stokes equations by the Reynolds averages Navier-Stokes equations. The application of Reynolds stress models to compressible flows has a long history and will not be discussed in this paper. Reviews can be found in Cebeci and Smith (1974) and Speziale (1991).

The second approach is to decompose the flow field into its energy containing eddies (large scale), and the presumably universal small scale eddies. While the dynamics of the large scale eddies satisfy known evolution equations, there remain source terms, called subgrid-scale stress terms which must be modeled. This forms the basis of subgrid-scale modeling. Subgrid-scale models are expected to be more robust to different large-scale flow conditions than their Reynolds stress counterparts. The price to pay for this increased generality, is the higher expense.

It is still too early to consider Large-Eddy Simulations (LES) of compressible flows as an engineering tool. But if reliable models can be found, the large-eddy simulation databases can be used as a testbed against which the cheaper Reynolds stress models can be evaluated. This is pretty much the same relationship that exists between the DNS databases and the LES models (which of course must be tested before they are generally accepted).

In this paper, we consider the advances in both the Direct Numerical Simulation and in the Large Eddy Simulation of compressible turbulence. These subjects are treated together since the numerical techniques that are used to perform the simulations are identical for both types of problems. In fact the LES models are often incorporated into the DNS codes. To date, LES modeling of compressible turbulence is based less on theory, and more on

extensions of incompressible models to the compressible regime. As we demonstrate, these models, in the absence of shocks and/or shocklets, are quite capable of predicting reasonably well the decay rates of the turbulence and of the thermodynamics fluctuation rms levels. We conclude with some current issues that should be addressed in the near future. A discussion on recent LES advances can be found in Ferziger (1984).

The full paper will be provided in the final issue of the proceedings. In this extended abstract, many issues not mentioned will be addressed in the final manuscript.

1 DIRECT NUMERICAL SIMULATION

When one speaks of direct numerical simulations, one refers to the fully resolved solutions of the complete set of Navier-Stokes equations without any modeling. For reference, these equations are (in dimensional form)

$$\frac{\partial \rho}{\partial t} + \frac{\partial(\rho v_k)}{\partial x_k} = 0 \quad (1)$$

$$\frac{\partial(\rho v_k)}{\partial t} + \frac{\partial(\rho v_k v_l)}{\partial x_l} = - \frac{\partial p}{\partial x_k} + \frac{\partial \sigma_{kl}}{\partial x_l} \quad (2)$$

$$\frac{\partial(\rho h)}{\partial t} + \frac{\partial(\rho h v_k)}{\partial x_k} = \frac{\partial p}{\partial t} + v_k \frac{\partial p}{\partial x_k} + \frac{\partial}{\partial x_k} (\kappa \frac{\partial T}{\partial x_k}) + \Phi \quad (3)$$

respectively, where ρ is the mass density, \mathbf{v} is the velocity vector, p is the thermodynamic pressure, μ is the dynamic viscosity, h is the enthalpy, T is the absolute temperature, and κ is the thermal conductivity. The viscous stress σ_{kl} and the viscous dissipation Φ are defined by

$$\sigma_{kl} = - \frac{2}{3} \mu \frac{\partial v_j}{\partial x_j} \delta_{kl} + \mu \left(\frac{\partial v_k}{\partial x_l} + \frac{\partial v_l}{\partial x_k} \right) \quad (4)$$

$$\Phi = - \frac{2}{3} \mu \left(\frac{\partial v_j}{\partial x_j} \right)^2 + \mu \left(\frac{\partial v_k}{\partial x_l} + \frac{\partial v_l}{\partial x_k} \right) \frac{\partial v_k}{\partial x_l} \quad (5)$$

respectively. Equations (1)-(3) must be supplemented with the equations of state

$$P = \rho R T, \quad h = C_p T \quad (6)$$

for an ideal gas where R is the ideal gas constant and C_p is the specific heat at constant pressure. Likewise, the dependence of the viscosity and thermal conductivity on the temperature must be provided (i.e., relationships of the form $\mu = \mu(T)$ and $\kappa = \kappa(T)$ are needed and these depend on the gas under consideration). Typically Sutherland's law is appropriate for the viscosity when the medium is air. The Prandtl number is set to a constant by most investigators.

The majority of DNS of compressible turbulence have been concerned with homogeneous turbulence (either isotropic or homogeneous shear). In all cases, the boundary conditions

are periodic in all directions. Homogeneous shear flow simulations are rendered periodic through the Rogallo transformation (Rogallo 1981). For a long time, only spectral methods were considered accurate enough for the numerical solution to the full Navier-Stokes equations. This was due to the low dissipation and dispersion errors of the method, which are very desirable characteristics of the numerical algorithm when performing direct simulations. Indeed, one wishes to protect the structure of the smallest turbulent eddies from numerical dissipation and dispersion. If these eddies were smeared out by the numerics, the simulation would take the character of a large-eddy simulation which seeks to model the small-scale dissipation as a function of the large scale characteristics of the turbulence. Recently however, high order finite-difference methods (Lele 1990, Shu, Erlebacher, Zang and Osher 1991) are gaining acceptance in the DNS community. Tests at Langley confirm the high accuracy of the method when applied to turbulence calculations (Shu 1991). Moreover, the 6th order compact scheme is two times faster than the spectral algorithm when compared on identical numerical grids. However, except for the recent work of Lele, Lee and Moin (1990) on shock turbulence interaction, all investigators still opt for the Fourier collocation schemes (Canuto, Hussaini, Quarteroni and Zang 1988).

Passot and Pouquet (1987) use the non-conservative form of the momentum equations and the conservative enthalpy equation. All terms are treated explicitly, except for the viscous terms which are partially implicit. Time advancement is a combination of Crank-Nicolson and 3rd order Adams-Basforth. Erlebacher et al. (1987) considered initial conditions with very low turbulent Mach number, and therefore required a low error scheme capable of treating the acoustic terms implicitly. They use a time-split scheme. The first step integrates (with an explicit third-order Runge-Kutta scheme) the full equations with a set of linear acoustic terms subtracted off. In the second step, the remaining set of equations (linear) is solved exactly in Fourier space. Thus, large time steps do not sacrifice accuracy, since the proper acoustic behaviour is accounted for in the implicit step. The only errors incurred are the splitting error, and the error due to the (small) variation of the average sound speed during the implicit stage. The homogeneous shear flow simulations of Sarkar et al. (1989) are currently fully explicit.

Feiereisen (1981) was the first to perform DNS of compressible homogeneous turbulence. He pointed out potential problems which could occur if the convective terms were not discretized properly. He advocated that the convective terms be rewritten in the form

$$\frac{1}{2} \left[\frac{\partial(\rho v_k v_l)}{\partial x_l} + \rho v_l \frac{\partial v_k}{\partial x_l} + v_k \frac{\partial(\rho v_l)}{\partial x_l} \right]. \quad (7)$$

As noted by Feiereisen, Reynolds and Ferziger (1981), when this form is employed together with a symmetric differencing method in space (for example Fourier collocation), then in addition to mass, and momentum, energy is also conserved for the ideal compressible equations (zero viscosity and thermal conductivity) in the absence of time differencing (and splitting) errors. Fornberg (1975) discusses the conditions under which the non-symmetric form of the convective equations maintains numerical stability. Recently, numerical simulations of supersonic boundary-layer flows undergoing laminar to turbulent transition have

demonstrated the unstable nature of both the conservation form ($\frac{\partial}{\partial x_j} \rho v_i v_j$) and the non-conservative forms ($\rho v_i \frac{\partial v_j}{\partial x_j}$) using a spectral collocation algorithm. Stability was achieved with the expression (7). Note that the alternative form

$$\frac{1}{2} \left[\frac{\partial(\rho v_k v_l)}{\partial x_l} + \rho v_k \frac{\partial v_l}{\partial x_l} + v_l \frac{\partial(\rho v_k)}{\partial x_l} \right] \quad (8)$$

is also subject to instabilities. The reasons are not known. In a recent paper, Zang (1988) discusses the relative merits of the different forms that can be taken by the convective operator in incompressible flows. He conclude that aliasing errors decrease substantially when the skew-symmetric is used instead of either the rotational form or the non-conservative form. However, he does not demonstrate an actual instability similar to the one recently observed in the supersonic transition simulations.

1.1 Initial Conditions

Different initial conditions have been used by different investigators. Often, they can be traced back to their roots in incompressible flow simulations. This is clearly the origin of the initial conditions used by Feiereisen et al. (1981) and Erlebacher et al. (1987). Both sets of authors chose a divergence-free initial velocity field, and computed the initial pressure to insure that the time-derivative of the divergence of velocity also be zero initially. Furthermore, the initial fluctuating density rms was zero. As explained by Erlebacher et al. (1990), these conditions lead to a very slow build-up of the compressibility effects on a convective $O(1)$ time scale. If one relaxes the condition that the initial time derivative of $v_{i,i}$ be zero, and specify instead random fluctuations for pressure, the flow will reach a quasi-equilibrium on an $O(M_t)$ time scale instead.

More general initial conditions are considered by Passot and Pouquet (1987), and adopted by Erlebacher et al. (1990). These allow the generation of weak and strong shocks, or simply the existence of acoustic waves of prescribed strength superimposed on an essentially nonlinear incompressible flow field. These initial conditions are based on a Helmholtz decomposition of the velocity field:

$$u = u^I + u^C \quad (9)$$

where u^I, u^C are respectively the solenoidal and irrotational components of velocity. At $t = 0$, the reference turbulent Mach number M_{t0} , the Reynolds number, Re , the Prandtl number, Pr , the rms levels of $u_0^C, u_0^I, \rho_0, T_0$, and the autocorrelation spectrum for ρ, T, u^C and u^I are imposed. The zero subscript refers to the initial state. The energy spectrum of the density, temperature and velocity fluctuations are all given by

$$E(k) = k^4 e^{-\frac{2k^2}{k_0^2}} \quad (10)$$

where k_0 corresponds to the spectrum peak. Strictly speaking the initially irrotational component of velocity should have an autocorrelation spectrum proportional to k^2 for low k to guarantee analyticity (Batchelor 1953). However, Erlebacher et al. (1990) did not feel that this would qualitatively influence the numerical results.

1.2 Results

In this section we present an abbreviated section on some fundamental results found in the last couple of years by DNS of compressible turbulence. A more complete version of this section will appear in the full paper.

Passot and Pouquet performed 2-D and 3-D DNS of compressible isotropic turbulence on 256^3 and 64^3 grids and were able to produce both weak and strong shocks. The presence or absence of the shocks was controlled solely by the initial conditions, whose influence can never completely vanish in decaying isotropic flow. They found three separate regimes. The weak Mach number regime ($M_t < 0.3$) has two sub-components. If $\delta\rho/\rho \leq M_t^2$, the flow remains quasi-incompressible for all time. However, if $\delta\rho/\rho > M_t^2$, even by a small amount, the flow switches to a state which is mostly irrotational. Under these conditions weak shocks (negligible entropy jumps) can appear which propagate at the velocity of sound across the domain. The third regime is the strong shock regime characterized by $M_t = O(1)$. Passot and Pouquet considered the decay laws of their spectra compared to that of predicted by various theories. Results were inconclusive, mainly because the simulations are still not capable of producing an inertial range. They also find that in the strong shock regime, there is a strong influence of the baroclinic torque in the vicinity of the shocks (for 2-D flows). In these cases, the $\nabla\rho$ and ∇p were found to be nearly perpendicular.

Erlebacher et al. (1990) were primarily concerned with the weak shock regime treated by Passot and Pouquet (1987). They sought to explain and quantify rigorously the relationship between initial conditions and the subsequent evolution of turbulence. While it is a widely accepted fact that in the absence of shocks, compressible turbulence is the superposition of a nonlinear incompressible turbulent flow and of linear acoustic waves isotropically distributed, it was never made clear under what conditions such flows were actually realized. By a careful asymptotic analysis, Erlebacher et al. (1987) found that the presence of weak shocks is linked to initial flow conditions which were out of acoustic equilibrium. More precisely they determined that in the absence of shocks, the flow evolves towards a state where the compressible potential energy and the irrotational kinetic energy are in equipartition (see also Sarkar et al. 1989). If the initial conditions violate this equipartition in the direction of higher potential energy, weak shocks will occur. From a practical standpoint, this situation can arise for the initial conditions: $M_t = 0.04$, $p_{rms} = 10\%$, and $\chi = 0.1$ where χ is the ratio of irrotational to solenoidal kinetic energy.

The compressible simulations of Kida and Orszag (1990b) highlight some interesting differences with Passot and Pouquet (1987). For example, Kida and Orszag find that in

3-D decaying turbulence, $\nabla \rho$ and ∇p are almost aligned in strong shock regions. These alignment properties in two-dimensional and three-dimensional turbulence are not currently explained. In the three-dimensional simulations, they find that the production of vorticity is dominated (overall) by the vortex stretching and the dissipation terms. However, in the shock regions, the compression and baroclinic terms produce vorticity, while the dissipation term depletes it.

2 Large-Eddy Simulation

The large-eddy simulations are based on the following Favre-filtered continuity, momentum, and energy equations (Speziale 1988):

$$\frac{\partial \bar{\rho}}{\partial t} + \nabla \cdot (\bar{\rho} \bar{u}) = 0 \quad (11)$$

$$\begin{aligned} \frac{\partial}{\partial t}(\bar{\rho} \bar{u}) + \nabla \cdot (\bar{\rho} \bar{u} \bar{u}) &= -\nabla \bar{p} + \nabla \cdot \bar{\sigma} + \nabla \cdot \tau \\ \frac{\partial}{\partial t}(C_v \bar{\rho} \tilde{T}) + \nabla \cdot (C_v \bar{\rho} \bar{u} \tilde{T}) &= -\bar{p} \nabla \cdot \bar{u} + \bar{\sigma} \cdot \nabla \bar{u} + \nabla \cdot \kappa \nabla \tilde{T} - \nabla \cdot Q \end{aligned} \quad (12)$$

where R is the ideal gas constant, C_v is the specific heat at constant volume, τ is the subgrid scale stress tensor, Q is the subgrid scale heat flux, and I is the identity tensor. In Eqs. (11)-(12), an overbar represents a spatial filter whereas a tilde represents a mass weighted or Favre filter, i.e.

$$\tilde{\mathcal{F}} = \frac{\bar{\rho} \mathcal{F}}{\bar{\rho}} \quad (13)$$

where \mathcal{F} is any flow variable. These equations are obtained by applying a Gaussian filter to the full Navier-Stokes equations. The subgrid scale stress tensor and subgrid scale heat flux are modeled as follows (Speziale et al. 1988 and Erlebacher et al. 1990):

$$\tau = -\bar{\rho}(\tilde{\bar{u}\bar{u}} - \bar{u}\bar{u}) + 2C_R \bar{\rho} \Delta_f^2 II_S^{1/2} (\tilde{\bar{S}} - \frac{1}{3}(\tilde{\bar{S}} : I) I) - \frac{2}{3}C_I \bar{\rho} \Delta_f^2 II_S I \quad (14)$$

$$Q = C_v \bar{\rho}(\tilde{\bar{u}\tilde{T}} - \tilde{\bar{u}}\tilde{T} - \frac{C_R}{Pr_T} \Delta_f^2 II_S^{1/2} \nabla \tilde{T}) \quad (15)$$

where $II_S \equiv \tilde{\bar{S}} : \tilde{\bar{S}}$, Δ_f is the filter width, and C_R and C_I are constants which assume the values of 0.012 and 0.0066, respectively. The turbulent Prandtl number Pr_T is taken to be 0.7. In the incompressible limit, the subgrid scale stress model (14) reduces to the linear combination model of Bardina et al (1983). The solution technique is essentially the numerical method discussed in Erlebacher et al. (1990) modified to account for the eddy viscosity term.

This subgrid-scale model was tested both by Erlebacher et al. (1990) and Zang et al. (1990). They compared the results of 96^3 DNS of isotropic decaying compressible turbulence

with the results of LES on 32^3 grids. The initial conditions were spectrally interpolated from the DNS results after the first peak in the time history of total enstrophy. Results show that the subgrid-scale model is capable of correctly predicting the decay rates of kinetic energy (both compressible and solenoidal), and of the thermodynamic variables (ρ, T, p).

DNS were also performed on 32^3 grids to directly measure the effect the subgrid-scale model. Furthermore, runs were made to establish the sensitivity of the subgrid statistics on the actual values of the model constants. To this end, they were varied up to 50% above and below their nominal values. It was found that such variations can influence the modeled flow characteristics substantially. Therefore, the actual functional form of the LES model are an important consideration, even for this simple flow. The effect of filter width on the LES was also studied.

3 Conclusions

We are today at the threshold of a new beginning in the understanding compressible turbulent flows. One can only hope that the interest expressed by the fluid dynamics community and the industry at large will continue on its present track.

It is clear that there are many questions that remain unanswered, and many controversies yet to come. The following ten years promise to be very exciting for anyone actively involved in the field of compressible turbulence research.

References

- Bardina, J.; Ferziger, J.H.; and Reynolds, W.C. 1983 - Improved Turbulence Models Based on Large-Eddy Simulation of Homogeneous, Incompressible Turbulent Flows. Stanford University Technical Report, TF-19.
- Blaisdell, G. 1990 - Numerical Simulation of Compressible Homogeneous Turbulence. Ph.D Thesis, Stanford University.
- Canuto, C.; Hussaini, M. Y.; Quarteroni, A.; and Zang, T. A. 1988 - *Spectral Methods in Fluid Dynamics*, Springer-Verlag, Berlin.
- Cebeci, T.; and Smith, A.M.O. 1974 - *Analysis of Turbulent Boundary Layers*. New York: Academic Press.
- Chu, B.T.; and Kovasznay, L.S.G. 1958 - Nonlinear Interactions in a Viscous Heat-Conducting Compressible Gas. *J. Fluid Mech.* 3, 494.
- Erlebacher, G.; Hussaini, M.Y.; Speziale, C.G.; and Zang, T.A. 1990 - Toward the Large-Eddy Simulation of Compressible Turbulent Flows. ICASE Report No. 90-76.

- Erlebacher, G; Kreiss, H.O.; Sarkar, S. and Hussaini, M.Y. 1990 - The Analysis and Simulation of Compressible Turbulence. *Theor. and Comput. Fluid Dyn.*, to appear.
- Erlebacher, G.; Hussaini, M.Y.; Speziale, C.G.; and Zang, T.A. 1990 - On the large-eddy simulation of compressible turbulence. Proceedings of the 12th International Conference of Numerical Methods in Fluid Dynamics, University of Oxford.
- Feiereisen, W. J.; Reynolds, W. C. and Ferziger, J. H. 1981 - Numerical Simulation of Compressible, Homogeneous, Turbulent Shear Flow. Report TF-13, Dept. Mech. Eng., Stanford University.
- Ferziger, J.H. 1984 - Large Eddy Simulation: Its Role in Turbulence Research. In *Theoretical Approaches to Turbulence*, edited by D.L. Dwyer, M.Y. Hussaini, and R.G. Voigt (Springer Verlag, New York).
- Fornberg, B. 1975 - On a Fourier Methods for the Integration of Hyperbolic Equations. *Siam J. Numer. Anal.* 12, No. 4, pp. 509-528.
- Kadomtsev, B.B.; and Petviashvili, V.I. 1973 - Acoustic Turbulence. *Sov. Phys. Dokl.* 18, 115.
- Kida, S.; and Orszag, S. 1990a - Energy and Spectral Dynamics in Forced Compressible Turbulence. In press.
- Kida, S.; and Orszag, S. 1990b - Enstrophy Budget in Decaying Compressible Turbulence. In press.
- Kovasznay, L.S.G 1957 - Turbulence in Supersonic Flows. *J. Aero. Sciences* 20, No. 10, 657-682.
- Lele, S. K. 1990 Compact Finite-Difference Schemes with Spectral-like Resolution. Submitted to *Journal of Computational Physics*. ????====
- Lele, S.K.; Lee, S.; and Moin, P. 1990 - Compressible Turbulence and Shock Waves. Presented at the Lumley Symposium: Recent Developments in Turbulence, held in Hampton, Va. Nov. 12-13, 1990.
- L'vov, V.S.; and Mikhailov, A.V. 1978a - Sound and Hydrodynamic Turbulence in a Compressible Liquid. *Sov. Phys. J. Exp. Theor. Phys.* 47, 756.
- L'vov, V.S.; and Mikhailov, A.V. 1978b - Scattering and Interaction of Sound with Sound in a Turbulent Medium. *Sov. Phys. J. Exp. Theor. Phys.* 47, 840.
- Moiseev, S.S.; Sagdeev, R.Z.; Tur, A.V.; and Yanovskii, V.V. 1977 - Structure of Acoustic-Vortical Turbulence. *Sov. Phys. Dokl.* 22, 582.
- Moyal, J.E. 1952 - The Spectra of Turbulence in a Compressible Fluid; Eddy Turbulence and Random Noise. *Proc. of the Cambridge Phil. Soc.*, 48, part 1, 329-344.

- Passot, T.; and Pouquet, A. 1987 - Numerical Simulation of Compressible Homogeneous Flows in the Turbulent Regime. *J. Fluid Mech.* **181** 441-466.
- Rogallo, S. 1981 - Numerical Experiments in Homogeneous Turbulence. *NASA TM-81315*.
- Sarkar, S.; Erlebacher, G.; Hussaini, M.Y.; and Kreiss, H.O. 1989 - The Analysis and Modeling of Dilatational Terms in Compressible Turbulence. *ICASE Report No. 89-79*.
- Shu, C-W; Erlebacher, G.; Zang, T.A.; and Osher, S. - 1991 High Order ENO Schemes Applied to Two and Three Dimensional Compressible Euler and Navier-Stokes Equations. To be published.
- Speziale, C.G. 1991 - Analytical Methods for the Development of Reynold-Stress Closures in Turbulence. *Annual Review of Fluid Mechanics*, **23**, 107-157.
- Speziale, C.G.; Erlebacher, G.; Zang, T.A.; and Hussaini, M.Y. 1988 - The subgrid scale modeling of compressible turbulence. *Phys. Fluids* **31**, 940-942.
- Yoshizawa, A. 1986 - Statistical Theory for Compressible Turbulent Shear Flows, with the Application to Subgrid Modeling, *Phys. Fluids* **29**, 2152-2164.
- Zakharov, V.E.; and Sagdeev, R.Z. 1970 - Spectrum of Acoustic Turbulence. *Sov. Phys. Dokl.* **15**, 439.
- Zang, T.A; Dahlburg, R.B.; and Dahlburg, J.P. 1990 Direct and Large-Eddy Simulations of Compressible, Isotropic Navier-Stokes Turbulence. *NASA TP*, in press.

LARGE-EDDY SIMULATIONS OF COMPRESSIBLE MIXING LAYERS

Saad A. Ragab

Department of Engineering Science and Mechanics
Virginia Polytechnic Institute and State University
Blacksburg, VA 24061.

1. INTRODUCTION

The large-eddy simulations technique is pursued as a promising method for the prediction of flows of technological and scientific interest. Successful applications of LES to flows of engineering interest demand developing and testing proper subgrid-scale models and adapting high-order finite-difference methods to complex geometries.

Our effort is concentrated on evaluating the performance of different subgrid-scale models for compressible turbulence, and on developing finite-difference methods for large eddy-simulations.

In this paper we present preliminary results obtained for a temporally developing mixing layer. The linear combination model developed by Bardina et al [1] for incompressible flows and generalized to compressible flows by Erlebacher et al [2] (see also Speziale [3]) is used in this study. The eddy viscosity coefficient is determined from the Smagorinsky formula. The numerical method is an explicit fourth-order finite-difference method developed by Gottlieb and Turkel [4]. This method has been used by Tang et al [5,6] for the direct simulations of the instabilities of supersonic mixing layers.

2. EQUATIONS OF COMPRESSIBLE LARGE-EDDY SIMULATIONS

Using standard notation, the compressible Navier-Stokes equations are

$$\frac{\partial \rho}{\partial t} + \frac{\partial}{\partial x_j} (\rho u_j) = 0 \quad (1)$$

$$\frac{\partial}{\partial t} (\rho u_i) + \frac{\partial}{\partial x_j} (\rho u_i u_j + p \delta_{ij} - \tau_{ji}) = 0 \quad (2)$$

$$\frac{\partial}{\partial t} (\rho E) + \frac{\partial}{\partial x_j} [(\rho E + p) u_j - u_i \tau_{ji} + q_j] = 0 \quad (3)$$

where E is the total energy per unit of mass,

$$E = e + \frac{1}{2} u_i u_i \quad (4)$$

τ_{ij} is the viscous stress tensor,

$$\tau_{ij} = \lambda \frac{\partial u_k}{\partial x_k} \delta_{ij} + \mu \left(\frac{\partial u_i}{\partial x_j} + \frac{\partial u_j}{\partial x_i} \right) \quad (5)$$

and q_j is the heat-flux vector,

$$q_j = -\kappa \frac{\partial T}{\partial x_j} \quad (6)$$

A perfect gas with constant specific heats c_v and c_p is assumed, hence the equations of state are

$$e = c_v T \quad (7)$$

and

$$p = R \rho T \quad (8)$$

The resolvable flow field is defined by

$$\bar{f}(\mathbf{x}, t) = \int_D G(\mathbf{x} - \boldsymbol{\xi}) f(\mathbf{x}, t) d\boldsymbol{\xi} \quad (9)$$

where D is the flow domain, and G is a function that satisfies the normalization condition:

$$\int_D G(\mathbf{x} - \boldsymbol{\xi}) d\boldsymbol{\xi} = 1 \quad (10)$$

It is assumed that the function G is such that filtering and differentiation with respect to space and time commute, hence

$$\overline{\frac{\partial f}{\partial t}} = \frac{\partial \bar{f}}{\partial t} \quad (11)$$

$$\overline{\frac{\partial f}{\partial x_j}} = \frac{\partial \bar{f}}{\partial x_j} \quad (12)$$

Following Erlebacher et al [2], we introduce the Favre-filtered field,

$$\tilde{f} = \bar{\rho} \bar{f} / \bar{\rho} \quad (13)$$

and decompose the total flow field into a resolvable flow field and a subgrid-scale flow field,

$$f = \tilde{f} + f' \quad (14)$$

Note that, in general,

$$\tilde{f} \neq \bar{f} \quad (15)$$

and

$$\tilde{f}' \neq 0 \quad (16)$$

Filtering the mass and momentum equations, we obtain

$$\overline{\frac{\partial \bar{\rho}}{\partial t}} + \frac{\partial}{\partial x_j} (\bar{\rho} \tilde{u}_j) = 0 \quad (17)$$

and

$$\frac{\partial}{\partial t} (\bar{\rho} \tilde{u}_i) + \frac{\partial}{\partial x_j} (\bar{\rho} \tilde{u}_i \tilde{u}_j + \bar{p} \delta_{ij} + R_{ij} + L_{ij} + C_{ij} - \bar{\tau}_{ji}) = 0 \quad (18)$$

where

$$R_{ij} = \bar{\rho} \tilde{u}'_i \tilde{u}'_j \quad (19)$$

$$L_{ij} = \bar{\rho} (\tilde{u}_i \tilde{u}_j - \tilde{u}_i \tilde{u}_j) \quad (20)$$

$$C_{ij} = \bar{\rho} (\tilde{u}_i \tilde{u}'_j + \tilde{u}_j \tilde{u}'_i) \quad (21)$$

are referred to as the Reynolds-stress, Leonard-stress, and cross-stress terms. The filtered pressure is given by

$$\bar{p} = R \bar{\rho} \bar{T} \quad (22)$$

Filtering the energy equation, we obtain

$$\frac{\partial}{\partial t} (\bar{\rho} \tilde{E} + q) + \frac{\partial}{\partial x_j} [(\bar{\rho} \tilde{E} + \bar{p}) \tilde{u}_j + K_j + Q_j - \bar{u}_i \bar{\tau}_{ji} + \bar{q}_j] = 0 \quad (23)$$

where

$$\tilde{E} = \tilde{e} + \frac{1}{2} \tilde{u}_i \tilde{u}_i \quad (24)$$

$$q = \frac{1}{2} (R_{kk} + L_{kk} + C_{kk}) \quad (25)$$

$$K_j = \frac{1}{2} \bar{\rho} (\tilde{u}_i \tilde{u}_i \tilde{u}_j - \tilde{u}_i \tilde{u}_i \tilde{u}_j + \tilde{u}'_i \tilde{u}'_i \tilde{u}_j + \tilde{u}_i \tilde{u}'_i \tilde{u}_j + \tilde{u}'_i \tilde{u}'_i \tilde{u}_j + 2 \tilde{u}'_i \tilde{u}_i \tilde{u}_j + 2 \tilde{u}'_i \tilde{u}_i \tilde{u}'_j) \quad (26)$$

$$Q_j = c_p \bar{\rho} (\bar{T}' \tilde{u}'_j + \tilde{T} \tilde{u}_j - \tilde{T} \tilde{u}_j + \bar{T}' \tilde{u}_j + \tilde{T} \tilde{u}'_j) \quad (27)$$

3. A SUBGRID-SCALE MODEL

Here, we summarize the subgrid-scale model of Erlebacher et al [2] (see also Speziale et al [3]). This model is an extension to compressible flows of a linear-combination model developed by Bardina et al [1] for incompressible flows.

The Leonard-stress term needs no modelling, while the cross-stress term is modelled by a scale similarity model,

$$C_{ij} = \bar{\rho} (\tilde{u}_i \tilde{u}_j - \tilde{u}'_i \tilde{u}'_j) \quad (28)$$

Therefore, the sum of the two terms can be written as

$$L_{ij} + C_{ij} = \bar{\rho} (\tilde{u}_i \tilde{u}_j - \tilde{u}'_i \tilde{u}'_j) \quad (29)$$

The Reynolds-stress term is modelled by an eddy-viscosity model where the eddy-viscosity coefficient is given by the Smagorinski formula,

$$R_{ij} = -2C_R \Delta^2 \bar{\rho} \sqrt{\Pi} (\tilde{S}_{ij} - \frac{1}{3} \tilde{S}_{kk} \delta_{ij}) - \frac{2}{3} C_I \Delta^2 \bar{\rho} \Pi \delta_{ij} \quad (30)$$

where

$$\tilde{S}_{ij} = \frac{1}{2} \left(\frac{\partial \tilde{u}_i}{\partial x_j} + \frac{\partial \tilde{u}_j}{\partial x_i} \right) \quad (31)$$

is the rate of strain tensor of the resolvable flow field, and

$$\Pi = \tilde{S}_{ij} \tilde{S}_{ij} \quad (32)$$

In Eq(30), Δ is the filter width.

The temperature-velocity correlation terms are modelled as follows:

$$\tilde{T}' u'_j = -C_T \Delta^2 \sqrt{\Pi} \frac{\partial \tilde{T}}{\partial x_j} \quad (33)$$

that is a gradient-transport model, and

$$\tilde{T}' \tilde{u}_j + \tilde{T} u'_j = \tilde{T} \tilde{u}_j - \tilde{T} \tilde{\tilde{u}}_j \quad (34)$$

that is a scale similarity model. Substituting Eqs (34) and (35) into Eq(27), we obtain

$$Q_j = c_p \bar{\rho} (-C_T \Delta^2 \sqrt{\Pi} \frac{\partial \tilde{T}}{\partial x_j} + \tilde{T} \tilde{u}_j - \tilde{T} \tilde{\tilde{u}}_j) \quad (35)$$

where the constant C_T is written as

$$C_T = C_R / Pr_T \quad (36)$$

and Pr_T is a turbulent Prandtl number.

We model the third and last term in Eq(26) as

$$\bar{\rho} \overline{u'_i \tilde{u}_j u'_j} \approx \bar{\rho} \overline{u'_i u'_j} \tilde{u}_i = R_{ij} \tilde{u}_i \quad (37)$$

where R_{ij} is given by Eq(30). We note that the first two terms of Eq(26) can be computed directly, whereas a scale similarity model may be used for the remaining three terms.

In the present preliminary investigation, we neglected all the terms in Eq(26) except the last term for which we used Eq(37). Also, we neglected the q term in Eq(24) and the Leonard and cross terms. Because free shear layers are treated in this paper, the viscous and the heat conduction terms are also neglected.

4. RESULTS

Temporal simulations are obtained for compressible mixing layers at a convective Mach number of 0.4 and density ratio of 1. The initial mean velocity profile is assumed to be a hyperbolic tangent profile, $u = U_0 \tanh(y/\delta)$, where U_0 and δ are used as reference velocity and length throughout the simulations. The mean temperature profile is obtained from the Busemann-Crocco energy equation, and the mean pressure is assumed to be uniform. Disturbance fields are then superimposed on these mean profiles. In the first case of a two-dimensional simulation, the velocity disturbance field is a white-noise divergence-free field. No density or pressure disturbances are used. In the second case of a three-dimensional simulation, the disturbance fields are specified by the eigenfunctions of the linear stability theory.

4.1 Two-Dimensional Simulations

According to the linear stability theory, the most amplified 2D wave has a wave-number of 0.4, and hence the corresponding wave length is $\lambda=5\pi$. To be able to predict the pairing phenomena, we choose a computational box that extends 4λ in the streamwise direction, and over the range $-30 \leq y \leq +30$ in the transverse direction. A uniform grid of (257,301) points is used. Periodic boundary conditions are imposed in the x-direction, and zero derivative boundary conditions are imposed in the y-direction.

A Fourier analysis in the x-direction is performed at selected time steps, and the modal energy,

$$E_k(t) = \int_{y_{\min}}^{y_{\max}} (\widehat{uu}^* + \widehat{vv}^*)_k dy \quad (38)$$

is computed, where k is the mode number.

The initial spectrum of E_k is shown in Fig(1); a white-noise spectrum is evident. As time progresses, the most amplified wave ($k=4$) extracts energy from the mean flow and dominates the large scale structure of the mixing layer. This is clearly evident in Fig.(2) which shows vorticity contours at time $t = 51.2 (\delta/U_0)$. The corresponding modal energy spectrum is shown in Fig.(3). As this mode saturates, the first subharmonic mode ($k=2$) grows and becomes the most energetic mode. This mode is responsible for the first pairing that is shown by the vorticity contours at time $t = 83.2 (\delta/U_0)$ in Fig. (4). The energy spectrum at this time is shown in Fig. (5). At a much later time, $t = 128 (\delta/U_0)$, the second subharmonic ($k=1$) becomes the most energetic mode, and a second pairing appears in the vorticity contours as shown in Fig. (6) and Fig. (7) of the modal energy. We also note that the spectra shown in Figs. (3), (5), and (7) suggest that the energy-containing eddies follow a power law of exponent of (-4). Such a power law has been reported by Lesieur et al [7] in their 2D large-eddy simulations of an incompressible mixing layer.

4.2 Three-Dimensional Simulations

The second case of simulation is a temporal 3D mixing layer. The computational box extends over 2λ in both the streamwise and spanwise directions, and covers the range $-15 \leq y \leq +15$ in the transverse direction. A uniform grid of (65,151,65) points is used. Periodic boundary conditions are imposed in the x- and z- directions, and zero derivative boundary conditions are imposed in the y-direction.

In this case, the initial fields are given by the linear superposition of the hyperbolic tangent profile, the most amplified 2D and 3D waves and their first subharmonics and superharmonics. A Fourier analysis in the x-z plane is performed at every time step, and the modal kinetic energy

$$E_{mn}(t) = \int_{y_{min}}^{y_{max}} (\hat{u}\hat{u}^* + \hat{v}\hat{v}^* + \hat{w}\hat{w}^*)_{mn} dy \quad (39)$$

is computed, where m and n are the mode numbers in the streamwise and spanwise directions, respectively, of the Favre-averaged velocity field. The time development of this energy for different modes is shown by Figs. 8-10. Evident in Fig. 8 is the dominance of the two-dimensional mode (1,0) which saturates at time $t = 60$. In Fig. 9, we see that the most important 3D mode is the (1,1) mode which gives the streamwise vorticity.

At time $t=75$, the spectrum $E(m,n)$ is shown in Fig. 11 as a function of m for different n , and in Fig. 12 as a function of n for different m. These figures suggest a power law of the energetic eddies with slopes between -3 and -4.

ACKNOWLEDGEMENTS

We thank Professor L. Sankar, Georgia Institute of Technology, for providing us with a copy of his direct simulation computer code. This work is supported by the Office of Naval Research under Grant No. N00014-89-J-1544.

REFERENCES

- [1] Bardina, J., Ferziger, J. H., and Reynolds, W. C., (1983), "Improved subgrid-scale models based on large-eddy simulation of homogeneous, incompressible, turbulent flows," Stanford Report No. TF-19, Stanford.
- [2] Erlebacher, G., Hussaini, M. Y., Speziale, C. G., and Zang, T. A., (1987), "Toward the large-eddy simulation of compressible turbulent flows," ICASE Report No. 87-20.
- [3] Speziale, C. G., Erlebacher, G., Zang, T. A., and Hussaini, M. Y., (1987), "The subgrid-scale modeling of compressible turbulence," The Physics of Fluids, Vol. 31, No. 4, April 1988, pp. 940-942.
- [4] Gottlieb, D. and Turkel E., "Dissipative two-four methods for time-dependent problems," Math. Compt., vol. 30, No. 136, 1976, pp. 703-723.
- [5] Tang, W., Komerath, N., and Sankar, L., "Numerical simulation of the growth of instabilities in supersonic free shear layers," AIAA Paper No. 89-0376, January 1989.
- [6] Tang, Sankar, L., and Komerath, N., "Mixing enhancement in supersonic free shear layers," AIAA Paper No. 89-0981, March 1989.
- [7] Lesieur, M., Staquet, C., Le Roy, P., and Comte, P., "The mixing layer and its coherence examined from the point of view of two-dimensional turbulence," J. Fluid Mech., vol. 192, July 1988, pp. 511-534.

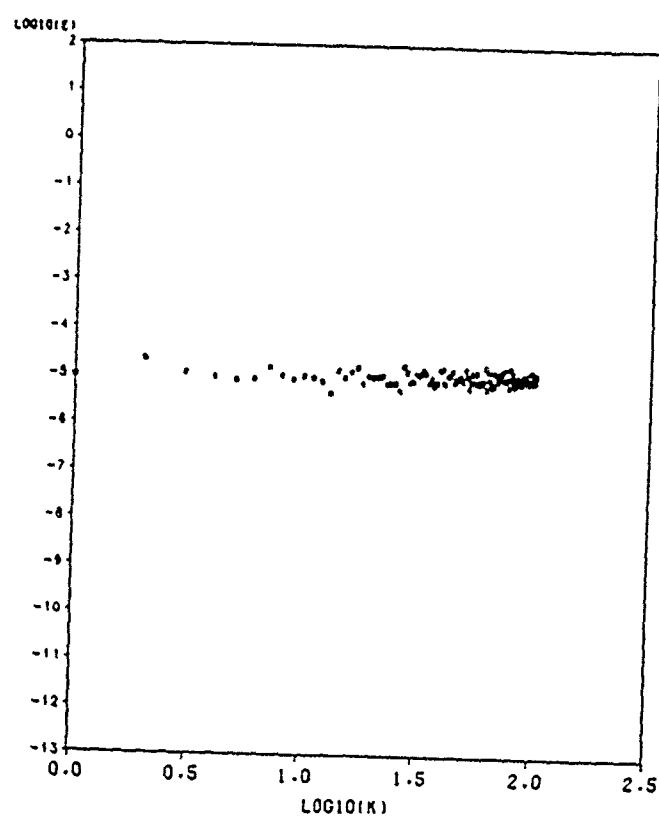


Fig. (1) Modal energy spectrum at $t=0$, two-dimensional simulation.

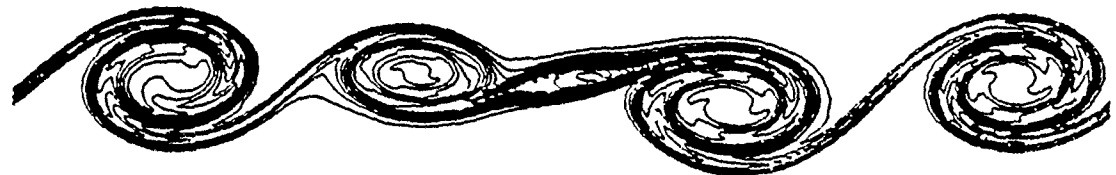


Fig. (2) Vorticity contours at $t = 51.2 (\delta/U_0)$, two-dimensional simulation.

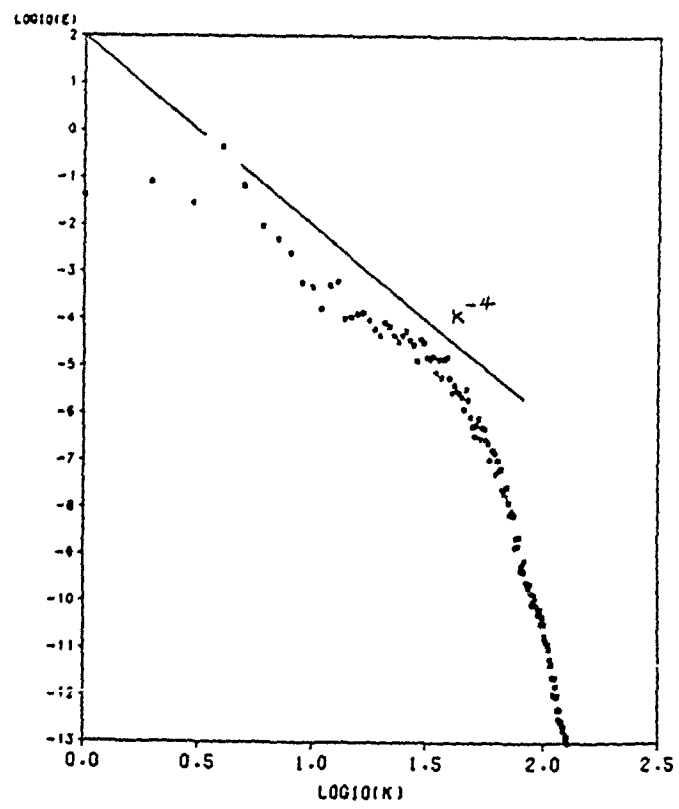


Fig. (3) Modal energy spectrum at $t = 51.2 (\delta/U_0)$, two-dimensional simulation.

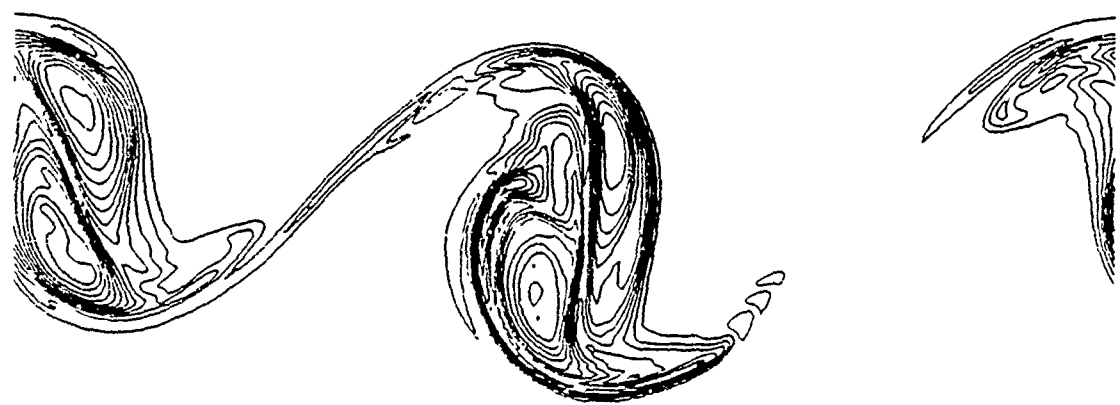


Fig. (4) Vorticity contours at $t = 83.2 (\delta / U_0)$, two-dimensional simulation.

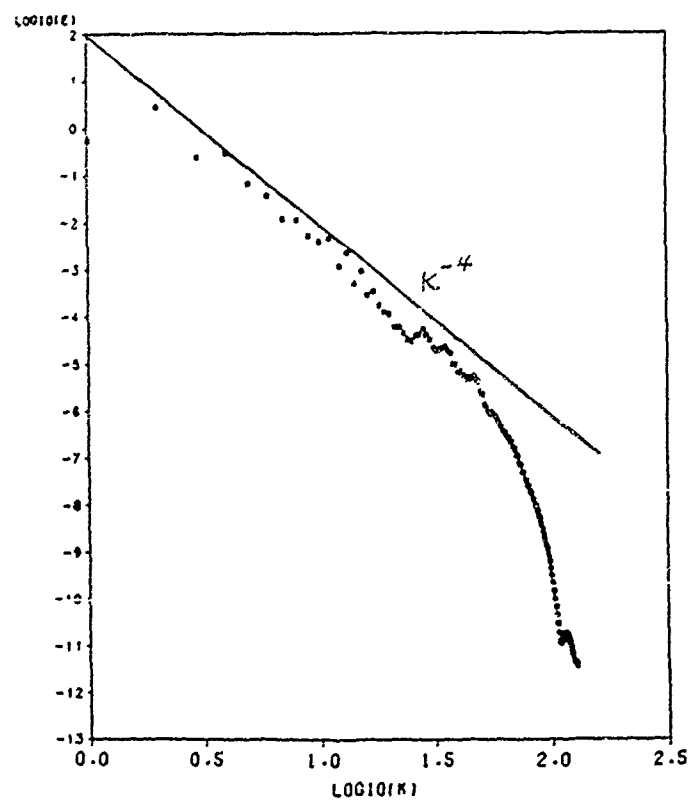


Fig. (5) Modal energy spectrum at $t = 83.2 (\delta / U_0)$, two-dimensional simulation.

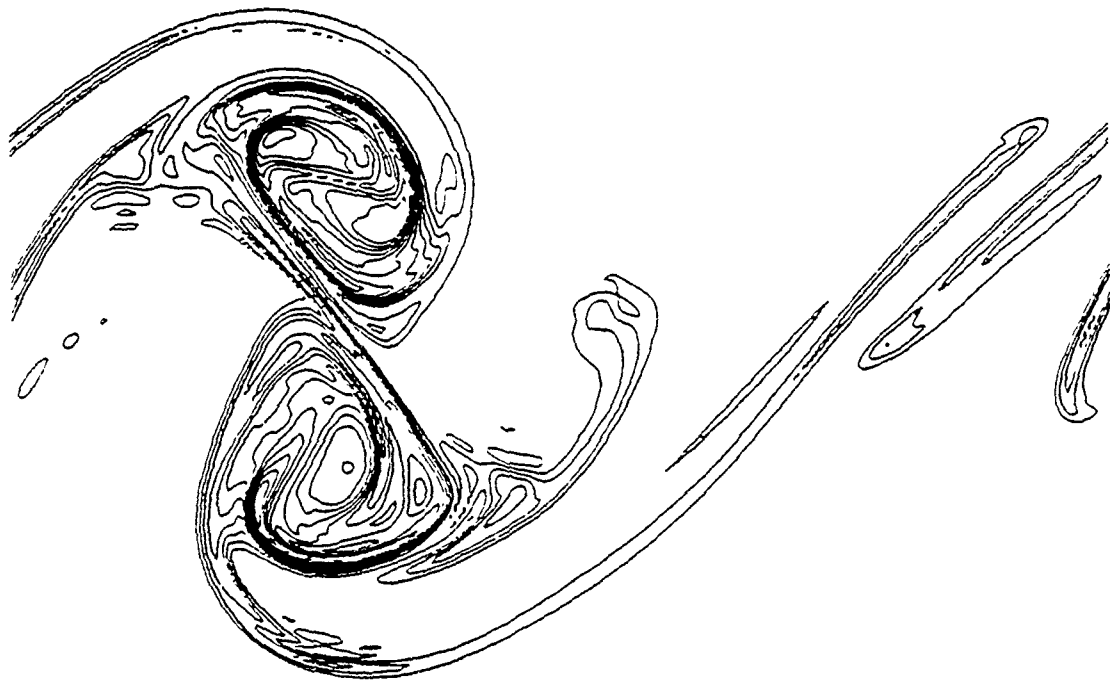


Fig. (6) Vorticity contours at $t = 128 (\delta/U_0)$, two-dimensional simulation.

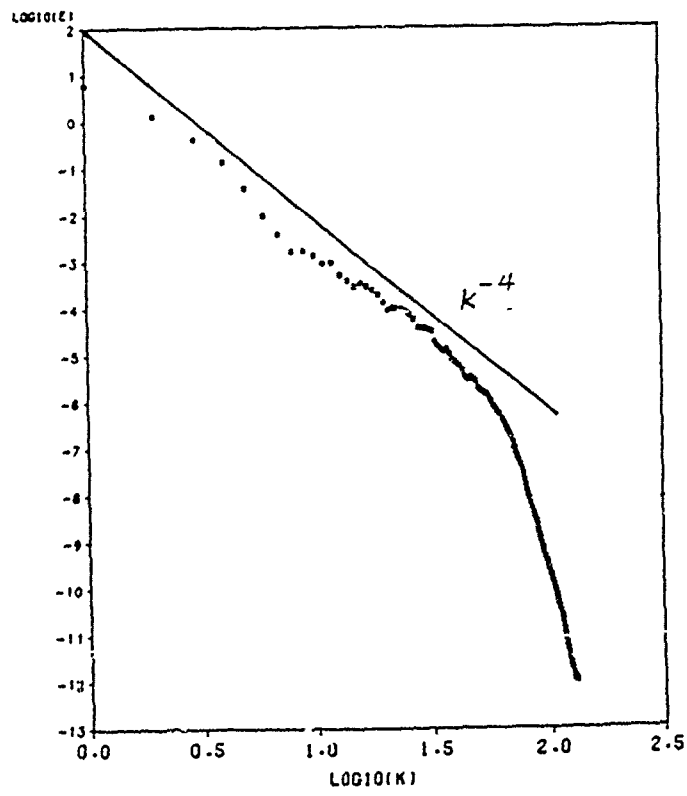
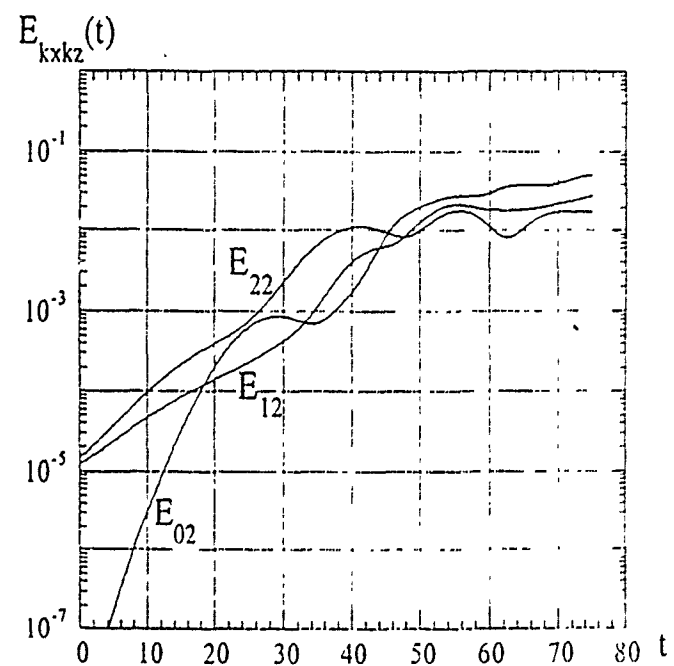
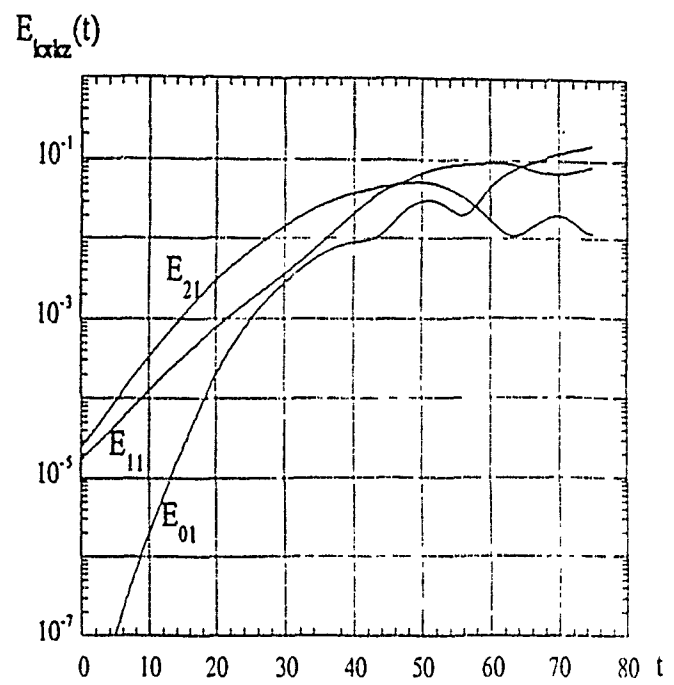
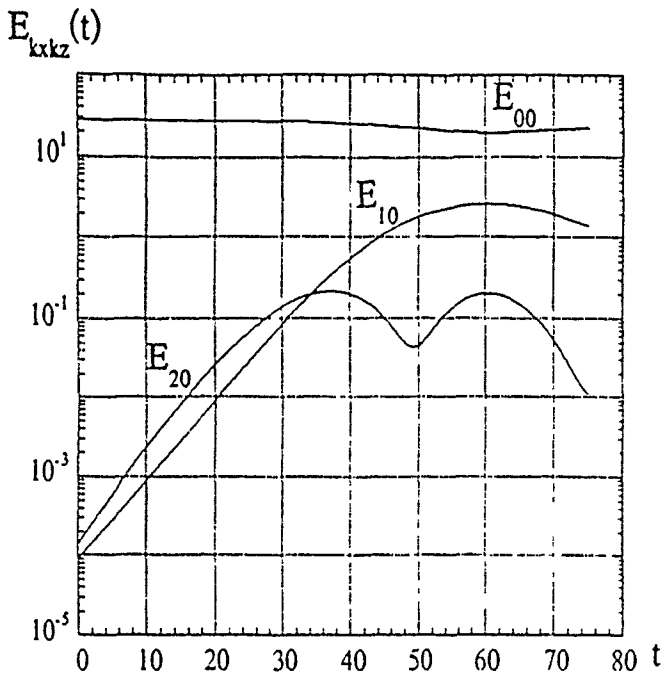


Fig. (7) Modal energy spectrum at $t = 128 (\delta/U_0)$, two-dimensional simulation.



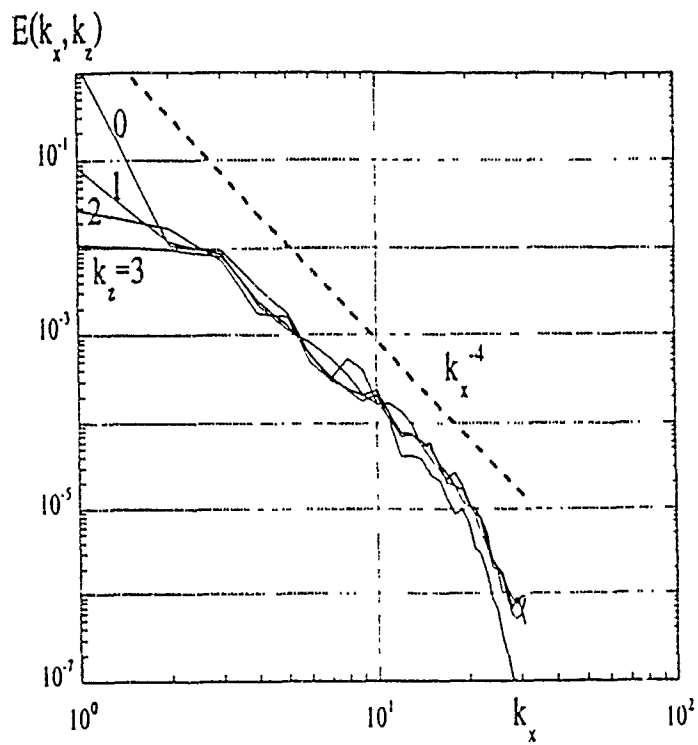


Fig. 11 Energy spectrum at time $t=75$.
 k_x = streamwise wavenumber, k_z = spanwise wavenumber.

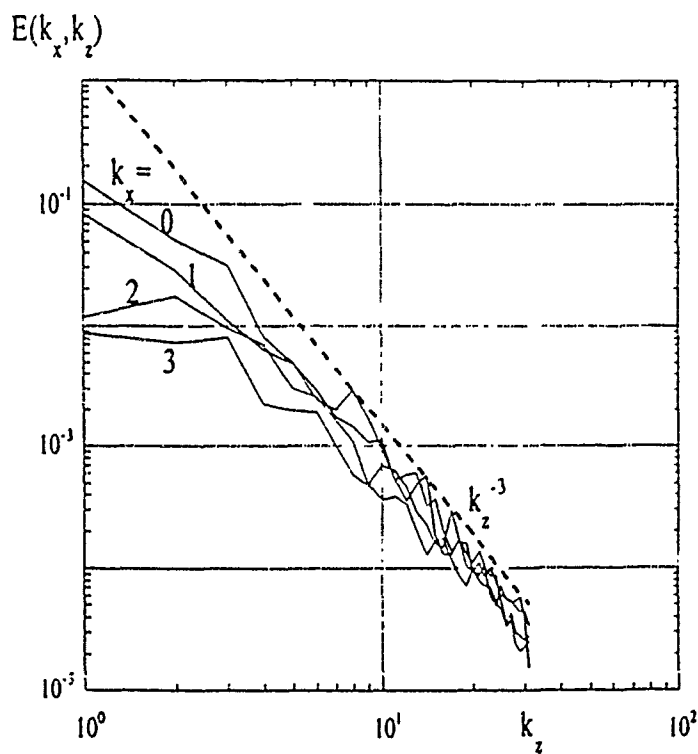


Fig. 12 Energy spectrum at time $t=75$.
 k_x = streamwise wavenumber, k_z = spanwise wavenumber.

Some Issues in Computation of Turbulent Flows

Parviz Moin

Stanford University & NASA-Ames

The presentation will address the key problems and solutions for the large eddy simulation of turbulent flows. Specifically, we will argue that high order finite difference methods give comparable results to spectral methods with *the same resolution*. The problem of prescribing turbulence at the inflow of the computational domain will be addressed in conjunction with examples from direct simulation of compressible isotropic turbulence and the flow over a backward facing step.

The main part of the presentation will be devoted to subgrid scale modeling. Among the deficiencies of the widely used eddy viscosity models in large eddy simulations are the variation of model constant in different flows, incorrect or ad hoc imposition of limiting behavior of the stresses near walls, and strictly dissipative nature of the models. Recent direct simulations of wall-bounded and homogeneous flows show that there is energy transfer from small scales to large scales (backscatter) at about 40-60% of the grid points (Piomelli, Cabot, Moin & Lee, 1990). Eddy viscosity models (with positive eddy viscosity) remove energy from large scales at each point in the physical space. In the past, improvements for SGS models have been sought in the same manner as in phenomenological modeling, that is to resort to additional moment equations. This practice ignores the wealth of information available from the computed large scale field.

Using the notion of subgrid stress similarity of Germano (1990) and Bardina *et al.* (1980), a new eddy viscosity subgrid scale model has been developed which overcomes the aforementioned drawbacks (Germano, Piomelli, Moin & Cabot, 1990). The model coefficient is a function of space and time and is computed dynamically during the computation using the spectral information in the resolved field. With this model the subgrid scale stresses have the proper asymptotic behavior near the wall and vanish in laminar flow without the use of ad hoc damping functions. In this formulation, the subgrid scale dissipation can become positive which would act as production for the large scales. The model has been tested in large eddy simulation of transitional and turbulent channel flow. The agreement with the experimental data and direct simulations are good.

Bardina, J., Ferziger, J. H. & Reynolds, W. C. (1980) Improved subgrid scale models for large eddy simulation. *AIAA Paper 80-1357*.

Germano, M. (1990) Averaging invariance of the turbulent equations and similar subgrid modeling. *CTR Manuscript 116*, Center for Turbulence Research, Stanford University and NASA-Ames Research Center.

Germano, M., Piomelli, U., Moin, P. & Cabot, W. H. (1990) A dynamics subgrid-scale eddy viscosity model. In *Studying Turbulence Using Numerical Simulation Databases-III*. Proc. of the 1990 Summer Program of the Center for Turbulence Research, Stanford University and NASA-Ames Research Center, pp. 5-18.

Piomelli, U., Cabot, W. H., Moin, P. & Lee, S. (1990) Subgrid scale backscatter in transitional and turbulent flows. In *Studying Turbulence Using Numerical Simulation Databases-III*. Proc. of the 1990 Summer Program of the Center for Turbulence Research, Stanford University and NASA-Ames Research Center, pp. 19-29.

SPECTRAL LARGE-EDDY SIMULATION
OF TURBULENT-SHEAR FLOWS

by

M. LESIEUR, P. COMTE, X. NORMAND
O. METAIS and A. SILVEIRA

Institut de Mécanique de Grenoble, France
B.P. 53X, 38041 Grenoble-Cedex

*To be presented at the International Workshop: "Large-eddy simulations, where do we stand?"
St Petersburg, Florida, 19-21 December 1990*

We present first the formalism of a spectral large-eddy simulation of isotropic three-dimensional turbulence, based on the concept of spectral eddy-viscosity developed by Kraichnan. For decaying turbulence at high Reynolds number, it yields a self-similar decaying kinetic-energy spectrum, of slope close to the Kolmogorov $k^{-5/3}$ law. For a passive scalar, a spectral eddy-diffusivity of the same genre allows to obtain an inertial-convective range at the cutoff, as well as a k^{-1} shear dominated range in the large energetic scales.

This subgrid-scale model gives satisfactory results in the case of stably-stratified decaying turbulence: here, the dynamic coupling between momentum and temperature implies for the latter a loss of its anomalous character. For a temporal mixing layer involving two fundamental Kelvin-Helmholtz vortices, we show that the model allows for the formation of thin longitudinal vortices, with a Kolmogorov spectrum developing in the small scales, and with turbulent intensities in good agreement with the experimental observations.

Afterwards, we reformulate the model in terms of the local second-order velocity structure function, in order to take into account the intermittency of turbulence in physical space. This new subgrid-scale model is then applied to three-dimensional numerical simulations of:

- a) isotropic incompressible or compressible decaying turbulence.
- b) flow above a backwards-facing step.
- c) temporal mixing layer.
- d) spatially developing compressible boundary layer (Mach 5).

In the last two cases, we show how a three-dimensional random perturbation of weak amplitude allows to trigger the development of a staggered array of coherent vortices.

Anisotropic Representation of Subgrid-scale Reynolds Stress in LES

Kiyoshi Horiuti

Institute of Industrial Science, University of Tokyo
7-22-1 Roppongi, Minato-ku Tokyo 106 Japan.

Abstract

The Smagorinsky model which has been commonly used in Large Eddy Simulation (LES) of turbulent flows is investigated. Although various numerical simulations using the Smagorinsky model yielded good results,¹⁻⁵⁾ several issues on the model remain unsolved:

- (a) A poor correlation of the model value of the Reynolds stresses using the Smagorinsky model with the exact value computed from the Direct Numerical Simulation (DNS) data.
- (b) Universality of the Smagorinsky constant involved in the model.
- (c) Development of the damping function with a wide applicability and theoretical foundations, in place of the ad hoc Van Driest type.

The aim of the present paper is to propose a new model which partially resolves these issues.

1. Introduction

The basic approach adopted in the present study is an incorporation of higher order terms in anisotropic representation (AR)⁶⁾ into the subgrid scale (SGS) Reynolds stresses, supplementing new terms to the conventional eddy viscosity. The same approach has already been taken to Reynolds averaged model of $k-\varepsilon$ type.⁷⁾ As is well known, conventional $k-\varepsilon$ models have several drawbacks.⁷⁾ First of all, models based on isotropic eddy viscosity representation inevitably fail to predict the anisotropy of the Reynolds stresses, i.e., the inability to accurately forecast the normal stresses degrades model applicability. Secondly, numerical studies indicate that the conventional eddy viscosity magnitude is too large and excessively dissipative, thus the model is unable to provide a detailed prediction of the fine turbulence structures.⁷⁾ To overcome the first deficiency, 2nd order anisotropic representation (AR) models of the Reynolds stresses have been introduced by Leslie,⁸⁾ Yoshizawa,⁹⁾ Speziale.¹⁰⁾ These models provide acceptably good predictions of the anisotropy of turbulence intensities,^{10,11)} and statistically this representation is found in the 2nd order terms

in the scale parameter expansion of the two scale direct interaction approximation (DIA) approach.⁹⁾ When 2nd order AR is incorporated, however, the eddy viscosity, a proportional coefficient between the Reynolds shear stress and the mean strain, remains unchanged. AR can be mathematically extended to higher orders. In Horiuti,⁶⁾ 3rd order AR was used to develop supplementary eddy viscosity terms which effectively reduce its magnitude, therefore counteracting this $k-\epsilon$ model drawback. The most prominent finding was that as a energy scale in the eddy viscosity, the normal shear stress is more preferable than the total turbulent energy. Besides, it was found that 3rd order AR may be used as an alternative method to reduce the magnitude of the eddy viscosity in the buffer layer region by acting similarly to the Van Driest damping function,¹²⁾ commonly used in $k-\epsilon$ models. The present study extends the same approach to the SGS modeling in LES.

Large Eddy Simulations (LES) involve the modeling of various stress terms, which arise in filtering the Navier-Stokes (NS) equations. The raw variables u_i are divided into filtered [or grid scale (GS)] components and the subgrid (SGS) components. GS variables \bar{u}_i are defined as follows:

$$\bar{u}_i(x_1, x_2, x_3) = \int_D \prod_{i=1}^3 G_i(x_i - x_i') u_i(x_1', x_2', x_3') dx_1' dx_2' dx_3' \quad (1)$$

where u_i denotes the velocity component in the i -th direction, $i=1, 2, 3$ correspond to the x (downstream), y (normal to the walls), z (spanwise) directions, respectively. G_i is a filter function in the i -th direction.³⁻⁵⁾ In the present study, the Gaussian filter is used as G_i ($i=1, 3$) in homogeneous directions and the top-hat filter is used as G_2 in the y direction.³⁻⁵⁾ The SGS component is defined as $u_i = u_i - \bar{u}_i$. The length in wall units is denoted by $(\cdot)_w$, the horizontal average by $\langle \cdot \rangle$. The governing equations in LES for incompressible flow become

$$\frac{\partial \bar{u}_i}{\partial t} + \frac{\partial}{\partial x_j} (\bar{u}_i \bar{u}_j) = -\frac{\partial \tau_{ij}}{\partial x_j} - \frac{\partial \bar{p}}{\partial x_i} + \frac{1}{Re} \nabla^2 \bar{u}_i + 2 \delta_{ii}, \quad (2)$$

$$\frac{\partial \bar{u}_i}{\partial x_i} = 0. \quad (3)$$

When raw variables are divided into GS and SGS components, the SGS stresses (τ_{ij}) consist of the three components : $\tau_{ij} = L_{ij} + C_{ij} + R_{ij}$, the Leonard terms ($L_{ij} = \bar{u}_i \bar{u}_j - \bar{u}_i u_j$), the cross stress terms ($C_{ij} = u_i \bar{u}_j + \bar{u}_i u_j$), and the SGS Reynolds stress terms ($R_{ij} = u_i u_j$). Recent direct tests of the models in LES using Direct Numerical Simulations (DNS) data base^{6, 13-16)} revealed that among these terms, C_{ij} , which have been neglected in most of previous computations,^{3, 4)} have a significant contribution. In a priori test,^{5, 16)} it is shown that the Bardina model¹³⁾ for C_{ij} is compatible with the Gaussian filter, and the inclusion of the models for C_{ij} significantly improves the correlation with DNS. The Bardina model approximates C_{ij} and R_{ij} as follows:

$$C_{ij} \sim C_{ij}^B = \bar{u}_i(\bar{u}_j - \bar{u}_i) + (\bar{u}_i - \bar{u}_j)\bar{u}_i, \quad R_{ij} \sim (\bar{u}_i - \bar{u}_j)(\bar{u}_j - \bar{u}_i) \quad (4)$$

One of most significant contributions of the Bardina model is a recovery of Galilean Invariance.¹⁷⁾ In 'a posteriori' test,^{5, 16)} it is

found that the statistical values such as turbulence intensities are considerably improved.

2. Anisotropic representation of the Reynolds stress

Reynolds stresses up to the 2nd order expansion in a scale parameter⁹⁾ can be expressed as

$$\begin{aligned} \overline{u_i' u_j'} &= \delta_{ij} \left[\frac{2}{3}k - \frac{1}{3}\frac{k^3}{\varepsilon^2} \left\{ (C_{r1} + C_{r3}) \frac{\partial \bar{u}_1}{\partial x_m} + C_{r2} \frac{\partial \bar{u}_m}{\partial x_l} \right\} \frac{\partial \bar{u}_l}{\partial x_m} \right] \\ &\quad - C_v \frac{k^2}{\varepsilon} \left(\frac{\partial \bar{u}_i}{\partial x_l} + \frac{\partial \bar{u}_j}{\partial x_i} \right) \\ &\quad + \frac{k^3}{\varepsilon^2} \left\{ C_{r1} \frac{\partial \bar{u}_i}{\partial x_l} \frac{\partial \bar{u}_j}{\partial x_l} + \frac{C_{r2}}{2} \left(\frac{\partial \bar{u}_i}{\partial x_l} \frac{\partial \bar{u}_l}{\partial x_j} + \frac{\partial \bar{u}_j}{\partial x_l} \frac{\partial \bar{u}_l}{\partial x_i} \right) + C_{r3} \frac{\partial \bar{u}_l}{\partial x_i} \frac{\partial \bar{u}_l}{\partial x_j} \right\}, \end{aligned} \quad (5)$$

where k is the turbulent kinetic energy, ε the dissipation rate of k , $C_v, C_{r1}, C_{r2}, C_{r3}$ are constant coefficients, and δ_{ij} is the Kronecker delta symbol. After continuing to a 3rd order expansion some noteworthy terms are produced,⁶⁾ i.e., in the products of first order terms and second order terms:

$$- \frac{k^4}{\varepsilon^3} \left[C_{A1} \frac{\partial \bar{u}_i}{\partial x_m} \frac{\partial \bar{u}_l}{\partial x_m} + C_{A2} \frac{\partial \bar{u}_i}{\partial x_m} \frac{\partial \bar{u}_m}{\partial x_l} \right] \left(\frac{\partial \bar{u}_i}{\partial x_l} + \frac{\partial \bar{u}_j}{\partial x_i} \right). \quad (6)$$

Combining with (5), the eddy viscosity ν_e (the coefficient of mean strain $(\partial \bar{u}_i / \partial x_j + \partial \bar{u}_j / \partial x_i)$), is rearranged to

$$\nu_e = \frac{3}{2} C_v \frac{k}{\varepsilon} \left[\frac{2}{3}k - \frac{1}{3} \frac{k^3}{C_v \varepsilon^2} \left\{ \frac{C_{A1} - C_{A2}}{4} \left(\frac{\partial \bar{u}_i}{\partial x_m} + \frac{\partial \bar{u}_m}{\partial x_l} \right)^2 + \frac{C_{A1} - C_{A2}}{4} \left(\frac{\partial \bar{u}_i}{\partial x_m} - \frac{\partial \bar{u}_m}{\partial x_l} \right)^2 \right\} \right]. \quad (7)$$

The second term in (7) is always positive and reduces the magnitude of the eddy viscosity. Note that the terms within the square bracket ([]) in eq.(7) correspond to the 2nd order AR turbulence intensities, and that the theoretical values of C_{A1} and C_{A2} are respectively 0.119 and 0.0424. The relationship between AR and ASM¹⁸⁾ will now be referred to. ASM approximates the transport equation for the Reynolds stress $\overline{u_i' u_j'}$ as follows:

$$\begin{aligned} \overline{u_i' u_j'} \frac{P - \varepsilon}{k} &= P_{ij} - \frac{2}{3} \delta_{ij} \varepsilon - C_1 \frac{\varepsilon}{k} (\overline{u_i' u_j'} - \frac{2}{3} \delta_{ij} k) \\ &\quad - \gamma k \left(\frac{\partial \bar{u}_i}{\partial x_j} + \frac{\partial \bar{u}_j}{\partial x_i} \right) - \alpha (P_{ij} - \frac{2}{3} \delta_{ij} P) - \beta (D_{ij} - \frac{2}{3} \delta_{ij} D), \end{aligned} \quad (8)$$

where,

$$P_{ij} = -\overline{u_i' u_l} \frac{\partial \bar{u}_j}{\partial x_l} - \overline{u_j' u_l} \frac{\partial \bar{u}_i}{\partial x_l}, D_{ij} = -\overline{u_i' u_l} \frac{\partial \bar{u}_l}{\partial x_j} - \overline{u_j' u_l} \frac{\partial \bar{u}_l}{\partial x_i}, P = P_{mm}/2.$$

The left hand side of (8) is a model for convection and diffusion terms,¹⁸⁾ whereas the 3rd to 6th terms in the right hand side are for pressure-strain terms.¹⁹⁾ Usually these coupled equations are numerically solved iteratively by setting the initial values of $\overline{u_i' u_j'}$ ⁽⁰⁾ equal to $2\delta_{ijk}/3$, and successively inserting them into (8), with the superscript denoting the number of iterations. After the 2nd iteration, an expression for $\overline{u_i' u_j'}$ is obtained,

$$\overline{u_i u_j}^{(2)} = \delta_{ij} \left[\frac{2}{3} k - \frac{2}{3} \frac{1}{C_1^2} \bar{\gamma} (1-\alpha-\beta) \frac{k^3}{\varepsilon^2} \left(\frac{\partial \bar{u}_l}{\partial x_m} + \frac{\partial \bar{u}_m}{\partial x_l} \right) \frac{\partial \bar{u}_l}{\partial x_m} \right] \quad (9)$$

$$- \left[\left(1 - \frac{1}{C_1} (1 + \frac{1}{C_1}) \bar{\gamma} \frac{k^2}{\varepsilon} - \frac{1}{C_1^3} \bar{\gamma}^2 \frac{k^4}{\varepsilon^3} \left(\frac{\partial \bar{u}_l}{\partial x_m} + \frac{\partial \bar{u}_m}{\partial x_l} \right) \frac{\partial \bar{u}_l}{\partial x_m} \right) \left(\frac{\partial \bar{u}_l}{\partial x_i} + \frac{\partial \bar{u}_i}{\partial x_l} \right) \right]$$

$$+ \left[\frac{\bar{\gamma}}{C_1^2 \varepsilon^2} \left\{ 2(1-\alpha) \frac{\partial \bar{u}_l}{\partial x_i} \frac{\partial \bar{u}_j}{\partial x_l} + (1-\alpha-\beta) \left(\frac{\partial \bar{u}_l}{\partial x_i} \frac{\partial \bar{u}_l}{\partial x_j} + \frac{\partial \bar{u}_j}{\partial x_l} \frac{\partial \bar{u}_l}{\partial x_i} \right) + 2\beta \frac{\partial \bar{u}_l}{\partial x_i} \frac{\partial \bar{u}_l}{\partial x_j} \right\} \right],$$

where $\bar{\gamma}$ denotes $\bar{\gamma}-2(1-\alpha-\beta)/3$. Notice AR and ASM are similar, with the exception that (7) contains terms related to vorticity, possibly violations the principle of having the SGS Reynolds stresses indifferent under frame rotations.²⁰⁾ This similarity has also been noted recently in Rubinstein et al.,²¹⁾ however, no reference is made to the new eddy viscosity terms pointed out here. The origin of each term can not be easily traced with the DIA approach, and thus ASM was utilized to do this. The eddy viscosity on the 3rd iteration becomes

$$\nu_e^{(3)} = \frac{\bar{\gamma} k^2}{C_1 \varepsilon} - \frac{1}{C_1} \nu_e^{(2)} \frac{P^{(2)} - \varepsilon}{\varepsilon} - \frac{1}{C_1^2} (1-\alpha-\beta)^2 \frac{k^2}{\varepsilon^2} P^{(1)}, \quad (10)$$

where

$$P^{(2)} = - \overline{u_l u_m}^{(2)} \frac{\partial \bar{u}_l}{\partial x_m}.$$

Both the second and 3rd terms in (10) include 3rd order AR. The second term results from the imbalance between production and dissipation, whereas the third term is from the products of δ_{il} terms in (8) with $\partial \bar{u}_l / \partial x_i$, and the δ_{il} terms in (8) with $\partial \bar{u}_i / \partial x_l$, and is consequently related to the anisotropy of turbulence intensities. Based on these observations, it is assumed that 3rd order AR arises from the deviation from equilibrium, and also the anisotropy of turbulence intensities. For details, see Horiuti.⁶⁾

Here, we refer to the relationship between the Leonard term, the Bardina model and the 2nd order AR. By using the Taylor expansion,¹⁴⁾ L_{ij} and C_{ij}^B are expressed as follows:

$$L_{ij} = -\frac{\Delta^2}{24} \bar{u}_i \frac{\partial}{\partial x_k} \frac{\partial}{\partial x_k} \bar{u}_j + \frac{\Delta^2}{24} \bar{u}_i \frac{\partial}{\partial x_k} \frac{\partial}{\partial x_k} \bar{u}_i + \frac{\Delta^2}{12} \frac{\partial \bar{u}_i}{\partial x_k} \frac{\partial \bar{u}_j}{\partial x_k} + O(\Delta^4), \quad (11)$$

$$C_{ij}^B = -\frac{\Delta^2}{24} \bar{u}_i \frac{\partial}{\partial x_k} \frac{\partial}{\partial x_k} \bar{u}_j - \frac{\Delta^2}{24} \bar{u}_i \frac{\partial}{\partial x_k} \frac{\partial}{\partial x_k} \bar{u}_i + O(\Delta^4).$$

The first and second terms of each expansion have a same form with opposite signs, thus the total summation of L_{ij} and C_{ij}^B recovers the Galilean Invariance.¹⁷⁾ This, however, does not necessarily mean that the remainder is negligibly small. Besides, the remainder

$$\frac{\Delta^2}{12} \frac{\partial \bar{u}_i}{\partial x_k} \frac{\partial \bar{u}_j}{\partial x_k}, \quad (12)$$

corresponds to a part of AR of the SGS Reynolds stress eq.(5). AR consists of three types of terms, namely

$$\Delta^2 \frac{\partial \bar{u}_i}{\partial x_k} \frac{\partial \bar{u}_j}{\partial x_k}, \quad \Delta^2 \frac{\partial \bar{u}_i}{\partial x_k} \frac{\partial \bar{u}_k}{\partial x_j}, \quad \Delta^2 \frac{\partial \bar{u}_k}{\partial x_i} \frac{\partial \bar{u}_k}{\partial x_j}. \quad (13)$$

The last two terms of (13) are absent in (11), thus the incorporation of AR by combining the Leonard terms and the Bardina model ignores these terms. Among these three terms in (13), the last term in particular is from D_{ij} , in the pressure-strain approximation terms in ASM. In this respect, the neglect of this term may result in a poor approximation of the pressure-strain terms, if the model employed in ASM is accurate. Inclusion of D_{ij} , however, violates the invariance of the SGS Reynolds stress under the frame rotation,²⁰⁾ unless appropriate constants are chosen. Based on his statistical theory, Leslie²¹⁾ objects to the inclusion of D_{ij} in (8). Practically, in LES of plane channel flow, the magnitude of modeled values by D_{ij} is marginally small, if the recommended values¹⁹⁾ are chosen for the model constants. It seems that the neglect of the last term in (13) does not seriously degrade the computation.

3. 'A priori' test of subgrid scale models

In LES, k and ε in the previous section are replaced by the SGS turbulent energy $K_G = u_1 u_1 / 2$ and $C_\varepsilon K_G^{3/2} / \Delta$, respectively, giving the time scale as $\Delta / C_\varepsilon / K_G^{1/2}$ and the eddy viscosity as follows:

$$\nu_e = C_N \frac{\Delta}{K_G^{1/2}} E, \quad (14)$$

where E denotes the energy scale and C_N is a model constant. If K_G is chosen as E , the conventional Smagorinsky model

$$\nu_e = (C_S \Delta)^2 [\frac{1}{2} e_{11} e_{11}]^{1/2}, \quad e_{11} = \frac{\partial \bar{u}_1}{\partial x_1} + \frac{\partial \bar{u}_1}{\partial r_1}, \quad (15)$$

can be obtained, assuming the equilibrium of SGS energy production and dissipation.

We begin with 'a priori' validation of the Smagorinsky model, using the DNS data base of turbulent channel flow at Reynolds number (Re ; based on the wall friction velocity and the channel width) of 360 with grid points of $128 \times 129 \times 128$ in the x, y, z directions, respectively, generated employing Fourier-Chebyshev polynomials expansions. The data is filtered with the Gaussian filter in the r and z directions and the top-hat filter in the y direction, and divided into GS and SGS components, reducing the LES grid point numbers to 32, 65, 32 in the x, y, z directions, respectively. The y -distribution of the correlation coefficient (C.C.) between the model value for $u_1 u_2$ by the Smagorinsky model and exact value is shown in Fig.1. C.C. is generally very low and, in particular, becomes negative at $y \sim 0.04$ and 0.96 . Figure 2 shows the y -distribution of average of $u_1 u_2$ in the $x-z$ plane. The model value shows a prohibitively large peak at the locations where negative C.C. is found in Fig.1. This large peak had to be suppressed by multiplying the length scale Δ by the Van Driest damping function $(1 - \exp(-y_1/A_1))^{1/2}$ with $A_1=25$,³⁻⁵⁾ implying that K_G may not be a proper energy scale. Here, we find a proper energy scale E , while inserting the exact value obtained from DNS data as K_G into eq.(14). As is noted before, the terms within the square bracket $([])$ in eq.(7) corresponds to the (2nd order) AR of SGS Reynolds stresses. It is, however, not practical in LES to directly

compute all of the terms, optimizing model constants C_{A1} and C_{42} . Here, the fact pointed out in the previous section that the total sum of the Leonard term and the Bardina model corresponds to (a part of) 2nd order AR is utilized to approximate the 2nd term in the square bracket. In this model, the new term

$$C_{A3} \Delta^2 (\overline{u_i u_j} - \overline{u_i} \overline{u_j}), \quad (16)$$

is superposed to the conventional Smagorinsky model. This term can be readily computed when the Gaussian filter is used combined with the spectral method. For an implementation of the finite difference method to the approximation of these terms, see Horiuti.²³⁾ C.C. between the model value for $\overline{u_i u_j}$ by this model and the exact value showed no noteworthy improvement over the Smagorinsky model. (The figure is omitted here.) Noting that in the $k-\varepsilon$ model,⁶⁾ the optimized values for C_{A1} and C_{42} in (7) were rather close to those to approximate the normal shear stress,¹¹⁾ next validation is made on the model which chooses the wall normal shear stress $\overline{u_2 u_2}$ as the energy scale E . A similar idea has already been adopted in Reynolds averaged models by Rodi.²⁴⁾ When the exact value of $\overline{u_2 u_2}$ obtained from the DNS data is used as E in eq.(14), C.C. has been considerably improved as is shown in Fig.3, particularly at $y \sim 0.4$ and 0.96. As can be depicted in the y -distribution of $\langle u_1 u_2 \rangle$ in Fig.4, the mean model value is in a good agreement with the exact value. It should be noted that no damping function is introduced in eq.(14), confirming the previous finding in the $k-\varepsilon$ model⁶⁾ that the normal shear stress is more preferable as the energy scale.

To incorporate the proposed model into actual LES computations, $\overline{u_2 u_2}$ and K_C must be represented by GS variables and accurately approximated. As is evidenced in the previous validation using the model eq.(16), the 2nd order AR is not sufficiently accurate to approximate the anisotropy of turbulence intensities for the use in LES. In place of AR, the Bardina model

$$\overline{u_i u_j} = (\overline{u}_i - \overline{\bar{u}}_i)^2, \quad (17)$$

is adopted in the present study. K_C is approximated in the same manner. Piomelli et al.⁵⁾ noted the model which uses K_C approximated by eq.(17) as E in (14) combined with the Van Driest damping function. The y -distribution of C.C. and the mean values are shown in Figs. 5 and 6, respectively. Although C.C. is a little lower than in Fig.3, the negative C.C. in the Smagorinsky model is eliminated. As in Fig.4, without introducing any ad hoc damping functions, the mean values are in a remarkably good agreement with the DNS data. It must be noted here that the wall limiting behaviour of the SGS Reynolds stress is not well satisfied by the models eq.(14) and (17). Although most of commonly used damping functions do not satisfy the limiting behaviour except for the one proposed by Piomelli et al.,⁵⁾ it seems that incorrect wall behaviour does not lead to inaccurate computation results. Now, a qualitative explanation to the difference in the optimized Smagorinsky constant in homogeneous flow ($C_S \sim 0.23$),¹⁴⁾ mixing layer ($C_S \sim 0.16$)²⁵⁾ and channel flow ($C_S \sim 0.10$)¹⁻⁵⁾ can be given: The anisotropy of GS turbulence intensities becomes larger in this order and this fact will be

reflected in the SGS turbulent energy, when the grid resolution is not sufficient. Because of the wrong choice of the energy scale in the Smagorinsky model, C_S had to be adjusted depending on the flow. It may be possible that C_N becomes universal independent on the flow, but C_S may not be so.

4. 'A posteriori' test of the proposed model

In this section, numerical results of LES when the SGS model proposed in the previous section (eqs.(14) and (17)) is incorporated into the actual computation, are briefly presented. Re is chosen equal to 1280, and 128, 129 and 128 grid points are employed in the x, y, z directions, respectively. Model constant C_N in eq.(14) is selected equal to 0.125, and no damping function is included.

Fig.7 displays the mean velocity profile. The von karman constant ($\kappa=0.4$) and another constant ($B=5.0$) are in a good agreement with experimental measurement.²⁵⁾ GS turbulence intensities of streamwise and normal components are shown in Figs.8 and 9, respectively. Note that the contributions from the Bardina model are included in the intensities. For a comparison, experimental measurement²⁷⁾ and numerical results²⁸⁾ obtained by using the Smagorinsky model combined with the Van Driest damping function are included in the figures. Overall agreement with experimental measurement is good. The peak positions of turbulence intensities using the proposed model are closer to the wall than in the previous result, confirming the validity of the presented model.

5. Summary and discussions

A new subgrid scale Reynolds stress model is proposed. The prominent feature of the proposed model lies in the incorporation of 3rd order terms in the anisotropic representation of SGS Reynolds stresses to the eddy viscosity, choosing the normal shear stress as the energy scale. In the present model, previously found discrepancy in the optimized values for the Smagorinsky model constant can be explained, and the use of the empirical damping functions can be avoided, while maintaining a higher correlation with the DNS data than in using the Smagorinsky model. Unlike commonly used damping function of Van Driest type which globally reduces the eddy viscosity magnitude at the same level of y_+ , this model can make a local reduction of the magnitude. The relationship between the Leonard term, the Bardina model and the 2nd order AR is pointed out. The validity of the proposed model is confirmed in 'a posteriori' test. Although the normal shear stress can be almost uniquely chosen in plane channel flow, further refinement is needed for its proper selection in complex geometry, such as in a corner flow or backward facing step, which will be left to the future work.

Acknowledgement

This work was partially supported by a Grant-in-Aid for Scientific Research Nos. 01613002 and 02302043 from the Ministry of Education of Japan, and University of Tokyo-Hitachi Joint

Research Program.

References

1. J.W. Deardorff, J. Fluid Mech. 41, 453 (1970).
2. U. Schumann, J. Comp. Phys. 18, 376 (1975).
3. P. Moin and J. Kim, J. Fluid Mech. 118, 341 (1982).
4. K. Horiuti, J. Comp. Phys. 71, 343 (1987).
5. U. Piomelli, P. Moin and J.H. Ferziger, Phys. Fluids 31, 1884 (1988).
6. K. Horiuti, Phys. Fluids A2, No.10 (1990).
7. H. Tennekes and J.L. Lumley, A First Course in Turbulence The MIT Press, Cambridge 1972.
8. D.C. Leslie, "Developments in the theory of turbulence", Clarendon Press, Oxford (1973).
9. A. Yoshizawa, Phys. Fluids 27, 1377 (1984).
10. C.G. Speziale, J. Fluid Mech. 175, 459 (1987).
11. S. Nisizima and A. Yoshizawa, AIAA J. 25, 414 (1987).
12. E. R. Van Driest, J. Aero. Sci. 23, 1007 (1956).
13. J. Bardina, Ph.D. dissertation, Stanford University, 1983.
14. R.A. Clark, J.H. Ferziger, and W.C. Reynolds, J. Fluid Mech. 91, 1 (1979).
15. C.G. Speziale, G. Erlebacher, T.A. Zang and M.Y. Hussaini, Phys. Fluids 31, 940 (1988).
16. K. Horiuti, Phys. Fluids A1, 462 (1989).
17. C.G. Speziale, J. Fluid Mech. 156, 55 (1985).
18. W. Rodi, ZAMM 56, T219 (1976).
19. B.E. Launder, G.J. Reece and W. Rodi, J. Fluid Mech. 68, 537 (1975).
20. C.G. Speziale, Geophys. Astrophys. Fluid Dyn. 33, 199 (1985).
21. D.C. Leslie, J. Fluid Mech. 98, 435 (1980).
22. R. Rubinstein and J.M. Barton, Phys. Fluids A2, 1472 (1990).
23. K. Horiuti, Proc. of Int. Symp. on Comp. Fluid Dyn.-Nagoya, Nagoya, Aug. 1989, p.233.
24. W. Rodi, AIAA J. 20, 872 (1982).
25. N.N. Mansour, J.H. Ferziger and W.C. Reynolds, Ph.D. Thesis, Report No. TF-11, Stanford Univ. 1978.
26. A.K.M.F. Hussain and W.C. Reynolds, J. Fluid Eng. 97, 568 (1975).
27. H. Kreplin and M. Eckermann, Phys. Fluids 22, 1233 (1979).
28. K. Horiuti, submitted to J. Fluid Mech. (1990)

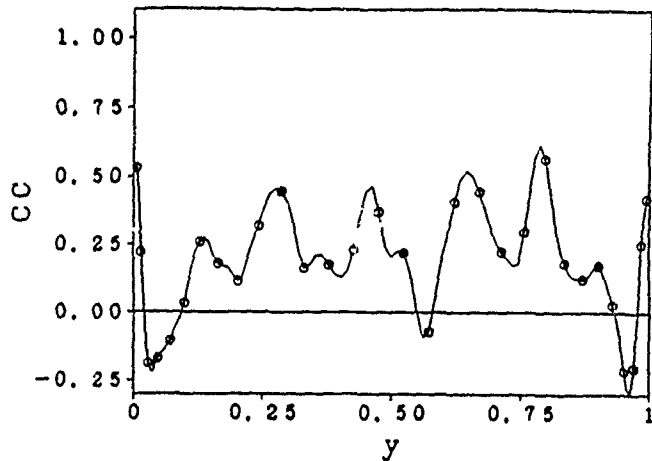


Fig. 1: The y -distribution of C.C. between the model value for $u_1 u_2$ by the Smagorinsky model (Eq.(15)) and the exact value.

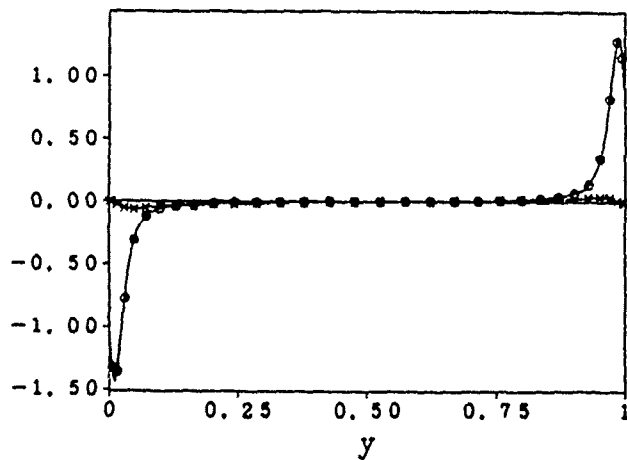


Fig. 2: The y -distribution of $\overline{\langle u_1' u_2' \rangle}$ of the model value by the Smagorinsky model (—○—) and the exact value (---X---).

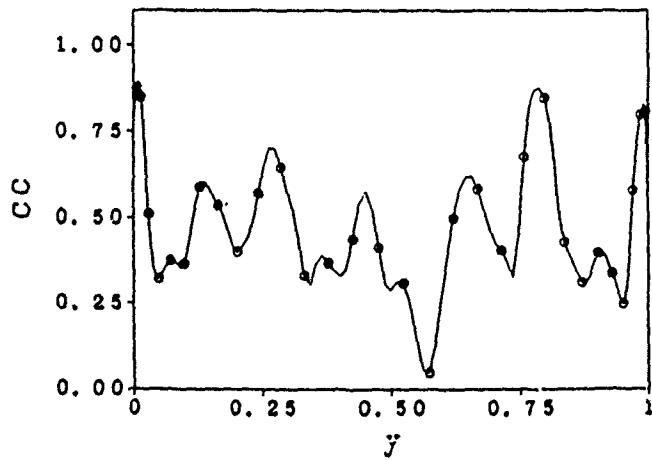


Fig. 3: The y -distribution of C.C. between the exact value for $u_1 u_2$ and the model value by Eq.(14) using K_c and $u_2 u_2$ computed from the DNS data.

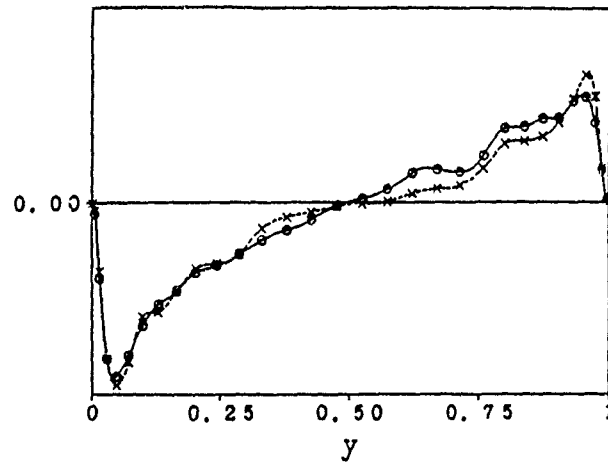


Fig. 4: The y -distribution of the exact value for $\langle u_1' u_2' \rangle$ (---*---) and the model value by Eq.(14) using K_C and $u_1' u_2'$ computed from the DNS data (—○—).

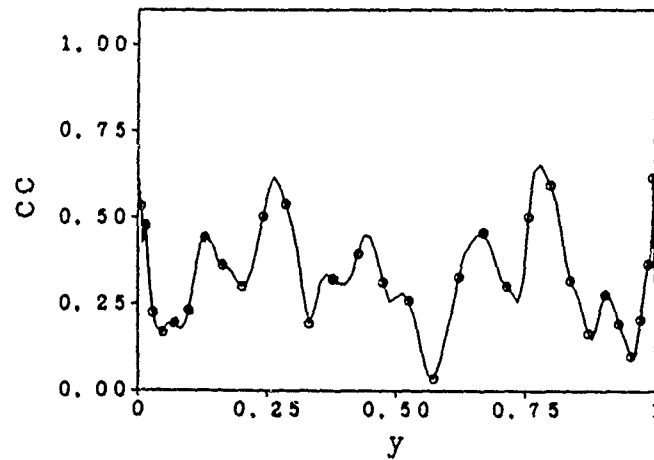


Fig. 5: The y -distribution of C.C. between the model value for $u_1' u_2'$ by Eqs.(14) and (17) and the exact value.

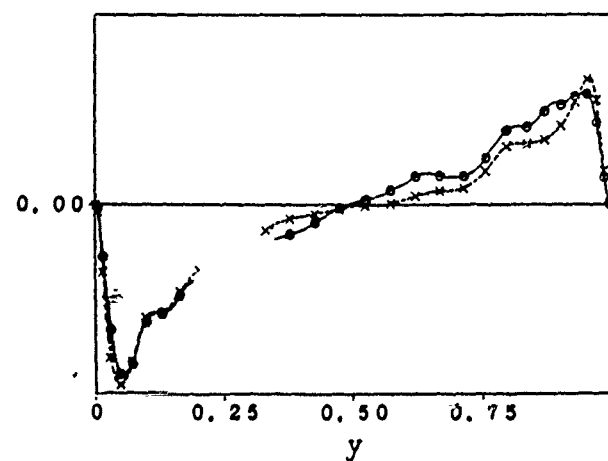


Fig. 6: The y -distribution of the model value for $\langle u_1' u_2' \rangle$ by Eq.(14) and (17) (—○—) and the exact value (---*---).

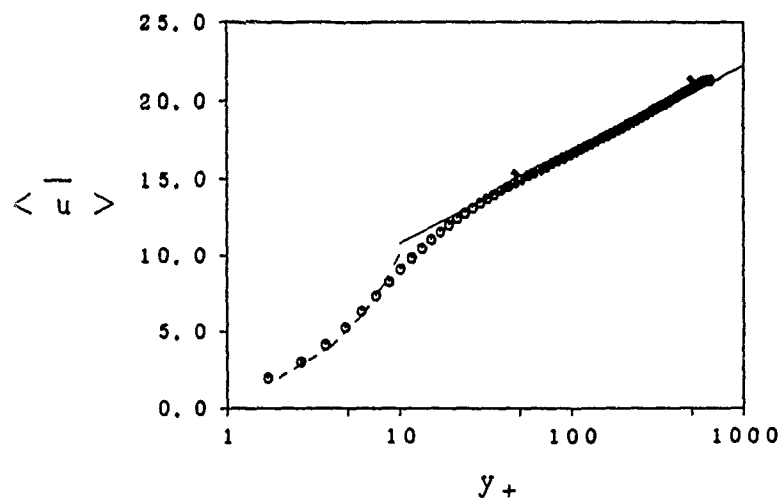


Fig. 7: Mean streamwise velocity profile $\langle \bar{u} \rangle$; \circ , computation; \cdots , $\langle \bar{u} \rangle = y_+$; --- , $\langle \bar{u} \rangle = 1/0.4 \log y_+ + 5.0$.

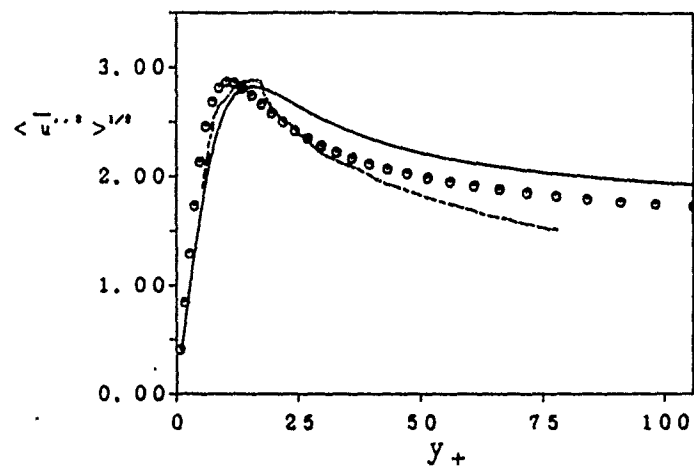


Fig. 8: Streamwise component of GS turbulence intensities in the vicinity of the lower wall (\circ); \cdots , experimental data²⁷; --- , computational data using the Smagorinsky model.

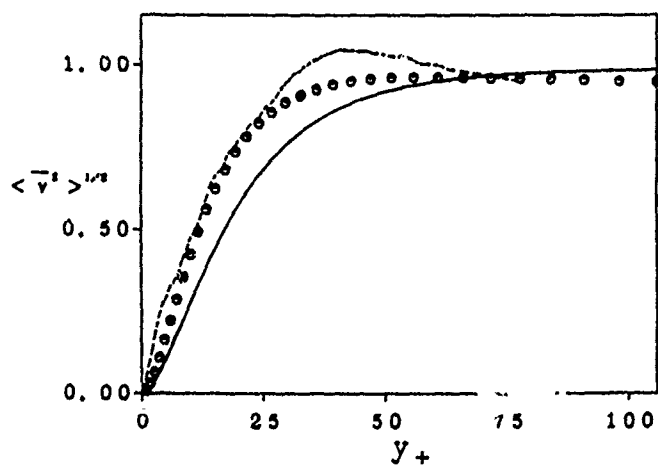


Fig. 9: Normal component of GS turbulence intensities in the vicinity of the lower wall (\circ); \cdots , experimental data²⁷; --- , computational data using the Smagorinsky model.

Large-Eddy/RNG Simulation of Flow Over a Backward-Facing Step

Karniadakis G.E., Orszag S.A., and Yakhout V.

Mechanical and Aerospace Engineering
and Applied and Computational Mathematics
Princeton University, Princeton, N.J. 08544

Abstract

In this paper we combine spectral element methodology with a subgrid scale model based on renormalization (RNG) group theory to formulate an algorithm appropriate for simulating turbulent flows in complex geometries. The method is then applied to flow over a backward-facing step in transitional and turbulent flow regime. Preliminary results suggest that the RNG model can be applied faithfully even in the transitional and early turbulent regime, where other turbulence models fail.

1 INTRODUCTION

Renormalization group theory (RNG) has found its way into fluid mechanics relatively recently, particularly in developing turbulence theory [1], however it has already provided a series of interesting theoretical and numerical results. A milestone for RNG theory in fluid mechanics was the establishment of the so-called correspondence principle, stating that in the inertial range the behavior of the small-scale Navier-Stokes turbulence is statistically equivalent to the modeled Navier-Stokes equation with the addition of a random noise term. This principle makes it possible to use all the formalism of classical RNG theory. Recently, renormalization group methods have been developed [1], [2], [3] to analyse a variety of turbulent flow problems. For homogeneous turbulent flows, such important quantities as the Kolmogorov constant, Batchelor constant, turbulent Prandtl number, rate of decay to isotropy, skewness factor, etc. have been obtained directly from this theory in good agreement with available data.

RNG methods involve systematic approximations to the full Navier-Stokes equations that are obtained by using perturbation theory to eliminate or decimate infinitesimal bands of small scale modes, iterating the perturbation procedure to eliminate finite bands of modes by constructing recursion relations for the renormalized transport coefficients, and evaluating the parameters at a fixed point in the lowest order of a dimensional expansion around a certain critical dimension. The decimation procedure, when applied successively to the entire wavenumber spectrum leads to the RNG equivalent of full closure of the Reynolds averaged Navier-Stokes equations. The resulting RNG transport coefficients are differential in character as opposed to ad hoc algebraic coefficients of conventional closure methods. All constants and functions appearing in the RNG closures are fully determined by the RNG analysis. Briefly, the RNG method provides an analytical method to eliminate small scales from the Navier-Stokes equations, thus leading to a dynamically consistent description of the large-scales. The formal process of successive elimination of small scales together with re-scaling of the resulting equations results in a calculus for the derivation of transport approximations in turbulent flows.

An obvious advantage of RNG models over other standard models is that they apply also in the low Reynolds number limit and thus potentially can be used to describe the late stages of transition and early turbulence. This result has been reconfirmed in the recent simulations of Yakhot et al. [4] and Piomelli et al. [5] who studied turbulent channel flow and boundary layers. Despite the fact that the initial conditions employed corresponded to laminar flow, transition to turbulence was faithfully simulated as in standard direct simulations. The RNG subgrid model provides an expression for the eddy viscosity with correct limits both in the high and low Reynolds number range, namely the molecular viscosity and the Smagorinsky equation respectively. Application of the subgrid scale model to complex-geometry flows where a broader range of scales typically exists has not been performed yet.

In this work we consider the flow over a backward-facing step and employ RNG/large-eddy computations to simulate transitional and early turbulent states. A parallel study by Kaiktsis et al. [6] investigates transitional states of the same flow using direct simulations. The paper is organized as follows: In section 2, we present a review of the RNG formalism for homogeneous turbulence and its extension to finite systems. In section 3 we describe the discretization procedure in solving the renormalized equation of motions; and finally, in section 4, we present some preliminary results based on spectral element/large-eddy simulations.

2 RENORMALIZATION GROUP THEORY

In this section we develop a subgrid scale model for inhomogeneous turbulence following the derivation presented first in [1]. To this end, we first review the infrared limit of RNG theory for homogeneous turbulence. In particular, we consider the following system of equations describing the motion of an incompressible fluid stirred by an external force \mathbf{f} ,

$$\frac{\partial \mathbf{v}}{\partial t} + \mathbf{v} \cdot \nabla \mathbf{v} = -\frac{\nabla p}{\rho} + \nu_0 \nabla^2 \mathbf{v} + \mathbf{f} \quad (1a)$$

$$\nabla \cdot \mathbf{v} = 0 \quad (1b)$$

where p is the pressure, ν_0 is the molecular viscosity, and ρ is the density. The force has an energy spectrum given by

$$\langle f_i(k\omega) f_j(k'\omega') \rangle = 2(2\pi)^4 D_0 k^{-3} [\delta_{ij} - \frac{k_i k_j}{k^2}] \delta(\mathbf{k} + \mathbf{k}') \delta(\omega + \omega') \quad (1c)$$

The idea of the infrared RNG method is to eliminate modes from the wavenumber strip defined by $\Lambda e^{-r} < k < \Lambda$, near the ultraviolet cutoff Λ . The system resulting from the elimination of these modes involves modified interaction coefficients and new nonlinearities, as well as modified viscosities and forces. The resulting equations are also rescaled and recasted in a form similar to the original system (1). The first step of the RNG procedure is to Fourier transform equations (1) and solve for the transformed velocity field as follows,

$$v_l(\hat{k}) = G^0 f_l(\hat{k}) - \frac{i\lambda_0}{2} G^0 P_{lmn}(\hat{k}) \int v_m(\hat{q}) v_n(\hat{k} - \hat{q}) d\hat{q} \quad (2a)$$

where $\hat{k} = (k, \omega)$ and the harmonic propagator $G^0 = (-i\omega + \nu_0 k^2)^{-1}$. The rest of the parameters are defined as

$$P_{lmn}(k) = k_m P_{ln}(k) + k_n P_{lm}(k); P_{lm}(k) = \delta_{lm} - \frac{k_l k_m}{k^2} \quad (2b)$$

Here λ_0 is a formal parameter introduced for the iterative procedure.

Next, the transformed velocity field v is split into two components: $v^<(\hat{k})$ with $0 < k < \Lambda e^{-r}$ and $v^>(\hat{k})$ with $\Lambda e^{-r} < k < \Lambda$, the former being the *resolvable* part, while the latter is to be eliminated by repeated substitution. This process of elimination generates an infinite expansion for $v^<$ in powers of λ_0 . Keeping only terms up to second order in λ_0 then a correction term to the bare viscosity $\nu_0 k^2$ is generated, which after the integration over the frequency space $-\infty$ to ∞ and the wave space Λe^{-r} to Λ has the form,

$$\Delta\nu = A_d \frac{\lambda_0^2 D_0}{\nu_0^2 \Lambda^4} \frac{e^{4r} - 1}{4} \quad (3)$$

and A_d is a constant computed exactly in terms only of the space dimensions (d) [1]. Thus, the viscosity resulting from elimination of the modes $v^>$ is,

$$\nu = \nu_0 \left(1 + A_d \bar{\lambda}_0^2 \frac{e^{4r} - 1}{4}\right) \quad (4a)$$

where the dimensionless coupling constant $\bar{\lambda}_0$ is

$$\bar{\lambda}_0 = \lambda_0 \frac{D_0^{1/2}}{\nu_0^{3/2} \Lambda^2} \quad (4b)$$

The above results are valid in the limit $r \rightarrow 0$. It is possible, however, to eliminate a finite band of modes by iterating the above procedure of eliminating an infinitesimally narrow band of modes; this will result in wave-dependent viscosity $\nu = \nu(r)$ and coupling constant $\bar{\lambda} = \bar{\lambda}(r)$. These functions can then be determined by taking the limit $r \rightarrow 0$ in equation (3) in order to obtain the differential equation,

$$\frac{d\nu}{dr} = A_d \nu(r) \bar{\lambda}^2(r) \quad \text{and} \quad \bar{\lambda}^2(r) = \frac{\lambda_0^2 D_0}{\nu^3(r) \Lambda^4} e^{4r} \quad (5a)$$

The solution to this equation is,

$$\nu(r) = \nu_0 \left(1 + \frac{3}{4} A_d \bar{\lambda}_0^2 (e^{4r} - 1)\right)^{1/3} \quad (5b)$$

$$\bar{\lambda}(r) = \bar{\lambda}_0 e^{2r} \left(1 + \frac{3}{4} A_d \bar{\lambda}_0^2 (e^{4r} - 1)\right)^{1/3} \quad (5c)$$

This equation gives a k -dependent viscosity in the infrared limit ($r \rightarrow \infty$) which leads to an energy spectrum similar to the Kolmogorov $k^{-5/3}$ spectrum for the inertial-range. An exact comparison, in fact, with the Kolmogorov spectrum provides the relation between the amplitude of the stirring force D_0 and the mean dissipation rate ($\bar{\epsilon} \propto D_0$) and thus equation (5b) can be rewritten as

$$\nu(r) = \nu_0 \left(1 + a \frac{\bar{\epsilon}}{\nu_0^3 \Lambda^4} (e^{4r} - 1)\right)^{1/3} \quad (6)$$

where $a = 0.120$ as computed in terms of A_d .

It can be shown that a more realistic model whose stirring force satisfies:

$$\langle f_j(k\omega) f_i(k'\omega') \rangle \propto \bar{\epsilon} k^{-d} [\delta_{ij} - \frac{k_i k_j}{k^2}] \delta(k + k') \delta(\omega + \omega'), \forall k \geq k_c \quad (7)$$

$\forall k_c > L^{-1}$ (where L is an integral scale of the flow) also gives a Kolmogorov spectrum in the limit $k \rightarrow \infty$. This is true since all contributions originating from the strip $L^{-1} < k < k_c$ are negligible in the limit $k \rightarrow \infty$. This result is the key idea in extending the above theory in finite systems and inhomogeneous turbulence. In particular, we assume that a turbulent fluid in a finite system in which the flow is locally homogeneous exhibits the Kolmogorov behaviour in the intermediate range $k_c < k < k_d$, where k_d denotes the dissipation cutoff. In addition, it can be shown directly from the equations (1) and the definition of $\bar{\epsilon}$ that $\bar{\epsilon} \approx \epsilon^<$, which in turn can be expressed in terms of the resolvable field and the (enhanced) viscosity, i.e.

$$\epsilon^<(x, t) = \nu(r) \left(\frac{\partial v^<_i}{\partial x_i} + \frac{\partial v^<_j}{\partial x_i} \right)^2 \quad (8)$$

In order to construct a subgrid scale model based on the above formulation we identify the mesh size $\tilde{\Delta}$ as the smallest unrenormalized scale ($\tilde{\Delta} = \Lambda^{-1} e^r$) and employ a Gaussian filter of width $\Delta = 2\tilde{\Delta}$ to obtain,

$$\nu = \nu_0 [1 + H\left(\frac{a\bar{\epsilon}}{(2\pi)^4 \nu_0^3} \Delta^4 - C\right)]^{1/3} \quad (9)$$

where $H(x)$ is the Heaviside function, and $C \approx 100$. An alternative equation for evaluating Δ in the case of nonuniform meshes is the following

$$\Delta^4 = \int^{\Lambda_1} \int^{\Lambda_2} \int^{\Lambda_3} \frac{dk dp dq}{(k^2 + p^2 + q^2)^{7/2}} \quad (10)$$

Here $\Lambda_i = \pi/\Delta_i$ (for $i = 1, 2, 3$) and $\Delta_i = 2\tilde{\Delta}$ equals twice the computational mesh in each direction respectively. The above integral can be readily evaluated by breaking it up to three asymptotic integrals and a finite triple integral that can be computed numerically. In cases of simple geometries (i.e. plane channels) the integral can be evaluated through algebraic relations [4].

The assumption of local homogeneity implies that the eliminated scales are much smaller than the distance y from the nearest wall, for only such scales can be isotropic. Thus Δ must decrease as the distance to the nearest wall decreases (this is of course automatically true for all spectral type discretizations). It follows then from (9) that $\nu \rightarrow \nu_0$ as $y \rightarrow 0$. On the other hand, in regions far from the wall equation (9) reduces to

$$\nu = C_s \Delta^2 \left| \frac{\partial v^<_i}{\partial x_i} + \frac{\partial v^<_j}{\partial x_i} \right| \quad (11)$$

where $C_s = 0.005$. This last equation is the same as the classical Smagorinsky eddy viscosity model [7].

The corresponding renormalized equation of motion (incorporating the full stress tensor) for $v^<$ is,

$$\frac{\partial v^<}{\partial t} + v^< \cdot \nabla v^< = -\frac{\nabla p}{\rho} + \nabla \cdot \nu [\nabla v^< + \nabla^T v^<] + f^< \quad (12)$$

where $f^<$ refers to the renormalized force of the original system in equation (1). It can be shown that $f^< \propto k^2$ and thus is negligible (compared to the bare force which scales as k^{-3}) everywhere but in the buffer region. In the next section we discuss the discretization of this equation subjected to the incompressibility constraint.

3 SPECTRAL ELEMENT METHODOLOGY

To simplify the notation in the following we omit the superscripts, and rewrite the equation of motion as follows

$$\frac{\partial \mathbf{v}}{\partial t} = -\frac{\nabla p}{\rho} + \bar{\nu} \nabla^2 \mathbf{v} + \mathbf{N}(\mathbf{v}) \quad (13a)$$

where the last term includes all nonlinear and forcing terms as well as the viscous terms, i.e.

$$\mathbf{N}(\mathbf{v}) = -\frac{1}{2}[\mathbf{v} \cdot \nabla \mathbf{v} + \nabla \cdot (\mathbf{v} \cdot \mathbf{v})] + \mathbf{f} + \nabla \cdot (\nu - \bar{\nu})[\nabla \mathbf{v} + \nabla^T \mathbf{v}] \quad (13b)$$

where ν here denotes the total viscosity given by equation (9), while $\bar{\nu}$ is an artificial (constant in space) viscosity introduced here for stability reasons. The convective terms are written in skew-symmetric form for aliasing control purposes [8]. Numerical solution of the above system of equations will be obtained in a three-dimensional computational domain Ω . Before we proceed to the spatial discretization of the equations we first review briefly the time-stepping algorithm.

3.1 Semi-Discrete Formulation

The separation of terms in equation (13) leads naturally to a splitting scheme of mixed explicit/implicit type. In particular, the recently developed high-order splitting algorithm based on mixed stiffly stable schemes is used [9]. Considering first the nonlinear terms \mathbf{N} we obtain,

$$\frac{\hat{\mathbf{v}} - \sum_{q=0}^{J-1} \alpha_q \mathbf{v}^{n-q}}{\Delta t} = \sum_{q=0}^{J-1} \beta_q [-\mathbf{N}(\mathbf{v}^{n-q})] \quad (14a)$$

where α_q, β_q are implicit/explicit weight-coefficients for the stiffly stable scheme of order J (see [9]). The next substep incorporates the pressure equation and enforces the incompressibility constraint as follows,

$$\frac{\hat{\mathbf{v}} - \hat{\mathbf{v}}}{\Delta t} = -\nabla p^{n+1}/\rho \quad (14b)$$

$$\nabla \cdot \hat{\mathbf{v}} = 0 \quad (14c)$$

Finally, the last substep includes the viscous corrections and the imposition of the boundary conditions, i.e.

$$\frac{\gamma_0 \mathbf{v}^{n+1} - \hat{\mathbf{v}}}{\Delta t} = \bar{\nu} \nabla^2 \mathbf{v}^{n+1} \quad (14d)$$

where γ_0 is a weight-coefficient of the backwards differentiation scheme employed [9].

The above time-treatment of the system of equations (13) results in a very efficient calculation procedure as it decouples the pressure and velocity equations as in (14bc) and (14c) respectively. As regards time-accuracy of this splitting scheme a key element

in this approach is the specific treatment of the pressure equation, which can be recasted in a form

$$\nabla^2 p^{n+1} = \nabla \cdot \left(\frac{\hat{v}}{\Delta t} \right) \quad (15a)$$

along with the consistent high-order pressure boundary condition (see [9])

$$\frac{\partial p^{n+1}}{\partial n} = n \cdot \left[- \sum_{q=0}^{J-1} \beta_q N(v^{n-q}) - Re^{-1} \sum_{q=0}^{J-1} \beta_q [\nabla \times (\nabla \times v^{n-q})] \right] \quad (15b)$$

where n denotes the unit normal to the boundary Γ . Equation (15) therefore is a Poisson equation with constant coefficients, which can be rewritten in the standard form

$$\nabla^2 \phi = g(x) \quad (16)$$

where we have defined $\phi = p^{n+1}$, and $g(x) = \nabla \cdot \left(\frac{\hat{v}}{\Delta t} \right)$. In the following section we will refer to this equation in order to discuss the spatial discretization of equations (14) in three dimensions using the spectral element method.

3.2 Spatial Discretization

The spatial discretization of (14) is obtained using the spectral element methodology [10], [11], [12]. In the standard spectral element discretization the computational domain Ω is broken up into general brick elements (hexahedra) in three-dimensions, which are mapped isoparametrically to canonical cubes. The accuracy of interpolating the geometry therefore is of the same order as the accuracy of interpolating the field unknowns. Geometry, unknowns and data are then expressed as tensorial products in terms of Legendre-Lagrangian interpolants. The final system of equations to be solved is obtained via a Galerkin variational statement. In particular, the computational domain Ω is covered with $K = 48$ spectral elements of resolution $N_1 = N_2 = N_3 = 12$ in each direction.

To illustrate the spectral element methodology in more detail let us first consider the model equation (16) which represents the elliptic contributions of the governing equations. If we define H_0^1 the standard Sobolev space that contains functions which satisfy homogeneous boundary conditions, and introduce testfunctions $\psi \in H_0^1$, we can then write the equivalent variational statement of (16) as,

$$\int_{\Omega} \frac{\partial \psi}{\partial x_j} \frac{\partial \phi}{\partial x_j} ds = - \int_{\Omega} \psi g ds. \quad (17)$$

The conforming spectral element discretization corresponds to numerical quadrature of the variational form (17) restricted to the space $X_h \subset H_0^1$. The discrete space X_h is defined in terms of the spectral element discretization parameters (K, N_1, N_2, N_3) , where K is the number of spectral elements, and $N_1 - 1, N_2 - 1, N_3 - 1$ are the degrees of piecewise high-order (Legendre) polynomials in the three directions respectively that fill the space X_h . By selecting appropriate Gauss-Lobatto points $\xi_{pq,l}^k$ and corresponding weights $\rho_{pq,l} = \rho_p \rho_q \rho_l$, equation (17) can be replaced by,

$$\sum_{k=1}^K \sum_{p=0}^{N_1} \sum_{q=0}^{N_2} \sum_{l=0}^{N_3} \rho_{pq,l} J_{pq,l}^k \left[\frac{\partial \psi}{\partial x_j} \frac{\partial \phi}{\partial x_j} \right]_{\xi_{pq,l}^k} = - \sum_{k=1}^K \sum_{p=0}^{N_1} \sum_{q=0}^{N_2} \sum_{l=0}^{N_3} \rho_{pq,l} J_{pq,l}^k [\psi g]_{\xi_{pq,l}^k}. \quad (18)$$

Here $J_{pq,l}^k$ is the Jacobian of the transformation from global to local coordinates $(x, y, z) \Rightarrow (r, s, t)$, for the three-dimensional element k . The Jacobian is easily calculated from the

partial derivatives of the geometry transformation at the nodal point (pql) via collocation as follows

$$J = z_t(x_r y_s - x_s y_r) + z_s(x_t y_r - x_r y_t) + z_r(x_s y_t - x_t y_s) \quad (19a)$$

The partial derivatives are calculated from standard Lagrangian interpolations as for example

$$(x_p)_{pql} = D_{pm} x_{mql} \quad (19b)$$

where x_{mql} is the x global coordinate of node (pql); here the derivative operator is defined as $D_{ij} = \frac{dh_i}{ds}(\xi_j)$, and h_i is the Lagrangian interpolant.

The next step in implementing (18) is the selection of a basis which reflects the structure of the piecewise smooth space X_h . We choose an interpolant basis with components defined in terms of Legendre-Lagrangian interpolants, $h_i(r_j) = \delta_{ij}$. Here, r_j represents local coordinate and δ_{ij} is the Kronecker-delta symbol. It was shown in [10], [13] that such a spectral element implementation converges spectrally fast to the exact solution for a fixed number of elements K and $N_{1,2,3} \rightarrow \infty$, for smooth data and solution, even in non-rectilinear geometries. Having selected the basis we can proceed in writing the local to the element spectral element approximations for test functions, data, and geometry and obtain the system matrix; details are presented in [12].

The natural choice of solution algorithm for equation (18) is an iterative procedure; in this case the large matrices (i.e. $P_{ijmn,pq}^k$) need not be stored, but instead compute during the time-stepping the matrix-vector products (i.e. $P_{ijmn,pq}^k \phi_{mnq}$). Two different iterative techniques have been implemented in this context: conjugate gradient techniques, and multigrid methods [13]. A difference of the formulation proposed here as compared to the formulation in [13] is that the high-order splitting scheme adopted in this work results in separate, elliptic equations for the pressure and velocity that can be very efficiently and robustly solved using those iterative techniques without the need of case-dependent preconditioners or other convergence acceleration techniques.

4 RESULTS

Here we report the results of applying the RNG based subgrid LES model to predict transition in complex geometry flows. Earlier work by Yakhot et al. [4] and by Piomelli et al. [5] in channel flows and boundary layer flows respectively suggests that transitional states can be faithfully simulated by this LES model. The problem we consider here is flow over a backward-facing step of the same geometry (expansion ratio approximately two) as the one studied by Armaly et al. [14]. The size of the separation zone is a unique function of the Reynolds number Re for fixed inflow conditions, and thus this flow is a prototype for transition in massively separated wall-bounded flows [6]. The Reynolds number is defined as $Re = \frac{2}{3}U_{max}(2h)/v_0$, where $h = 1$ is the height of the inlet channel, and U_{max} is the maximum velocity at the inlet. The computational domain is described in detail in [6]; briefly, the domain is 35 units long and the spanwise length is $L_z = 2\pi$ corresponding to a wave number $\beta = 1$. The inflow prescribed velocity profile is a blunt profile of the form $U_i(y) = 1 - (2y)^4$, periodic boundary conditions are imposed in span, while Neumann/sponge type conditions are imposed at outflow [15].

In all the results reported here, the RNG subgrid model was active throughout the computation; the production of non-zero eddy viscosity ($\nu > v_0$) is then an indication of transition. The first run is at Reynolds number $Re = 2222$; instantaneous streamlines are plotted in Figure 1 showing the existence of multiple eddies inside the separation

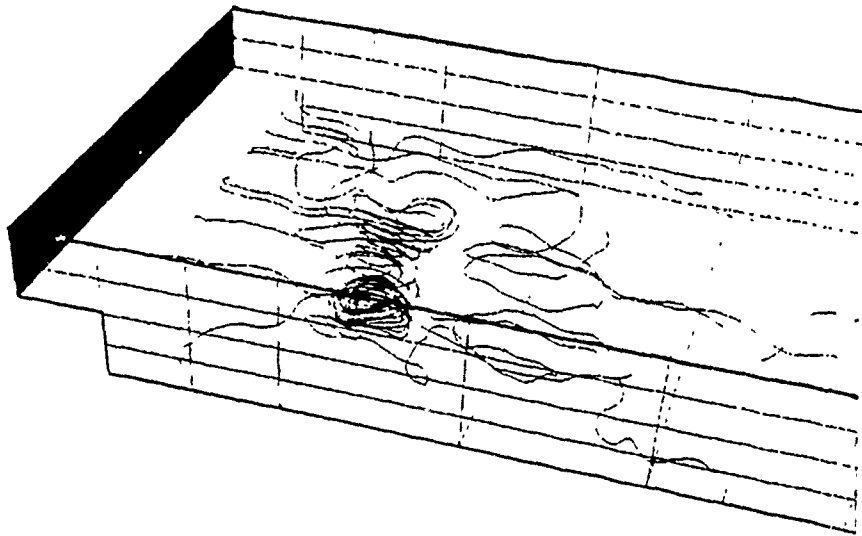


FIG. 1. Instantaneous streamlines at $Re = 2222$.

region. In this case the subgrid model does not produce any eddy viscosity at resolution ($K = 48; N_1 = N_2 = N_3 = 12$). The flow therefore is sufficiently resolved using direct simulation only. The instantaneous multi-eddy structure of the time-averaged flow at this Reynolds number (Figure 2) has disappeared and only a smaller size eddy is present at the step corner. This feature seems to be a high Reynolds number effect and persists to the fully turbulent regime. At Reynolds number $Re = 1000$ which marks the beginning of the transition process the flow does not reverse sign inside the separation zone. This is seen in Figure 3, where we plot the streamwise profile very close to the lower wall from the step location to the outflow.

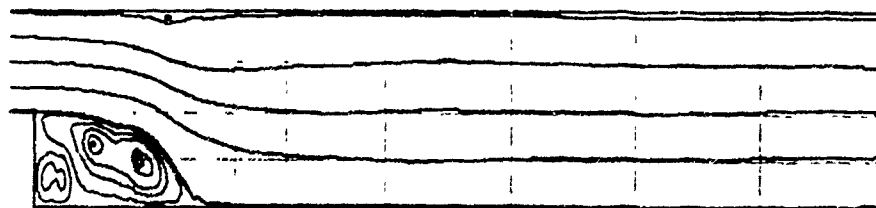


FIG. 2. Streamlines of time-average flow at $Re = 2222$.

Starting the simulation from the velocity field generated at $Re = 2222$ and increasing the Reynolds number to $Re = 4444$, a non-zero eddy viscosity distribution is established at the high-strain regions of the flow, i.e. the shear layer emanating from the step corner and near the walls. Increasing the Reynolds number further to $Re = 8888$ (inside the fully turbulent regime) the eddy-viscosity distribution becomes much broader as seen in the sequence of Figure 4, which show instantaneous values of the total viscosity in different planes parallel to walls. The corner eddy resolved by the direct simulation at $Re = 2222$ is also captured by the large eddy simulation for the fully turbulent regime (in agreement with the experimental results of Tani et al. [16]). This is shown in Figure 5a-b where we plot the streamwise velocity profile very close to the lower wall at Reynolds number $Re = 4444$ and $Re = 8888$, respectively. The positive values very close to the step corner indicate the existence of the eddy, while the further zero gives the value of the reattachment length. This value is in agreement with the experimental results of Armaly et al. [14] within ten percent accuracy. The reason for this discrepancy as explained in detail in [6] relate to variations of the inflow velocity profile.

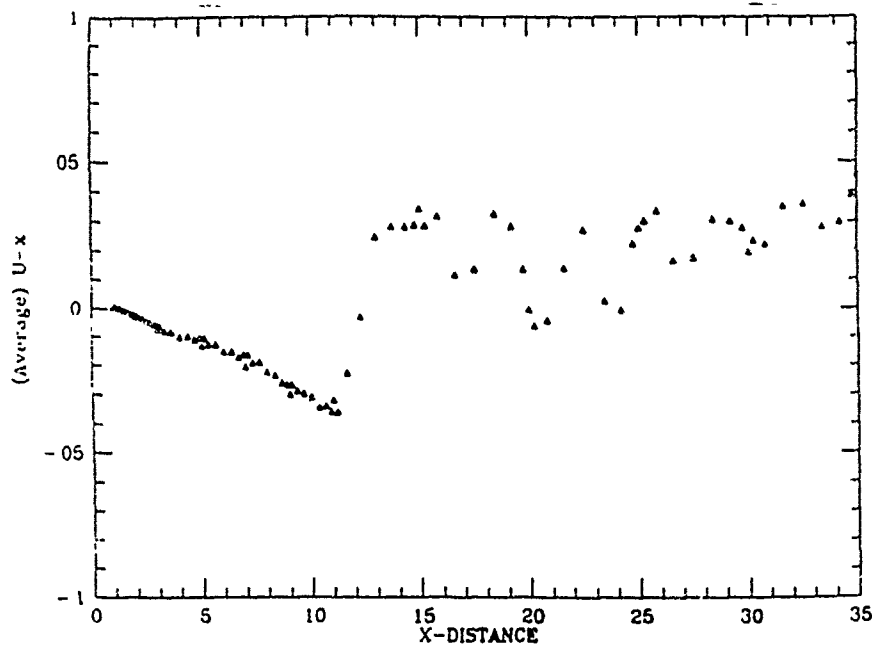


FIG. 3. Streamwise velocity profile through the nearest to the lower wall collocation points. ($\text{Re} = 1000$, direct simulation)

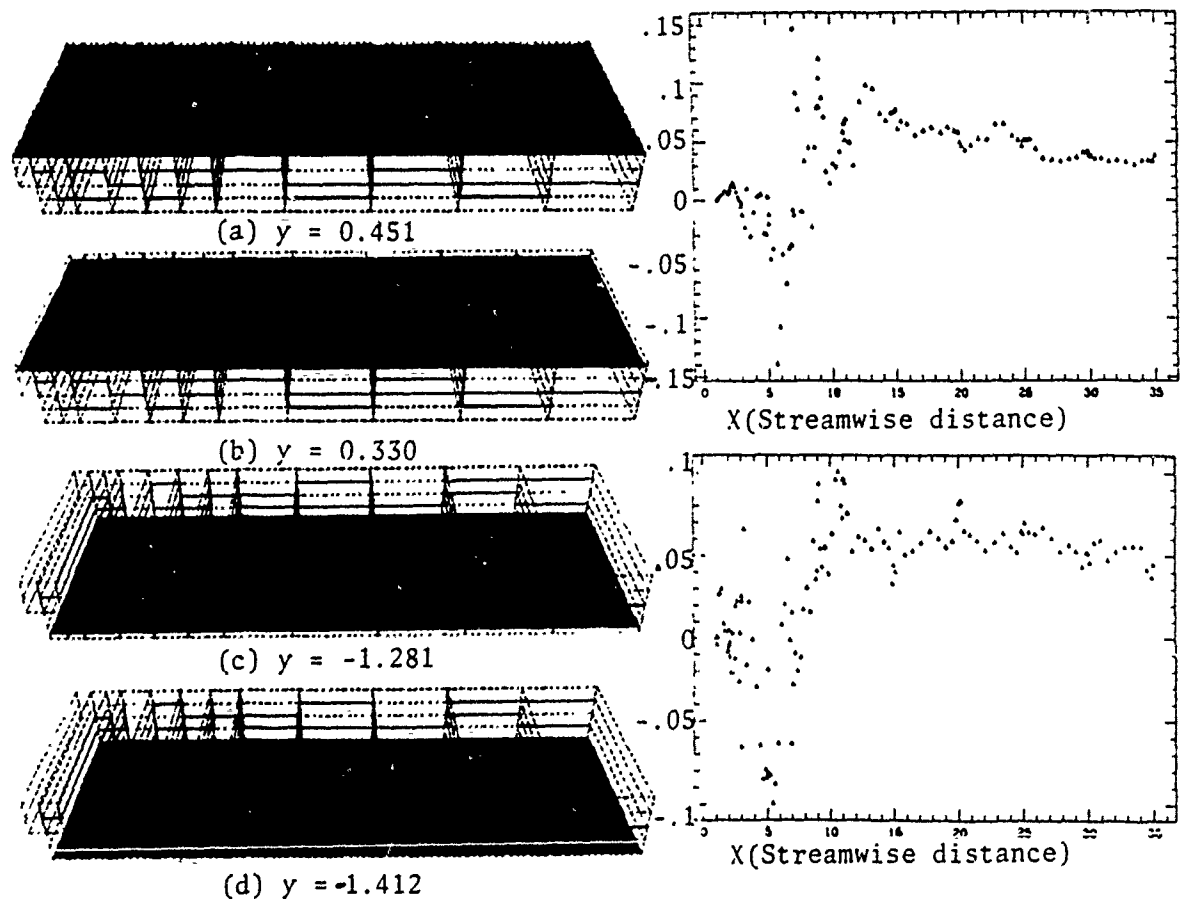


FIG. 4(a-d). Instantaneous total viscosity distribution at $\text{Re} = 8888$. (Blue corresponds to molecular viscosity).

FIG. 5. Streamwise velocity profile through the nearest to the lower wall collocation points (a) $\text{Re} = 4444$, large-eddy simulation; (b) $\text{Re} = 8888$, large-eddy simulation.

The results presented in this paper are preliminary and can only provide a qualitative assessment of the resolution capabilities of the RNG subgrid model in describing inhomogeneous turbulence and, in particular, separated flows. Work still underway addresses

the issue of mesh dependence and compares in detail results of large eddy simulations with direct simulations for the same flow.

5 ACKNOWLEDGEMENTS

Financial support for the current work was provided by grants from NSF (CTS-8906911 and CTS-8906432), by AFOSR Grant AFOSR-90-0124, and DARPA Contract N00014-86-K-0759. Most of the computations were performed on the Cray-Y/MP at Pittsburgh Supercomputing Center, and at the Numerical Aerodynamic Simulation Facility at NASA Ames.

REFERENCES

- [1] Yakhot, V. and Orszag, S.A., Renormalization group analysis of turbulence. I. Basic theory. *J. Sc. Comp.*, 1, 3 (1986).
- [2] Yakhot, V. and Orszag, S.A., Renormalization group analysis of turbulence. *Phys. Rev. Lett.*, 57, 1722 (1986).
- [3] Yakhot, V. and Orszag, S.A., Relation between Kolmogorov and Batchelor constants. *Phys. Fluids*, 30, 3 (1987).
- [4] Yakhot, A., Yakhot, V. and Orszag, S.A., Renormalization group formulation of large-eddy simulations. *J. Sc. Comp.*, 4, 139 (1989).
- [5] Piomelli, U., Zang, T.A., Speziale, C.G., and Lund, T.S. Application of renormalization group theory to the large-eddy simulation of transitional boundary layers. In *ICASE/LaRC Workshop on Instability and Transition*, pp. May 15 – June 9, 1989.
- [6] Kaitksis, S., Karniadakis, G.E., and Orszag, S.A., Onset of three-dimensionality, equilibria, and early transition in flow over a backward-facing step. *J. Fluid Mech.*, submitted 1989.
- [7] Smagorinsky, J., General circulation experiments with the primitive equations. I. The basic experiment. *Monthly Weather Review*, 91, 99 (1963).
- [8] Horiuti, K., Comparison of conservative and rotational forms in large eddy simulations of turbulent channel flow. *J. Comput. Phys.*, submitted 1989.
- [9] Karniadakis, G.E., Israeli, M., and Orszag, S.A., High-order splitting methods for the incompressible Navier-Stokes Equations. *J. Comput. Phys.*, submitted 1989.
- [10] Patera, A.T., A spectral element method for fluid dynamics; Laminar flow in a channel expansion. *J. Comput. Phys.*, 54, 468 (1984).
- [11] Karniadakis, G.E., Bullister, E.T., and Patera, A.T., A spectral element method for solution of two- and three-dimensional time dependent Navier-Stokes equations. In *Finite Element Methods for Nonlinear Problems*, Springer-Verlag, p. 803 (1985).
- [12] Karniadakis, G.E., Spectral element simulations of laminar and turbulent flows in complex geometries. *Appl. Num. Math.*, 6, 85 (1989).
- [13] Ronquist, E.M. *Optimal spectral element methods for the unsteady three-dimensional incompressible Navier-Stokes equations*. Ph.D. thesis, Massachusetts Institute of Technology (1988).
- [14] Armaly, B.F., Durst, F., Pereira, J.C.F., and Schonung, B., Experimental and theoretical investigation of backward-facing step flow. *J. Fluid Mech.*, 127, 473 (1983).
- [15] Karniadakis, G.E. and Israeli, M., Viscous outflow boundary conditions. In preparation (1990).
- [16] Tani, I., Inchi, M., and Komoda, H., Experimental investigation of flow separation associated with a step of a groove. Technical Report 364, Aero. Res. Inst. Tokyo Univ. (1967).

Large-Eddy Simulation of Transitional Flow

Thomas A. Zang

*NASA Langley Research Center
Hampton, VA 23665, USA*

and

Ugo Piomelli*

*Department of Mechanical Engineering
University of Maryland
College Park, MD 20742, USA*

Abstract

The large-eddy simulation technique is applied to the problem of transition to turbulence. The focal example is transition in plane channel flow. Both *a priori* and *a posteriori* analyses are presented. In the former the results of a well-resolved direct numerical simulation of transition are examined for their implications for subgrid-scale models, and in the latter the results of actual large-eddy simulations of transition are compared with those of the direct simulation. Subgrid-scale backscatter (that is, energy flow from small to large scales) is found to be significant at all stages of transition; the dynamic eddy viscosity model [Germano *et al.*, *Proc. Summer Prog. 1990*, pp. 5-17, Stanford U., 1990], which can account for backscatter, predicts transition to turbulence more accurately than two other models which do not have this capability.

*This research was partly supported by the NASA Langley Research Center under Grant NAG-1-1089 and partly by the National Aeronautics and Space Administration under NASA Contract No. NAS1-18605 while the second author was in residence at the Institute for Computer Applications in Science and Engineering (ICASE), NASA Langley Research Center, Hampton, VA, 23665

1 Introduction

Transition from laminar to turbulent flow has many facets. The specific phenomena of particular interest to us pertain to the technological issues of the prediction, modeling and control of transition on aerospace vehicles. Accurate prediction and modeling is especially crucial to the forthcoming generation of advanced aerospace vehicles such as the High Speed Civil Transport and the National Aerospace Plane [1]. For design purposes one needs to know not only the location of transition onset, but also the extent and properties of the transitional zone. In most cases the peak skin friction and wall heat transfer occur near the end of the transitional zone. Accurate predictions of these peak values are especially crucial.

Transitional zone models can be developed both for the Reynolds-averaged Navier-Stokes (RANS) equations and for large-eddy simulations (LES). In the RANS approach models are developed for the higher-order moments of the *ensemble-averaged* Navier-Stokes equations, whereas subgrid-scale (SGS) models for large-eddy simulations are directed towards the small spatial scales of the *spatially-averaged* Navier-Stokes equations. For engineering applications, of course, one wants a RANS transitional zone model and there is a strong practical preference for a model which blends smoothly into an acceptable model for the fully turbulent zone. Virtually all the extant models for the transitional zone are modifications of RANS turbulence models. For recent reviews of RANS transitional models consult [2,3,4].

The opportunities for calibrating RANS models of the compressible transitional zone are quite limited. Until recently experimental data has been the only benchmark. Surface measurements are essentially all that is currently available from supersonic flight and quiet tunnel measurements and there are virtually no suitable measurements whatsoever at hypersonic speeds. It is only at essentially incompressible speeds that detailed flow field data are available.

Fortunately, numerical simulations of transition appear on the verge of providing an alternative source of reliable, detailed flow-field data for the transitional zone. The current status of this field is summarized by Kleiser and Zang[5]. To date, direct numerical simulation (DNS) of transition in wall-bounded flows has been employed primarily for studying the basic physics of laminar-to-turbulent transition. Such computations, based on the Navier-Stokes equations without recourse to any type of physical model, are extremely demanding computationally for the later stages of transition. In simple low-speed (essentially incompressible) flows it is now possible to compute reliably the entire transition process from laminar to fully-developed turbulent flow in extremely simple situations [6,7]. However, at present this is still only feasible for forced rather than for natural transition, *i.e.*, for flows in which transition develops from imposed, specific waves with finite amplitude (on the order of 1%) rather than from the natural disturbance background (which is composed of a broad spectrum of waves). Due to the massive computational effort required by this technique, however, direct simulation of the governing equations is, for the foreseeable future, limited to simple flows and low Reynolds numbers. The computational demands of the *compressible*

transition problem are even more severe: the length scales are shorter, the transitional zones are longer, the equations themselves are more complex, and, ultimately, shock wave and real gas effects must be taken into account. For the solution of problems of engineering interest, other, less computationally intensive, methods are required, and these will necessarily involve some degree of modeling.

A less intensive numerical technique that has been successfully applied to the study of turbulent flows is large-eddy simulation (LES). In LES only the large, energy-containing scales of the motion are computed directly; the effect of the small scales (subgrid scales), which appears in a residual (or subgrid-scale) stress term, is modeled. Since, in turbulent flows, the small scales tend to be more isotropic and homogeneous than the large scales and do not depend very strongly on the boundary conditions, their effect can be represented by fairly simple models. This approach offers better hope of furnishing data on the transitional zone for compressible flow than does DNS. Indeed, a conceivable path to the objective of supplying transitional zone flow-field data for high-speed flow starts with validating LES for incompressible transitional flow against both experimental data and DNS results, continues with validating LES for simple compressible transitional flow against the very limited set of experimental and DNS data, and concludes with applying LES to general compressible transitional problems. At present only the first tentative steps along this path have been taken.

Large-eddy simulations have been successfully applied to a variety of incompressible turbulent, wall-bounded flows such as plane channel flow [8,9,10], boundary layers [11] and channel flow with transpiration [12], but only recently have efforts been made to study transition to turbulence using LES. Early work [13,14,15] was characterized by the application of well-established subgrid-scale (SGS) stress models to the simulation of laminar-turbulent transition. From the technological point of view, however, the issue is not whether LES can start with a laminar flow and end up with a turbulent flow, but rather whether it computes the transition *correctly*, *i.e.*, with the proper duration and properties. Piomelli and co-workers were the first to use the databases generated by well-resolved direct numerical simulations of transition to study the behavior of the SGS stress tensor during transition and to evaluate actual LES of the transitional zone. Piomelli *et al.* [16] observed that during the nonlinear stages, and in particular during the second-spike stage, the subgrid-scale dissipation (*i.e.*, the energy transfer from large to small scales) is significantly smaller than in turbulent flow. They devised an intermittency-like modification of the Smagorinsky [17] model which allowed accurate prediction of the early stages of transition in a flat-plate boundary layer [16] and plane channel flow [18]. Subsequently, in [19], they again calculated a transitional boundary layer flow using a subgrid-scale stress model based on the renormalization group (RNG) theory [20]. This predicts zero eddy viscosity as long as the magnitude of the strain rate tensor is less than some threshold value. A recently devised dynamic subgrid-scale model was also successfully applied to plane channel flow [21].

This article will describe these particular subgrid-scale models for incompressible transitional flow, review the *a priori* tests of the models against direct numerical simulation of plane channel flow, and present *a posteriori* results of actual LES using the various models.

2 Formulation

In large-eddy simulations of incompressible flow the dependent variables (velocity u_i and pressure p) are decomposed into a large-scale component (denoted by an overbar) and a subgrid-scale (SGS) component. The large-scale field is defined by the filtering operation:

$$\bar{f}(\mathbf{x}) = \int G(\mathbf{x}, \mathbf{x}') f(\mathbf{x}') d\mathbf{x}', \quad (1)$$

where the integral is extended over the entire spatial domain and $G = \bar{G}_1 \bar{G}_2 \bar{G}_3$, where \bar{G}_i is the filter function in the i th direction. In the present work x_1 (or x) is the streamwise direction, x_2 (or y) is the wall-normal direction, and x_3 (or z) is the spanwise direction; u_1 , u_2 and u_3 (or u , v and w) are the velocity components in the coordinate directions. The subgrid-scale component is denoted by a prime, and is defined as

$$f' = f - \bar{f}. \quad (2)$$

In the present work, a sharp cutoff filter [22] has been applied in all directions.

The filtered Navier-Stokes and continuity equations, which describe the evolution of the large, energy-carrying eddies, can be obtained by applying the filtering operation to the incompressible Navier-Stokes and continuity equations to yield

$$\frac{\partial \bar{u}_i}{\partial t} + \frac{\partial}{\partial x_j} (\bar{u}_i \bar{u}_j) = - \frac{\partial \bar{p}}{\partial x_i} + \frac{1}{Re} \frac{\partial^2 \bar{u}_i}{\partial x_i \partial x_j} - \frac{\partial \tau_{ij}}{\partial x_j} \quad (3)$$

$$\frac{\partial \bar{u}_i}{\partial x_i} = 0, \quad (4)$$

in which a reference length and velocity scale are used to make \bar{u}_i , \bar{p} , x_i , t and the molecular kinematic viscosity ν dimensionless and to define the Reynolds number Re ; repeated indices denote summation. The effect of the subgrid scales appears in the SGS stress, $\tau_{ij} = \bar{u}_i \bar{u}_j - \bar{u}_i \bar{u}_j$, which must be modeled. For example, in eddy viscosity models, the SGS stress is approximated as

$$\tau_{ij}^m = -2\nu_T \bar{S}_{ij} + \delta_{ij} q_{sgs}^2 / 3, \quad (5)$$

where δ_{ij} is the Kronecker delta function, $q_{sgs}^2 = \tau_{kk}$ is the subgrid-scale energy (which is added to the pressure), \bar{S}_{ij} is the large-scale strain-rate tensor

$$\bar{S}_{ij} = \frac{1}{2} \left(\frac{\partial \bar{u}_i}{\partial x_j} + \frac{\partial \bar{u}_j}{\partial x_i} \right), \quad (6)$$

and ν_T is an eddy viscosity. The eddy viscosity originally proposed by Smagorinsky [17], denoted here by ν_S , is

$$\nu_S = C_S \Delta^2 \sqrt{2\bar{S}_{ij}\bar{S}_{ij}}, \quad (7)$$

in which C_S is a constant and Δ is a length scale, usually taken as

$$\Delta = (\Delta x \Delta y \Delta z)^{1/3}. \quad (8)$$

We have departed here from the usual convention in which C_S appears in Eq. (7) as C_S^2 because we wish to admit models in which C_S is negative, at least locally.

To examine the effect of the SGS stress model on the resolved scales, consider the transport equation for (twice) the resolved kinetic energy $\bar{q}^2 = \bar{u}_i \bar{u}_i$:

$$\begin{aligned} \frac{\partial \bar{q}^2}{\partial t} + \frac{\partial}{\partial x_j} (\bar{q}^2 \bar{u}_j) &= \frac{\partial}{\partial x_j} \left(-2\bar{p} \bar{u}_j - 2\bar{u}_i \tau_{ij} + \frac{1}{Re} \frac{\partial \bar{q}^2}{\partial x_j} \right) \\ &- \frac{2}{Re} \frac{\partial \bar{u}_i}{\partial x_j} \frac{\partial \bar{u}_i}{\partial x_j} + 2\tau_{ij} \bar{S}_{ij}. \end{aligned} \quad (9)$$

One half of the last term on the right-hand side of Eq. (10) will be referred to as “subgrid-scale dissipation”, $\epsilon_{sgs} = \tau_{ij} \bar{S}_{ij}$; it represents the energy transfer between resolved and subgrid scales. If it is negative, the subgrid scales remove energy from the resolved ones (forward scatter); if it is positive, they release energy to the resolved scales (backscatter). The backward and forward scatter components of ϵ_{sgs} , respectively denoted by ϵ_+ and ϵ_- , are defined as

$$\epsilon_+ = \frac{1}{2} (\epsilon_{sgs} + |\epsilon_{sgs}|), \quad \epsilon_- = \frac{1}{2} (\epsilon_{sgs} - |\epsilon_{sgs}|). \quad (10)$$

It is easy to see that eddy viscosity SGS stress models of the Smagorinsky type are absolutely dissipative, so long as $C_S > 0$, since they then assume that the eddy viscosity ν_T is positive, which gives

$$\tau_{ij}^m \bar{S}_{ij} = -2\nu_T \bar{S}_{ij} \bar{S}_{ij} < 0. \quad (11)$$

To study the behavior of the SGS stresses and dissipation in transitional flow we have used the databases obtained from the direct simulation of transition in a plane channel at $Re = 8,000$ (based on the channel half-width δ and the laminar centerline velocity, U_c), with periodic boundary conditions in the streamwise and spanwise directions. Initial conditions consisted of the parabolic mean flow, on which a 2-D Tollmien-Schlichting (TS) mode of 2% amplitude and a 3-D TS mode of 0.02% amplitude were superimposed. The periodicity lengths in the streamwise and spanwise directions were $L_x = 2\pi$ and $L_z = 4\pi/3$, respectively. The initial conditions and Reynolds number matched those of the direct simulation described in [23]. This finely-resolved DNS used $216 \times 162 \times 216$ grid points, and the truncation errors in the primitive variables was less than 0.03% at all times. The spanwise symmetry of the initial conditions was exploited to reduce the computational effort by a factor of two. For

details on the particular numerical method, the physics of channel flow transition, and results for closely related problems, see [24].

We should note that this is a *temporal* transition problem, as opposed to the *spatial* transition problem of technological interest. The extension of LES from temporal to spatial transition problems is a necessary task, whose prime complication is the increased computing demands (by about an order of magnitude) for the spatial problem.

This simulation has been conducted to date up to a time of 330 (made dimensionless by δ and U_c). The results of the present DNS at $Re = 8000$ are qualitatively similar, in both the transitional and turbulent regions, to the pioneering simulation of Gilbert & Kleiser [7] at $Re = 5000$ (see [23]). From $t = 0$ to $t = 165$ the evolution is well-described by a combination of linear stability theory and secondary instability theory [25]. The strongly nonlinear, so-called “one-spike stage” occurs between $t \approx 165$ and $t \approx 175$, the “multi-spike stages” between $t \approx 175$ and $t \approx 185$, the “laminar breakdown” phase commences at $t \approx 185$, the peak wall shear stress occurs near $t = 220$, and fully-developed turbulent flow ensues at about $t = 240$. The fully-turbulent flow is characterized by a Reynolds number based on the wall shear velocity of $Re_\tau = 320$, a Reynolds number based on mean centerline velocity of $Re_{CL} = 6200$, and it has a computational domain in wall units of $L_x^+ 2010$ and $L_z^+ = 1340$. The “transitional zone”, between $t = 165$ and $t = 240$, is the focus of the present work.

3 A Priori Analysis

Piomelli *et al.* [16] performed an *a priori* analysis of channel flow transition for $t \leq 200$ using DNS data in which they focused on the early part of the transitional period. They found that the SGS stresses τ_{ij} and the SGS dissipation ϵ_{sgs} were significantly different from their counterparts in fully-developed turbulent flow. They noted that there were substantial regions of the flow with negative SGS dissipation, indicating the presence of a reversed energy cascade. In other words, transitional flow exhibits backscatter.

The issue of backscatter has been addressed recently by Piomelli *et al.* [26], with an emphasis on turbulent flows, but with some results extracted from the transitional data base described in the preceding section. To investigate the character of backscatter the velocity fields obtained from the direct numerical simulation of channel flow transition were filtered to yield the exact resolved and subgrid-scale velocities, and the exact subgrid-scale dissipation. Figure 1 shows the SGS dissipation at 3 representative times: $t = 170$ (the one-spike stage), $t = 200$ (during laminar breakdown), and $t = 220$ (near the peak wall shear stress). SGS dissipation and backscatter are normalized by the volume-averaged viscous dissipation $\langle \epsilon_v \rangle_V$:

$$\langle \epsilon_v \rangle_V = \frac{1}{2L_x L_z} \int_0^{L_x} \int_0^{L_z} \int_{-1}^{+1} \frac{2}{Re} S_{ij} S_{ij} dx dy dz. \quad (12)$$

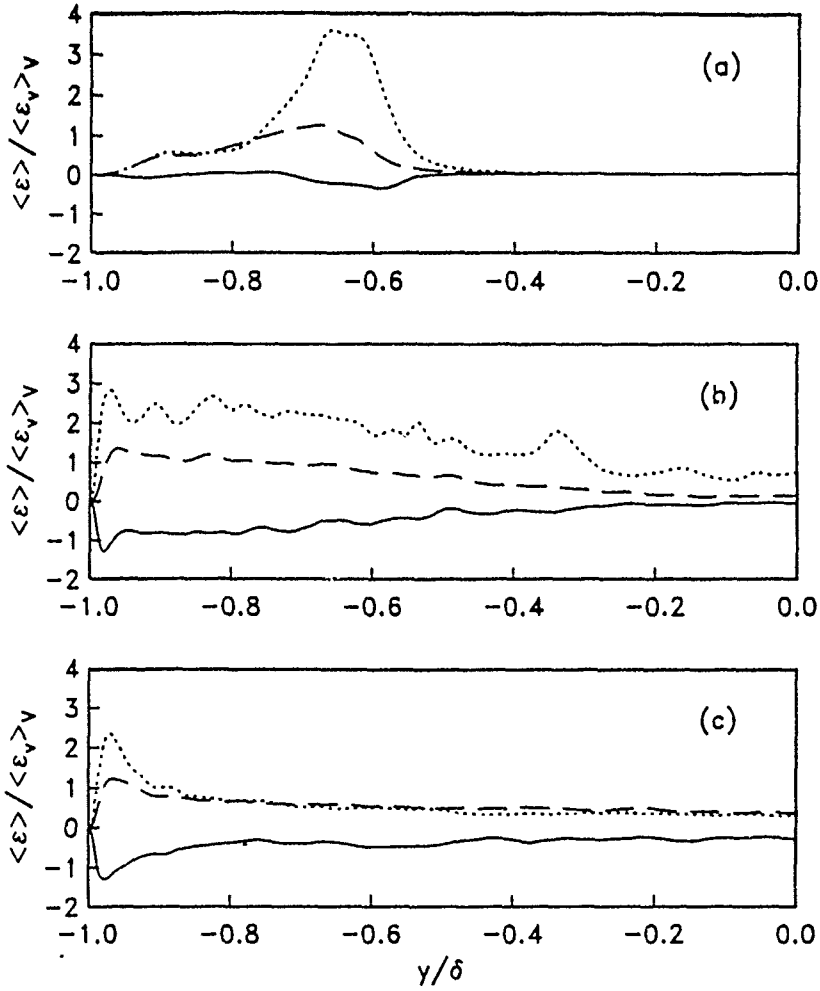


Figure 1: Subgrid-scale dissipation normalized by $\langle \epsilon_v \rangle_V$; cutoff filter. — Plane-averaged dissipation $\langle \epsilon_{sgs} \rangle$; --- root-mean-square fluctuation of ϵ_{sgs} ; plane-averaged backscatter $\langle \epsilon_+ \rangle$. (a) $t = 170$, $\Delta_i = 8\Delta x_i$, $\alpha = 0.01$; (b) $t = 200$, $\Delta_i = 6\Delta x_i$, $\alpha = 0.07$; (c) $t = 220$, $\Delta_i = 6\Delta x_i$, $\alpha = 0.11$.

The amount of filtering is characterized by α , the ratio of subgrid scale kinetic energy, $\langle q_{sgs}^2 \rangle_V$, to total turbulent kinetic energy, $\langle q^2 \rangle_V$, and by the ratio of filter width, Δ_i , to grid size, Δx_i . Since filtering was only applied in the plane parallel to the wall, the ratios $\Delta_i/\Delta x_i$ reported here only refer to the streamwise and spanwise directions. Unless otherwise noted, all quantities are made dimensionless by the channel halfwidth δ , the fluid density ρ and the centerline velocity in laminar flow U_c .

Figure 1 indicates that the backscatter contribution to ϵ_{sgs} is much larger than the mean at all times (and also independent of filter width). Although the subgrid scales extract energy from the large scales in the mean, large values of ϵ_+ and ϵ_- can be expected. The fraction of points in each plane which experience backscatter (shown in Figure 2) is close to 50%, virtually independent of time and distance from the wall.

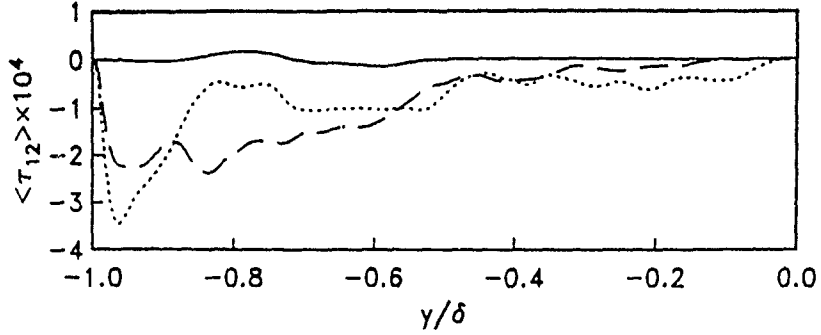


Figure 2: Fraction of grid points at which $\epsilon_{sgs} > 0$; cutoff filter. — $t = 170$, $\Delta_i = 8\Delta x_i$, $\alpha = 0.01$; --- $t = 200$, $\Delta_i = 6\Delta x_i$, $\alpha = 0.07$; $t = 220$, $\Delta_i = 6\Delta x_i$, $\alpha = 0.11$.

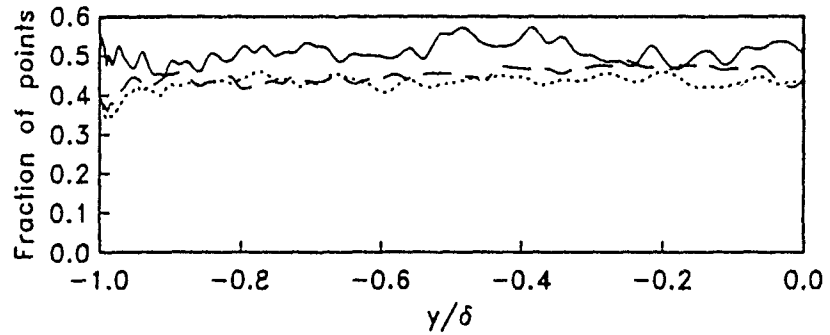


Figure 3: Plane-averaged SGS stress $\langle \tau_{12} \rangle$; cutoff filter. — $t = 170$, $\Delta_i = 8\Delta x_i$, $\alpha = 0.01$; --- $t = 200$, $\Delta_i = 6\Delta x_i$, $\alpha = 0.07$; $t = 220$, $\Delta_i = 6\Delta x_i$, $\alpha = 0.11$.

Figure 3 shows the plane-averaged SGS shear stress $\langle \tau_{12} \rangle$ at the same instants. Initially, the stress is very small, reflecting the absence of small scales in the flow. The positive stress which is observed for $t = 170$ at $y/\delta = -0.8$ is to a large extent responsible for the positive mean SGS dissipation which also occurs around this location.

4 Subgrid-scale Stress Models

The model considered by Piomelli *et al.* [16] and Piomelli and Zang [18] for the subgrid-scale stress in transitional flow was the scaled Smagorinsky model, which has the form of Eq. (5) with the eddy viscosity given by

$$\nu_T = [\gamma (1 - e^{-y^+ / 25})]^2 C_S \Delta^2 \sqrt{2 \bar{S}_{ij} \bar{S}_{ij}}. \quad (13)$$

A superscript + indicates a quantity made dimensionless by the kinematic viscosity ν and the shear velocity $u_r = (\tau_w / \rho)^{1/2}$, where $\tau_w = \mu[\partial \bar{u} / \partial y]_w$ is the wall shear stress and ρ the fluid density. The scaling factor $\gamma = (H_l - H)/(H_l - H_t)$ (in which H is the shape factor, given

by the ratio of the displacement thickness to the momentum thickness, and the subscripts l and t refer, respectively, to laminar and fully-developed turbulent flow) was introduced to decrease the dissipation by the subgrid scales during the early stages of transition [16].

Piomelli *et al.* [19] modeled the SGS stress with an algebraic eddy viscosity model based on the renormalization group theory of Yakhot and Orszag [20]. With this approach the total viscosity, $\nu_{tot} = \nu + \nu_T$ [where ν_T is the eddy viscosity to be used in Eq. (5)] is given by the RNG formula [20]

$$\nu_{tot} = \nu \left[1 + H \left(\frac{\nu_S^2 \nu_{tot}}{\nu^3} - C \right) \right]^{1/3} \quad (14)$$

where $H(x)$ is the ramp function:

$$H(x) = \begin{cases} x & \text{for } x > 0 \\ 0 & \text{otherwise,} \end{cases} \quad (15)$$

C is a constant, ν is the molecular viscosity, and ν_S is the Smagorinsky [17] eddy viscosity, given by Eq. (7).

If the argument of the ramp function $H(x)$ is greater than zero, Eq. (14) has the appearance of a cubic equation for the total viscosity. In reality, however, it is a functional equation, since ν_{tot} and ν_S are related through the renormalized Navier-Stokes equations. The numerical implementation of the model chosen in [19] was the explicit formula of evaluating the total viscosity at the present time step, ν_{tot}^n , by substituting the viscosity at the previous time step, ν_{tot}^{n-1} , in the right-hand side of (14) to yield

$$\nu_{tot}^n = \nu \left[1 + \frac{\nu_S^2 \nu_{tot}^{n-1}}{\nu^3} - C \right]^{1/3}. \quad (16)$$

The filter width Δ was given by Eq. (8). Recent results [27] for LES of turbulent flows suggest that an alternative length scale formula specifically tuned for RNG models might be preferable.

An alternative model, the dynamic eddy viscosity model, was developed recently by Germano *et al.* [21] and applied to both turbulent and transitional channel flows. They defined two filtering operators: one is the *grid* filter, \bar{G} , defined in Eq. (1), with characteristic filter width $\bar{\Delta}$, while the other, the *test* filter, \tilde{G} , is associated with the filter width $\tilde{\Delta}$. In addition, let $\bar{G} = \bar{G}\tilde{G}$ and $\eta = \tilde{\Delta}/\bar{\Delta} > 1$.

In the dynamic eddy viscosity model the eddy viscosity is given by Eq. (7), in which C_S is replaced by a coefficient, C , which is computed from the instantaneous state of the flow. The use of the two filters allows extraction of information regarding the smallest resolved

scales, which is then used to optimize the parameterization of the subgrid scales. The form of the coefficient C used in [21] is

$$C(y, t) = -\frac{1}{2} \frac{\langle \mathcal{L}_{kl} \bar{S}_{kl} \rangle}{\tilde{\Delta}^2 \langle |\tilde{S}| \tilde{S}_{mn} \bar{S}_{mn} \rangle - \tilde{\Delta}^2 \langle |\tilde{S}| \tilde{S}_{pq} \bar{S}_{pq} \rangle}, \quad (17)$$

in which the resolved turbulent stress, \mathcal{L}_{ij} , is defined as

$$\mathcal{L}_{ij} = \tilde{u}_i \tilde{u}_j - \tilde{\bar{u}}_i \tilde{\bar{u}}_j, \quad (18)$$

a tilde indicates the application of the test filter, and a planar average is denoted by $\langle \cdot \rangle$. The coefficient C used in [21] is not completely localized; the average over planes parallel to the wall could, however, be relaxed to a more localized average, although some sort of average is necessary to avoid ill-conditioning arising from pointwise vanishing of the denominator in Eq. (17). The modeled SGS stress tensor is then given by

$$\tau_{ij}^m = \frac{\langle \mathcal{L}_{kl} \bar{S}_{kl} \rangle}{\left(\tilde{\Delta}/\bar{\Delta}\right)^2 \langle |\tilde{S}| \tilde{S}_{mn} \bar{S}_{mn} \rangle - \langle |\tilde{S}| \tilde{S}_{pq} \bar{S}_{pq} \rangle} |\tilde{S}| \bar{S}_{ij}. \quad (19)$$

Note that the model gives zero SGS stress everywhere that \mathcal{L}_{ij} vanishes (as long as the denominator remains finite). Such is the case in laminar flow. As Germano *et al.* [21] observed, this model also produces the correct near-wall behavior of the SGS stress, and the modeled subgrid-scale dissipation, $\epsilon_{sg}^m = \tau_{ij}^m \bar{S}_{ij}$, can be either positive or negative. Thus, the model does not rule out backscatter. The only adjustable parameter in the model is the ratio η .

5 LES Results

The three transitional SGS stress models described above have been applied to the channel flow transition problem described at the end of Section 2. The sharp cutoff filter was employed. The meshes for the LES used up to $48 \times 72 \times 48$ grid points (smaller meshes were used for the early part of the evolution – until $t = 165$ – during which the flow could be computed reliably with no SGS model; as increased resolution was required, the mesh was refined to its final value). The DNS imposed spanwise symmetry, the LES calculations were free of this constraint; although the initial condition which was spanwise symmetric, the LES results eventually became asymmetric due to the influence of round-off errors.

In the case of the scaled Smagorinsky model, the model constant C_S was set equal to 0.01, and the values 5/2 and 1.7 were used for H_l and H_t . The numerical results, at least in the fully-developed turbulent regime, are not expected to depend much on the values of H_l and H_t : turbulent statistics are insensitive to changes in C_S of the order of 20% [9]. For the RNG model, the values recommended by Yakhot and Orszag [20] were chosen for the

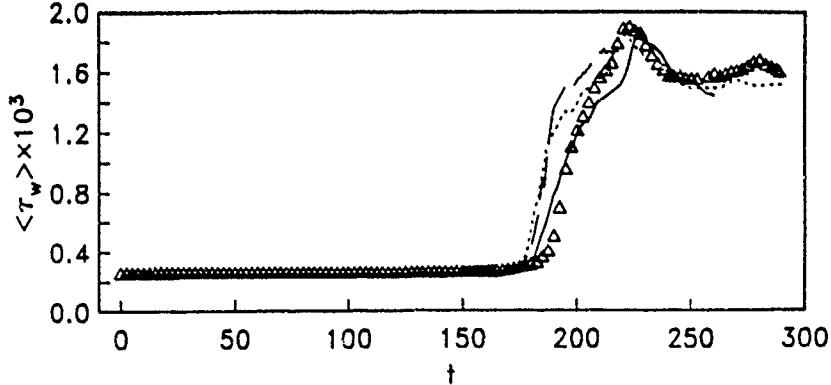


Figure 4: Time evolution of the wall shear. Scaled Smagorinsky model (13) [18]; --- RNG model (14); —— dynamic eddy viscosity model (19) [21]; Δ fine direct simulation [23].

model constants: $C = 100$ and $C_S = 0.015625$. For the dynamic eddy viscosity model, the parameter η was chosen to be 2. The results in [21] suggested that this value was close to an optimal choice for this problem.

Figure 4 presents a comparison of wall shear stress, τ_w , for the well-resolved DNS and the LES using the three different SGS models. In the following, time is normalized by δ/U_c , velocities by U_c , and lengths by δ ; moreover, $U_i = \langle \bar{u}_i \rangle$, and the resolved fluctuations are defined as $u_i'' = \bar{u}_i - U_i$.

Some remarks regarding the evolution of the wall shear stress in the DNS are in order. There is no perceptible change in the wall shear stress during the stages dominated by linear and secondary instability. It is only after the one-spike stage is underway that the wall shear stress rises above its laminar value. During the later part of the transitional zone the wall shear stress overshoots the turbulent value by roughly 20%. Although these results were obtained for a highly idealized simulation of forced transition, this sort of evolution of the wall shear stress is typical of natural transition in a low disturbance environment and accurate prediction of this overshoot as well as the length of the transitional zone are significant indicators of the usefulness of the LES for transition.

During the linear and secondary instability stages all simulations agree very well. Indeed, the eddy viscosity in all three LES is negligible up to this point ($t = 165$). All three LES exhibit a slightly premature rise in wall shear stress near $t = 175$; this rise occurs earlier with the scaled Smagorinsky and the RNG models than with the dynamic eddy viscosity model. Both the scaled and the dynamic eddy viscosity models produce an overshoot in the wall shear stress that agrees well with the actual overshoot and they also produce reasonable agreement for the time-averaged wall shear stress in the fully turbulent state. The peak wall shear stress computed with the scaled Smagorinsky model is within 3% of the DNS prediction. The RNG model performs less well in both of these respects.

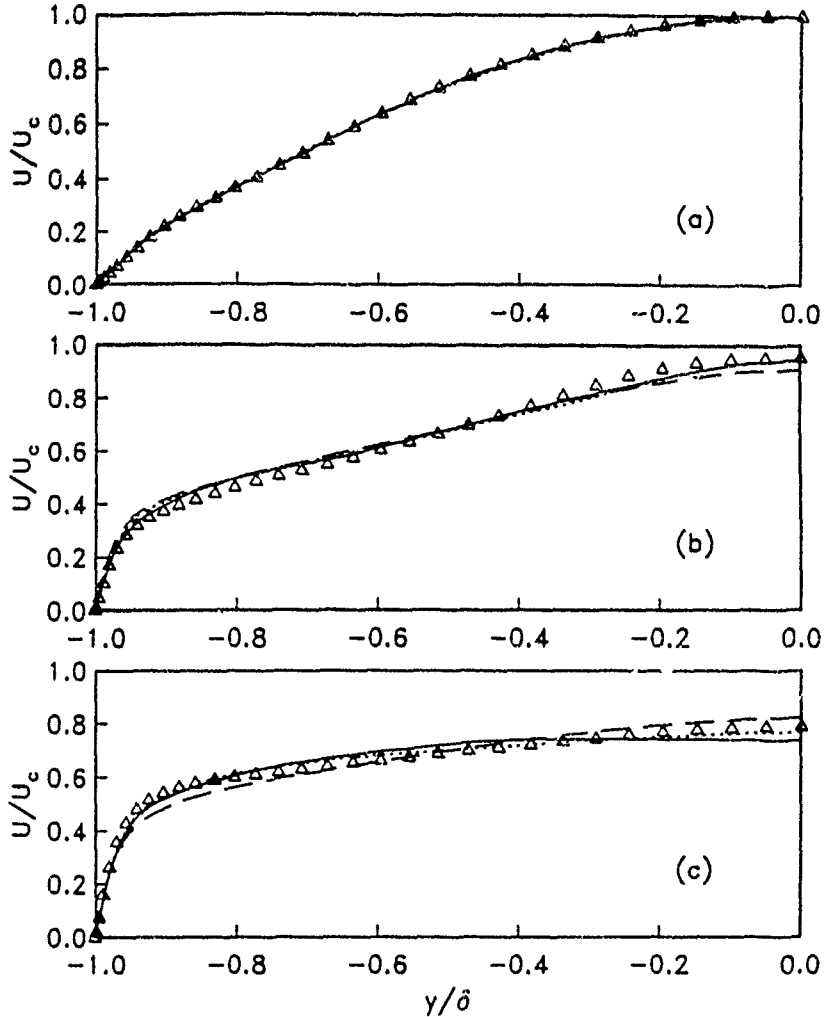


Figure 5: Plane-averaged velocity. Scaled Smagorinsky model (13) [18]; -·- RNG model (14); — dynamic eddy viscosity model (19) [21]; Δ fine direct simulation [23]. (a) $t = 175$; (b) $t = 200$; (c) $t = 220$.

In earlier work [18], the LES results for the scaled Smagorinsky model were compared with both the well-resolved DNS results and with those of a coarse DNS which used the same number of points as the LES, but no model. The coarse-grid DNS results were decidedly inferior to those with the SGS model: the prediction of the peak wall stress from the coarse-grid DNS, for example, was in error by approximately 12%.

In the transitional zone, the eddy viscosity begins to increase for all the models; for example, in the calculation which used the scaled Smagorinsky model the eddy viscosity at $t = 220$ is approximately 40% larger than in it is fully-developed turbulent flow. This is due to the large velocity fluctuations that occur during laminar breakdown, which cause oscillations of the large-scale strain rate tensor of greater amplitude than in turbulent flow. Similar results were observed with all models.

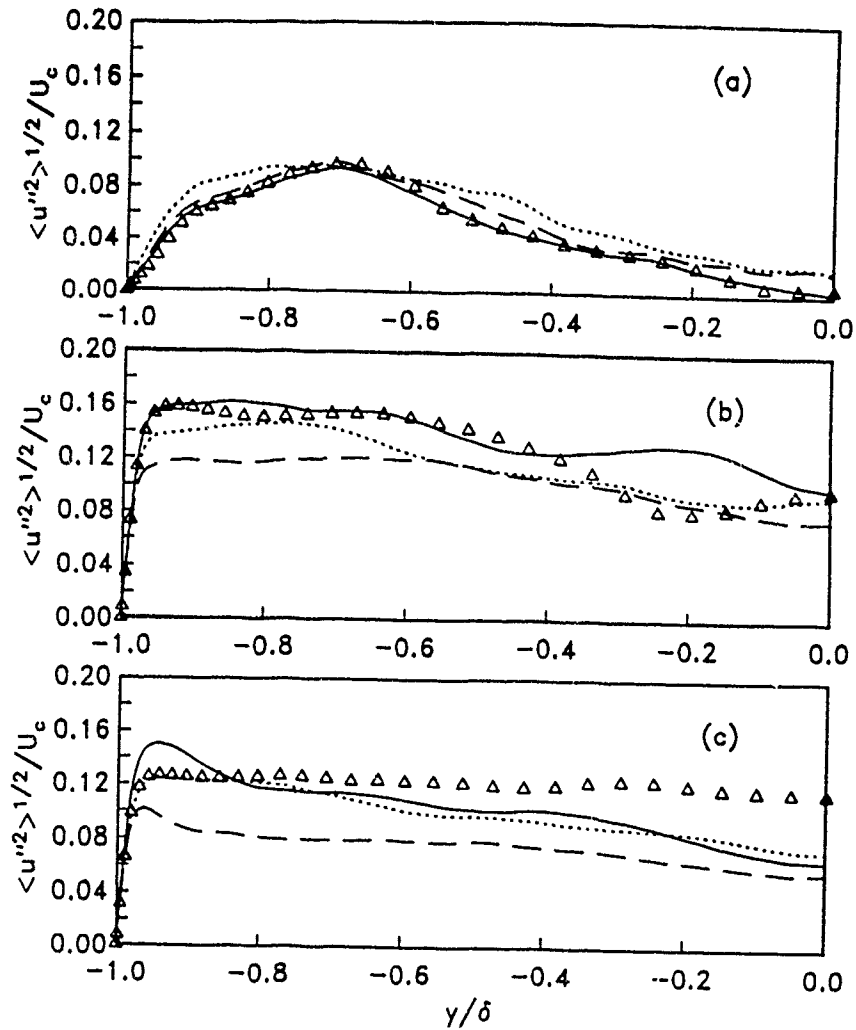


Figure 6: Plane-averaged rms turbulent fluctuations $\langle u''^2 \rangle^{1/2}$ Scaled Smagorinsky model (13) [18]; --- RNG model (14); —— dynar. eddy viscosity model (19) [21]; Δ fine direct simulation [23]. (a) $t = 175$; (b) $t = 200$; (c) $t = 220$.

Figure 5 displays the mean flow at selected times as predicted by the DNS and the various LES calculations. The LES results obtained with all models agree well with the DNS results. Streamwise velocity fluctuations and Reynolds shear stress profiles are shown in Figures 6 and 7, respectively. Some differences between the predictions of the various models can be observed here. For $t = 170$ the scaled Smagorinsky model is the least accurate; the errors are caused primarily by its prediction of slightly premature transition. For $t \leq 200$ the dynamic eddy-viscosity model is significantly more accurate than the other two models studied. At $t = 220$ the profiles of the rms fluctuations of u that are predicted by the LES calculations are peakier than those calculated by the DNS; the level predicted by the RNG model is also lower than the DNS result.

During the late stages of transition the Reynolds stresses can be several times larger than their counterparts in turbulent flow, perhaps due to the highly intermittent character

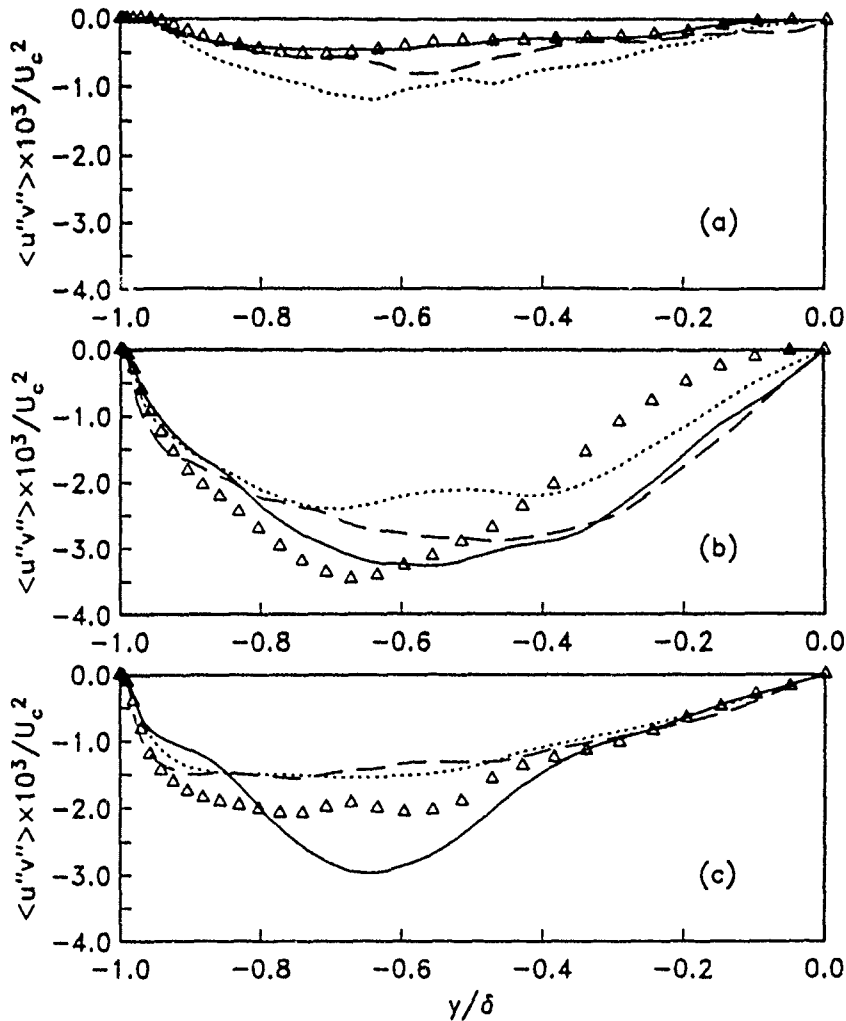


Figure 7: Plane-averaged shear Reynolds stress $\langle u''v'' \rangle$ Scaled Smagorinsky model (13) [18]; --- RNG model (14); —— dynamic eddy viscosity model (19) [21]; Δ fine direct simulation [23]. (a) $t = 175$; (b) $t = 200$; (c) $t = 220$.

of the late stages of the transition process, which results in large velocity gradients and increased turbulent kinetic energy production. The large-eddy simulations were carried out into the turbulent regime, and their results were found to compare well with experimental and numerical results [29,30]. Little difference was observed, in turbulent flow, between the various models, with the dynamic eddy viscosity model giving slightly more accurate results (especially in the near-wall region) than the other two.

When the RNG model was used for LES of boundary-layer transition [19], the eddy viscosity was found to depend very much on the length scale employed. If the length scale was changed by a factor of two due to increased mesh resolution, for example, the first term in the argument of the ramp function in Eq. (14) would change by a factor of sixteen. This may have very significant effects, especially at the early stages of transition, in which the

model is switched on only locally and part of the time. If too coarse a mesh was used, moreover, Eq. (14) yielded a non-zero eddy viscosity even in laminar flow.

As mentioned earlier, the dynamic eddy viscosity is capable of predicting backscatter. With the formulation presented here, backscatter is not localized: if it occurs, it occurs over an entire plane. In their calculation Germano and coworkers [21] observed backscatter (evidenced by a negative eddy viscosity) during transition (for $t \leq 185$).

The LES of channel flow transition reported here were nearly two orders of magnitude less expensive (in terms of CPU time) than the highly-resolved DNS with which they were compared. Thus, LES of transitional flow offers a realistic prospect of producing important information for RANS transition models in more complex geometries and for compressible flow.

6 Conclusions

The behavior of the subgrid-scale stresses has been studied *a priori*. It was found that, during transition, backscatter (*i.e.*, energy flow from small to large scales) is significant. The standard Smagorinsky SGS stress model, which cannot account for this phenomenon is, however, capable of predicting transition to turbulence fairly accurately, as long as the subgrid-scale dissipation predicted by the model is decreased by the introduction of some form of intermittency function.

Alternatively, a model based on renormalization group theory has been used which does not require an *ad hoc* intermittency function. With this model the SGS stresses are essentially zero throughout the linear and early nonlinear stages of transition. This model also is absolutely dissipative, but still captures most of the physical features of transition. Previous experience with this model, however, has shown it to be quite grid-dependent.

Finally, a subgrid-scale model which is not strictly dissipative was used. This model gives more accurate prediction of mean velocity and Reynolds stresses than the others, indicating that use of models capable of predicting backscatter may be beneficial for the study of laminar-turbulent transition.

reflected in the SGS turbulent energy, when the grid resolution is not sufficient. Because of the wrong choice of the energy scale in the Smagorinsky model, C_S had to be adjusted depending on the flow. It may be possible that C_N becomes universal independent on the flow, but C_S may not be so.

4. 'A posteriori' test of the proposed model

In this section, numerical results of LES when the SGS model proposed in the previous section (eqs.(14) and (17)) is incorporated into the actual computation, are briefly presented. Re is chosen equal to 1280, and 128, 129 and 128 grid points are employed in the x, y, z directions, respectively. Model constant C_N in eq.(14) is selected equal to 0.125, and no damping function is included.

Fig.7 displays the mean velocity profile. The von karman constant ($\kappa=0.4$) and another constant ($B=5.0$) are in a good agreement with experimental measurement.²⁵⁾ GS turbulence intensities of streamwise and normal components are shown in Figs.8 and 9, respectively. Note that the contributions from the Bardina model are included in the intensities. For a comparison, experimental measurement²⁷⁾ and numerical results²⁸⁾ obtained by using the Smagorinsky model combined with the Van Driest damping function are included in the figures. Overall agreement with experimental measurement is good. The peak positions of turbulence intensities using the proposed model are closer to the wall than in the previous result, confirming the validity of the presented model.

5. Summary and discussions

A new subgrid scale Reynolds stress model is proposed. The prominent feature of the proposed model lies in the incorporation of 3rd order terms in the anisotropic representation of SGS Reynolds stresses to the eddy viscosity, choosing the normal shear stress as the energy scale. In the present model, previously found discrepancy in the optimized values for the Smagorinsky model constant can be explained, and the use of the empirical damping functions can be avoided, while maintaining a higher correlation with the DNS data than in using the Smagorinsky model. Unlike commonly used damping function of Van Driest type which globally reduces the eddy viscosity magnitude at the same level of y_+ , this model can make a local reduction of the magnitude. The relationship between the Leonard term, the Bardina model and the 2nd order AR is pointed out. The validity of the proposed model is confirmed in 'a posteriori' test. Although the normal shear stress can be almost uniquely chosen in plane channel flow, further refinement is needed for its proper selection in complex geometry, such as in a corner flow of backward facing step, which will be left to the future work.

Acknowledgement

This work was partially supported by a Grant-in-Aid for Scientific Research Nos. 01613002 and 02302043 from the Ministry of Education of Japan, and University of Tokyo- Hitachi Joint

References

- [1] M.R. Malik, T.A. Zang and D.M. Bushnell. Boundary layer transition in hypersonic flows. *AIAA Paper No. 90-5232*, 1990.
- [2] R. Narasimha. The laminar-turbulent transition zone in the boundary layer. *Prog. Aerospace Sci.*, 22:29-80, 1985.
- [3] D. Arnal. Laminar-Turbulent Transition Problems at High Speeds. *The Second Joint Europe/U.S. Short Course on Hypersonics*, 1989.
- [4] R. Narasimha and J. Dey. Transition-zone models for 2-dimensional boundary layers: a review. *Sādhanā, Acad. Proc. Eng. Sci.*, 14:93-120, 1989.
- [5] L. Kleiser and T.A. Zang. Numerical simulation of transition in wall-bounded shear flows. *Ann. R. Fluid Mech.* 23:495-537, 1991.
- [6] N. Gilbert. Numerische Simulation der Transition von der laminaren in die turbulente Kanalströmung. DFVLR-FB 88-55, 1988.
- [7] N. Gilbert and L. Kleiser. Near-wall phenomena in transition to turbulence. In *Near-Wall Turbulence: 1988 Zoran Zaric Memorial Conference*, (S.J. Kline and N.H. Afgan, eds.), pp. 7-28, Hemisphere, Washington, 1989.
- [8] J.W. Deardorff. A numerical study of three-dimensional turbulent channel flow at large Reynolds numbers. *J. Fluid Mech.* 41:453-480, 1970.
- [9] P. Moin and J. Kim. Numerical investigation of turbulent channel flow. *J. Fluid Mech.* 118:341-377, 1982.
- [10] U. Piomelli, P. Moin and J.H. Ferziger. Model consistency in large eddy simulation of turbulent channel flows. *Phys. Fluids* 31(7):1884-1891, 1988.
- [11] L. Schmitt, K. Richter and R. Friedrich. A study of turbulent momentum and heat transport in a boundary layer using large eddy simulation technique. In *Finite Approx. in Fluid Mech.* (E.H. Hirschel, ed.), pp. 232-247, Vieweg, Braunschweig, 1985.
- [12] U. Piomelli, P. Moin and J.H. Ferziger. Large eddy simulation of the flow in a transpired channel. *AIAA Paper No. 89-0375*, 1989.
- [13] K. Horiuti. On the use of SGS modeling in the simulation of transition in plane channel flow. *J. Phys. Soc. Japan*, 55(5):1528-1541, 1986.
- [14] K. Dang and V. Deschamps. Numerical simulation of transitional channel flow. In *Numerical Methods in Laminar and Turbulent Flows*, (C. Taylor, W.G. Habashi and M.M. Hafez, eds.), pp. 423-434, Pine Ridge, Swansea, 1987.
- [15] V. Deschamps and K. Dang. Evaluation of subgrid-scale models for large-eddy simulation of transitional channel flows. In *6th Symp. on Turbulent Shear Flows*, Toulouse, France, September 1987.
- [16] U. Piomelli, T.A. Zang, C.G. Speziale, and M.Y. Hussaini. On the large eddy simulation of transitional wall-bounded flows. *Phys. Fluids A* 2(2):257-265, 1990.
- [17] J. Smagorinsky. General circulation experiments with the primitive equations. I. The basic experiment. *Monthly Weather Review*, 91:99-164, 1963.

- [18] U. Piomelli and T.A. Zang. Large-eddy simulation of transitional channel flow. In press, *Computer Physics Comm.*, 1990.
- [19] U. Piomelli, T.A. Zang, C.G. Speziale and T.S. Lund. Application of renormalization group theory to the large-eddy simulation of transitional boundary layers. In *Instability and Transition*, (M.Y. Hussaini, and R.G. Voigt, eds.), Vol. 2, pp. 480–496, Springer, New York, 1990.
- [20] V. Yakhot and S.A. Orszag. Renormalization group analysis of turbulence. I. Basic theory. *J. Sci. Computing*, 1(1):3–51, 1986.
- [21] M. Germano, U. Piomelli, F. Moin and W. H. Cabot. A dynamic subgrid-scale eddy viscosity model. In *Proc. 1990 Summer Program*, pp. 5–17, Center for Turbulence Research, Stanford, 1990.
- [22] A. Leonard. Energy cascade in large-eddy simulations of turbulent fluid flows. *Adv. Geophys.*, 18A:237–248, 1974.
- [23] T.A. Zang, N. Gilbert and L. Kleiser. Direct numerical simulation of the transitional zone. In *Instability and Transition*, (M.Y. Hussaini, and R.G. Voigt, eds.), Vol. 2, pp. 283–299, Springer, New York, 1990.
- [24] T.A. Zang and S.E. Krist. Numerical experiments on stability and transition in plane channel flow. *Theoret. Comput. Fluid Dynamics* 1:41–64, 1989.
- [25] T. Herbert. Secondary instability of boundary layers. *Ann. Rev. Fluid Mech.* 20:487–526, 1988.
- [26] U. Piomelli, W. H. Cabot, P. Moin and S. Lee. Subgrid-scale backscatter in transitional and turbulent flows. In *Proc. 1990 Summer Program*, pp. 19–29, Center for Turbulence Research, Stanford, 1990.
- [27] A. Yakhot, S.A. Orszag, V. Yakhot and M. Israeli. Renormalization group formulation of large-eddy simulation. *J. Sci. Computing*, 4(2):139–150, 1989.
- [28] M. Germano. Averaging invariance of the turbulent equations and similar subgrid scale modeling. *CTR Manuscript 116*, Center for Turbulence Research, Stanford, 1990.
- [29] R.B. Dean. Reynolds number dependence of skin friction and other bulk flow variables in two-dimensional rectangular duct flow. *Jour. Fluids Engng.*, 100:215–223, 1979.
- [30] J. Kim, P. Moin and R.D. Moser. Turbulence statistics in fully developed channel flow at low Reynolds number. *J. Fluid Mech.* 177:133–166, 1987.

Extended Abstract

LES IN GEOPHYSICAL TURBULENCE PARAMETERIZATION

J. C. Wyngaard and C.-H. Moeng

National Center for Atmospheric Research*
Boulder, Colorado 80307

Numerical models of the ocean and atmosphere on virtually all scales require parameterizations of turbulence effects. These effects are not confined to the oceanic and atmospheric boundary layers, but occur in clouds and in free flows (e.g., "clear-air turbulence") as well. The state of this parameterization science has not been particularly healthy but is improving, thanks in part to turbulence simulation.

We have begun a planetary boundary layer (PBL) model evaluation project at NCAR. Sanctioned by the World Climate Research Program, its focus is the PBL models used within general circulation codes. We have surveyed virtually all approaches to PBL modeling used to date and have separated them into a half-dozen general categories. We have begun defining and coding a representative version of each type. We will then evaluate the performance of each "generic" model against a data base built in part from LES results.

This use of LES is prompted by the rather different situations in geophysics and engineering with regard to direct measurements of flow structure. Geophysical flows are much less accessible to experiment—and are likely to remain so for the foreseeable future. Thus, LES can play a very important role in generating reliable PBL "data bases" from which parameterizations are developed.

In this talk we focus on the convective PBL, first studied by Deardorff in the early 1970s and revisited by others in the mid-1980s. We review the strong and weak points of LES in PBL applications. We discuss other approaches to PBL modeling, and indicate why LES could be characterized as "the worst form of PBL modeling—except for all the others that have been tried."

We then discuss some of the research applications for LES of the convective PBL. We cover the "top-down, bottom-up" diffusion studies of Moeng, Brost, and Wyngaard, including the generalized mixed-layer similarity scaling that they have inspired. An interesting parameterization of these results, which stems from Lumley's 1978 attempt to generalize the eddy-diffusion constitutive equation, is discussed. We show how LES has given the first good insight into the fidelity of contemporary second-order closures for pressure covariances, third moments, and dissipation rates in the convective PBL.

We survey the prospects for LES studies of other important PBL states and conclude with an assessment of the feasibility of treating cumulus cloud systems, whose transport is important for global dynamics and trace constituent balances.

* The National Center for Atmospheric Research is sponsored by the National Science Foundation.

Numerical Simulation of Turbulent Convection over Wavy Terrain

Ulrich Schumann and Kilian Krettenauer
DLR, Institute of Atmospheric Physics,
W-8031 Oberpfaffenhofen, Germany

October 1990

Abstract

Thermal convection of a Boussinesq fluid in a layer confined between two infinite horizontal walls is investigated by direct numerical simulation (DNS) and by large eddy simulation (LES) for zero horizontal mean motion. The lower surface height varies sinusoidally in one direction with an amplitude δ up to $0.15 H$ and a wavelength λ of $1.0 H$ to $4.0 H$ (inclination up to 43°) in different cases, where H is the mean fluid layer height. Constant heat flux is prescribed at the lower surface of the initially resting and isothermal fluid layer. In the LES, the surface is treated as rough surface ($z_0/H = 1 \cdot 10^{-4}$) using the Monin-Obuchow relationships. At the flat top an adiabatic frictionless boundary-condition is applied which approximates a strong capping inversion of an atmospheric convective boundary layer. In both horizontal directions, the model domain extends over the same length (from 4 to $3 H$) with periodic lateral boundary conditions.

We compare DNS of moderate turbulence (Reynolds number based on H and on the convective velocity is 100, Prandtl number is 0.7) with LES of the fully developed turbulent state in terms of turbulence statistics and characteristic large-scale motion-structures. The LES results for a flat surface agree very well with the measurements of Adrian et al. (1986). The gross features of the flow statistic such as profiles of turbulence variances and fluxes are found to be not very sensitive to the variations of wavelength, amplitude, domain-size and resolution and even the model type (DNS or LES) whereas details of the flow structure are changed considerably. The LES for infinite Reynolds number shows more turbulent structures and somewhat larger horizontal scales than the DNS for the finite Reynolds number. To a weak degree, the orography enforces rolls both with axis perpendicular and parallel to the wave crests and with horizontal spacings

between the axis of about 2 to 4 H . The orography has the largest effect for $\lambda = 4H$ in the LES and for $\lambda = 2H$ in the DNS. The results do not change much when the size of the computational domain is doubled in both horizontal directions. Most of the motion energy is contained in the large-scale structures and these structures are persistent in time over periods of the order five convective time scales or longer. The time scales are considerably larger over wavy terrain than over flat surfaces.

1. Introduction

Much is known about thermal convection over ideally homogeneous horizontal surfaces (Busse, 1978, Stull, 1988). Land surfaces are, however, rarely homogeneous. They are often undulated and form hilly terrain. Even when the amplitude of such hilly terrain stays below the mean height of the atmospheric boundary layer, one might expect that the topography has appreciable effect on the flow structure. In this paper, we investigate the effect of terrain on turbulent convection within a boundary layer of finite depth over a wavy surface with zero mean horizontal motion.

In the atmosphere, a convective boundary layer (CBL) forms between the surface and an inversion which is topped by stably stratified air (Stull, 1988). The properties of such a CBL depend at least weakly on the effective Brunt-Väisälä frequency of the stable layer above the turbulent CBL and the time scale of convective motions within the CBL. Moreover, the CBL is non-steady because of growing boundary layer depth; it is however quasi steady in the sense that normalized turbulence profiles become stationary. In this study, we limit the boundary layer by an adiabatic free-slip rigid wall. Such a wall mimics the properties of a very strong temperature inversion above the CBL. For constant surface heat flux such a layer approaches a state in which all statistics of motions approach a strictly steady state. Only the mean temperature remains to increase linearly with time but this does not matter because the flow is driven solely by temperature differences. Hence, the parameter space for this problem is smaller than for the CBL and this property is attractive because of the large number of additional parameters which enter the problem due to the wavy surface. For the same reason we concentrate this study on the fully turbulent case of infinite Reynolds or Rayleigh number. Only for comparisons we also show results of DNS for a finite Reynolds number which is about 9 times the critical for the onset of convection over flat surfaces ($Re_{crit} = (Ra_{crit}/Pr^2)^{1/3}$, $Ra_{crit} = 720$, Krettenauer and Schumann, 1989). The simulations over a flat surface can be compared with the laboratory experiments of Adrian et al. (1986) in a water tank.

Relatively little is known about the impact of heterogeneity of the bounding surfaces. The problem of periodic horizontal disturbances has been inves-

tigated analytically for laminar flow by Kelly and Pal (1978). They showed that the linear analysis of a case with periodic temperature variation at flat walls is closely related to the constant temperature but undulated surface problem. They consider small two-dimensional "resonant" perturbations at a wavelength which equals the critical wavelength of the unperturbed Rayleigh-Bénard problem. The heat-transfer rate increases with the square of the perturbation amplitude. Pal and Kelly (1979) further considered three-dimensional convection. They found that the two-dimensional flow pattern produced by two-dimensional thermal forcing becomes unstable with respect to three-dimensional disturbances, consisting of two sets of oblique rolls.

Hadfield (1988), Schmidt (1988), Graf and Schumann (1990) and Hechtel et al. (1990) have investigated the effects of inhomogeneous surface heating on the turbulent CBL over a flat surface by means of LES. Hadfield (1988) observed a general increase of velocity fluctuations due to an idealized two-dimensional surface heat-flux perturbation. Schmidt (1988) found considerable increase of horizontal velocity fluctuations with increasing inhomogeneity but a small reduction in the vertical velocity component. Graf and Schumann (1990) supported this result from simulations in comparison with field observations including a weak mean wind. Hechtel et al. (1990) simulated an observed case of the CBL with weak mean wind including moisture effects; they found little influence of inhomogeneity on the turbulence statistics. Schädler (1990) found larger effects from variations in surface moisture variations at scales of the order 10 to 20 km using two-dimensional simulations. Briggs (1988) reported on steady downdrafts of 0.4 times the convective velocity scale induced by inhomogeneities in urban areas within rural surroundings at horizontal scales of the order of 30 km.

From field observations on the structure of the atmospheric convective boundary layer, Kaimal et al. (1982) found that "gently rolling terrain" does not seem to affect the turbulence spectra except for a 30 % increase in the length-scale of the spectrum of vertical velocity and a 60 % reduction of the length-scale of temperature. The terrain had an irregular shape with amplitude of about 50 m and horizontal scale of about 10 km while the boundary layer depth is of order 1 km. Druilhet et al. (1983a) made measurements both over homogeneous and over a heterogeneous site with ter-

rain elevations of 48 m standard deviation and a wavelength of about 2 km in convective boundary layers with a depth between 540 and 1360 m. They found that dissipative and spectral length-scales are smaller (about half) over complex domain while all other statistics show smaller differences. Jochum (1988) found only small differences in the vertical velocity variance and temperature fluxes at various scales over smooth and gently modulated terrain. Huynh et al. (1990) compared mean profiles of variances and fluxes of moisture, temperature and vertical velocity fluctuations in convectively mixed layers over homogeneous and over rugged terrain with amplitudes of order 100 m and wavelengths of order 1 km. They did not find any systematic differences in comparison to results obtained over homogeneous terrain.

In a previous paper (Krettenauer and Schumann, 1989), we investigated the present problem for various finite Reynolds numbers. It was shown that for isothermal no-slip boundaries, two-dimensional convection sets in at sub-critical Rayleigh numbers in close quantitative agreement with linear theory of Kelly and Pal (1978). For the problem with boundary conditions as considered in this study, two-dimensional direct simulations show oscillatory roll convection which becomes almost stationary if the Rayleigh number is of order 7000 or less. The two-dimensional convection is unstable with respect to three-dimensional disturbances and a cross-role pattern evolves even over a surface which is undulated in one direction only. For Rayleigh numbers exceeding about 15000, the flow becomes turbulent. The results exhibit little sensitivity of the convection to the wavy surface for a 10% amplitude. These simulations were limited in the Reynolds number and in the domain size; the wavelength was $\lambda = 2H$ and equal to the domain size in all cases.

In this paper, we extend the previous method to large eddy simulations and study the convection over a surface which is sinusoidally undulated in one direction at infinite Reynolds or Rayleigh number. Most previous LES considered flows over plane surfaces (Mason, 1989, Moeng and Wyngaard, 1989, Nieuwstadt, 1990). We implemented a subgrid-scale (SGS) model into a numerical scheme which uses terrain following coordinates. The SGS-model is similar to that used by Schmidt (1988), Schmidt and Schumann (1989), Ebert et al. (1989) and Schumann (1989). It is simplified in

comparison to that of Schmidt and Schumann (1989) in that buoyancy enters the SGS model only through the transport equation of kinetic energy and not through a second-order closure for the SGS fluxes. The same simplification was used with success also by Schumann (1990, 1991). On the other hand, the terrain following coordinates complicate the SGS-model but allow for accurate representation of wavy surfaces.

2. Method

2.1 Equations

As in Clark (1977), the equations of motion are formulated for the Cartesian velocity components u_i as a function of curvilinear coordinates \vec{x}^r which are related to the Cartesian coordinates x_i , according to the transformation

$$\vec{x}^r = f^j(x_i). \quad (1)$$

The actual transformation used in this study is given in the appendix. For an arbitrary scalar field ψ (including the individual Cartesian velocity components) the derivatives with respect to the Cartesian coordinates can be expressed as

$$\frac{\partial}{\partial x_i} (\psi) = \frac{\partial \vec{x}^r}{\partial x_i} \cdot \frac{\partial}{\partial \vec{x}^r} (\psi) \equiv G^{ri} \frac{\partial}{\partial \vec{x}^r} (\psi). \quad (2)$$

Although we are not transforming vector or tensor quantities, we use the common tensor notation where upper indices correspond to contravariant coordinates. This simplifies comparisons with literature in which the tensor version is being used (Pielke, 1984). The summation convention applies to repeated indices. The matrix G^r of differential quotients was called "metric tensor" by Clark (1977) but this term has a different meaning in tensor calculus. Using the Jacobi-determinant

$$V = (\det(G^{ij}))^{-1}, \quad (3)$$

allows to transform derivatives in a "conservative form" (as discussed by Schumann and Volkert, 1984) due to the identity

$$V \frac{\partial}{\partial x_i} (\psi) = \frac{\partial}{\partial \bar{x}^r} (VG^{ri}(\psi)). \quad (4)$$

In the discretized form, the Jacobi-determinant V measures the volume of a grid cell within the curvilinear coordinates in Cartesian space which corresponds to a unit cube in the transformed space.

With these definitions, the model equations are formed by the continuity equation for time-independent density ρ ,

$$\frac{\partial}{\partial \bar{x}^d} (\rho VG^{dq} u_q) = 0, \quad (5)$$

by the momentum balance in terms of the Cartesian velocity components u_i , pressure p , SGS momentum fluxes F_{ij} , buoyancy coefficient βg and temperature T ,

$$\begin{aligned} \frac{\partial}{\partial t} (\rho Vu_i) + \frac{\partial}{\partial \bar{x}^d} (\rho VG^{dq} u_q u_i) &= - \frac{\partial}{\partial \bar{x}^g} (VG^{gi} p) \\ &\quad - \frac{\partial}{\partial \bar{x}^d} (G^{ds} (VF_{is})) \\ &\quad + \beta g \delta_{3i} T. \end{aligned} \quad (6)$$

and by the heat balance in terms of temperature (for constant specific heat capacity) for given SGS heat fluxes Q_r ,

$$\frac{\partial}{\partial t} (\rho VT) + \frac{\partial}{\partial \bar{x}^d} (\rho VG^{dq} u_q T) = - \frac{\partial}{\partial \bar{x}^d} (G^{dr} (VQ_r)). \quad (7)$$

The diffusive fluxes of momentum are driven by the deformation of the velocity field

$$(VD_{ij}) = - \frac{\partial}{\partial \bar{x}^r} (VG^{rj} u_i + VG^{ri} u_j). \quad (8)$$

In case of DNS, the diffusive fluxes are

$$(VF_{ij}) = - \rho v (VD_{ij}). \quad (9)$$

$$(VQ_i) = - \rho \mu \frac{\partial}{\partial \bar{x}^g} (VG^{gi} T). \quad (10)$$

For the LES we use

$$(VF_{ij}) = - \rho K_M (VD_{ij}) + \frac{2}{3} \delta_{ij} \rho V e, \quad (11)$$

$$(VQ_i) = - \rho K_H \frac{\partial}{\partial \bar{x}^g} (VG^{gi} T). \quad (12)$$

The turbulent diffusivities for momentum and heat are computed from

$$K_M = c_v e^{1/2} l, \quad K_H = c_y e^{1/2} l, \quad (13)$$

with the mixing lengths related to the grid spacing $\Delta x, \Delta y, \Delta z$ in real space as appropriate for LES.

$$l = \min\{ 1/3(\Delta x + \Delta y + \Delta z); c_L z \}. \quad (14)$$

The height dependent part becomes effective only in the lowest grid layer and accounts for the limitation of turbulent eddies by the wall. The diffusivities depend also on a characteristic velocity which we compute from the square root of the kinetic energy e of SGS turbulent motions. For this energy we solve the transport equation

$$\begin{aligned} \frac{\partial}{\partial t} (\rho V e) + \frac{\partial}{\partial \bar{x}^d} (\rho V G^{dq} u_q e) &= - \frac{1}{2V} (VF_{qr})(VD_{qr}) \\ &\quad + \beta g (VQ_3) \\ &\quad - \frac{\partial}{\partial \bar{x}^d} (G^{dr} (VS_r)) \\ &\quad - c_{EM} \rho V \frac{e^{3/2}}{l}. \end{aligned} \quad (15)$$

with diffusive fluxes

$$(VS_i) = - \rho \frac{5}{3} c_{3M} e^{1/2} l \frac{\partial}{\partial \bar{x}^g} (VG^{gi} e). \quad (16)$$

The model contains various coefficients for which we use the values as found appropriate by Schmidt (1988).

$$c_{3M} = 0.2, \quad c_{EM} = 0.845, \quad c_v = 0.057, \quad c_y = 0.136, \quad c_L = 1. \quad (17)$$

The coefficients c_x and c_y are slightly smaller than those derived and used by Schmidt and Schumann (1989) and Schumann (1990). Our experience is that such differences are unimportant.

2.2 Discretization

The differential equations are approximated by finite differences. In space we use a staggered grid which allows for a compact representation of the continuity equation, at least for Cartesian coordinates. The momentum equation is integrated using the Adams-Basforth scheme in time and second-order finite differences in space. This scheme conserves momentum and, to a high degree, kinetic energy. The transport equations for temperature and SGS kinetic energy are integrated using the second-order upwind scheme proposed by Smolarkiewicz (1984) which guarantees positivity and exhibits only weak numerical diffusion. The pressure is computed implicitly such that the continuity equation is satisfied after each time step.

Subsequently, some details are reported. Here, Δt denotes the time step increment. Superscripts (n) identify the time step number. Intermediate results between the time-steps are symbolized by a tilde, $\tilde{\cdot}$. Finite differences in space are denoted by δ_r , e.g.,

$$\frac{\partial}{\partial x^r} (\dots) \equiv \delta_r \{ \dots \}. \quad (18)$$

The temperature at the next time level $t^{(n+1)}$ can be computed explicitly.

$$\rho V(T)^{(n+1)} = \rho V(T)^{(n)} - \Delta t \delta_d \left\{ \rho V G^{dq} (u_q T)^{(n)} + G^{dr} (V Q_r)^{(n)} \right\}. \quad (19)$$

Here, the advective fluxes with the transporting velocity $\rho V G^{dq} u_q$ are computed according to the Smolarkiewicz-scheme. The same scheme is used to compute the advective parts of the SGS-energy transport,

$$\rho V(e)^\sim = \rho V(e)^{(n)} - \Delta t \delta_d \left\{ \rho V G^{dq} u_q (e)^{(n)} + G^{dr} (V S_r)^{(n)} \right\}. \quad (20)$$

To this intermediate result we add the energy production rate by shear and buoyancy

$$\rho V(e)^{(n+1)} = K_E \rho V(e)^\sim - \Delta t \left(\frac{1}{2V} (V F_{rs} V D_{rs})^{(n)} - \beta g (V Q_3)^{(n)} \right) \quad (21)$$

and account for the action of dissipation by the damping factor,

$$K_E = \left(1 + \frac{1}{2} c_{EM} \frac{(e^{1/2})^{(n)}}{I} \Delta t \right)^{-2} \quad (22)$$

This factor describes the exact solution in a purely dissipating situation and avoids negative energy results in regions with strong dissipation.

With respect to velocity, we first compute accelerations

$$(b_i)^{(n)} = \delta_d \left\{ \rho V G^{dq} (u_q u_i)^{(n)} + G^{ds} (V F_{is})^{(n)} \right\}, \quad (23)$$

which enter the new (intermediate) velocity according to the Adams-Basforth scheme

$$\begin{aligned} \rho V(u_i)^\sim &= \rho V(u_i)^{(n)} \\ &- \Delta t \left(\gamma_0 (b_i)^{(n)} - \gamma_1 (b_i)^{(n-1)} + \delta_g \left\{ V G^{gi} (p)^{(n)} \right\} - \beta g \delta_3 (T)^{(n+1)} \right), \end{aligned} \quad (24)$$

with $\gamma_0 = 3/2$, $\gamma_1 = 1/2$. Note that the buoyancy is calculated from the new temperature; this is necessary for numerical stability when temperature is computed from an Euler-type time-integration scheme like that of Smolarkiewicz (1984). The final new velocity field has still to be corrected by means of the gradient of the pressure change Δp ,

$$\rho V(u_i)^{(n+1)} = \rho V(u_i)^\sim - \Delta t \delta_g \left\{ V G^{gi} (\Delta p) \right\}, \quad (25)$$

such that it satisfies the continuity equation. The new pressure result is

$$p^{(n+1)} = p^{(n)} + \Delta p.$$

The pressure change Δp is the solution of the linear system of equations corresponding to a discretized elliptic partial differential equation

$$\frac{1}{\Delta t} \delta_d \left\{ \rho V G^{dq} (u_q)^\sim \right\} = \delta_d \left\{ G^{dq} \delta_g \left\{ V G^{gq} (\Delta p) \right\} \right\}_q = L \{ \Delta p \}, \quad (27)$$

to which q enters as a function of the divergence of the intermediate field. The second line in the above equation represents an operator equation, where L denotes the Laplace operator in the transformed coordinates.

As in Schumann and Volkert (1984), the elliptic equations are solved using the following iteration

$$\begin{aligned} H \{ \Delta p^{v+1} - \Delta p^v \} &= (q - L \{ \Delta p^v \}), \\ \Delta p^{v+1} &= 0, \end{aligned} \quad (28)$$

for iterations $v = 1, \dots, 5$. Here L is the operator for the curvilinear system and

$$H \{ \dots \} \equiv \delta_d \left\{ \bar{G}^{dq} \delta_g \{ \bar{V} \bar{G}^{gq} (\dots) \} \right\} \quad (29)$$

is a similar operator which one obtains if the surface height $h(x,y)$ is replaced by its horizontal mean value. The operator H allows for application of fast direct solvers (Schumann and Sweet, 1988).

2.3 The boundary conditions

In the present application, we use cyclic boundary conditions at the lateral boundaries. At the surface, we implement boundary conditions which approximate the noslip condition with zero tangential velocity and prescribed heat flux. The condition selected prescribes constant heat flux per horizontal unit area. This should approximate the fact that a sun in the zenith would provide uniform heating over a horizontal area. In the DNS, the no-slip condition is implemented by second-order finite differences. In the LES, the Monin-Obuchow relationships are used for that purpose as described in Schmidt and Schumann (1989) with adaptions to curvilinear coordinates as documented by Krettenauer (1991). The pressure boundary condition at the surface is defined such that the normal velocity stays zero at the surface. As a consequence of Eq. (25), this implies that the pressure increment has to satisfy the condition

$$\frac{\partial(\Delta p)}{\partial n} = \rho \tilde{u}_n. \quad (30)$$

In curvilinear coordinates, this is a rather complicated condition and discussed in detail by Krettenauer (1991). At the rigid top surface, as it is considered in this study, we prescribe zero vertical momentum fluxes and zero heat flux.

2.4 Initialization and parameters

Subsequently we report results as obtained from a set "D" of direct simulations (DNS) and a set "L" of large eddy simulations (LES), see Table 1. The cases are denoted by a string "mddIL", where $m \in D, L$, identifies the method, $dd \in 0, 10, 15$, the wave-amplitude in percent, $I \in U, 1, 2, 4$, the wavelength (U for undefined), and $L \in 4, 8$, denotes the domain size. All length-scales are measured in units of H . In order to point out that the undulation is strong, we note that the maximum slope $2\pi\delta/\lambda$ reaches 0.942 with an inclination of 43° for $\delta/H = 0.15$. For set L, we have to specify the surface roughness height z_0 . We use $z_0 = 10^{-4}H$.

The results are normalized by the characteristic velocity, height, temperature and time scales,

$$w_* = (\beta g Q_s H)^{1/3}, \quad H, \quad T_* = Q_s / w_*, \quad t_* = H / w_*. \quad (31)$$

which are the "convective" scales as proposed by Deardorff (1970). Here, β is the volumetric expansion coefficient, g gravity, Q_s is the prescribed vertical temperature flux at the surface, and H is the mean height of the flow domain. In the atmosphere, typical values are of the order $w_* = 1.3 \text{ ms}^{-1}$, $H = 1000 \text{ m}$, $T_* = 0.05 \text{ K}$, $t_* = 13 \text{ min.}$.

The set D is run for a Reynolds number Re and Prandtl number Pr ,

$$Re = w_* H / v = 100, \quad Pr = v / \gamma = 0.7. \quad (32)$$

This Reynolds number-value is selected based on the experience from Krettenauer and Schumann (1989), because it is large enough to produce turbulent solutions but small enough to have all scales resolved with the selected discretization. Results from direct simulations for Reynolds numbers 100, 150 and 250 have been reported by Krettenauer and Schumann (1989). It has been found that the flow approaches a turbulent state for all these values.

From the final LES results we estimate that the average SGS kinetic energy is about $0.1 w^2$. Hence the average turbulent diffusivity for momentum can be computed from Eq. 13 and this value can be used to quantify an equivalent Reynolds number which belongs to such a diffusivity. Its value is 888. It is large enough to expect fully turbulent solutions.

In the laboratory experiment of Adrian et al. (1986) the scale-values for the case with largest heat flux $Q_s = 0.450 \text{ K mm/s}$, $Re = 1736$, were $w = 6.96 \text{ mms}^{-1}$, $H = 200 \text{ mm}$, $T = 0.082 \text{ K}$, $t = 29 \text{ s}$.

The initial conditions prescribe zero mean velocities, constant mean temperature and constant SGS kinetic energy. Random perturbations are added to the temperature and velocity field to initiate turbulent convective motions. The actual (non-dimensional) values are

$$T = 10 + 0.1(1 - z/H)\text{ranf}(), \quad w = (1 - z/H)(\text{ranf}() - 0.5). \quad (33)$$

Here, $\text{ranf}()$ is a random number generator, $0 \leq \text{ranf} \leq 1$. The absolute value 10 of the initial temperature, which is large in comparison to the fluctuations, has been selected because it helps to reduce numerical diffusion in the (nonlinear) Smolarkiewicz scheme.

The computations are run until a maximum time of $35 t$. This is a rather large time. For an atmosphere of 1000 m thickness and a heat flux of about 100 Wm^{-2} or 0.1 K ms^{-1} this corresponds to about 6 hours. Schmidt and Schumann (1989) ended their simulations of the atmospheric convective boundary layer at $t = 7 t$. Hence we can expect that our final results are close to steady state.

Figure 2 shows the temporal development of the kinetic energy averaged over the total computational domain versus time for four cases of the LES and the DNS. We see that the initial energy provided by the random perturbations is small. The energy increases in the cases with and without a wavy surface at about the same rate, in particular for the LES cases. In the initial period the energy reaches rather large values according to dominant roll circulations driven by the wavy surface. Later, however, the energy tends to an asymptotic state. The final energy is larger in the LES cases than in the DNS cases because of stronger dissipation at lower Reynolds numbers. Because of the finite domain size, the final energy is not strictly

steady. Therefore, we will present results which are in addition averaged over the last five time units of the simulations.

3. Results

3.1 LES of the flat case, comparison with Adrian et al. (1986)

The present method has been validated by comparison to atmospheric and laboratory measurements for the convective boundary layer which is topped by a stable fluid layer (Schmidt and Schumann, 1989). These comparisons have shown that the results are at least as accurate as measurements for high grid resolution ($160 \cdot 160 \cdot 48$). Graf and Schumann (1990) have compared LES results with recent field observations for a convective boundary layer with nonzero mean wind; they found good comparisons for much larger grid spacings. Further parameter studies and comparisons with LES of F. Nieuwstadt, P. Mason and C.-H. Moeng (personal communication, 1990) have shown that mean profiles of first, second and third-order moments of turbulence quantities in the mixed layer of the CBL can be accurately represented even when using only $40 \cdot 40 \cdot 15$ grid cells in the CBL covering a domain of $4 \cdot 4 \cdot 1.5$ boundary layer depths. It still remains to validate the present code, because it contains many coding changes in order to treat curvilinear coordinates, contains a simplified SGS-model in comparison to that of Schmidt and Schumann (1989), and is applied with a lid at the top of the mixed layer instead of a stable fluid layer.

For this purpose, the LES results will be compared to the laboratory results obtained by Adrian et al. (1986) for convection between a heated lower and an adiabatic rigid upper surface. The experimental data are obtained for $Re = w.H/v$ in between 552 and 1736. The experimental results, scaled by the convective scales, were virtually independent of Re and therefore assumed to be representative to a case with infinite Reynolds number. Therefore, we compare these results to our LES, case L00U4. It should be noted, however, that we simulate a rigid free-slip top surface while the fluid layer in the experiment is bounded by a wall where the fluid comes to rest. Subsequently we compare mean profiles which are obtained by averaging over horizontal surfaces and over the time-period from $t/t_c = 30$ to 35, as a

function of the coordinate z with the experimental data. All results are normalized by the convective scales.

Figure 3 shows the mean kinetic energy. The SGS-part amounts to less than 25 % of the total energy and hence the results can be classified as LES in spite of the still rather coarse grid resolution. The energy is large near the upper surface, because of the free-slip condition; it is also large near the lower surface because there the buoyancy forcing takes its maximum value.

The mean temperature has increased from its initial value of 10 (in units of T_c) to 42.5 because of constant heating in the integration period, as required for heat conservation. The temperature profile is shown in Fig. 4. In this figure, the error bars denote the range of experimental results. We find satisfactory agreement. The larger temperatures measurements at $z/H = 0.03$ might be caused by the finite Reynolds number, in particular because of the rather large Prandtl of water (about 5). The temperature increases in the upper part of the layer with increasing height. This counter-gradient heat transport is caused, as explained in Krettenauer and Schumann (1989), by narrow and fast rising thermals which transport heat from the lower surface directly up to the upper part of the fluid layer from where the remainder of the fluid within the mixed layer is heated by turbulent diffusion and sinking motion from above.

In Fig. 5 we compare root-mean-square (rms) values of vertical and horizontal velocity fluctuations and of temperature fluctuations, as computed from the LES, with the measured results. The scatter of the experimental data characterizes approximately the standard deviation of these measurements. Note that T' is computed without SGS-contributions, which is very large near the lower surface, while SGS-contributions have been included in the velocity results. The vertical velocity is largest in the mid-channel, as expected, and of a magnitude which is only little larger than the value observed in the CBL (Schmidt and Schumann, 1989 pointed out that w' increases slightly with increasing stability; in this sense, the rigid top wall represents the infinite stability case). The measurements are close to the computed results. The systematic deviation to lower measured values in the upper part might be caused by friction at the top surface. Similar comments apply to the horizontal velocity fluctuations. The temperature fluctuations

are largest near the heated wall. Most of these fluctuations originate from very small-scale turbulent eddies, as is known for atmospheric boundary layers. With respect to the vertical temperature flux, which is largest at the lower boundary, the large temperature fluctuations balance the reduced vertical velocity fluctuations. Overall, Fig. 5 shows excellent agreement between LES and experiment.

The vertical temperature flux and the correlation coefficient of vertical velocity and temperature fluctuations are shown in Fig. 6. Obviously, the measured data underestimate the flux. This is most obvious near the lower surface because there the normalized flux is unity by definition. This result suggests that the LES gives higher accuracy than the measurements. The flux profile decreases linearly with height as required for steady state with constant heating rate according to the vertical divergence of the flux. The entrainment flux, which we usually observe in atmospheric cases, is absent for the present case because of the rigid lid. The correlation coefficient is quite high (Druilhet et al. 1983b find a correlation coefficient of 0.5 in the lower 30 % of an atmospheric CBL with linearly decreasing value above that height). The large correlation coefficient signifies that most of the motions are effective in transporting heat.

The cubed vertical velocity in Fig. 7 is of importance with respect to vertical transport of kinetic energy (in the vertical velocity component). Its value is positive throughout the mixed layer and this indicates that the flow structure is composed of narrow updrafts with large upward velocity surrounded by wide and slow downdrafts. The magnitude of this quantity is only a few percent smaller than that found for the CBL. In the CBL, we expect a larger energy transport because this is required to balance the increased energy sink from entrainment at the inversion. The LES shows a small but negative value in the lowest grid cell. This result should not be considered as realistic and is probably an effect of too large dissipation rate near the surface, as discussed by Schmidt and Schumann (1989). Otherwise, the experiment seems to underestimate the energy flux.

These results enter the energy budget. Figure 8 shows the complete budget of kinetic energy as computed from the LES. It shows, as expected, energy production by buoyancy which decreases linearly with height. On average,

the production rate equals the dissipation rate ε , but the dissipation rate is smaller than the production rate in the lower half of the layer. Consequently, there is upward energy transport by vertical motions (T) whereas the pressure acts counter this transport. The residuum characterizes the accuracy of these budget results. (As an exception, the results in Figs. 8 and 9 are obtained from the LES-results at $t = 30 t$, without time-averaging.) For steady state, the mean value of the dissipation should be exactly equal to the mean buoyancy forcing, i.e. equal to $0.5 w^3/H$. For this particular time, the dissipation is little larger, and Fig. 2 shows, in fact, decreasing energy at $t = 30 t$. In passing, we note that the results $\varepsilon \cong 0.5 w^3/H$, $E \cong 0.55 w^2$ (see Fig. 2), for $z > 0.1 H$ imply a dissipation scale $L_\varepsilon = E^{3/2}/\varepsilon \cong 0.82 H$, and this value is in close agreement with results obtained for the convective boundary layer (Schumann, 1991).

In Fig. 9, we compare some components of the energy budget with measured results. With respect to buoyancy forcing we refer to Fig. 6a. There, we had noted already, that the measurements underestimate the forcing considerably (by about 30 %). Also the flux w'^3 appears to be underestimated by the measurements, see Fig. 7. Therefore, it is not surprising to find considerable differences between measured and computed divergence of vertical turbulent fluxes, $-T$ in Fig. 9. The figure shows also $\varepsilon - P$. The data are determined as the residuum from the other measured results according to steady state. In view of these difficulties in the experiment, we still can classify the agreement as satisfactory.

In conclusion, the comparison between the LES results for the plane surface with the experimental results from Adrian et al. (1986) shows that the LES results can be taken to be as reliable as measurements.

3.2 Mean profiles over wavy terrain

In this section we compare mean profiles as computed with the LES for cases L00U4 (flat surface) and for cases L1014, L1024, L1044 with growing wavelength $\lambda/H = 1, 2, 4$. The mean profiles are averages at constant transformed coordinates $\eta = \text{const.}$ which are averaged in addition over the last five time units.

Figure 10 shows that the temperature results are more or less unchanged by the wavy surface. The black areas in the figure envelope the numerical results from the four cases. The differences were too small to become discernible. Small differences are also seen in the vertical velocity fluctuations, Fig. 11c. The heat flux results are affected very little, mainly because the heat flux is prescribed at the surface.

Somewhat larger differences can be seen in the rms-values of horizontal velocity fluctuations. We observe that the x-component increases with increasing wavelength. In the y-component, the changes are smaller and less systematic. Largest changes occur for $\lambda/H = 4$. The total turbulence energy, Fig. 12, shows that the wavy surface has largest effects at small altitudes, but in general the effects are small.

3.3 Turbulence structure

In this section we search for the effects of the wavy lower boundary on the turbulent flow structure. In view of the just presented mean profiles, we expect small influences. In fact, we have found that instantaneous flow fields are dominated by quite random motion components which hide the coherent parts induced by the boundary forcing. Therefore, we will present results averaged over a finite time period within the final part of the simulation period where the average filters out the small-scale and short-living random motions and emphasizes the large-scale and long-living parts of the turbulent motions. For this purpose, we average over the time period $30 \leq t/t_* \leq 35$. The limits of this interval are arbitrarily selected; the interval length of 5 convective time units is large enough to detect persistent structures but still small enough to show up turbulent motions. If one would average over an infinite time period, all motions parallel to the crests of the surface waves should average out.

In Fig. 13, we show the effect of averaging by comparing the results for an instantaneous time to those averaged. This figure applies to case L1014 with $\lambda/H = 1$. We see, that the flow fields are quite random. From the velocity vector plot at the top surface, it is hard to identify the direction of the wave crests (which is along the y-coordinate in the vertical). A regular structure becomes visible, however in the averaged vector plot and the averaged contour plots. Obviously, in this case, the flow is predominantly

composed of two rolls, one with axis parallel to the wave crests and one perpendicular to the crests. The roll diameters is, however, double that one would expect from the wavelength λ . In the time averaged results the motion amplitudes are roughly 60 to 70 % of those in the instantaneous fields. This can be measured in terms of the ratio of maximum velocity vectors (1.78/2.70) or the amplitude of the maximum contour lines. Hence, most of the motion energy is related to long-living flow structures and this structure is best seen from plots of time-averaged fields.

In Fig. 14, we show the results from our "largest" (in terms of domain size and computer effort) cases and compare DNS with LES. The basic structure looks the same. In both cases, the flow is dominated by the few strong updrafts that reached the top boundary. They cause the flow to diverge. Several such divergent flows collide along lines where the fluid sinks back to the mixed layer. Also similar is the amplitude of the maximum vectors, which is only little smaller in the DNS than in the LES. Hence the DNS for these Reynolds numbers come close to the state at infinite Reynolds number. However, some differences are obvious. As expected, the DNS results look smoother. Also, they show smaller horizontal structures. The characteristic horizontal scale can be estimated to be $2H$ for the DNS but $3H$ for the LES. Although these results are obtained for an undulated lower boundary, the results look isotropic and do not show up this forcing. For both simulations, the vertical cross-sections show clearly that the dominant turbulent scales are larger than the wavelength of the surface. It should be noted that the DNS-results have been obtained for the same parameters as in Krettenauer and Schumann (1989) except for larger domain size. The smaller domain size caused the solutions to show a more regular bimodal structure.

Short wavelengths excited by the surface get destroyed by the turbulent motions. Larger wavelengths require long distance forth and backwards flows with increased friction. Hence a certain wavelength will be that with maximum response to the surface wave. In Figs. 15 and 16 we show results from DNS and LES for flat and undulated surfaces with various wavelengths. These figures are selected to identify the effects of surface wavelength on the flow structure at finite and infinite Reynolds numbers. The DNS seems to have a preference with respect to $\lambda = 2H$, whereas the LES preferably

selects $\lambda = 4H$. Of course, these results will be affected by the finite domain size. However, the basic result that the LES gives rise to larger wavelengths than the DNS should be valid. In all cases, the effect of the surface structure on the flow structure is weak. It is strongest for $\lambda = 2H$ in the DNS and for $\lambda = 4H$ in the LES. The latter was shown also by the mean profiles.

In Fig. 17, we look again at the effect of wavelengths and of averaging on the flow structures. Plotted are velocity vectors in a vertical plane. Whereas the instantaneous flow result (top panels) shows little regular structure, coherent structures become obvious in time averaged (middle panels) and in time and y -direction averaged results (lower panels). The results show clearly, that a wavelength $\lambda = H$ is too small to match the dominant turbulent scales and therefore, the undulation has little effect. A wavelength of $\lambda = 4h$, however, seems to be close to the inherent length-scale of the large turbulent eddies and therefore the surface comes into sort of a resonance with the turbulent motion with the result that, on average (time and space), the surface controls a considerable part (but not all) of the motion field.

Up to now, we have discussed the velocity fields. Now, Fig. 18 shows the temperature field near the lower and upper surfaces for various surface wavelengths. Although these are again time-averaged results, the temperature field still looks very random, in particular near the lower surface. Only for the maximum wavelength, we see some systematic hot line along the surface of the wave crest. The temperature at the top surface indicates that large scale motions dominate there. For $\lambda = H$, the structure cannot be uniquely classified. For $\lambda = 2H$, the temperature field is consistent with the cross-roll convection pattern which produces maximum temperatures at the positions of updrafts. For $\lambda = 4H$, the pattern is more consistent with one dominant roll parallel to the wave crest. Hence, in conclusion, large scale coherent structures can be expected only if the surface wavelength is large in comparison to the boundary layer depth.

In Fig. 19, we investigate the effects of various wave amplitudes for fixed wavelengths on the flow structure. Here, we plot the velocity field at the upper surface and the vertical velocity component in a horizontal "plane" at $\eta = 0.5$. We see, that even without surface undulation, case L00U4, the largest scales dominate. With undulation, the flow selects rolls, but the axis

of these rolls are, surprisingly, not parallel rather than perpendicular to the waves and this effect gets enhanced by increasing wave-amplitude. The same qualitative effect was shown by Pal and Kelly (1979) and Krettenauer and Schumann (1989). Overall, this suggests, that short surface waves trigger rolls perpendicular to the crests and long surface waves drive rolls parallel to the surface wave-crests.

3.4 Length-scales, spectra and time correlations

Up to now we have discussed length-scales and time-scales based on the motion pictures. Now, we use correlations and spectra to provide a more quantitative analysis. From Fourier transforms of the turbulent fluctuations along horizontal lines in x or y -direction at fixed vertical coordinate η we compute cospectra $\Phi_{fg}(k)$ between any fluctuating components f and g as a function of horizontal wave-numbers k_x or k_y . The results to be shown represent averages over the free horizontal coordinate and over the time interval $30 \leq t/t_c < 35$. For instance, Fig. 20 shows the power spectra of vertical velocity and temperature fluctuations and their cospectrum, i.e. the vertical heat flux. The spectra are plotted in a form which was used by Schmidt and Schumann (1989) for the heat flux in the convective boundary layer over a plane surface. The present results are obtained for the case with undulated surface, $\lambda = H$, and for both the small computational domain ($L = 4H$) and the large domain ($L = 8H$). The wavelength λ and the wavenumber k are related to each other by $k = 2\pi/\lambda$. The smallest wavenumber depends on the domain size; it amounts to $k_{min}H = 0.78$ in case L1018 and 1.57 in case L1014. We observe from Fig. 20 that the spectra are in close agreement for both cases, i.e. even the largest scales are well approximated in the smaller domain. The surface wavelength $\lambda = 1$ corresponds to a nondimensional wavenumber 6.28 and one would expect that the spectra exhibit peaks of energy at this wavenumber, at least in the x -direction. Most spectra show, however, that this wavenumber is not dominant in the flow. On the contrary, the spectral maxima appear near a wavelength which is smaller than H near the surface but increases to values of the order $4H$ in the upper fluid layer. Only the temperature spectra show a pronounced peak at $k_xH = 6.28$ at least for the lowest grid layer. However, these coherent temperature patterns are only weakly correlated with vertical motions, as we see from the heat flux spectrum in which such a peak is not visible.

If the surface modulation would enforce two-dimensional roll motions, the x-spectra should be much larger than the y-spectra. This is, however, not the case, as we know already from the motion pictures. Instead, we see that the spectra in both directions have similar amplitudes and shapes and this supports, in a more quantitative manner, our previous insight that the motions are quite isotropic with respect to the vertical axis. The heat flux spectra near the surface look very similar to the results shown by Schmidt and Schumann (1989). However, the present case is free of entrainment at the upper boundary and hence the spectra are throughout positive in our case whereas negative flux contributions have been found in the atmospheric boundary layer.

Similar spectra have been computed for all other cases. However, space does not allow to show all details. Instead we follow common practice and present the wavelengths for which $k\Phi_{ww}(k)$ achieves its maximum value. For example, Fig. 21 shows this wavelength for the case with plane surface (L00U4) in comparison to results from measurements in atmospheric convective boundary layers. The results of Caughey and Palmer (1979) are obtained for homogeneous surfaces. Obviously, our numerical result agrees very well with the data which exhibit considerable scatter. The numerical results even agree with the data in the upper part where the boundary conditions in the atmosphere and in the simulations differ. Obviously, the characteristic wavelength increases from zero near the surface up to an order $2H$ in the upper third of the boundary layer and then decreases again to smaller values at the upper boundary. Figure 21 contains also the interpolating curve which Kaimal et al. (1982) found to represent measurements over hilly terrain. Their curve indicates somewhat larger wavelengths but the differences appear to be within the scatter of the data.

In Fig. 22 we report similar length-scales as obtained from spectra along x and y-coordinates and from vertical velocity, heat flux and temperature fluctuations. The individual curves are from three cases with different surface wavelengths. It should be noted that the finite domain size $L = 4H$ restricts the possible values of the wavelengths to integer fractions of the domain size. This explains the non-smooth behaviour of these results (Fig. 21 looked smoother because there we had plotted the mean of length-scales in x and y-direction). In order to make the curves distinguishable, some

of them have been reduced or increased by factors of 1.02. It is known that very long averaging periods are required to give reliable averages with respect to such length-scales. Hence, we cannot trust the results in all details. Nevertheless, we find that there is little systematic variation between the various cases and that the length-scales in x and y-direction are quite close to each other. This is consistent with the findings of Kaimal et al. (1982) and it supports again in a quantitative manner our previous finding that the surface wave has generally little effects on the flow structure. If any systematic trend is present than it consists of an increase in length-scales in x-direction with increasing surface-wavelength. At the same time, the length-scales in y-direction are decreasing, at least partly..

Finally, we evaluate the temporal persistence by means of time correlations, e.g. for the horizontal velocity fluctuations,

$$R_u(\Delta t, \eta) = \frac{\overline{u'(t_0) u'(t_0 + \Delta t)}}{\overline{u'(t_0) u'(t_0)}}, \quad (34)$$

where the averages are taken over the x and y-directions. This correlation coefficient depends on height η , time increment Δt , and the selected reference time t_0 . Here, we use $t_0 = 30 t$. Figure 23 shows, e.g., the correlation coefficient for $\Delta t = 4 t$ for two velocity components and for the temperature and for various cases. The full curves represent the correlations for the plane surface. We find that the correlation profiles have a shape very similar to the variances itself. This means, the motion components with largest energy have the largest correlation time. The correlations are quite small, however. This means, that most of a structure looses its form within a time period of about $4 t$. A similar result has been obtained by inspection of tracer diffusion by Ebert et al (1989). Considerable larger correlations are, however, found for the cases with surface wave. We observe that the correlation coefficients grow everywhere with increasing surface wavelength. The increase is particularly large with respect to vertical velocity fluctuations near the surface. Figure 23 shows also the "total" time correlation which is computed using averages over the whole computational domain. We see from Fig. 23 that the correlation decreases quite quickly with Δt . Again, we see that the correlations are considerably larger with surface waves, in particular for $\lambda = 4 H$.

4. Discussion and Conclusions

In summary, the comparison between the LES results for the flat surface with the experimental results from Adrian et al. (1986) shows that the LES results can be taken to be as reliable as laboratory measurements for high Rayleigh number flows. We find that the convection pattern is composed of large-scale components which persist over more than five convective time units plus small-scale random turbulent motions. The LES-results look less regular than the direct simulation results. The large-scale structures are similar in both models but the characteristic scale of the largest motions is about 50 % larger in the LES than in the DNS. The motion structures are persistent over longer time periods in the presence of surface waves which seem to "lock" the motions to fixed positions. Otherwise, the effect of the surface wave is weak within the limits $\delta \leq 0.15$, $\lambda/H \leq 4$, studied in this paper. In view of the fact that the maximum surface-slope reaches 43^0 , this is a noteworthy result. Terrain-induced coherent structures can be expected only if the surface wavelength is large in comparison to the boundary-layer depth. Shorter waves seem to preferably trigger rolls perpendicular to the crests whereas long surface waves drive rolls parallel to the surface wave-crests. However, in any case, the terrain-induced motion parts are rather small in comparison to the random turbulent components.

Our results confirm field observations (Kaimal et al., 1982, Druilhet et al., 1983a, Jochum, 1988, Huynh et al., 1990) which report little differences with respect to observations over homogeneous surfaces. In particular, we have found little systematic variation of length-scales with respect to terrain.

The present study was limited to the case of a boundary layer topped by a rigid free-slip adiabatic lid. As a consequence it does not experience the effects of entrainment at an inversion of finite stability or the interaction with gravity waves above the inversion. These effects may be important but we believe they are not. Our main argument is that all statistics which we reported and also those from LES of the CBL by other groups, as reviewed by Nieuwstadt (1990), are very similar to those measured for atmospheric convective boundary layers. The present method could easily be applied to

cases with a free stable troposphere above the mixed layer, however, then the results dependend on many more parameters so that a single additional case study would not be of much help.

In summary, we have investigated the structure of the convective layer above wavy terrain. We have identified some rather surprising effects of the two-dimensional terrain on three-dimensional motions. In particular we find that a two-dimensional model would be totally misleading. The results show that three-dimensional motions are enforced by terrain, like rolls perpendicular to the wave crests, which cannot be predicted with two-dimensional models. On the other hand, the results show that wavy terrain has rather small effects on the mean turbulence profiles as long as the wavelength is less than $4H$ and the wave amplitude less than $0.15H$. Note that such a wave has a height difference of $0.3H$ between valley and summit.

As a next step, we plan to investigate the effects of terrain on the turbulent boundary layer for cases with mean wind. Although the present code could be applied to this problem without any change, we expect problems from numerical approximation errors. The common "trick" of using a Galilean transformation, which is often used for LES of shear flows, cannot be applied for flow over wavy terrain.

Acknowledgments. This work was supported by the Deutsche Forschungsgemeinschaft.

Appendix. Transformation on terrain following coordinates

The transformation maps the domain above a wavy surface at height $h(x, y)$ and below a plane top surface at $z = H$ onto a rectangular transformed domain. It contains also transformation functions which allow for variable resolution along the three coordinate directions using monotonic functions f' . The general transformation $\bar{x}' = f'(x_i)$ is, hence, represented by the special transformation

$$\begin{aligned}\bar{x} &= f^1(x), \\ \bar{y} &= f^2(y), \\ \bar{z} &= f^3(\eta), \quad \eta = \eta(z, h) = H \frac{(z - h)}{(H - h)}, \quad h = h(x, y).\end{aligned}\tag{35}$$

Subsequently, differentials of any quantity ψ are denoted by commas,

$$\psi_{,x} \equiv \frac{\partial \psi}{\partial x}\tag{36}$$

With this notation, the differential matrix is

$$G^{ij} = \frac{\partial \bar{x}^i}{\partial x_j} = \begin{pmatrix} G^{11} & G^{12} & G^{13} \\ G^{21} & G^{22} & G^{23} \\ G^{31} & G^{32} & G^{33} \end{pmatrix} = \begin{pmatrix} f_x & 0 & 0 \\ 0 & f_y & 0 \\ f_{\eta} \eta_{,h} h_{,x} & f_{\eta} \eta_{,h} h_{,y} & f_{\eta} \eta_{,z} \end{pmatrix}\tag{37}$$

with

$$\eta_{,h} = \frac{(\eta - H)}{(H - h)}, \quad \eta_{,z} = \frac{H}{(H - h)},\tag{38}$$

and

$$f_x = \frac{df^1(x)}{dx}, \quad f_y = \frac{df^2(y)}{dy}, \quad f_{\eta} = \frac{df^3(\eta)}{d\eta}.\tag{39}$$

In the present paper, we actually use the equidistant transformations for which these abbreviations have the constant values $1/\Delta x$, $1/\Delta y$, and $1/\Delta \eta$, respectively. The Jacobi-determinant is

$$V = (G^{11} G^{22} G^{33})^{-1} = \left(\frac{1}{f_x} \cdot \frac{1}{f_y} \cdot \frac{1}{f_{\eta}} \cdot \frac{(H - h)}{H} \right).\tag{40}$$

References

- Adrian, R. J., Ferreira, R. T. D. S., Boberg, T., 1986: Turbulent thermal convection in wide horizontal fluid layers. *Experiments in Fluids* 4, 121-141.

- Briggs, G. A., 1988: Surface inhomogeneity effects on convective diffusion. *Boundary-Layer Met.* 45, 117-135.
- Busse, F. H., 1978: Non-linear properties of thermal convection. *Rep. Prog. Phys.*, 41, 1930-1967.
- Caughey, S. J., Palmer, S. G., 1979: Some aspects of the turbulent structure through the depth of the convective boundary layer. *Q. J. R. Met. Soc.* 105, 811-827.
- Clark, T., 1977: A small-scale dynamical model using a terrain-following coordinate transformation. *J. Comput. Phys.*, 24, 186-215.
- Deardorff, J. W., 1970: Convective velocity and temperature scales for the unstable planetary boundary layer and for Rayleigh convection. *J. Atmos. Sci.*, 27, 1211-1213.
- Druilhet, A., Noilhan, J., Benech, B., Dubosclard, G., Guedalia, D., Frangi, J., 1983a: Étude expérimentale de la couche limite au-dessus d'un relief modéré proche d'une chaîne de montagne. *Boundary-Layer Met.* 25, 3-16.
- Druilhet, A., Frangi, J. P., Guedalia, D. and Fontan, J., 1983b: Experimental studies of the turbulence structure parameters of the convective boundary layer. *J. Clim. Appl. Met.* 22, 594-608.
- Ebert, E. E., U. Schumann, and R. B. Stull, 1989: Nonlocal turbulent mixing in the convective boundary layer evaluated from large-eddy simulation. *J. Atmos. Sci.* 46, 2178-2207.
- Graf, J., Schumann, U., 1990: Simulation der konvektiven Grenzschicht im Vergleich mit Flugzeugmessungen beim LOTREX-Experiment. Subm. to Meteorol. Rdsch., Report DLR-IB-553-6/90.
- Hadfield, M. G., 1988: The response of the atmospheric convective boundary layer to surface inhomogeneities. Colorado State University , Atmospheric Science Paper No. 433
- Hechtel, L. M., Moeng, C.-H., Stull, R. B., 1990: The effects of nonhomogeneous surface fluxes on the convective boundary layer: A case study using large-eddy simulation. *J. Atmos. Sci.* 47, 1721-1741.
- Huynh, B. P., Coulman, C. E., Turner, T. R., 1990: Some turbulence characteristics of convectively mixed layers over rugged and homogeneous terrain. *Boundary-Layer Met.* 51, 229-254.
- Jochum, A., 1988: Turbulent transport in the convective boundary layer over complex terrain. Proc. Eighth Symposium on Turbulence and Diffusion, San Diego, Americ. Meteorol. Soc., Boston, Mass., p. 417-420
- Kaimal, J. C., Eversole, R. A., Lenschow, D. H., Stankow, B. B., Kahn, P. H., Businger, J. A., 1982: Spectral characteristics of the convective boundary layer over uneven terrain. *J. Atmos. Sci.* 39, 1098-1114.
- Kelly, R. E., Pal, D., 1978: Thermal convection with spatially periodic boundary conditions: resonant wavelength excitation. *J. Fluid Mech.*, 86, 433-456.

- Krettenauer, K., 1991: Numerische Simulation turbulenter Konvektion über gewellten Flächen. Dissertation, DLR-FB, in preparation.
- Krettenauer, K., Schumann, U., 1989: Direct numerical simulation of thermal convection over a wavy surface. Meteorol. Atmos. Phys. 41, 165-179.
- Mason, P. J., 1989: Large eddy simulation of the convective atmospheric boundary layer. J. Atmos. Sci. 46, 1492-1516.
- Moeng, C.-H., and J. C. Wyngaard, 1989: Evaluation of turbulent transport and dissipation closures in second-order modeling. J. Atmos. Sci., 46, 2311-2330.
- Nieuwstadt, F. T. M., 1990: Direct and large-eddy simulation of free convection. Proc. 9th Intern. Heat Transfer Conference, Jerusalem, 19-24 August 1990, Vol. I, pp. 37-47.
- Pal, D., Kelly, R. E., 1979: Three-dimensional thermal convection produced by two-dimensional thermal forcing. Amer. Soc. of Mech. Engineers, paper ASME 79-HT-109, 8 pp.
- Pielke, R. A., 1984: Mesoscale meteorological modeling. Academic press, Orlando, USA, 612 pp.
- Schädler G., 1990: Triggering of atmospheric circulations by moisture inhomogeneities of the earth's surface. Boundary-Layer Met., 51, 1-29.
- Schrnitzl, H., 1988: Grobstruktur-Simulation konvektiver Grenzschichten. Thesis, Univ. Munich, report DFVLR-FB 88-30, DLR Oberpfaffenhofen, 143 pp.
- Schmidt, H., Schumann, U., 1989: Coherent structure of the convective boundary layer deduced from large-eddy simulation. J. Fluid Mech., 200, 511-562.
- Schumann, U., 1989: Large-eddy simulation of turbulent diffusion with chemical reactions in the convective boundary layer. Atmos. Environ. 23, 1713-1727.
- Schumann, U., 1990: Large-eddy simulation of the upslope boundary layer. Q. J. R. Met. Soc. 116, 637-670.
- Schumann, U., 1991: Subgrid length-scales for large-eddy simulation of stratified turbulence. Theoretical and Computational Fluid Dynamics (T.B. Gatski and C.G. Speziale, eds.), Springer-Verlag, Berlin, in press.
- Schumann, U., Hauf, T., Höller, H., Schmidt, H., Volkert, H., 1987: A mesoscale model for the simulation of turbulence, clouds and flow over mountains: Formulation and validation examples. Beitr. Phys. Atmosph., 60, 413-446.
- Schumann, U., Sweet, R.A., 1988: Fast Fourier transforms for direct solution of Poisson's equation with staggered boundary conditions. J. Comput. Phys. 75, 123-137
- Schumann, U., Volkert, H., 1984: Three-dimensional mass- and momentum-consistent Helmholtz-equation in terrain-following coordinates. In: W. Hackbusch (Ed.), Notes on Numer. Fluid Mech. Vol. 10, Vieweg, Braunschweig, 109-131.
- Smolarkiewicz, P. K., 1984: A fully multidimensional positive definite advection transport algorithm with small implicit diffusion. J. Comput. Phys., 54, 325-362.

	case	L/H	λ/H	δ/H	grid cell no.	t_{\max}	N	CPU sec
Set D DNS	D1014	4	1	0.1	64x64x16	35	3500	3100
	D1024	4	2	0.1	64x64x16	35	3500	3100
	D1044	4	4	0.1	64x64x16	35	3500	3100
	D00U4	4	∞	0.0	64x64x16	35	3500	3100
	D1514	4	1	0.15	64x64x16	35	3500	3100
	D1018	8	1	0.1	128x128x16	35	3500	10700
Set L LES	L1014	4	1	0.1	64x64x16	35	3500	4400
	L1024	4	2	0.1	64x64x16	35	3500	4400
	L1044	4	4	0.1	64x64x16	35	3500	4400
	L00U4	4	∞	0.0	64x64x16	35	3500	3400
	L1514	4	1	0.15	64x64x16	35	3500	4400
	L1018	8	1	0.1	128x128x16	35	3500	14700

Table 1. Model parameters for the various cases. t_{\max} is given in units of t . N denotes the number of integration steps. The computer time refers to runs on a CRAY-YMP.

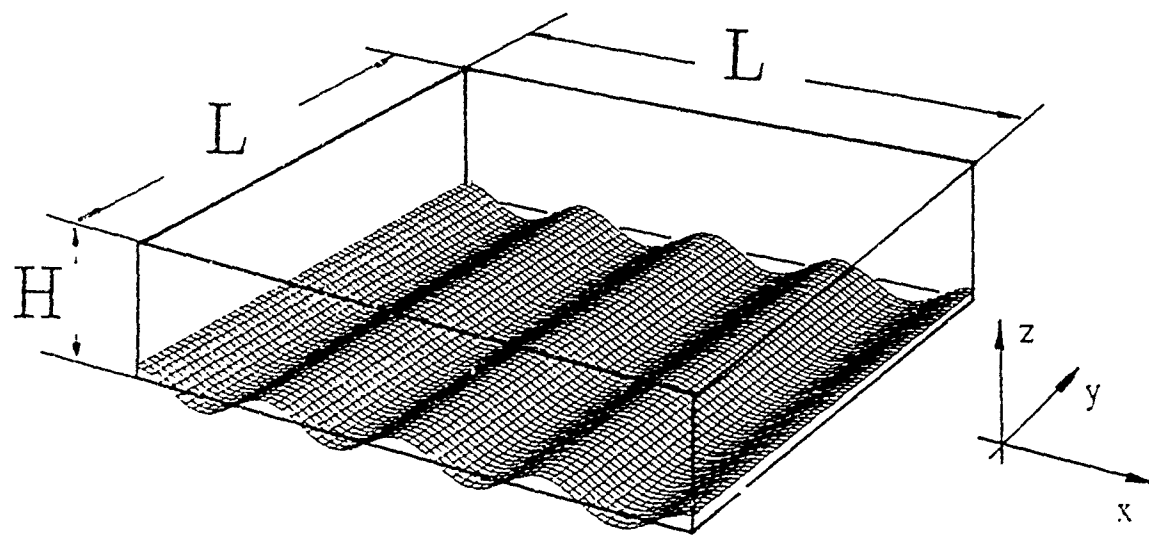


Fig. 1. Perspective sketch of the computational domain in three dimensions showing the sinusoidal surface-wave in x -direction; the surface height is constant in the y -direction. In the example, the wavelength is $\lambda = H$, the wave-amplitude is $\delta = 0.1 H$, and the domain-size is $L = 4 H$.

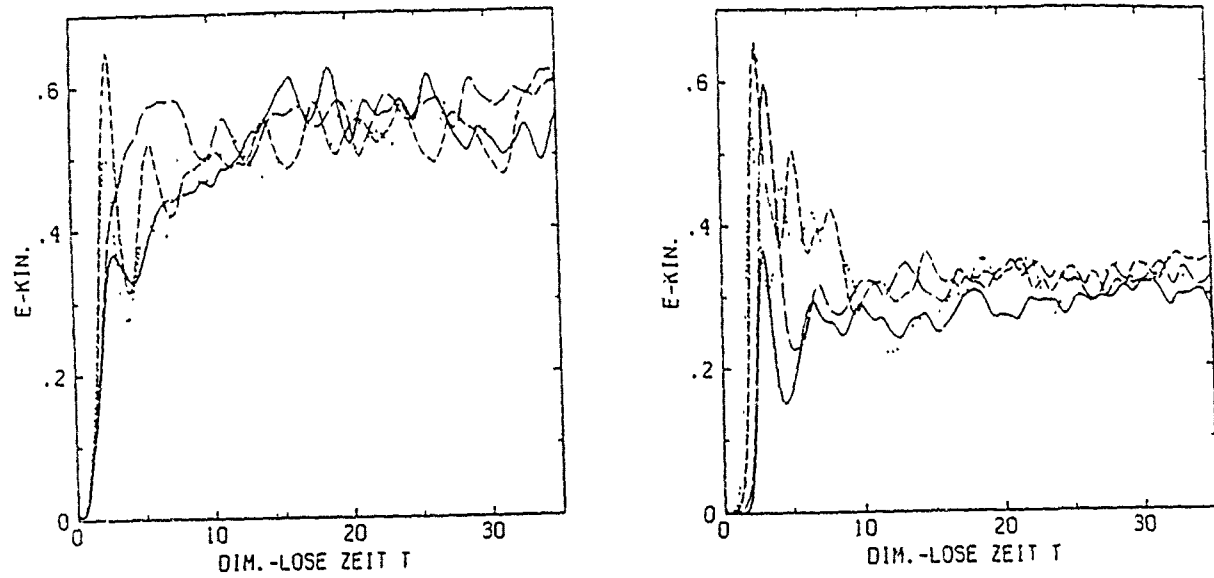


Fig. 2. Spatially averaged kinetic energy (normalized by w^2) versus time t/t_* for LES cases (left) and DNS cases (right). The curves are coded: full for L00U4/D00U4, dotted for L1014/D1014, short-dashed for L1024/D1024, long-dashed for L1044/D1044.

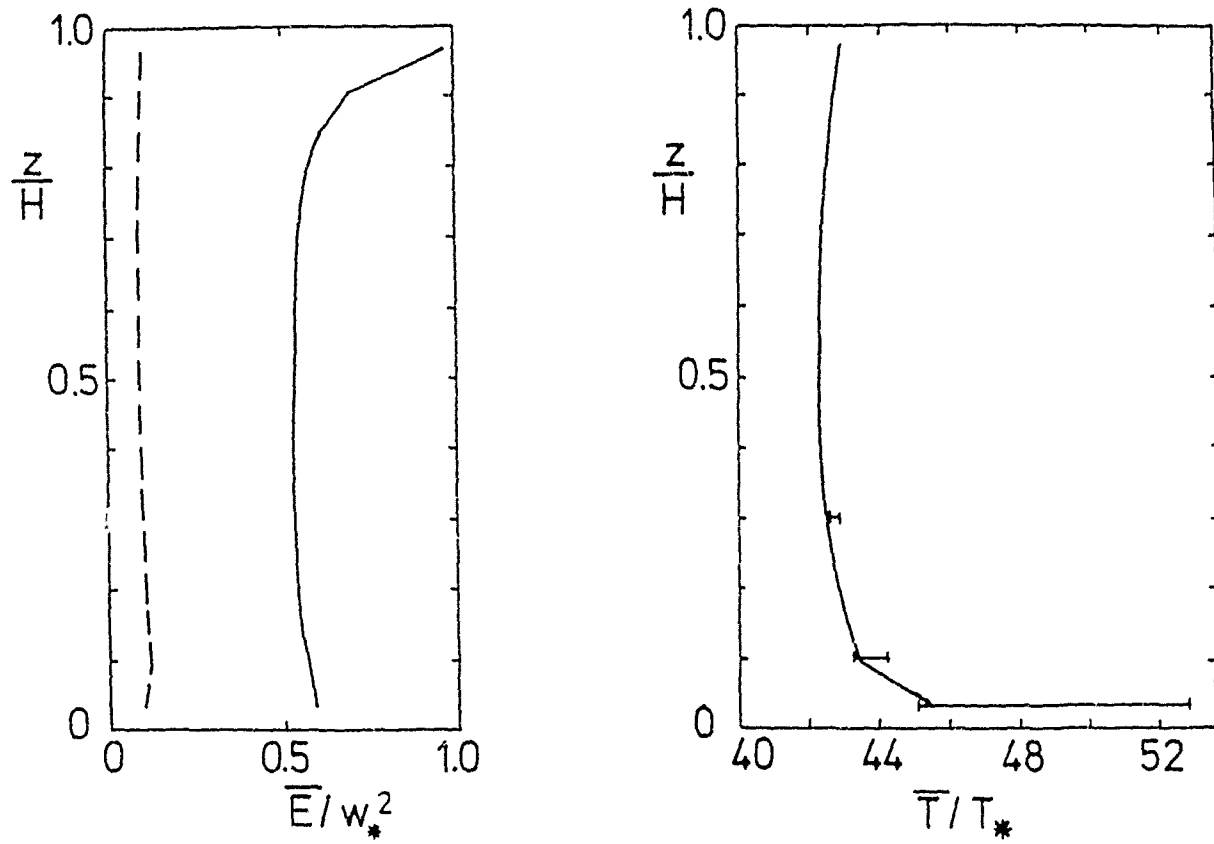


Fig. 3. Normalized mean kinetic energy $\bar{E} = (1/2)\bar{u'^2}$ of turbulent motions versus normalized height z/H , for the LES-case with flat surface. Dashed curve: SGS-contribution, full curve: total (SGS plus resolved) energy. The results are normalized with the convective velocity w_* and the height H of the fluid layer. The mean values represent averages over horizontal planes and over the time period from 30 to 35 t .

Fig. 4. Mean temperature profile versus height z/H , for the LES-case with flat surface. Full curve: LES-result, error bars enclose the experimental data for three heights from Adrian et al. (1986). The results are normalized with the convective temperature T_* and the height H of the fluid layer.

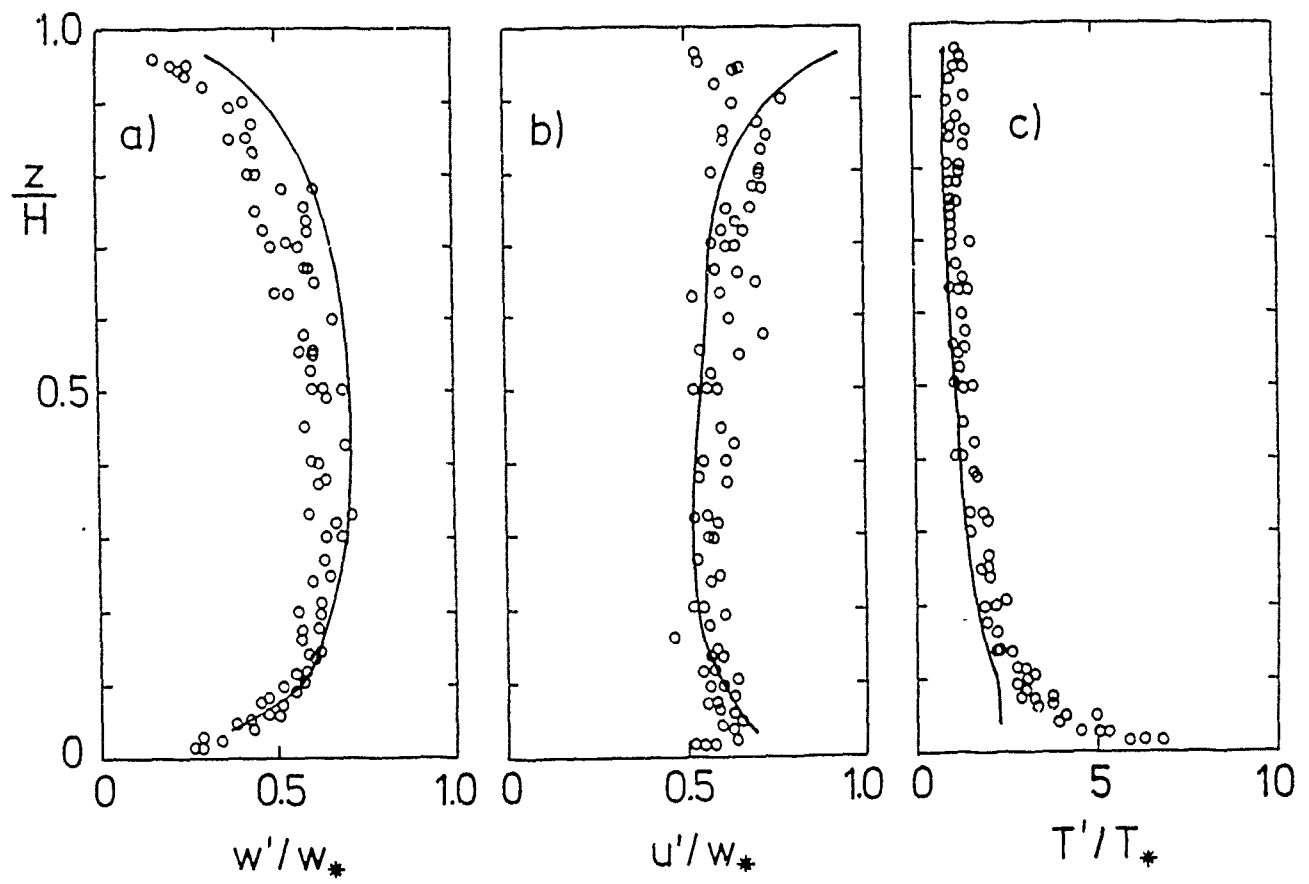


Fig. 5. Root-mean-square fluctuations of a) vertical velocity variance w' , b) horizontal velocity variance u' , c) temperature variance T' , versus height for the LES-case with flat surface. Full curves in a) and b) enclose the sum of resolved and SGS contributions, the curve c) depicts the resolved part only. The circles represent the experimental results of Adrian et al. (1986).

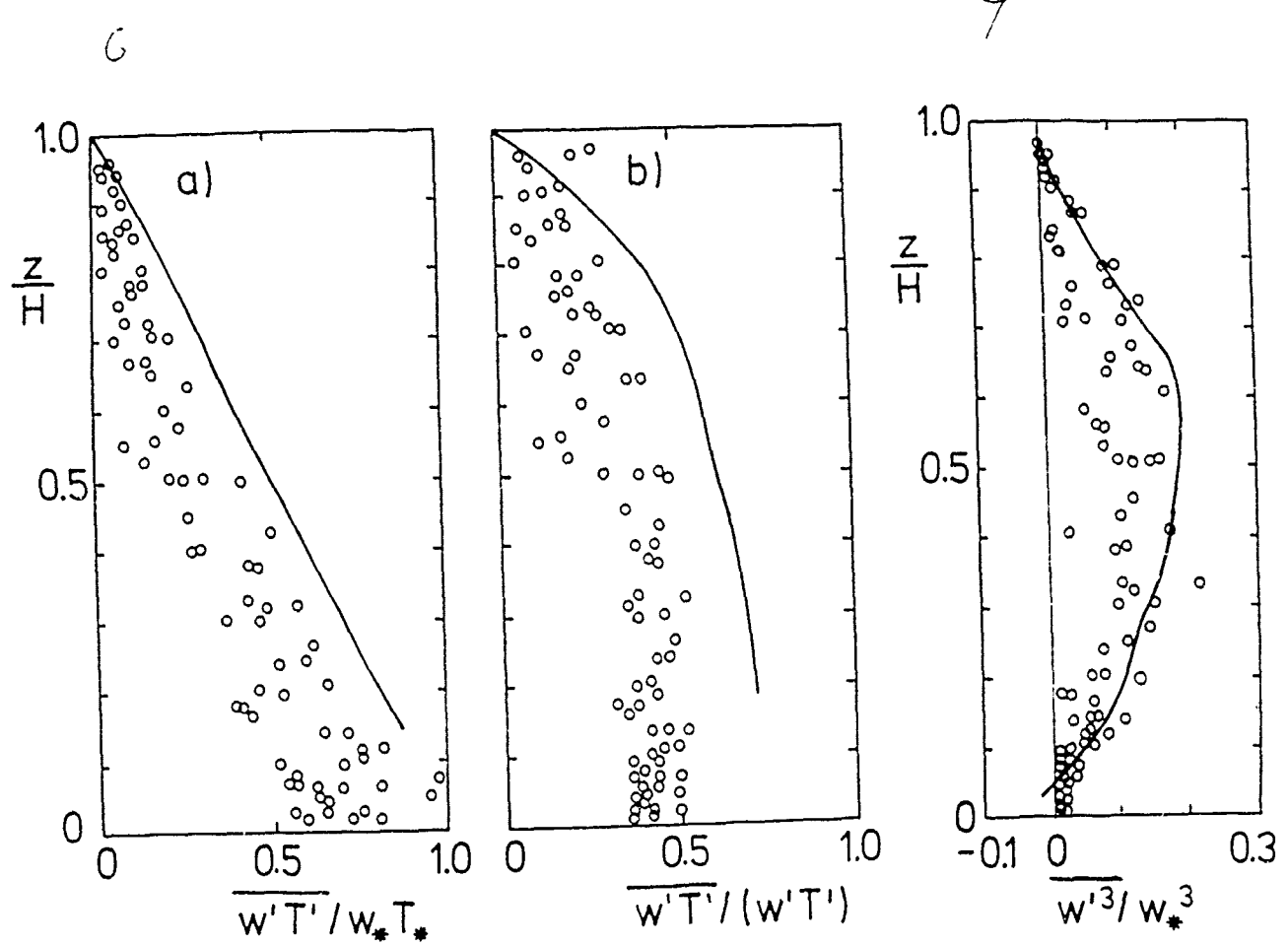


Fig. 6. Turbulent temperature flux and correlation coefficient versus height for the LES-case with flat surface. a) Flux normalized by surface temperature-flux, b) flux normalized by the rms-fluctuations of vertical velocity and temperature. The full curves represent the sum of resolved and SGS contributions. The circles represent the experimental results of Adrian et al. (1986).

Fig. 7. Vertical velocity cubed versus height for the LES-case with flat surface. The full curve represents resolved contributions. The circles represent the experimental results of Adrian et al. (1986).

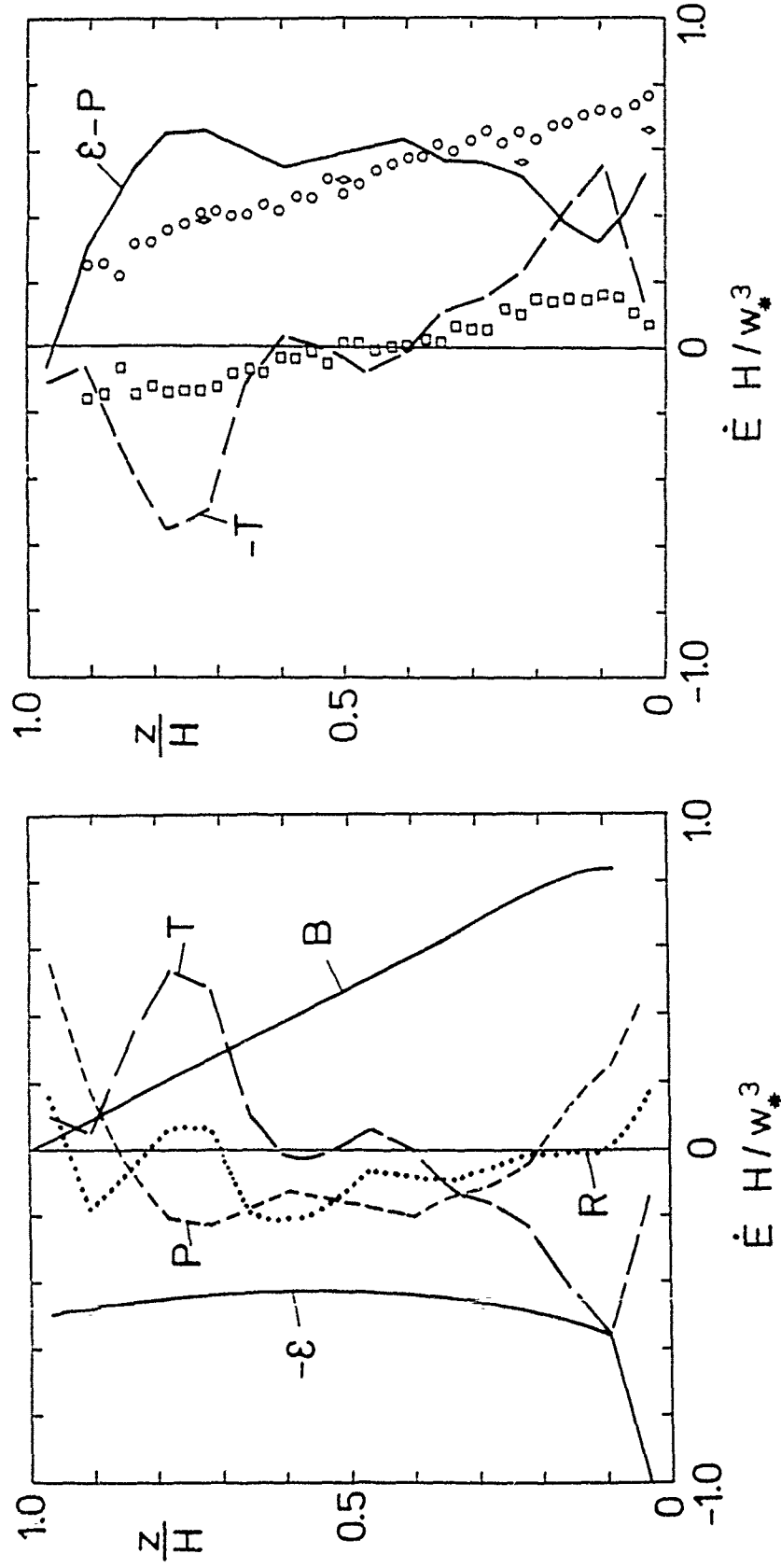


Fig. 8. Contributions to the budget of kinetic energy versus height for the LES-case with flat surface: $B = \beta g w' \bar{T}$, buoyancy flux; $T = -\partial w' u'^2 / 2 \partial z$, divergence of turbulent energy transport, $P = -\partial w' p' / \partial z$, divergence of pressure energy transport, $\varepsilon = C_{FM} e^{3/2} / f$, modelled dissipation rate, and $R = \partial E / \partial t = B + P + T - \varepsilon$, residuum. The results are obtained for $t = 30 t_*$, and plotted in the normalized form.

Fig. 9. Comparison of parts of the budget of kinetic energy as computed by the LES for the flat surface (curves) with experimental data (symbols) by Adrian et al. (1986) versus height. $T = -\partial w' u'^2 / 2 \partial z$, $P = -\partial w' p' / \partial z$, $\varepsilon = C_{FM} e^{3/2} / f$. The results are obtained for $t = 30 t_*$, and plotted in the normalized form. In the experiment, $\varepsilon - P$ is determined as the residuum from the momentum equation. The anomalous part of the energy budget is not included.

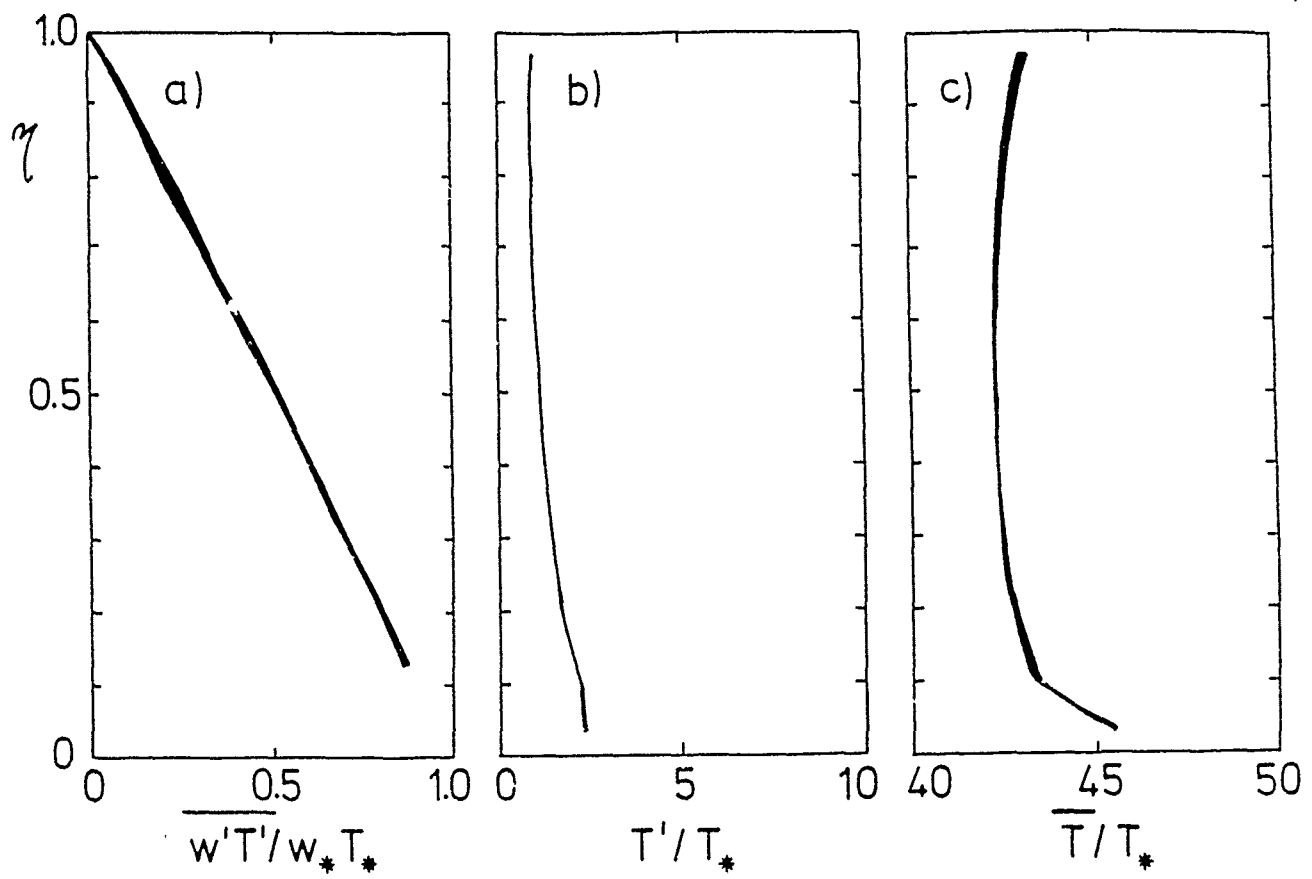


Fig. 10. a) Turbulent temperature flux (total), b) rms temperature fluctuations (resolved part only) and c) mean temperature profile versus vertical coordinate η for the LES-cases with flat or wavy surface. The thick curves enclose the results from cases L00U4, L1014, L1024, and L1044, i.e. without and with wavy surfaces and different wavelengths. The mean values represent averages over planes at $\eta = \text{const}$ and over the time period from 30 to 35 t .

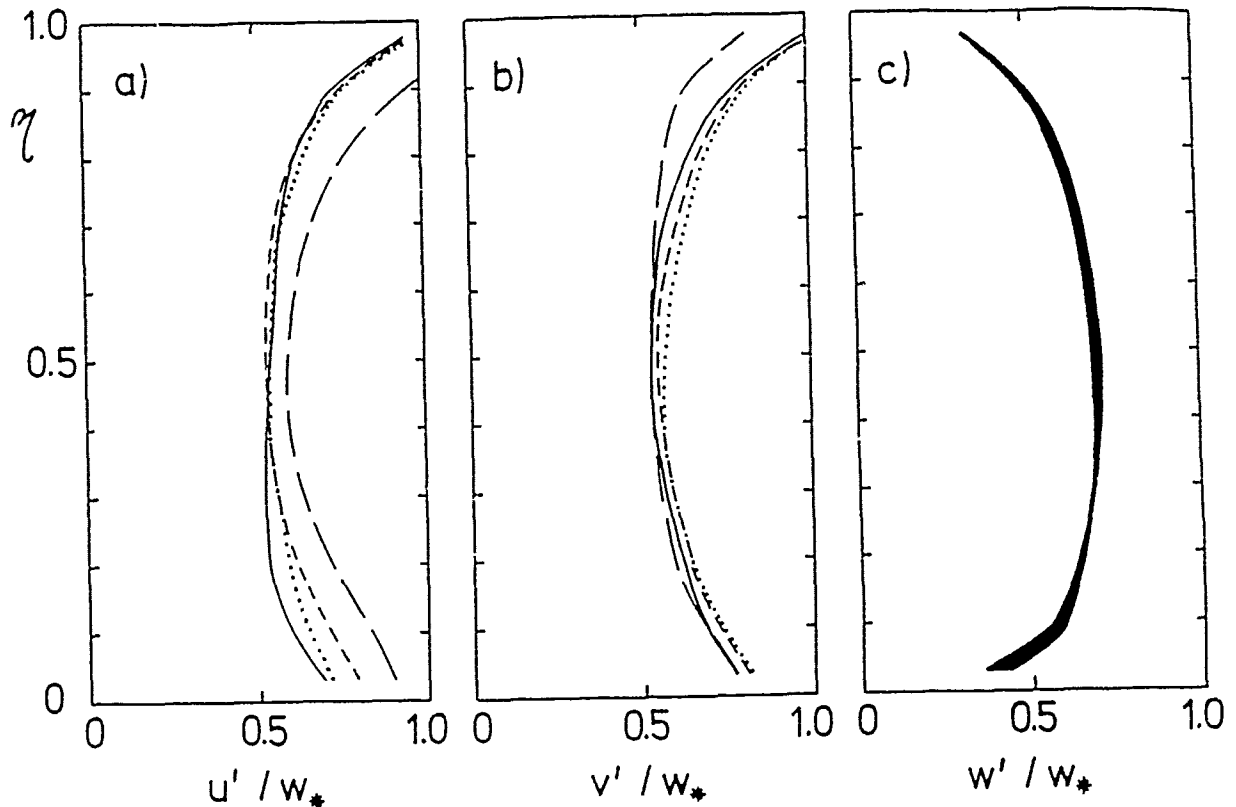


Fig. 11. Rms-values of a) the horizontal velocity fluctuation u' in x-direction, b) v' in y-direction and c) vertical velocity w' versus vertical coordinate η for the LES-cases with flat or wavy surface. Full curve: case L00U4, flat surface; dotted: L1014, $\lambda = H$, $\delta = 0.1$; short-dashed: L1024, $\lambda = 2H$, $\delta = 0.1$; long-dashed: L1044, $\lambda = 4H$, $\delta = 0.1$.

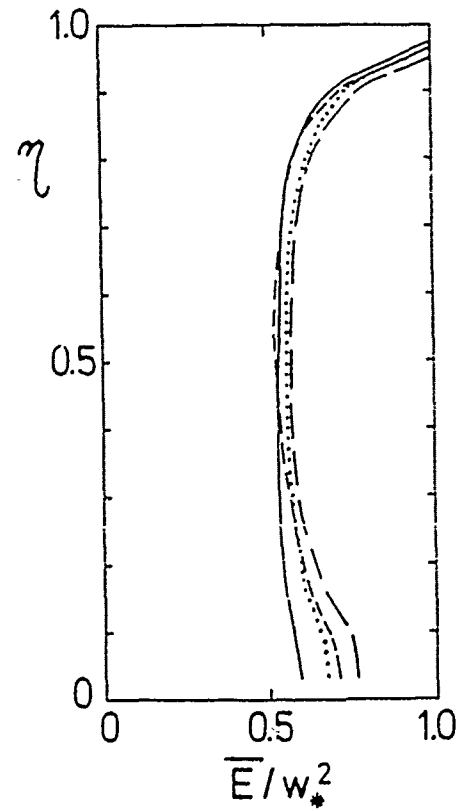


Fig. 12. Kinetic energy of turbulent velocities. $\bar{E} = (1/2)\bar{u'^2}$ versus vertical coordinate η for the LES-cases with flat or wavy surface. Line-coding as in

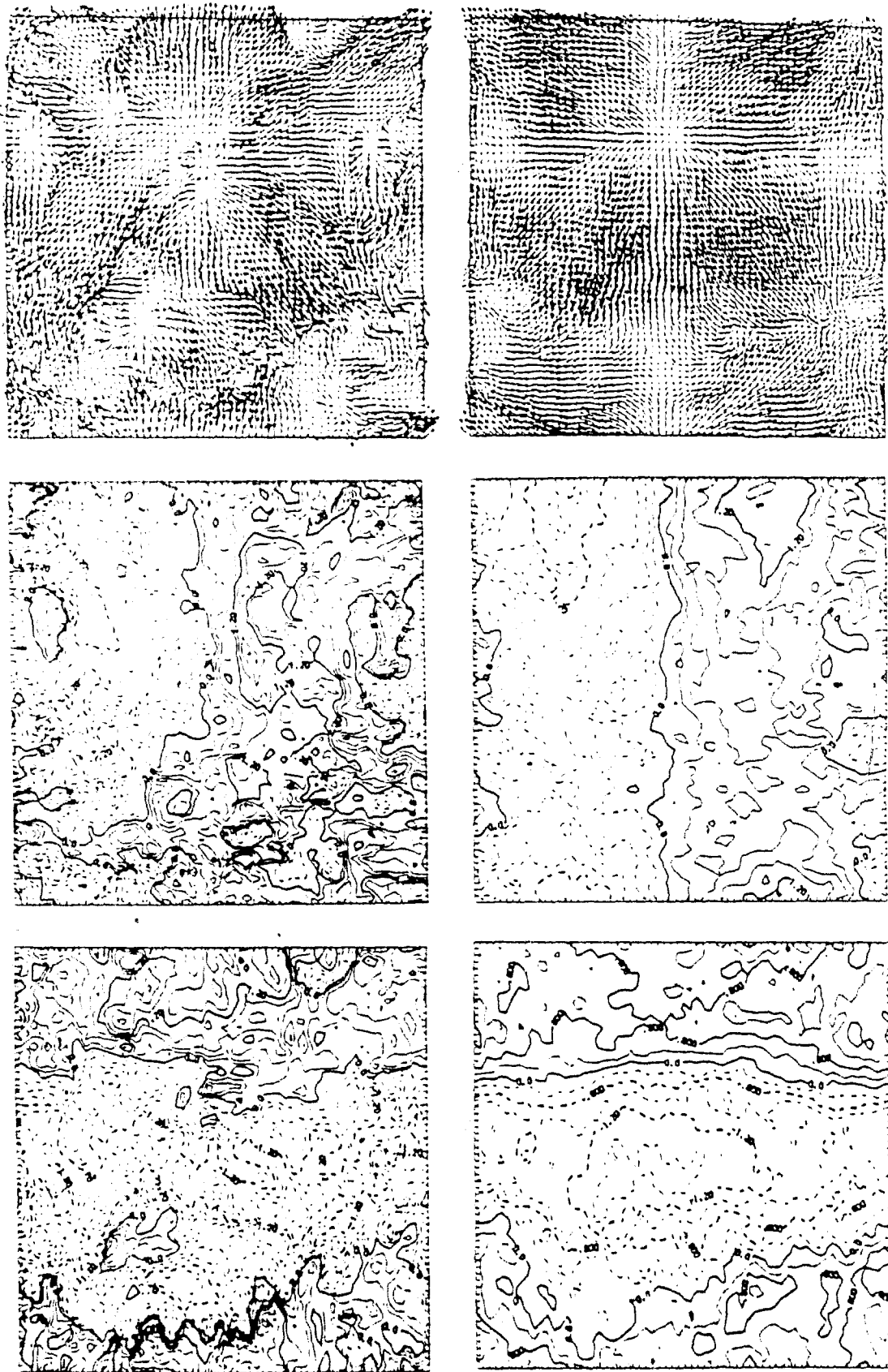


Fig. 13. LES-results at $t = 35 t^*$ (left), and averaged over $30 \leq t/t^* \leq 35$ (right) at $z = H$, for case L.1014 with $L/H = 4$, $\lambda = H$, $\delta = 0.1$. Top: $u - v$ -vectors (maximum vector corresponds to, left: $\bar{v}_{\max}/w = 2.70$, right: 1.78). Middle: u -velocity. Bottom: v -velocity. The contours increment is ~ 0.2 .

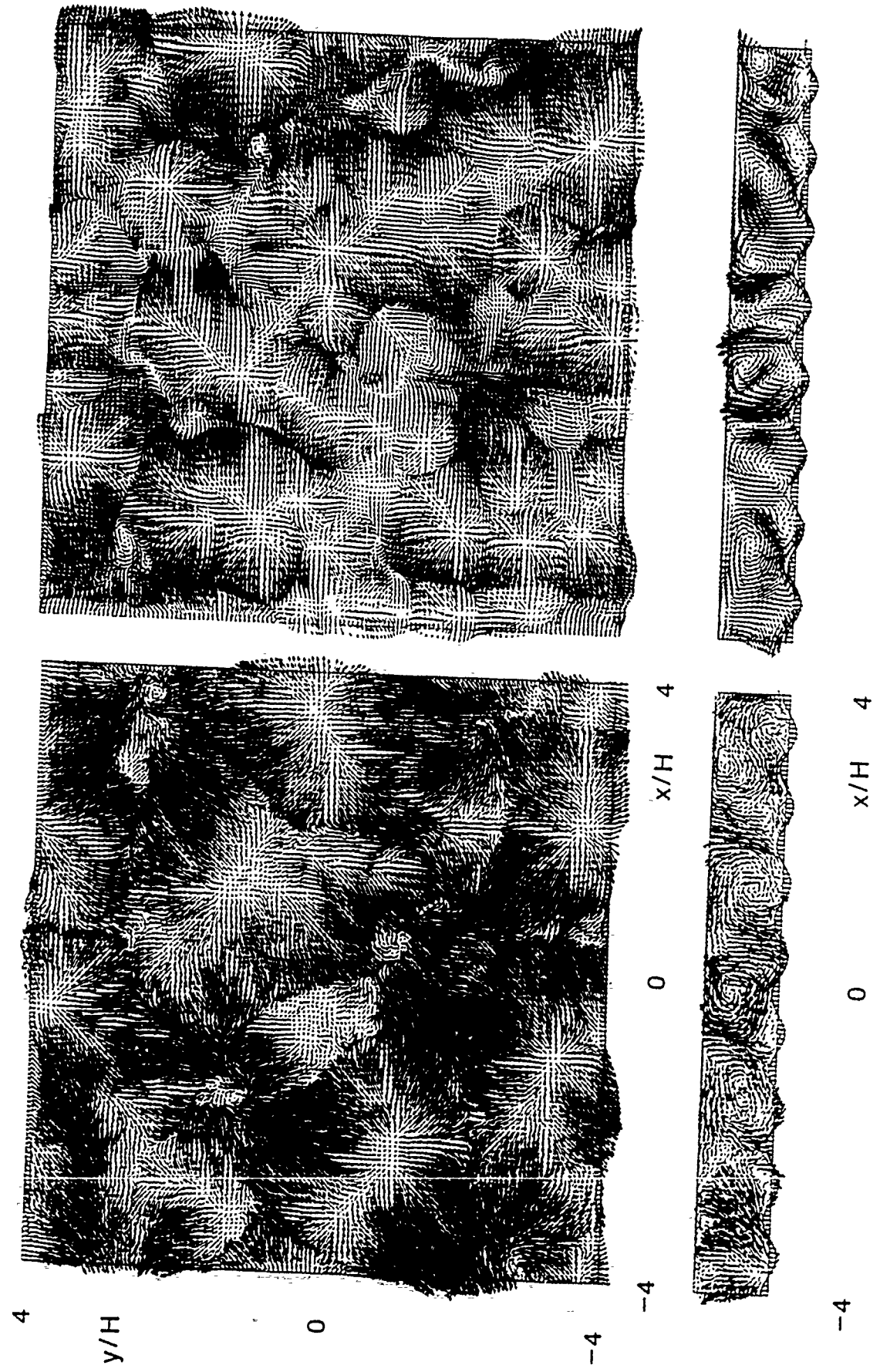


Fig. 14. Comparison between LES (left) and DNS (right) in terms of velocity field at $z = H$ (top) and at $y = -4H$ (bottom), averaged from $t/t_0 = 30$ to 35 in the case with $L/H = 8$, $\lambda = H$, $\delta = 0.1$ (cases D1018 and L1018). Maximum velocities are 1.72 w. (DNS) and 1.87 w. (LES).

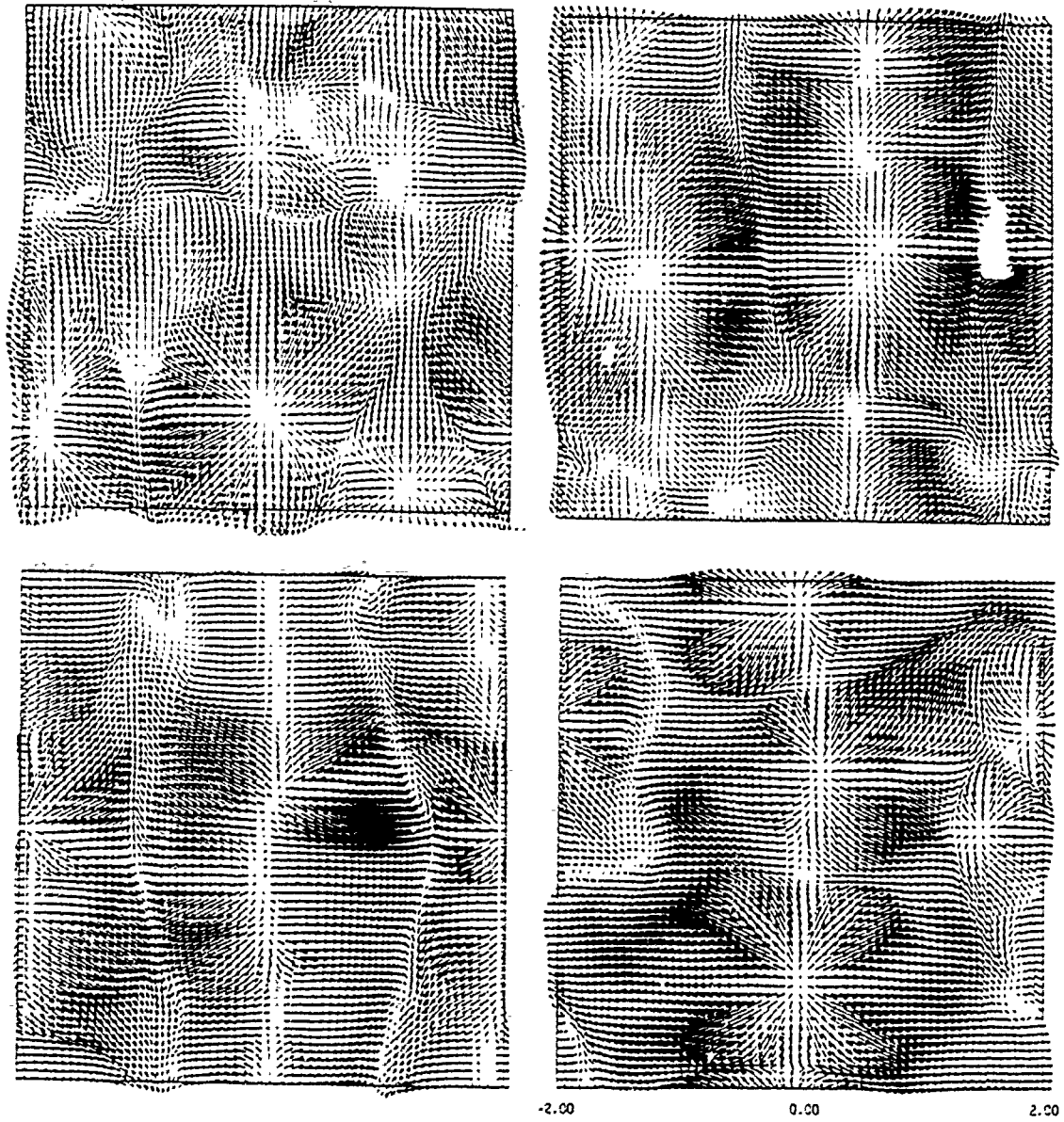


Fig. 15. Influence of wavelength of orography on velocity field in the DNS (time averaged from 30 to 35, at $z = H$). a) (top-left): flat surface, case D00U4, b) (top-right): $\lambda = H$, case D1014, c) (bottom-left): $\lambda = 2H$, case D1024, d) (bottom-right): $\lambda = 4H$, case D1044. In the wavy cases, $\delta = 0.1$. Maximum velocity vectors in units of w are 1.47, 1.77, 1.80, 1.51, for panels, a to d, respectively.

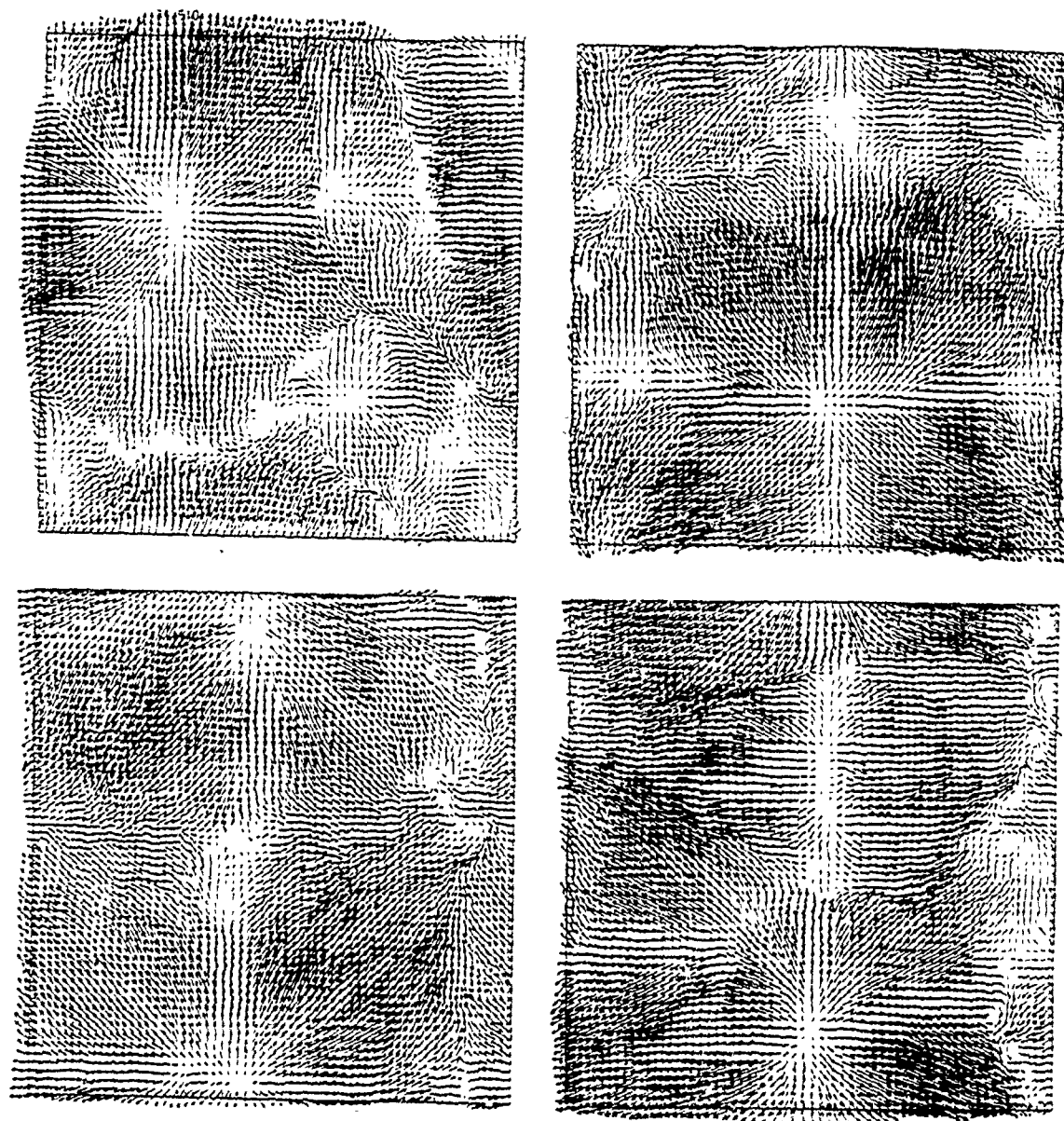


Fig. 16. Influence of wavelength of orography on velocity field in the LES, otherwise as in Fig. 15. Cases L00U4, L1014, L1024, L1044, maximum normalized velocities 1.69, 1.79, 1.93, 1.91, for panels, a to d, respectively.

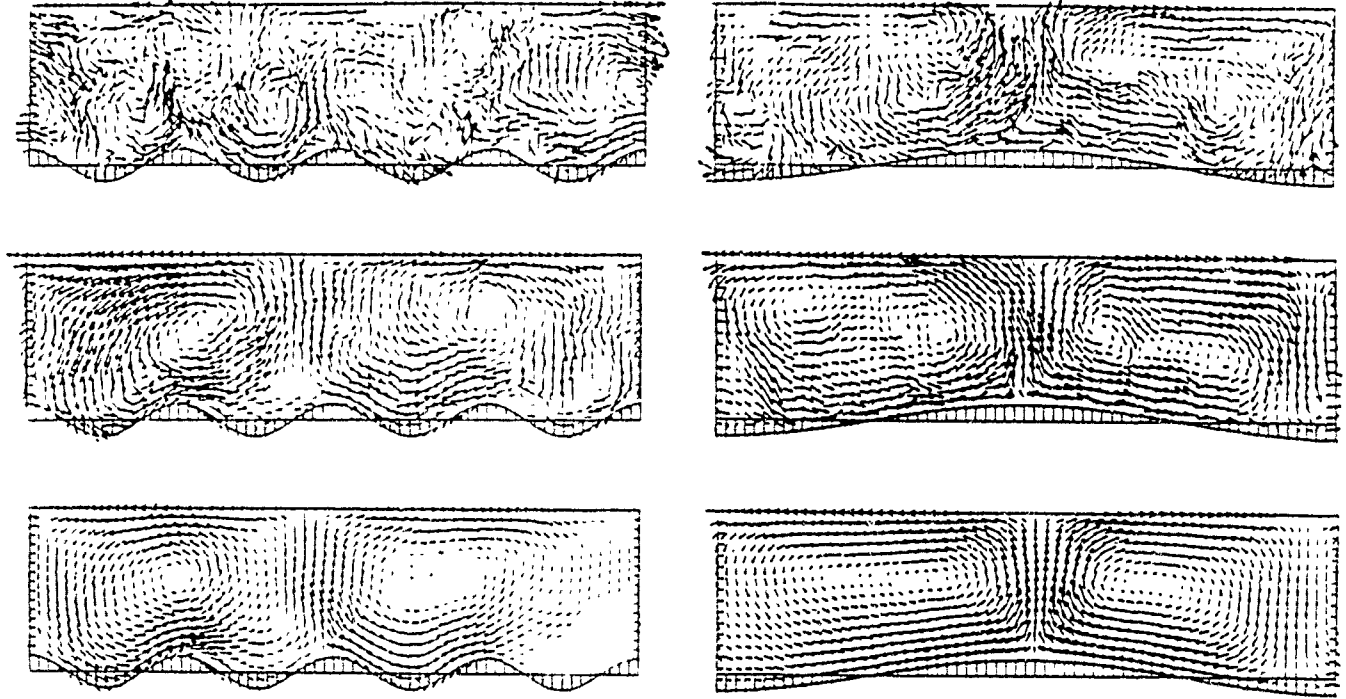


Fig. 17. Influence of wavelength of orography on velocity field in the LES in a vertical plane for various averages and wavelengths. Left: $\lambda = H$, case L1014. Right: $\lambda = 4H$, case L1044. Top: Instantaneous result at $t = 35t_0$. Middle: Result averaged from $t/t_0 = 30$ to 35. Bottom: Result averaged over the same time interval and in addition over the y -coordinate. Maximum normalized velocity vectors, from top to bottom, left: 2.20, 1.50, 1.03; right: 2.59, 1.63, 1.34.

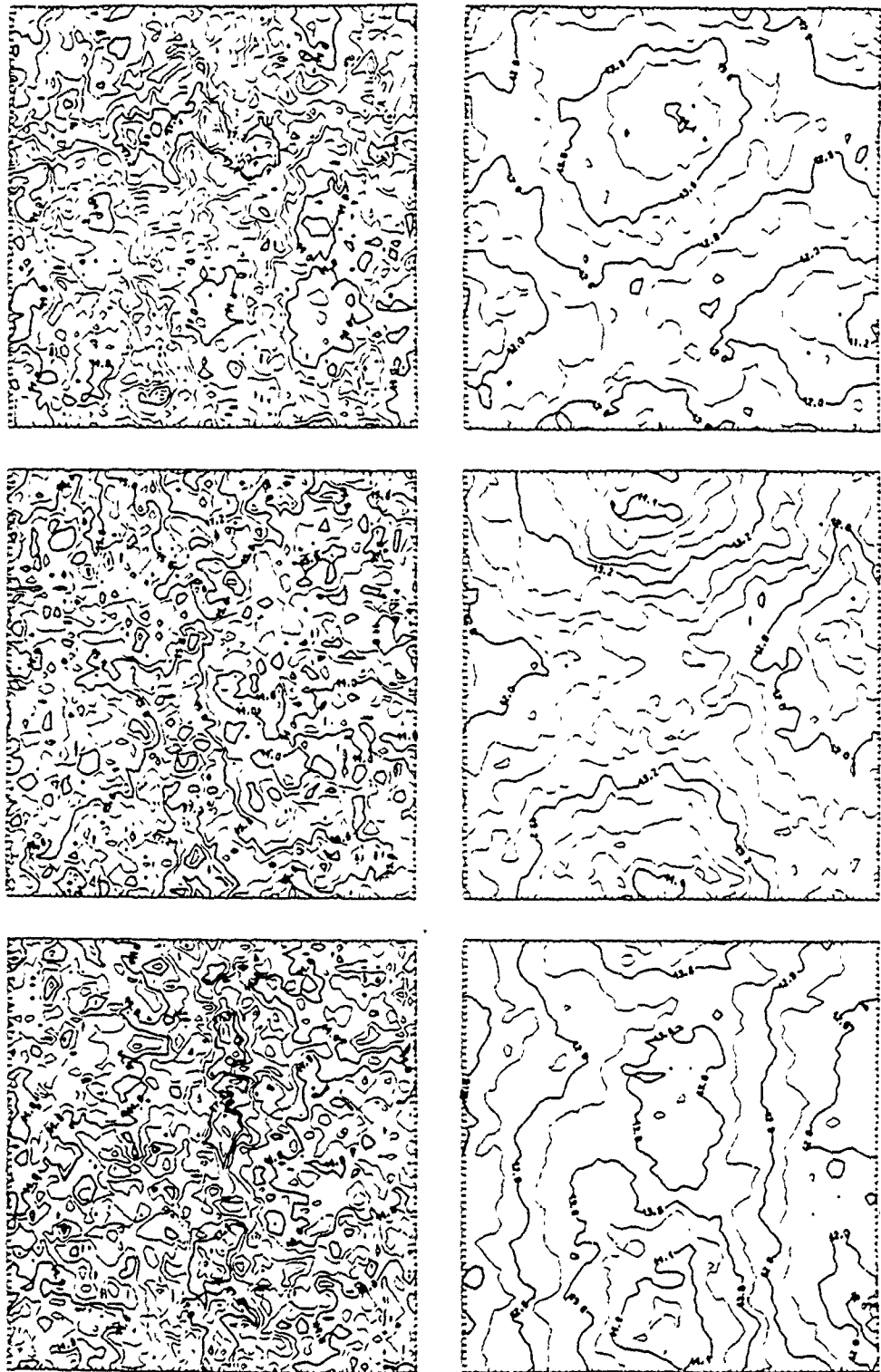


Fig. 18. Influence of wavelength of orography on temperature-field in the LES for $\lambda/H = 1, 2, 4$ (cases L1014, L1024, L1044) from top to bottom, respectively, time-averaged from $t/t_c = 30$ to 35. Left panels: temperature at the wavy surface ($\eta = 0.03$); contour increment are 0.8, 0.8, 0.7 T_c , from top to bottom panel, respectively. Right panels: temperature at the top

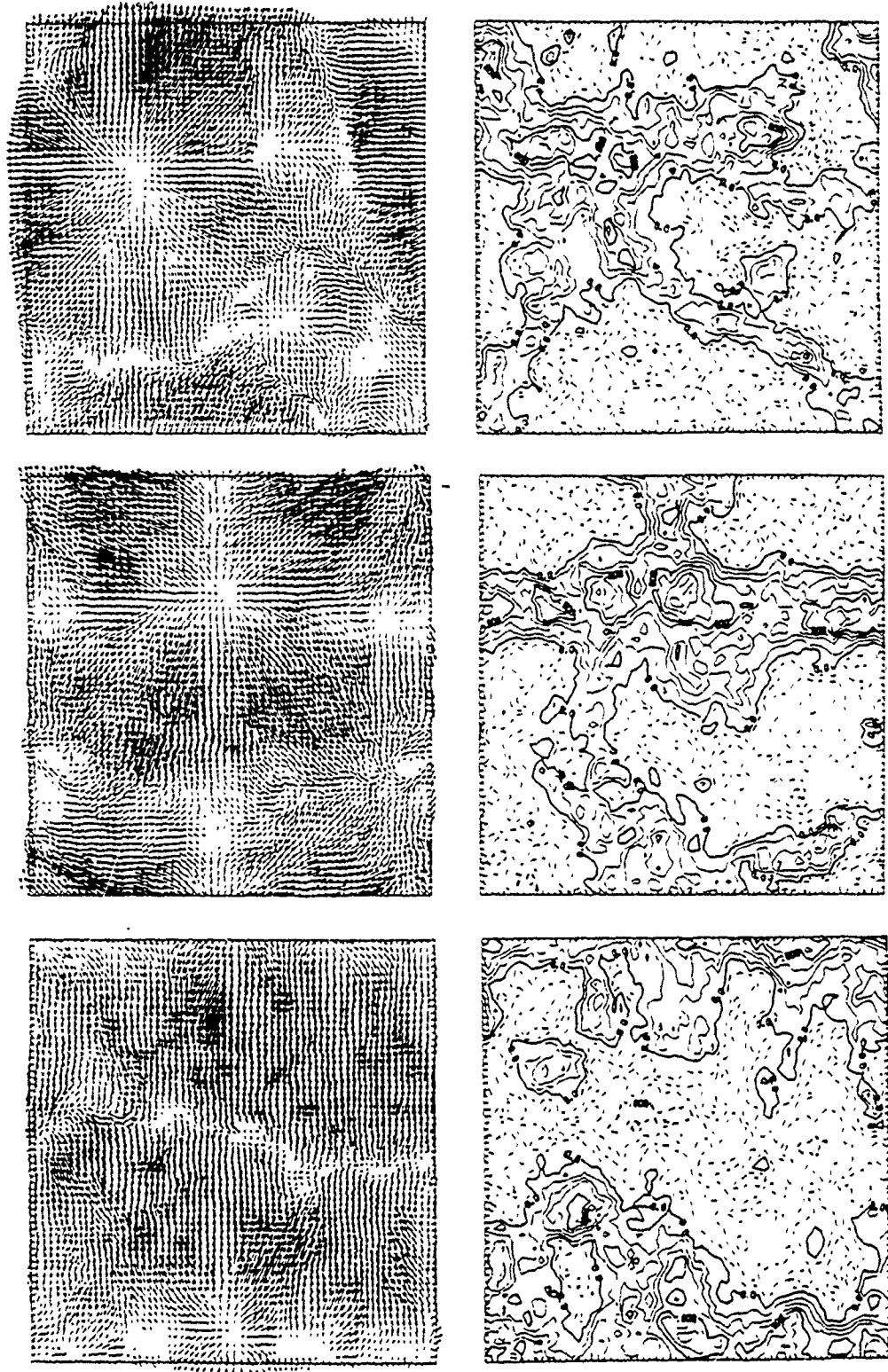


Fig. 19. Influence of wave amplitude δ of orography on horizontal velocity-vectors (left, at $z = H$) and on vertical velocity w (right, at $\eta = 0.5$) in the LES for $\delta = 0, 0.1, 0.15$ (cases L00U4, L1014, L1514) from top to bottom, respectively, in the time average from $t/t_* = 30$ to 35. Maximum velocity vectors in units of w , from top to bottom: 1.89, 1.78, 1.86. Contour increment

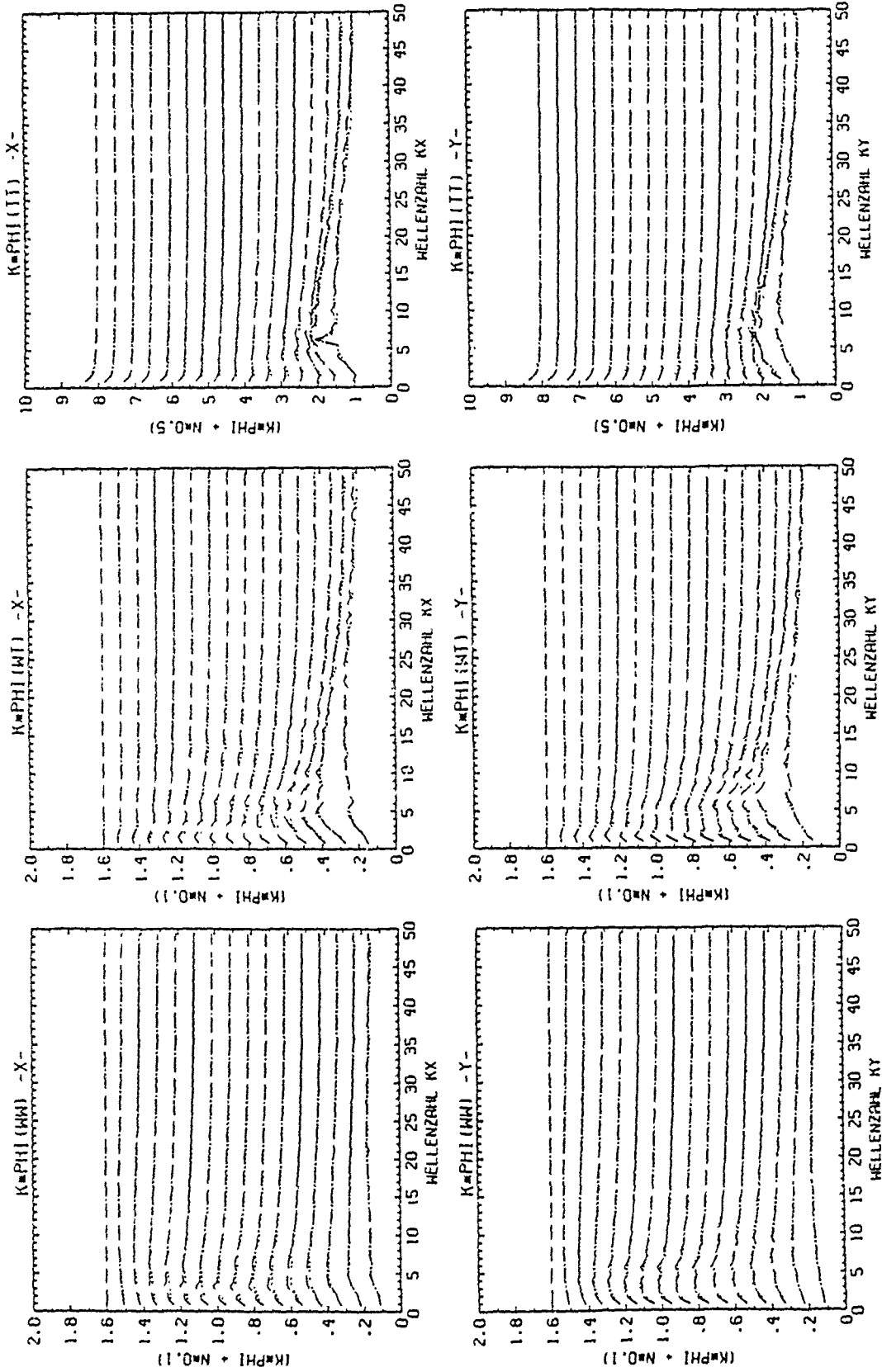


Fig. 20. Power-spectra of vertical velocity (left), cospectrum of heat flux (middle) and power-spectrum of temperature fluctuations (right) versus horizontal wavenumbers $k_x H$ (upper panels) and $k_y H$ (lower panels). The spectra are multiplied with wavenumber k . The curves belonging to increasing grid levels are separated by increments of 0.1 (left two columns) or 0.5 (right panels). The lowest curves correspond to the lowest level

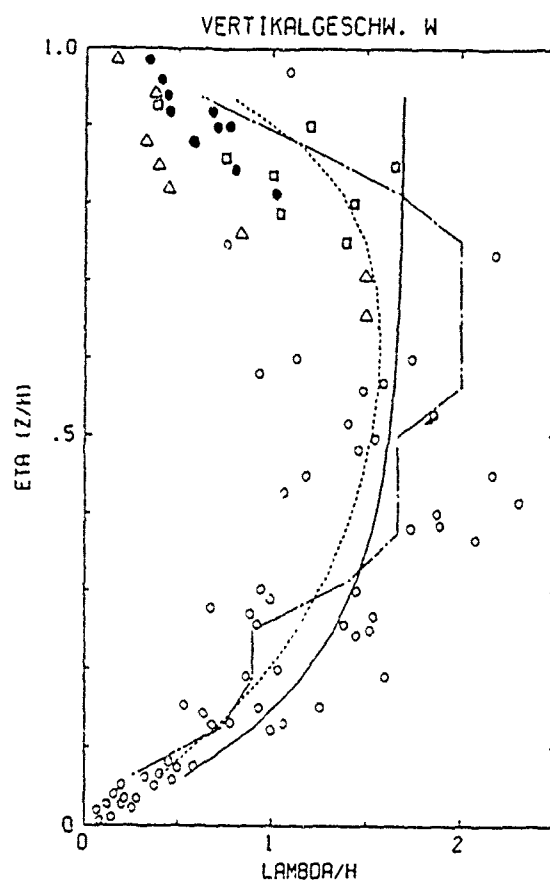


Fig. 21. Wavelength $\lambda = 2\pi/k$ of the spectral maximum of $kD_{ww}(k)$ versus height. Case L00U4: dash-dotted curve (the result shown is the mean value of those for spectra in x and y-directions); experimental data and fit from Caughey and Palmer (1979): symbols and dotted curve; fit from Kaimal et al. (1982): full curve.

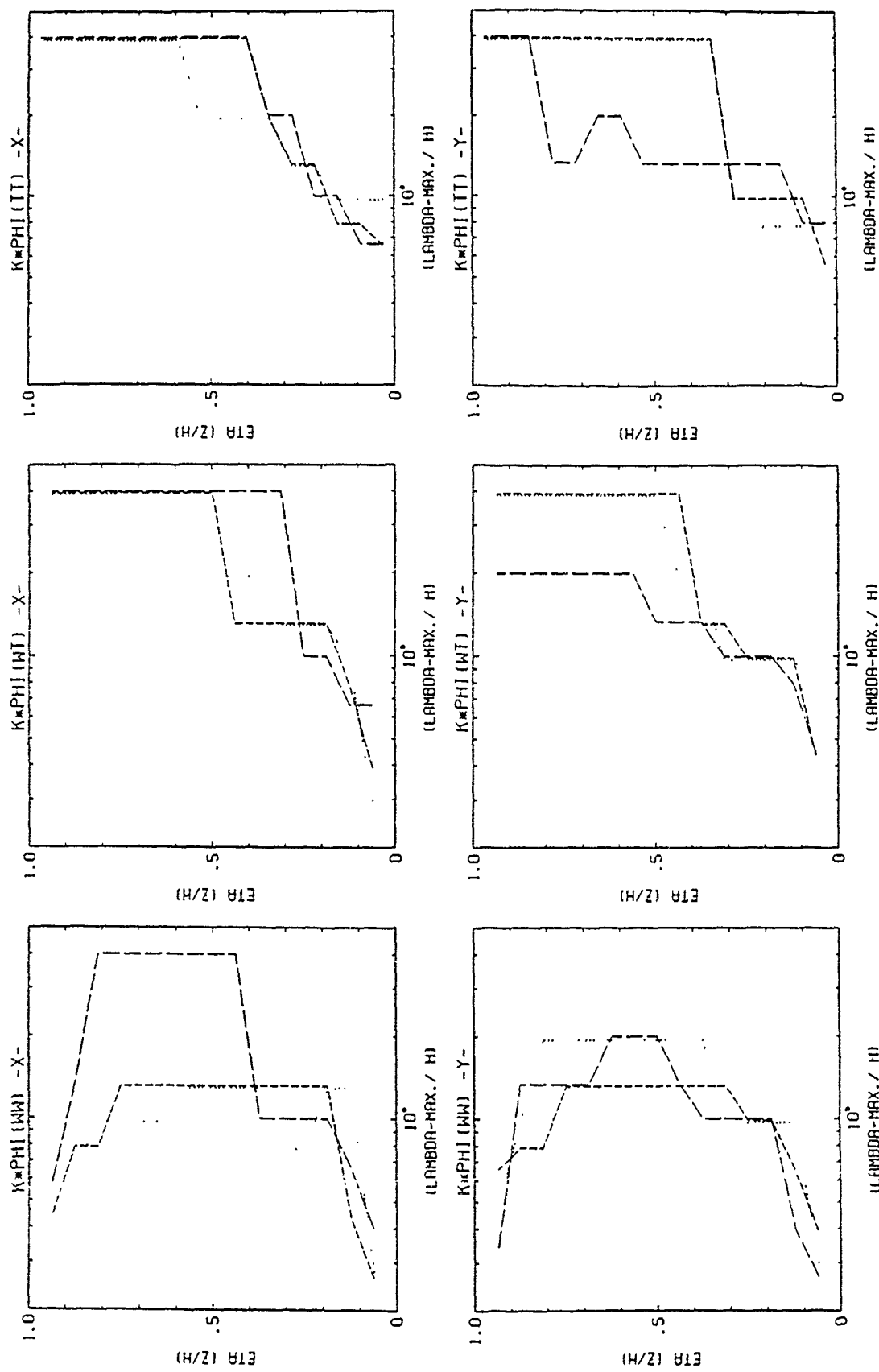


Fig. 22. Wavelengths of spectral maxima of vertical velocity (left), vertical heat flux (middle), and temperature fluctuations (right) along x and y-directions (upper and lower panels) versus vertical coordinate η . L1024: short-dashed, L1044: long dashed.

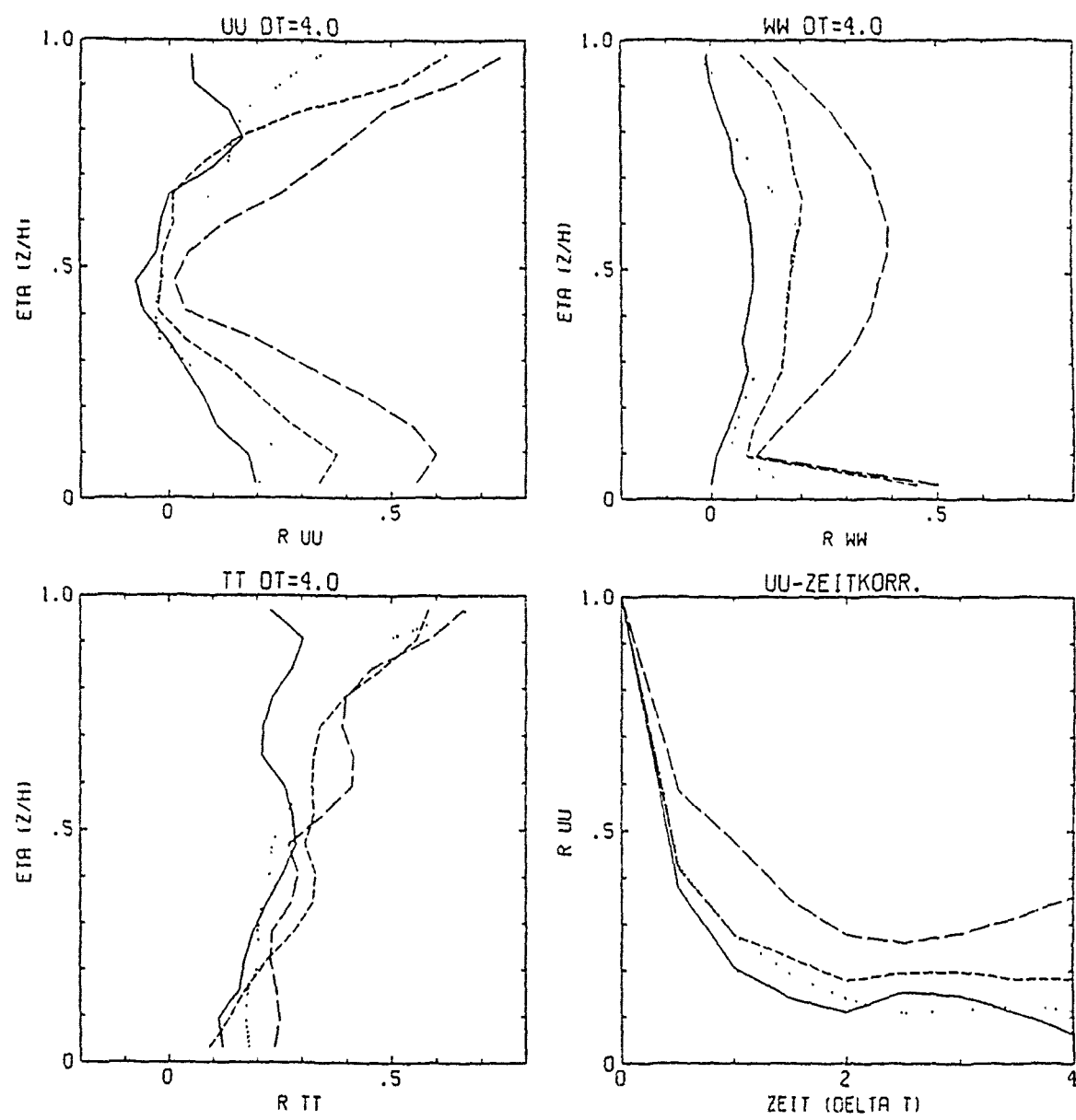


Fig. 23. Temporal correlations in the LES cases L00U4 (full curves), L1014 (dotted), L1024 (short dashed), L1044 (long dashed) a) Correlation between horizontal velocities u at times $t/t_c = 30$ and 34 versus vertical coordinate η , b) same for vertical velocity w , c) same for temperature fluctuations T' , d) volume averaged correlation between horizontal velocities u at times $t/t_c = 30$ and $t/t_c = 30 + \Delta t$ versus time difference Δt .

Using RAMS in LES mode – from inhomogeneous surfaces to cirrus clouds

W. R. Cotton, R. L. Walko, P. J. Flatau, and K. R. Costigan
Colorado State University

Overview

This talk gives an overview of applications of the Colorado State University Regional Atmospheric Modeling System (RAMS) in the Large Eddy Simulation (LES) mode. Several representative examples are given: the response of the atmospheric convective boundary layer to surface inhomogeneities, LES simulations in complex terrain using nested grids, plume and dispersion problems, LES simulations of hilly terrain, and LES modeling of upper-level clouds. This gives us a convenient framework to summarize our personal perspective on *Where Do We Stand* in atmospheric LES — one of the main theme of this workshop.

We extend this theme to discuss the *Where Do We Go* question. We digress to cover the ever increasing role of superworkstation technology on which RAMS is successfully implemented. The role of postprocessing and data visualization in analysis of LES data is covered. The speculative discussion includes data compression techniques such as empirical orthogonal functions and wavelet decomposition methods. Finally, plans for studying coherent structures and applying a multifractal description to SGS parameterization are mentioned.

Summary

The unique feature of the CSU RAMS is its versatility. RAMS includes numerous physics modules such as radiation, cloud microphysics, soil model, subgrid-scale turbulence, and cumulus parameterization. It can be run in non-hydrostatic or hydrostatic mode and has a two-way nested grid capability. This flexibility allows for a large range of RAMS applications to variety of atmospheric flows. The model has been ported to a number of computers ranging from the Stardent/Titan and IBM RISC6000 superworkstation boxes to CRAY Y-MP supercomputers.

The response of the atmospheric convective boundary layer to surface inhomogeneities was studied with RAMS (Hadfield, 1988) with a surface sensible heat flux that either was constant or varied on a spatial scale comparable to the boundary-layer depth. Several effects have been identified, though some are evident only after suitable averaging. They include mean circulations in phase with the surface perturbations, modulation of the turbulence throughout the boundary layer, and modifications to the profiles of horizontally

averaged quantities. Most of these effects increase as the wavelength of the surface perturbation is increased and decrease with an imposed mean wind. A time scale for kinetic energy transfer from the mean circulation to the turbulence has been defined and found to be surprisingly short in some cases. Elevated-plume dispersion has been studied using a Lagrangian particle model. Circulations driven by the surface heat-flux perturbations affect the ground-level concentrations.

The RAMS LES model has also been applied to the CBL over hilly terrain (Walko et al. 1990). This study has shown that LES over hilly terrain yields very similar statistical moments to those obtained over a flat surface when full horizontal averaging is performed on the statistical quantities. However, hilly cases exhibit strong positional preference for given phases of eddy circulations; in particular, rising motion is favored above higher terrain and subsidence over lower terrain. This tendency causes strong organized circulations to appear in time-averaged statistics, unlike simulations over a homogeneous surface. The mean circulations are highly thermally favorable, the upslope flow over the heated surface being a primary factor in determining the entire pattern of the circulation. We are continuing to investigate the effect of hilly terrain on the CBL, examining among other things additional terrain scales, more complex terrain, and the effect of mean wind. We are also investigating the effect of hilly terrain on dispersion of both point-source and homogeneously-distributed traces.

Another RAMS LES application (Costigan and Cotton, 1990) involves the simulation of the 22 June 1984 case study in the vicinity of the Boulder Atmospheric Observatory (BAO) tower on the high plains east of Boulder, Colorado. This date was chosen to coincide with the Phoenix II data. The unique feature of this work is an attempt to perform nested grid simulations with the Mellor-Yamada ensemble-averaged turbulence parameterization on the mesoscale grid and the Deardorff sub-grid closure on the small nested grid. Interactions between mesoscale circulations and turbulence have been simulated.

Cirrus cloud modelling presents a unique challenge for Large Eddy Simulation. Our recent work (Cotton et al 1990, Flatau et al. 1990) give extensive references to previous research in this field. Cirrus clouds develop in the stably stratified air of the upper troposphere (we hope it will prompt a discussion during the workshop about similarities between marine and atmospheric stable layer turbulence). Recently we analyzed aircraft measurements from the First ISCCP Regional Experiment (FIRE) and re-analyzed aircraft data from the Global Atmospheric Sampling Program (GASP). The spectra indicate higher levels of turbulent intensity inside cirrus clouds in comparison to the background atmosphere for both FIRE and GASP data. This indicates a transition between 2D turbulence of the environment to 3D turbulence inside radiatively forced clouds. Another challenging aspect of cirrus is its tendency to layering and prevalence of inhomogeneous structure. We study upper-level clouds in an LES framework to investigate the transition from a 3D convectively-forced cloud to a 2D ("collapsing") state. The emergence of coherent structures and behaviour of turbulence statistics is studied and discussed.

Plans are to take advantage of the RAMS nested grid capability by performing nested-grid simulations of cirrus clouds. In this application the large grids will establish mesoscale variations in vertical motions moisture, and wind shear, and a floating LES grid will move through this mesoscale field simulating variations in turbulent cloud

structure. By judicious selection of nested grids we hope to make major advances in our understanding of the behavior of turbulent cloud behavior in stably-stratified flow.

A major focus of our LES work is to establish a direct link between LES experiments and actual field experiments by developing the capability to simulate actual case study events rather than just idealized scenarios.

In the talk we will also describe our use of super-workstations in LES modeling including running of smaller simulations, post-processing of LES output data, and animation of individual realizations.

References

- Costigan, K. R. and W. R. Cotton, Large eddy simulations in complex terrain using nested grids, 1990, 104-106, Fifth conference on mountain meteorology, Boulder, Colorado, American Meteorological Society.
- Cotton, W. R., M. E. Nicholls, S. Heckman, P. J. Flatau, 1990, A modeling investigation of the 28 October 1986 FIRE cirrus case, Conference on cloud physics, San Francisco, Calif. 200-206, American Meteorological Society.
- Hadfield, M. G., The response of the atmospheric convective boundary layer to surface inhomogeneities, 1988, Colorado State University, Ph. D. dissertation, (also published as Atmospheric Science Paper 403).
- Flatau, P. J., I. Gultepe, G. Nastrom, W. R. Cotton, and A. J. Heymsfield, 1990, Cirrus cloud spectra and layers observed during the FIRE and GASP projects, 1990, Conference on cloud physics, San Francisco, Calif. 200-206, American Meteorological Society.
- Walko, R. L., W. R. Cotton, and R. A. Pielke, 1990, Large eddy simulation of the CBL over hilly terrain, 409-412, Ninth Symposium on Turbulence and Diffusion, April 30-May 3, 1990, Riso, Roskilde, Denmark, American Meteorological Society.

Helicity Revisited--Background and New Developments in an Erratic and Paradoxical Subject

Douglas Lilly

University of Oklahoma¹

**International Workshop on Large Eddy Simulation
December 19-21, St. Petersburg, Florida**

Helicity is a fundamental flow statistic which went unrecognized by the pioneers in fluid dynamics, and still remains of unclear significance except in certain sub-fields, notably magnetohydrodynamics and the meteorology of convective storms. I will here review briefly part of the history of studies of helical turbulence and some new developments in atmospheric applications.

It is recognized that in a purely helical flow, one in which the velocity and vorticity vectors are everywhere parallel, the "Lamb force", $\nabla \times \omega$, vanishes, so that vorticity cannot be generated by the advective terms in the equation of motion. This seems to preclude the development of a turbulent cascade and nearly eliminates dissipation in a large Reynolds number flow. Only a monochromatic flow can be purely helical, however. For a flow field containing components with more than one spatial wavenumber, non-linear transfer and generation of an inertial range is possible, though perhaps difficult. The degree of difficulty is suggested by the closure model calculations of Andre and Lesieur (1977), who simulated the decay of a flow initiated with a narrow but finite bandwidth energy spectrum with maximal helicity. From their results, the development of an inertial range occurs more slowly than normal. Even after an inertial range forms, the energy containing scales are somewhat isolated from it by the high helicity, so that the dissipation rate is reduced by a factor of 4 or more from that found for non-helical turbulence. Direct simulations of decay of a helical flow are presented by Shtilman and Polifke (1989), with results in general agreement with the Andre-Lesieur closure calculations, although the Reynolds number and resolution

¹Part of this work was accomplished while the author was visiting the National Center for Atmospheric Research.

available to the direct simulation are much less. Shtilman and Polifke also carry out simulations with the amount of helicity varied in the initial state. When it is less than 50% of the maximal value, they find that the helicity effect on downscale energy transfer is insignificant.

The suppressing effect of high helicity on the turbulent energy cascade process suggests that the turbulent energy in regions where helicity amplitude is larger than average should decay slower and survive longer than similar regions of low helicity. One might therefore suppose that a decaying high Reynolds number turbulent flow should ultimately consist of large volumes of highly helical flow of both signs, separated by thin boundaries where most of the dissipation is taking place. Such a Darwinian concept was introduced by Levich and Tsinober (1983, also Tsinober and Levich, 1983). It had the additional attractive feature of seeming to explain the increasing intermittency of dissipation at high Reynolds numbers.

The Levich-Tsinober hypothesis was dealt a severe blow by the publication of the results of a series of simulation experiments by Rogers and Moin (1987). Starting with initially isotropic flow, their results show a positive but weak tendency to generate helicity, but virtually no tendency for helicity to be locally correlated with dissipation rate. I'm not sure that the apparent failure of the hypothesis has yet been fully explained.

Meteorologists studying severe thunderstorms have for many years noted the spatial concurrence of vertical velocity and the vertical component of vorticity. Such vortex regions, when sufficiently strong and close to the ground, may lead to tornadoes. More recently, analyses of Doppler radar observations and convective storm simulations have shown that the horizontal components of velocity and vorticity also tend to be parallel. Further, it is found that the mean flow environments of such storms are usually also highly helical. The simplest presentation of such a flow configuration is the hodograph of horizontal mean flows as they vary with height. Helicity is indicated when the hodograph direction changes in the chosen frame of reference.

Figure 1 shows examples of two kinds of mean shear profiles that have produced helical storms. The upper frame is a flow with unidirectional shear, with a uniform southerly wind component and a

westerly component increasing with height. An often-observed storm motion is shown as the vector ending to the south of the hodograph. From the storm frame of motion, the mean flow has high helicity, especially near the level corresponding to the part of the hodograph just north of the storm motion vector. A second type of mean shear profile is indicated by the circular hodograph, with the storm motion indicated to be at the center of the circle. Here the mean flow helicity is complete, with the horizontal vorticity and velocity vectors parallel everywhere. Although both of the above wind hodographs are schematic and idealized, in many situations real mean wind flow hodographs resemble one of them or are somewhere between, for example describing a partial circle in the low levels with unidirectional shear above.

In very recently presented work, both research investigators and field forecasters have found that many storms which produced tornadoes developed in environments with circular type hodographs. An example shown in Fig. 2, is from a study by W. McCaul (1990) of tornadoes generated in the environments of recently landfallen hurricanes in the southeastern U. S. These environments are frequent generators of tornadic storms, for reasons which were elusive before McCaul's work, since the available buoyant energy is much less than that found typical for tornadic storms in the U. S. plains and other tornado-prone regions. He shows rather convincingly, however, that the principal regions where such storms generate are characterized by quasi-circular hodographs of very large amplitude. Similar results have been shown from observations of the environmental hodographs near other tornadic storms, several of which were unpredicted. These results indicate that thermodynamic energy is a less important contributor to tornado formation than is the source of vorticity available for vortex generation, which is what helicity seems to measure. In the latest Severe Storms Conference sponsored by the American Meteorological Society, 15 papers were presented reporting the role of mean flow helicity as a precursor and predictor of tornadoes.

The exact mechanism by which environmental vorticity and helicity are concentrated into the tornado vortex remains somewhat uncertain, and is the subject of ongoing research, much of it involving large eddy simulations. My belief is that it involves a combination of direct involvement of helical flow in strong vortex

generation plus some reduction of dissipation and mixing. With respect to the second component, I will present here some results of an LES study carried out by W.-S. Wu, R. Kerr, and myself. The idea is to generate buoyant convection within an environment containing mean flow helicity, without the usual atmospheric complications of moisture phase changes and microphysics.

The particular experimental environment chosen is a combination of Couette and Poisseuille flow and Benard cell convection. Two parallel plate boundaries (at $z=\pm H/2$) are assumed to move relative to each other in the x -direction, and a channel flow is generated between the plates in the y -direction. The lower plate is maintained at a higher temperature than the upper one. Viscosity and thermal diffusion are included, with a unit Prandtl number. No slip upper and lower boundary conditions are imposed, with periodic lateral boundaries. In a purely viscous and diffusive equilibrium, the velocity and temperature profiles are:

$$U = Az/H, \quad V = B(1-4z^2/H^2), \quad T = T_0 - Cz/H$$

where A, B, and C are the amplitudes of the plate and channel flow velocities and plate temperature differences, respectively. I will discuss simulations carried out within the above initial environment and also for environments which contain only one or none of the velocity shear components (A or B or both vanishing),

The conditions under which the above flow becomes unstable to perturbations are somewhat complicated, since there are four non-dimensional parameters, two Reynolds numbers, a Rayleigh number, and a Prandtl number. For the flow amplitudes used in most cases, the Rayleigh number,

$$Ra = g\alpha CH^3/v\kappa$$

is controlling, where α is the coefficient of expansion and v, κ are the viscosity and diffusion coefficients, here assumed equal. The critical Rayleigh number is generally of order 1500. Simulation experiments are carried out at two Rayleigh numbers, 15000 and 10^6 , corresponding to conditions only mildly supercritical and moderately turbulent, respectively.

The unique feature of the somewhat complicated initial state conditions imposed is a parabolic hodograph, as indicated by the

profiles on Fig. 3. Relative to any disturbance motion within the curve of the hodograph, the mean helicity is positive, highly so for stationary disturbances or those moving at the volume mean velocity, which is $u = 0$, $v = 2B/3$. For simulations carried out to a statistically steady state at the smaller Rayleigh number, the hodograph remains curved (Fig. 4), and the disturbances are found to be highly helical, as indicated by the map of vector velocity and vertical vorticity at $z = 0$ (Fig. 5). For simulations done with $B = 0$ (Couette flow) the disturbances are essentially downshear rolls with almost no helicity, and similarly for those with $A = 0$ (Poissonneille flow). With $A = B = 0$, the standard Benard cell results are found, with convective rolls.

The apparently most important result of this set of experiments is shown by comparison of the statistically steady mean flow profiles, on Fig. 6. For the Couette flow case the mean flow gradient is essentially eliminated (slightly reversed) in the middle of the channel, with increased gradients near the boundaries. This gradient reduction is much less for the helical flow case, indicating reduced turbulent stress and reduced transfer of energy from the mean flow to disturbances. Similar results are seen upon comparison of the helical and the Poisseuille flow cases (not shown here). The heat transfer, as measured by the Nusselt number, is also a little smaller for the helical flow case than any of the others. This indicates that mean flow helicity is indeed reducing turbulent transports. Analysis of the helicity budget (not shown) indicate that disturbance helicity is produced in about equal measure by transfer from the mean flow and by buoyancy effects.

The results of the larger Rayleigh number experiments are much less significant. The mean flow gradients in the middle part of the channel are so reduced that little mean flow helicity remains. Although a biased disturbance helicity is discernable in the results, its magnitude is small and its effects on energy transfer are undetectable.

An obvious question arising from these results is why the mean flow gradients which allow helical effects to be important in the atmosphere are not removed by continuing turbulent processes, as they are in large Rayleigh and Reynolds number flows in simpler environments. The apparent reason is the high intermittency of convective turbulence in the atmosphere. This is associated with

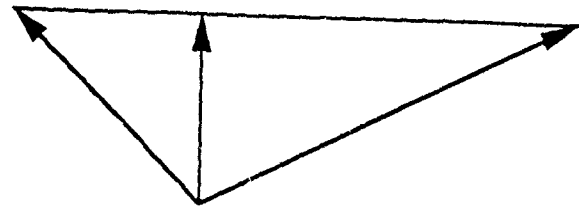
moisture effects, which usually allow convective cloud formation only for finite amplitude disturbances. Even so, in tropical environments, where dynamic generation processes tend to be weak, mean shears are generally insufficient to produce helical flow effects. In middle latitude environments, however, the dynamic forcing is stronger, and helical flows can be maintained in the presence of strong, but highly intermittent convection. This is probably the principal reason why helicity produces strong effects in atmospheric convection, but is found mostly insignificant in simpler fluid dynamics environments.

References:

- Andre, J. C. and M. Lesieur, 1977: Influence of helicity on the evolution of isotropic turbulence at high Reynolds number. *J. Fluid Mech.*, **81**, 187-207.
- Levich, E. and A. Tsinober, 1983: *Phys. Lett. A* **93**, 293.
- McCaul, E. W., Jr., 1990: Buoyancy and shear characteristics of hurricane tornado environments. Submitted to *Mon. Weather Rev.*
- Rogers, M. M., and P. Moin, 1987: Helicity in incompressible turbulent flow. *Phys. Fluids*, **30**, 2662-2671.
- Shtilman, L., and W. Polifke, 1989: On the mechanism of the reduction of nonlinearity in the incompressible Navier-Stokes equation. *Phys. Fluids*, **A1**, 778-780.
- Tsinober, A. and E. Levich, *Phys. Lett. A* **93**, 321.

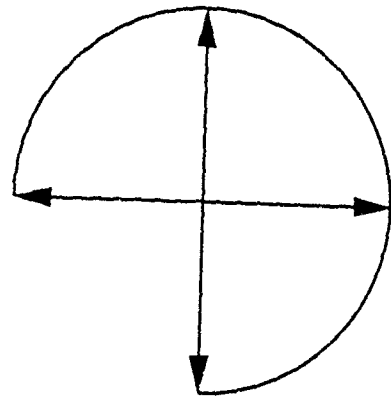
Figure Captions.

1. Hodographs of (a) a unidirectional shear, with the frame of reference to the right of the shear vector, (b) a circular shear, with the frame of reference at the center of the 3/4 circle.
2. Hodographs in the environments of tornadic storms generated in landfallen hodographs, from McCaul.
3. Initial profiles of U, V, and T for experiments done by Wu, Kerr, and Lilly. The hodograph is similar to the V profile, turned on edge.
4. Mean flow hodograph at a time when the flow has become statistically steady.
5. Map of vertical velocity vectors and vertical vorticity isolines at the mid level of the simulation done for $Ra = 15000$, with a helical initial flow.
6. Comparison of the U profiles for the helical initial flow profile (circles) and the Couette flow profile (+'s).



$$U_r = U(z) - c_x, V_r = -c_y$$

$$\xi = -\partial V \partial z = 0, \eta = \partial U \partial z$$



$$U_r = -M \cos mz, V_r = M \sin mz$$

$$\xi = -mM \cos mz, \eta = mM \sin mz$$

Figure 1

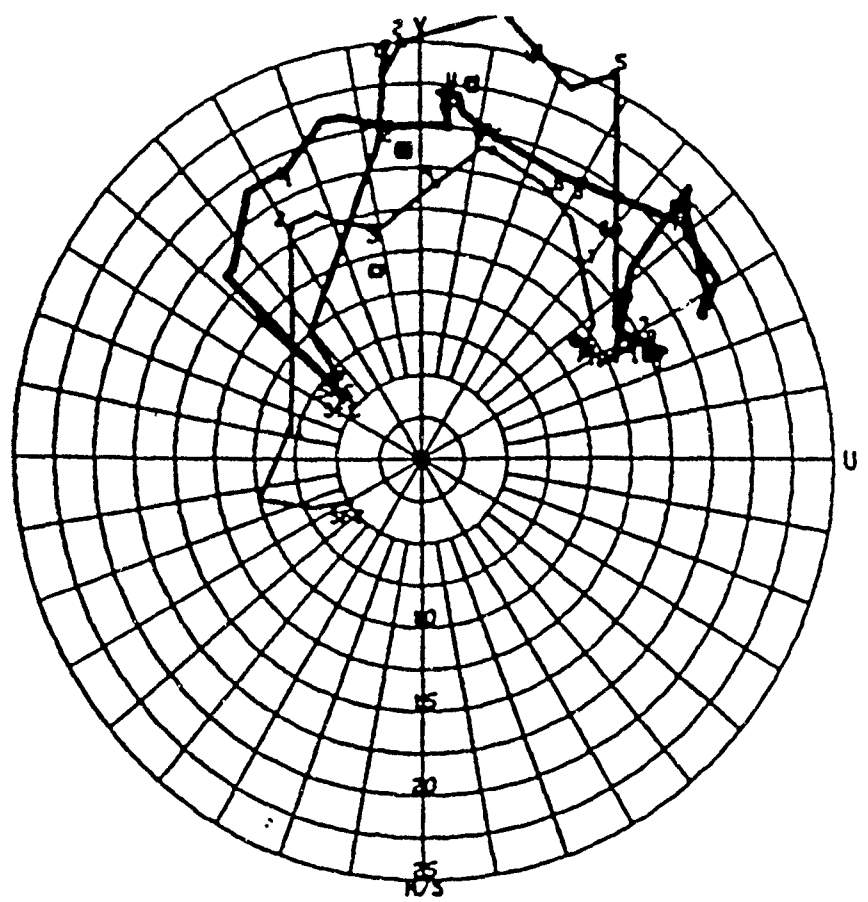


Figure 2

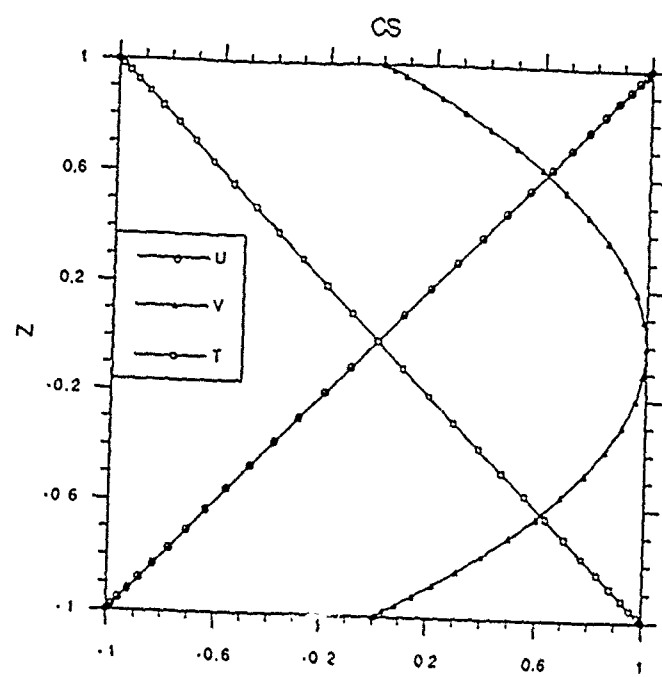


Figure 3

$\text{Ra}=15000 \text{ CS}$

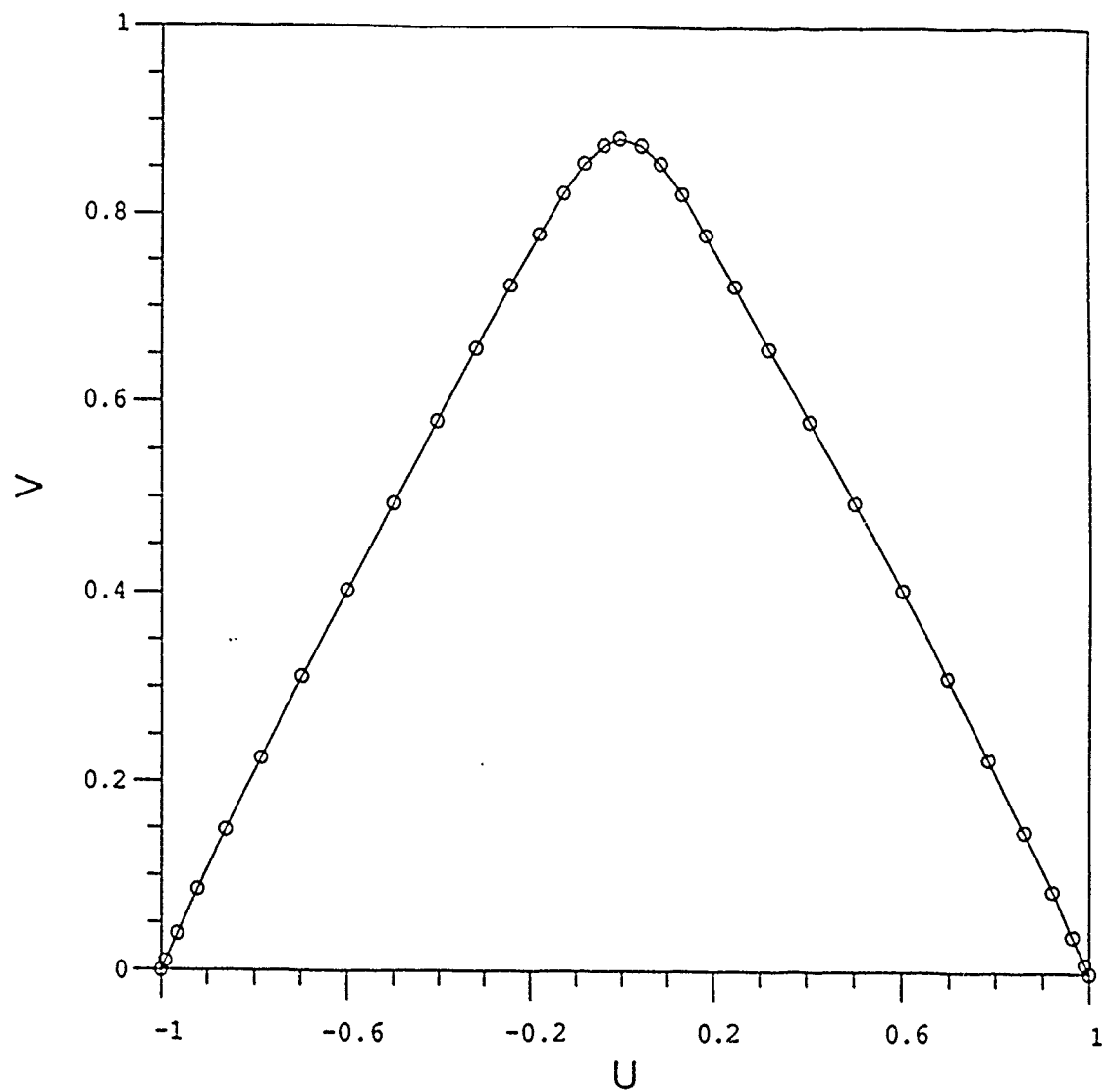


Figure 4

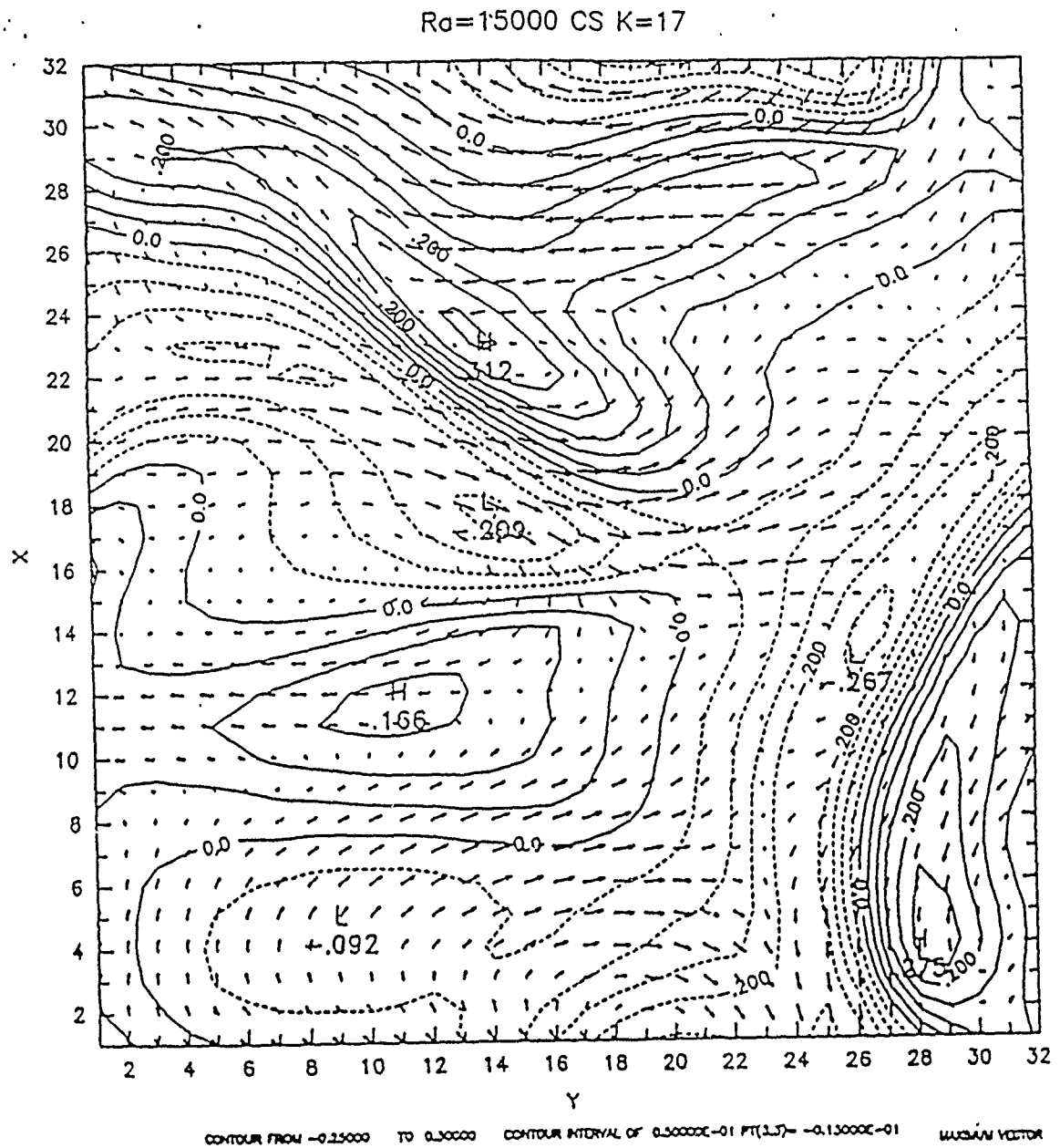


Figure 5

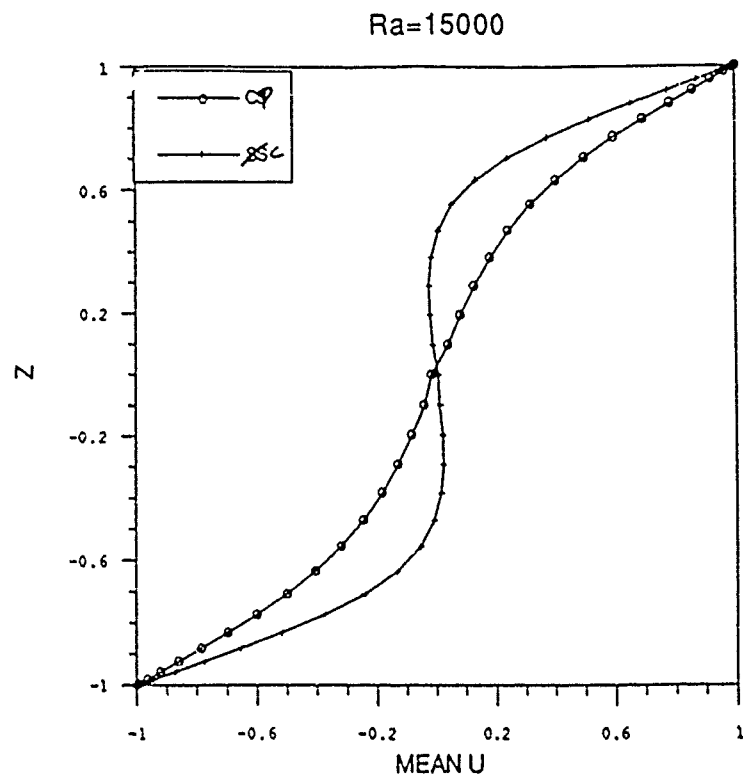


Figure 6

LARGE EDDY SIMULATION OF THE STABLY STRATIFIED ATMOSPHERIC BOUNDARY LAYER

Paul J Mason

Meteorological Office, Bracknell, Berks, U.K.

1. Introduction

Observations of stably stratified boundary layers are notorious for the appearance of both turbulent and wavelike features. The diversity of these observations has been linked to the sensitivity of stable boundary layers to terrain and other mesoscale influences. To advance modelling of stable boundary layers there is a clear need to seek data free of such complicating effects. Large eddy simulations of the stable boundary layer have been undertaken with both this objective to isolate salient features and also to provide detailed flow statistics.

Large eddy simulations use a three dimensional numerical model to explicitly describe the larger scale motions and attempt to parameterise the smaller scale motions. The technique is well established for convective and neutral flows but not for stably stratified flows. Stably stratified flows are not ideal for the technique as stable stratification promotes small rather than large eddies. As noted there is nevertheless a considerable motivation in seeking such application. The particular stable boundary layer chosen for study was the problem of evening transition over level horizontally homogeneous terrain.

2. The Large Eddy Model

The large eddy model used in this study was identical to the model used by Mason (1989) and previously applied to neutral and convective flows. The resolved scale motions are subject to a stability dependent subgrid scale mixing-length closure. This is an extension of the Smagorinsky model to include buoyancy effects and adopts a critical Richardson number of 0.33. The resolved motions were also subject to surface boundary conditions based on Monin Obukhov similarity. The cooling was achieved by either a prescribed heat flux or a prescribed rate of surface temperature change,

3. Initial Conditions

Initial condition proved to be very critical. No attempt to generate self sustaining turbulence in an initially stable boundary layer succeeded. With the small domain appropriate for the simulation of stable turbulence the neutral stability planetary boundary layer flow was linearly stable and required very large amplitude initial disturbances to generate self sustaining eddies.

4. Details of Parameters

The requirement for very long integration times comprising 60,000 time steps to first establish a statistically stable neutral boundary layer and subsequent 60,000 time steps for 3 hours of simulation after transition limited the mesh points to 40 x 32 x 62. The domain selected was 500m x 300m x 1000m and the vertical mesh was non-uniform. The typical resolution was 12m. The geostrophic wind speed was 10ms^{-1} and the surface roughness

0.1m. Results shown here are for a cooling due either to a flux of 10Wm^{-2} or a rate of 1°C per hour depending on the boundary condition. There are only minor differences between these cases. With a cooling rate of 30Wm^{-2} the turbulence collapsed. This may be realistic but with collapse the model no longer has large eddies in the very stable region and is dominated by a mixing length description.

5. Results

Statistics were obtained as averaged from 10 realisation within periods of 300s. Figure 1 shows the evolution of the temperature profile. The numerals I, II and III refer to times 1350s, 5500s and 8000s from the onset of cooling. In a comparable simulation with a passive scalar the "temperature" profile extended to greater heights than curve III after only 1350s. Figure 2 shows the corresponding velocity profiles. The velocity profiles show the usual characteristic evolution of wind profile after evening transition. Figure 3 shows the variation of surface stress with time; The inverted triangles are results with no cooling. The circles and diamonds are for the constant cooling rate and the constant heat flux respectively. The stress variations shows the establishment of a quasi-steady state roughly 1 hour after transition.

Figure 4 shows the heat flux profile after 8000s with the constant heat flux simulation and Figure 5 shows the corresponding shear stress profile (labelled B) together with the neutral (labelled A) boundary layer stress profile obtained prior to transition. The dashed curves are the subgrid part. Figures 6a and b shows the profiles of σ_w^2 and σ_v^2 for the final stable states (curve B) and the neutral boundary layer (curve A). Figure 7 shows profiles of the gradient Richardson number, the ratio $a_w = \sigma_w/u_*$, and the correlation coefficient for the heat flux. Figure 8 shows both the flux and gradient Richardson numbers. It is evident that the Richardson number rises to a value of around 0.25 at the top of the stable boundary layer. This has a depth of about 200 m and is the region in which turbulence is being maintained by shear production. Above this layer there is still significant turbulence but this is not being maintained and is due to the slow decay of the initial turbulence of the neutral boundary layer. It is significant that in the stable boundary layer the ratios of σ_u , σ_v and σ_w are similar to those in the neutral boundary layer. This similarity is borne out by the appearance of the flow fields. Figures 9a, b and c show horizontal sections with fields of flow directions, vertical velocity and temperature perturbation at a height of 67.5 m. In general the flow fields are of similar character to those in a neutral shear flow but have a smaller scale. There is little evidence for any wave motion in the simulations.

More detailed analysis of the statistics shows that the results match the expectations of local scaling and are well predicted by Second Order closure models. The production and dissipation terms in the kinetic energy budget are shown in Fig.10. There is a very close balance at all heights. Fig.11 compares the turbulence length scale in the model with those in closures. The resulting dissipation for and the Brost Wyngaard (1978) models and a length scale proposed by Hunt Spalopt and Mansour (1987) are compared. In the stable region there is good agreement with both models. The Brost Wyngaard model bases the length scale on the turbulence energy and stable stratification, whilst the Hunt et al model is based on the wind shear and vertical velocity variance. In the stable region these apparently different approaches should give very similar results, provided, as found here, the ratio a_w is constant. Above the stable region the Brost and Wyngaard model is outside its intended application but the Hunt et al

models works with useful generality.

These simulations do have one significant failing but this failing is a general problem with Large Eddy simulations and is not special to stable boundary layer. The match between the near surface, essentially subgrid flow, and the interior resolved region is imperfect. In particular the velocity and temperature gradients within this matching region are too great. This appears to be a common failing of all Large Eddy Simulations at high Reynolds number. If the wall region is not resolved with a refined mesh the problem appears as too great a velocity gradient on the mesh points closest to the surface. In low Reynolds number calculations the problem disappears as real molecular viscosity provides a correct description of the near wall match.

An initial extensive study of different procedures to match the resolved motion to the wall was conducted and lead to little improvement and the feeling that there is an inherent difficulty. One limitation to current subgrid scale models is their statistical determinism. This is not physically well based as the stress calculated in a filter volume should have a stochastic component. Such stochastic backscatter is liable to more important when the subgrid stresses are large. This occurs in the matching region close to the wall. In this region the mean velocity gradients are also large and the backscattered energy will lead to increased shear stress. Tentative tests suggest that backscatter may resolve the problem and give increased confidence to more widespread use of large eddy simulations. Figure 12 illustrates the problem and Figure 13 the improvement due to backscatter. Figure 12 shows an enlargement of the stress profile in the lowest one tenth of a neutral boundary layer Large-Eddy Simulation. There is no backscatter. The solid curve is the total stress and the thin dotted line is the resolved part of this stress. The other two lines denoted the resolved part plus an extra "steady" flow part. The long-dashed curve is with the stress due to the $l^2 u_r / KZ$ Where u_r is the square root of the prevailing stress and l the subgrid mixing length. The other dashed curve is the stress due to $l^2 \langle \partial U / \partial Z \rangle$. Where $\langle \partial U / \partial Z \rangle$ is the actual mean velocity gradient. This should equal u_r / KZ but at its worst is roughly twice as large. Figure 13 shows the an otherwise identical calculation with backscatter amounting to about 30% of the dissipative drain. This value of backscatter is little more than a guess of a value large enough to have impact yet not implausibly large. There are also various issues concerning the spectrum of back scatter. Much further work is required but the backscatter has clearly had a highly beneficial effect on this part of the flow. It seems that a suitably chosen value might eliminate the problem altogether. The impact in the flow interior is negligible but there is a beneficial impact on other near wall statistics.

Conclusions

A successful Large Eddy Simulation of the Stable planetary boundary layer has been obtained with the same model as previously applied to convective and neutral boundary layers. This gives encouragement to future refined application of Large Eddy Simulation to the Planetary Boundary Layer.

Equally encouraging progress has also been made in improving the match between the flow interior and the surface. Application of a stochastic backscatter from the subgrid scales is suggested to be required.

Acknowledgements

The author wishes to acknowledge collaboration with Dr Steven Derbyshire in the analysis of statistics of the Stable Boundary layer Simulation and collaboration with Dr David Thomson in the investigation of the errors in the near wall match and stochastic backscatter.

References

- Brost, R.A. and Wyngaard, J.C., 1978 "A model study of the Stably-Stratified Planetary Boundary Layer", *J.Atmos.Sci.* 35, 1427-40
- Hunt, J.C.R., Spalart, P and Mansour, N., 1987 "A general form for the dissipation length scale in turbulent shear flows". Proc (Stanford/NASA Ames) Center for Turbulence Research Summer Program, 1987
- Mason, P.J., 1989 "Large-Eddy Simulation of the convective Atmospheric Boundary Layer". *J.Atmos.Sci.* 46, 1492-1516

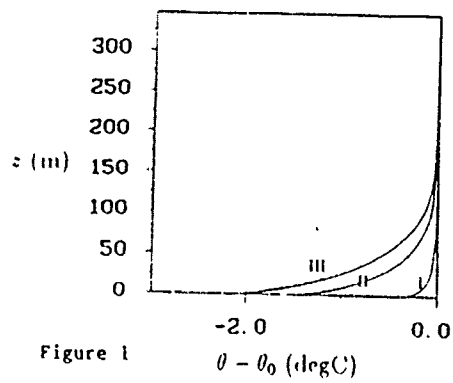


Figure 1 $\theta - \theta_0$ (deg C)

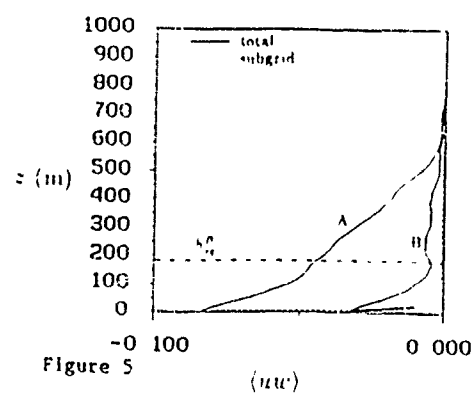


Figure 5 $\langle w \rangle$

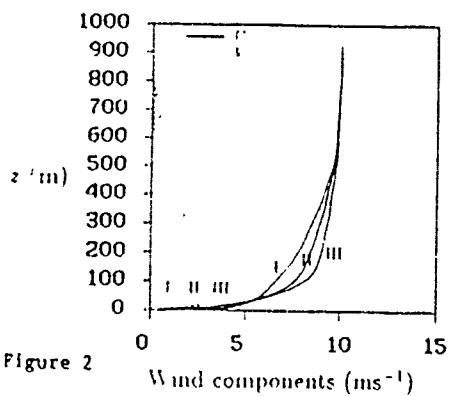


Figure 2 Wind components ($m s^{-1}$)

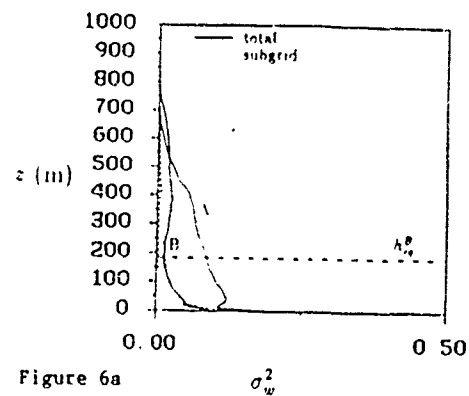


Figure 6a σ_w^2

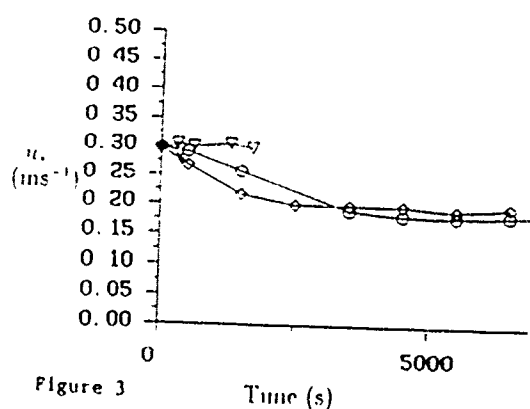


Figure 3 u_z ($m s^{-1}$)

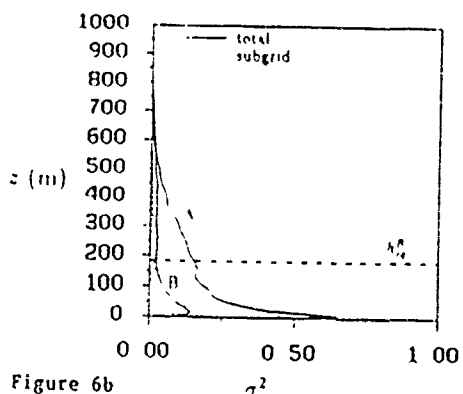


Figure 6b σ_u^2

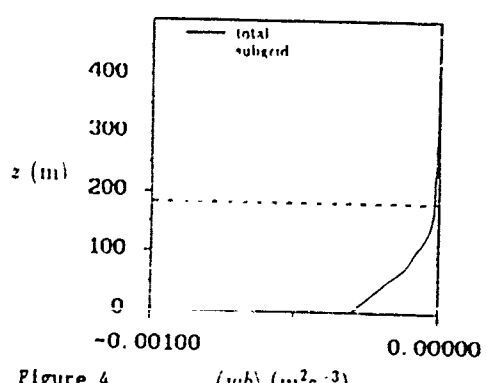


Figure 4 $\langle wb \rangle$ ($m^2 s^{-3}$)

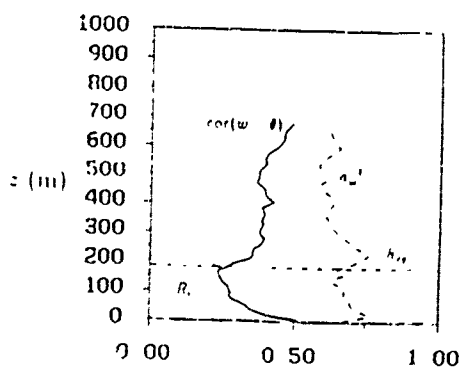


Figure 7

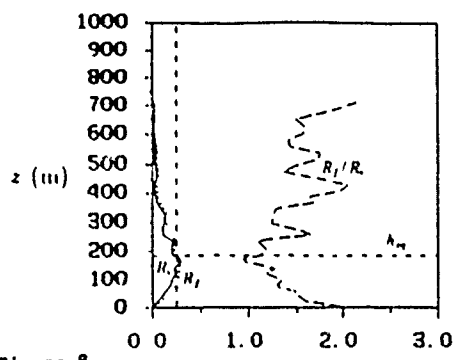


Figure 8

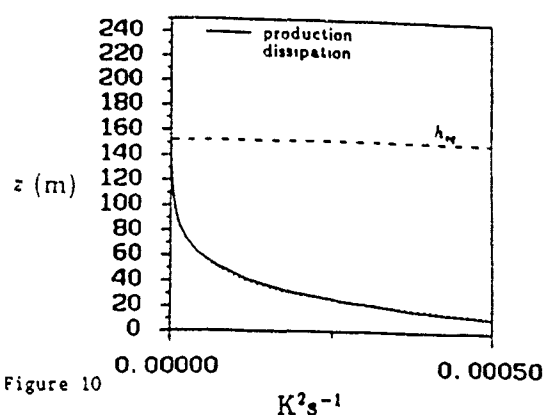


Figure 10

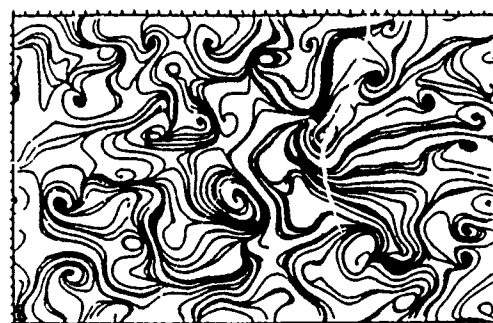


Figure 9a

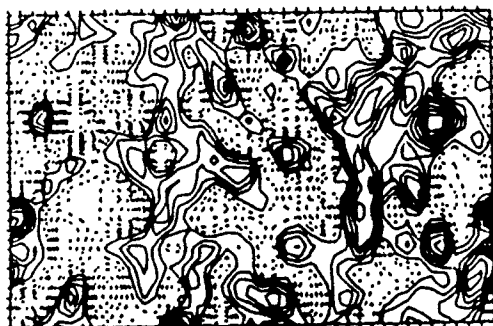


Figure 9b

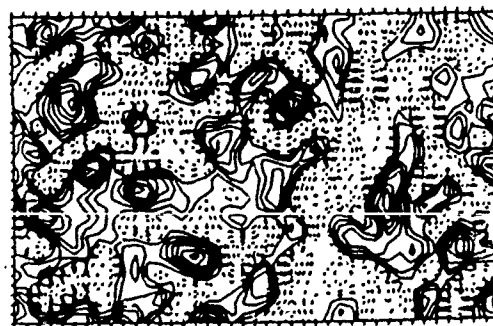


Figure 9c

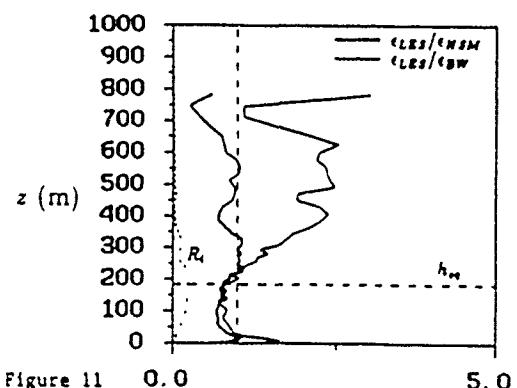


Figure 11

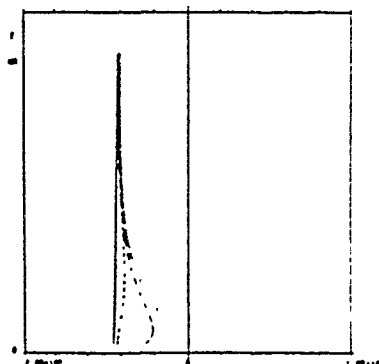


Figure 12

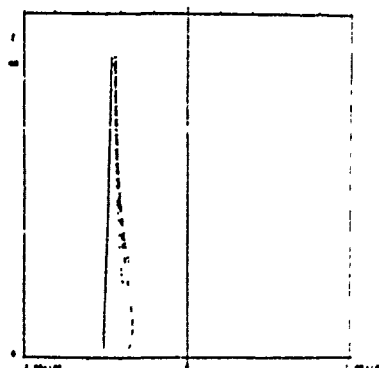


Figure 13

Subgridscale modeling for large scale ocean circulation

Greg Holloway

Institute of Ocean Sciences
Sidney BC Canada V8L4B2

Numerical modeling of 3D ocean circulation on space scales from ocean basin through global domain and over time scales from years to centuries poses an enormous computational challenge. To assess the significance of oceans for global climate and climate change, this challenge must be addressed. Perhaps this problem is an extreme of LES, where the "large eddies" are already the oceanic gyres themselves and the concern is to somehow represent a wealth of important processes that occur within the gyres.

Computational strategies divide into two approaches: (1) eddy-resolving and (2) non-eddy-resolving, where "eddy" refers here (and hereafter) to transient disturbances on scales smaller than the basin (gyre) scale.

1. The eddy-resolving approach

Conceptually this is the more straightforward approach, depending upon advances in computing technology together with sophistication in programming to resolve explicitly an ever greater portion of the eddy spectrum. As the unresolved (subgridscale, hereafter SGS) portion of the eddy field is reduced in total variance due to greater explicit resolution, it is hoped that relatively simple SGS representation may suffice. In practice, constant coefficient Laplacian and/or iterated Laplacian operators are used in both momentum and tracer equations. With presently available computational resource, this approach is feasible for domains as large as the North Atlantic with resolution as fine as $1/6^\circ$ in latitude or longitude, and 30 or more levels in the vertical. The

computation is also feasible in global domain with somewhat coarser resolution (1/4°) for model evolution over decadal timescales. Further advances in computing resource will enable both refinement of resolution and extended timescales for integrations.

Already, even in the global domain, encouraging results are in hand. Spontaneous eddy generation is seen, and the resulting eddy strengths and geographic distributions are similar to those inferred from satellite observations. So, are we done? Need we only await another generation in computing technology (and funding to enable use of that technology)? Answers to these questions are not clear. Although eddies appear in about the right places with about the right strengths, it is not clear that they do the right things. In particular, the explicit eddy transports of momentum, heat and other properties remain sensitive to the SGS; quantification of that sensitivity is an on-going, computationally intensive task.

It is seen that the mean states in model results exhibit systematic defects. Such features of ocean circulation as the Gulf Stream and Kuroshio are seen to overshoot their actual coastal separation latitudes. From the view of climate related studies, these overshoots are especially grievous because they predict warm, saline waters at latitudes where such waters are not found, implying grossly unrealistic atmospheric fluxes. Features of oceanic abyssal circulation are predicted that appear to be even farther from (poorly observed!) "reality". What is not known is how much these defects are due to the limited extent of eddy resolution or to the myriad other uncertainties that enter into large scale ocean models.

Questions of 'how much eddy resolution is enough?' and 'how much skill must be demanded of the SGS representation?' depend very much upon the time scale over which skill is required. For some sufficiently short time scale, relatively inexpensive, high resolution quasigeostrophic modeling may exhibit marginal skill (limited practically by uncertain initialization). For the longer term climate concerns (interannual, decadal and longer) the full range of SGS is felt, from "submesoscale" eddies (horizontal scales km to 10's of km) down to mixing processes on scales less than 1 m. Experimentation to improve SGS within eddy-resolving ocean circulation models has been limited by the high computational cost. Instead, SGS is more actively pursued within the non-eddy-resolving models.

2. The non-eddy-resolving approach

This is the more traditional approach to large scale ocean circulation, rooted historically in times when computational resource did not permit the eddy-resolving experiments. Today, despite enormous advances in computing power, a deliberate decision not to attempt to resolve eddies continues to offer opportunities to explore a range of ocean / climate possibilities evolving over significant timescales. However, the entire burden to represent eddy effects is then relegated to the SGS. For the most part, this has continued to be addressed in the form of Fickian gradient transport representations. Attention has been given to adaptive (nonlinear) eddy diffusion coefficients, such that the structure of the large scale fields determines those coefficients. An example is seen from modeling of the North Pacific Ocean. Other experimentation within non-eddy-resolving models is easily encouraged. Two particular aspects are highlighted in this talk.

a. Eddy-topographic rectification

The interaction of SGS eddies with SGS variations of bottom topography can, in principle, exert powerful forces on the larger scale flow. This is accomplished through correlations between eddy pressure anomaly and topographic slopes. The reaction on the mean flow tends to have a definite sense which may not oppose the mean flow, hence may not act as a drag. This phenomenon is termed "topographic stress". Due to inadequate resolution (presumably), ocean circulation models tend not to realize this stress. Such defects as overshoot in Gulf Stream and Kuroshio, too large Circumpolar transport, and weak or absent poleward undercurrents along eastern basin margins may reflect the model failures with respect to topographic stress.

Second order turbulence closure exhibits some skill at predicting this effect within the context of statistically homogenous environments. However, the results are not simple and not amenable to incorporation into large scale ocean models. An alternative approach is possible, recognizing that the closure results express an overall statistical

mechnaical tendency for flows to evolve toward higher system entropy. Since the maximum entropy state is relatively easily calculated, one may impose this tendency in ocean models simply as a relaxation toward maximum entropy. Ocean model tendency toward maximum entropy can be introduced either in a Rayleigh damping style or as a bias in a Laplacian-type eddy viscosity term.

b. Eddy transport of tracer fields

Gradient transport of passive tracers in statistically homogenous geostrophic turbulence is a tolerably tractable problem from the view of econd order closure theory. With the inclusion of Rossby wave propagation, a Fickian eddy diffusivity becomes anisotropic. Direct simulations tend to support the theory with respect to meridional transport; however, the simulations exhibit stronger zonal tracer transport than is predicted from simple theory. Applications for oceanic eddy transports of heat and salt, utilizing eddy statistics from satellite altimeters, are described.

DIAPYCNAL MIXING IN THE OCEAN: A REVIEW

by

Peter Müller

School of Ocean and Earth Science and Technology

University of Hawaii

ABSTRACT

Diapycnal mixing of buoyancy in the ocean interior is assumed to be caused by breaking internal gravity waves. Mixing coefficients are inferred from the diagnosis of large-scale hydrographic data, from tracer release experiments, from microstructure measurements, from the statistics of the Richardson number, and from calculations of the energy flux through the internal-wave field to high wavenumbers. All these inferences are indirect. Diapycnal buoyancy fluxes can neither be measured in the ocean nor calculated for realistic ocean conditions. Important unresolved issues include the energy conversions in a typical breaking event, the orientation of the diffusion tensor, the relevance of internal-wave-induced mixing in coarse-resolution oceanic general circulation models, and the importance of mixing in the ocean interior as compared to mixing at boundaries.

1. Introduction

The conventional wisdom is that

- diapycnal mixing of buoyancy in the ocean interior is due to intermittent patches of turbulence with a vertical extent of a few meters;
- mesoscale eddies and internal waves cannot mix buoyancy across isopycnals;
- the turbulent patches are caused by breaking internal gravity waves;
- internal-waves break by either shear or convective instabilities that are caused either by encounters of critical levels or by chance superpositions.

While these statements may be correct, this review will stress that all of our knowledge about the mixing process and mixing rates is indirect. Present-day instruments cannot measure diapycnal fluxes in the ocean. Theories and numerical models cannot calculate these fluxes for realistic ocean conditions. Thus, major basic issues are unresolved. Their resolution is necessary since, as we will demonstrate in the first section, oceanic general circulation models, prognostic and diagnostic ones, are extremely sensitive to the rate and functional dependence of mixing coefficients.

On the observational side, our knowledge about diapycnal mixing comes from diagnosing large-scale hydrographic data, from tracer release experiments, and from microstructure measurements. On the theoretical side, the statistics of the Richardson number and the energy flux through the internal-wave field to high wavenumbers have been calculated.

Among all these methods, the tracer release experiments provide perhaps the most direct evidence of diapycnal mixing. The interpretations of microstructure measurements, Richardson number statistics and energy flux calculations all rely on the notion that breaking internal waves convert fixed fractions of the available kinetic energy into mixing and dissipation. As already pointed out, the crucial quantity in

this scenario, the diapycnal buoyancy flux, can neither be measured nor calculated with confidence. This point will constitute our first major issue.

A second and related issue is the orientation of the diffusion tensor. It is usually assumed that it is diagonal in a horizontal/vertical coordinate system, but without any real physical basis. The orientation is an issue since horizontal mixing across sloping isopycnals becomes diapycnal mixing.

Inferences from hydrographic data depend on the specific assumptions made in the inference process. However, more importantly, the inferred diffusion coefficients are the ones that explain the large-scale hydrography and that are required in oceanic general circulation models which aim at prognosticating this hydrography. As our third issue we discuss whether or not diapycnal mixing by internal-wave breaking is relevant for coarse-resolution oceanic general circulation models.

Finally we address the question whether or not diapycnal mixing in the ocean interior is relevant at all. All of the admittedly indirect inferences of internal-wave-induced mixing in the ocean interior point to a value $O(10^{-5} \text{ m}^2\text{s}^{-1})$, an order of magnitude smaller than the value required to satisfy large-scale balances. One possible explanation is that most of the mixing happens near the boundaries of the oceans.

This review is by no means complete and thorough. Only a few examples are given and only some of the issues are discussed. A more complete discussion can be found in the proceedings of the 'Aha Huliko'a Workshop (Müller and Henderson, 1989) which is summarized in Müller and Holloway (1989) and in a review article by Gregg (1987). The difficulties and uncertainties of subgrid-scale representation are discussed with great insight in Holloway (1990).

A further limitation of this review is that we treat seawater as a one-component system and equate buoyancy and temperature. We therefore neglect the effects of double diffusion and the nonlinear equation of state on mixing. We also

assume that passive chemical traces behave like buoyancy. Finally, we do not distinguish between diapycnal and vertical mixing until this issue is discussed in Section 10.

2. Sensitivity Studies

Oceanic general circulation models (OGCMs) generally parameterize the subgrid-scale buoyancy fluxes by a Fickian diffusion term with a diffusion tensor which is diagonal in the horizontal/vertical coordinate system. The vertical diffusion coefficient K_v (supposed to model the diapycnal diffusion) is much smaller than the horizontal coefficient and is usually assumed to be constant. The value of K_v determines essential aspects of the thermohaline circulation. This has been most clearly demonstrated in a sensitivity study carried out by Bryan (1987) with a simplified OGCM. Figure 1 shows the calculated poleward heat flux (a quantity of importance for climate studies) as a function of latitude for various values of K_v . The heat transport increases approximately proportionally to the diffusion coefficient to the $2/3$ power. Following Bryan (1987), this power law dependence can be rationalized as follows: the thermal wind relation implies a horizontal velocity scale

$$u = \frac{\Delta \rho g H}{\rho_0 2 \Omega R} , \quad (2.1)$$

where g is the gravitational acceleration, Ω the earth's rotation rate, R the earth's radius, $\Delta \rho$ the imposed surface density difference, ρ_0 a reference density and H the vertical scale of the circulation. If a vertical advective-diffusive balance is assumed for the density field

$$w \frac{\partial}{\partial z} \rho = \frac{\partial}{\partial z} K_v \frac{\partial}{\partial z} \rho , \quad (2.2)$$

one finds

$$H = \frac{K_v}{w} = \frac{K_v R}{u H}, \quad (2.3)$$

where w is the vertical velocity scale and the incompressibility condition has been used. Solving (2.1) and (2.3) for u and H results in

$$u = \left(\frac{K_v \Delta \rho^2 g^2}{R^4 \Omega^2 \rho_0^2} \right)^{1/3} \quad (2.4)$$

$$H = \left(\frac{K_v R^2 \Omega \rho_0}{\Delta \rho g} \right)^{1/3}. \quad (2.4b)$$

The heat transport which is proportional to the product of u and H , then becomes

$$u \cdot H \sim K_v^{2/3} \quad (2.5)$$

as observed in the model calculation. This argument does not imply that the vertical advective-diffusive balance (2.2) holds locally, which it does not in the model, but only that it holds in some basin-wide integrated sense. Indeed, the horizontal advection terms in the density equation vanish upon integration over the area of the ocean, except for eddy-like terms.

While OGCMs with constant eddy viscosity and diffusivity coefficients of reasonable magnitude are capable of reproducing the broad features of the mid-latitude circulation, the same values do not allow reproduction of the complex structures of the equatorial circulation system which includes a narrow, intense equatorial undercurrent and a sharp thermocline. Modeling of these features becomes

more realistic when the vertical viscosity A_v and mixing coefficient K_v are assumed to depend on the Richardson number Ri in a manner proposed by Pacanowski and Philander (1981),

$$A_v = \frac{A_0}{(1 + \alpha Ri)^n} + \nu \quad (2.6)$$

$$K_v = \frac{A_v}{(1 + \alpha Ri)} + \kappa.$$

This form was motivated by the analysis of Munk and Anderson (1948), and is supposed to model the additional mixing caused by the strong undercurrent shear. In (2.6), A_0 , α , and n are adjustable parameters, and ν and κ are background values, in the absence of any shear-induced mixing.

Bryan's (1987) study demonstrates the sensitivity of prognostic calculations with respect to the value of the vertical diffusion coefficient. Inverse models show an even greater sensitivity. An argument advanced by Gargett (1984) demonstrates that the direction of the deep meridional circulation depends on such a subtle feature as the depth dependence of the diffusion coefficient. We repeat the argument here for it beautifully demonstrates possible pitfalls in our inference of the circulation from hydrographic data.

The observed density profile in most parts of the world's abyssal ocean is reasonably well approximated by

$$\rho(z) = \rho_0 - \Delta\rho \exp\{-z/b\} \quad (2.7)$$

where $\Delta\rho$ is the difference between the "surface" and bottom values of the density and b a scale depth, usually found to be $O(1.3 \text{ km})$. The associated Brunt-Väisälä frequency is

$$N^2(z) = - \frac{g}{\rho_0} \frac{\partial \rho}{\partial z} = \frac{g \Delta \rho}{b \rho_0} \exp \{z/b\}. \quad (2.8)$$

If this profile is interpreted as the result of the vertical advective-diffusive balance (2.2) we infer a vertical velocity

$$w = \frac{K_v}{b} + \frac{\partial}{\partial z} K_v. \quad (2.9)$$

If we assume

$$K_v(z) \sim N^{2q}(z), \quad (2.10)$$

the inferred vertical velocity becomes

$$w = \frac{K_v}{b} (1 + q). \quad (2.11)$$

If we further use the planetary geostrophic potential vorticity balance

$$\beta v = f \frac{\partial w}{\partial z}, \quad (2.12)$$

where f is the Coriolis and β the beta parameter, we find a meridional velocity

$$v = \frac{f}{\beta} \frac{(1 + q)q}{b^2} K_v, \quad (2.13)$$

which is equatorward for $-1 < q < 0$ and poleward otherwise. Observations discussed below have been interpreted as supporting values in the range from $q = 0$ to $q = -1/2$. Hence, inverse calculation might not even determine the sense of the meridional circulation.

A recent study by Cummins et al. (1990) shows that this dramatic effect does not occur in a prognostic calculation, partly because the vertical advective-diffusive balance (2.2) does not hold in that calculation and partly because explicit diapycnal mixing is overridden in some areas by implicit diapycnal mixing due to horizontal diffusion across sloping isopycnals.

3. Large-Scale Balances

Values of the diapycnal or vertical diffusion coefficients can be inferred from large-scale mass and heat balances. The original argument is due to Munk (1966), who applied it to the abyssal ocean in the following manner. Convection at high latitudes forms bottom water at a rate of $M = 50 \cdot 10^6 \text{ m}^3\text{s}^{-1}$. Conservation of mass requires that this water be upwelled with a velocity

$$w = \frac{M}{A} \sim 1.2 \text{ cm d}^{-1}, \quad (3.1)$$

where $A = 3.6 \cdot 10^{14} \text{ m}^2$ is the area of the ocean. If the vertical advective-diffusive balance (2.2) holds on average the scale height of the density field is given by

$$H = \frac{K_v}{w}. \quad (3.2)$$

The observed value of $H \sim 1.3 \text{ km}$ then leads to

$$K_v = 1.6 \text{ cm}^2\text{s}^{-1} \quad (3.3)$$

More recent estimates of the rate of bottom water formation are $O(20 \cdot 10^6 \text{ m}^3\text{s}^{-1})$ and would halve the values of the upwelling velocity and diapycnal mixing coefficient.

Nevertheless, $w = O(1 \text{ cm} \text{d}^{-1})$ and $K_v = O(1 \text{ cm}^2 \text{s}^{-1})$ are still the benchmark values today. The same type of argument has also been applied to abyssal basins where the inflow over a sill has been measured. Hogg et al. (1982) estimated $K_v = 3-4 \text{ cm}^2 \text{s}^{-1}$ for the Brazil Basin and Saunders (1987) $K_v \sim 1.5-4 \text{ cm}^2 \text{s}^{-1}$ for the Iberian Abyssal Basin.

4. Diagnostic Ocean Models

Any local estimate of the diffusion coefficient from the density equation must include the horizontal advection terms since $u/L \sim w/H$ because of incompressibility. The starting point of inverse estimates is hence the density equation in the form

$$u\partial_x\rho + v\partial_y\rho + w\partial_z\rho = D[\rho], \quad (4.1)$$

where $D[\rho]$ is the diffusion operator. Estimation of the diffusion coefficients from this equation requires knowledge of the three-dimensional velocity field and the gradient of the density. Hydrographic data provide the density field and, by virtue of the thermal wind relation, the vertical shear of horizontal velocity,

$$\partial_z u = \frac{g}{\rho_0 f} \partial_y \rho \quad (4.2)$$

$$\partial_z v = - \frac{g}{\rho_0 f} \partial_x \rho.$$

If additionally, validity of the planetary potential vorticity balance is assumed,

$$\partial_z w = \frac{\beta}{f} v, \quad (4.3)$$

one can calculate the complete three-dimensional velocity field up to three constants of integration, the reference velocities u_0 , v_0 and w_0 . This expresses the classical indetermination of the "level of no motion". If this velocity field is substituted into the density equation (4.1) one obtains an equation containing the three unknown reference velocities and the unknown diffusion coefficients. Since this equation holds for each vertical level one obtains a formally overdetermined system for the unknowns which can be solved by appropriate mathematical methods. This is the essence of the beta-spiral method first put forward by Stommel and Schott (1977). There are other diagnostic methods which differ in the dynamical principals and the type of data used.

The beta-spiral method has been applied by Olbers et al. (1985) to the North Atlantic using the Levitus (1982) atlas. Figure 2 shows maps of the estimated diapycnal diffusion coefficient for two depth ranges. The pattern of the diffusivities follows the pattern of the North Atlantic current system. The diffusivities are large where the currents are strong and small (or indistinguishable from zero) in the center of the gyre. Overall the values are small, less than $10^{-4} \text{ m}^2\text{s}^{-1}$ in most areas.

Much higher values of the diapycnal diffusivity are found by Olbers and Wenzel (1990) for the Antarctic Circumpolar Current, based on the Gordon et al. (1987) atlas. As seen in Fig. 3, values larger than $10^{-4} \text{ m}^2\text{s}^{-1}$ are found in most parts of the current.

5. Tracer Release Experiments

Another, perhaps more direct, estimate of the diapycnal diffusion coefficient can be obtained from tracer release experiments. In the deep ocean these experiments

have been pioneered by Ledwell et al. (1986). They inject sulfurhexafluoride (SF_6) on an isopycnal and follow the vertical spread of the tracer about the initial surface in time (see Fig. 4). A vertical diffusivity is then calculated from the formula

$$\sigma^2(t) = \sigma^2(t=0) + 2K_v t \quad (5.1)$$

where σ^2 is the variance of the vertical concentration distribution.

Their first experiment (in the Santa Monica Basin, release depth 800 m) yields a vertical diffusivity of about $0.25 \text{ m}^2\text{s}^{-1}$. Their second experiment (in the Santa Cruz Basin, release depth 1500 m) yields values larger than $1 \text{ cm}^2\text{s}^{-1}$ (Ledwell, 1989).

6. Microstructure Measurements

Though the vertical fluxes of buoyancy (and momentum) cannot be measured directly, microstructure profiling instruments are now capable of resolving the fluctuations of velocity and temperature in the centimeter range. From these microstructure profiles the dissipation rates of kinetic energy ϵ and of potential energy κ can be inferred if assumptions are made about the isotropy and statistics of the fluctuations. The dissipation rate κ is proportional to the dissipation rate of temperature or density variance.

Figure 5 (from Gregg, 1989) shows the kinetic energy dissipation ϵ as a function of depth for three experiments: Patchex, Patchexn and Ring 82I. These profiles suggest that the kinetic energy dissipation rate is proportional to the buoyancy frequency squared and to the 10 m vertical shear to the fourth power:

$$\epsilon = 7 \cdot 10^{-10} \frac{N^2}{N_o} \frac{S_{10}^4}{S_{GM}^4} \text{ WKg}^{-1}. \quad (6.1)$$

This scaling reduces the observed variability from a factor 58 to a factor 2. Other scalings have been suggested (e.g., Gargett, 1984) and there is dispute about the applicability of (6.1) (Gargett, 1990).

Dissipation rate estimates are used to infer diapycnal mixing rates according to an argument originally proposed by Lilly et al. (1974) and applied to the ocean by Osborn (1980). Consider the turbulent kinetic energy equation and assume the major balance to be between shear production, exchange with potential energy, and dissipation,

$$\overline{u'w'} \partial_z \bar{u} + \frac{g}{\rho_0} \overline{\rho'w'} + \epsilon = 0. \quad (6.2)$$

Define the flux Richardson number as

$$R_f = - \frac{g/\rho_0 \overline{\rho'w'}}{\overline{u'w'} \partial_z \bar{u}}. \quad (6.3)$$

The vertical buoyancy flux is then given by

$$\frac{g}{\rho_0} \overline{\rho'w'} = \gamma \epsilon, \quad (6.4)$$

with an efficiency factor

$$\gamma = \frac{R_f}{1 - R_f}. \quad (6.5)$$

Since, $\overline{\rho'w'} = -K_v \partial_3 \bar{\rho}$ we find a relation between the diapycnal diffusion coefficient K_v and the dissipation rate ϵ ,

$$K_v = \gamma \epsilon N^{-2}, \quad (6.6)$$

that involves only γ as an unknown. Laboratory experiments and oceanic measurements (Thorpe, 1973; Oakey, 1982) seem to suggest a value of $\gamma = 0.2$. Using this value Gregg's measurements shown in Fig. 5 imply

$$K_v = 5 \cdot 10^{-6} \text{ m}^2\text{s}^{-1} \frac{S_{10}^4}{S_{GM}^4}, \quad (6.7)$$

independent of depth.

Dissipation rates χ of potential energy have been used to infer the diapycnal diffusion coefficient by assuming a balance of the conversion and dissipation term (Osborn and Cox, 1972),

$$\frac{g}{\rho_0} \overline{\rho' w'} = \chi, \quad (6.8)$$

in the turbulent potential energy equation. This leads to

$$K_v = \chi N^{-2}. \quad (6.9)$$

Note that the assumed balances within the kinetic and potential energy equations are based on a scenario in which turbulent kinetic energy is generated by shear production. A fraction R_f of this kinetic energy is converted to potential energy and then dissipated. The other fraction $(1 - R_f)$ is dissipated directly.

7. Kinematic Estimates

If internal wave breaking is primarily shear driven, the Richardson number,

$$Ri = \frac{N^2}{(\partial_z u)^2 + (\partial_z v)^2}, \quad (7.1)$$

must be a key parameter. The rms Richardson number of the internal wave field is observed to be on the order of two (Munk, 1981), larger than the critical value $Ri = 0.25$. It was first recognized by Bretherton (1969) that a random superposition of internal waves would give a finite probability that $Ri < 1/4$ locally. This statistical approach was further pursued by Garrett and Munk (1972) and Garrett (1979b). The distribution function of the Richardson number has been derived by Desaubies and Smith (1982) for a Gaussian internal wave field. The distribution function depends on the rms strain λ of the wave field which is about $\lambda = 0.5$ for the ocean. Calculated and observed distributions agree fairly well as can be seen in Fig. 6 for two data sets from Evans (1982).

Using numerical simulations, Desaubies and Smith (1982) were also able to derive the statistics of the vertical distributions of regions where $Ri < 1/4$. However, estimates of a diapycnal mixing coefficient require two additional parameters: (i) the amount of mixing that occurs in these regions and (ii) the frequency in time with which these events occur. Both these parameters are poorly established although reasonable assumptions such as complete mixing and a frequency of occurrence proportional to N lead to reasonable values of K_v .

8. Dynamical Calculations

Nonlinear interactions among internal waves are a principal part of their dynamics and provide an important link in the overall energy cascade from large to small scales. Four approaches for their analysis are reviewed in Muller et al. (1986): (i) the evaluation of the transfer integral describing weakly and resonantly interacting waves, (ii) the application of closure hypotheses from turbulence theories to more strongly interacting waves, (iii) the integration of the eikonal equations describing the propagation of small-scale waves in a background of large-scale waves, and (iv) the direct numerical simulation of the basic hydrodynamic equations of motion. The weak interaction and eikonal calculations have provided most of the current wisdom about interactions within the oceanic internal wave field, notably, they have been used to explicitly calculate the energy flux F to high wave numbers. If one assumes again that a fraction R_f of this flux is used for mixing then the diapycnal diffusivity can be estimated according to

$$K_v = R_f F N^{-2} \quad (8.1)$$

The equation describing the nonlinear transfer of action or energy within an internal wave field due to weak resonant wave-wave interactions is given by

$$\begin{aligned} \frac{\partial}{\partial t} A(\mathbf{k}) &= \int d\mathbf{k}' d\mathbf{k}'' \{ T^+ \delta(\mathbf{k} - \mathbf{k}' - \mathbf{k}'') \delta(\omega - \omega' - \omega'') \\ &\quad \{ A(\mathbf{k}') A(\mathbf{k}'') - A(\mathbf{k}) A(\mathbf{k}'') - A(\mathbf{k}) A(\mathbf{k}'') \} \\ &\quad + 2T^- \delta(\mathbf{k} - \mathbf{k}' + \mathbf{k}'') \delta(\omega - \omega' + \omega'') \quad (8.2) \\ &\quad \{ A(\mathbf{k}') A(\mathbf{k}'') + A(\mathbf{k}) A(\mathbf{k}'') - A(\mathbf{k}) A(\mathbf{k}'') \}, \end{aligned}$$

where $A(\mathbf{k}) = E(\mathbf{k})/\omega(\mathbf{k})$ is the action density spectrum, $E(\mathbf{k})$ the energy density spectrum, \mathbf{k} the wavenumber vector, $\omega = \omega(\mathbf{k})$ the frequency (given by the dispersion relation), and T^+ and T^- are transfer functions depending on \mathbf{k} , \mathbf{k}' , and \mathbf{k}'' . Explicit expressions for T^+ and T^- can be found in Müller and Olbers (1975) and Olbers (1976). The transfer equation (8.2) is a closed equation for the spectrum $A(\mathbf{k})$. The basic statistical closure hypothesis in its derivation is the assumption that the correlation time of the wave field is smaller than the interaction time, so that interacting wave modes can always be treated as statistically independent (Hasselmann, 1966, 1967; Benney and Saffmann, 1966). Waves only interact if the resonance conditions

$$\mathbf{k}' + \mathbf{k}'' = \mathbf{k} \quad (8.3)$$

$$\omega' + \omega'' = \omega$$

are satisfied.

In analyzing the transfer equation (8.2) McComas and Müller (1981) assumed that internal wave energy is generated at low vertical wavenumbers $\beta < \beta_*$ and dissipated at high vertical wavenumbers $\beta > \beta_c$ (see Fig. 7). They then proved that an inertial range exists between β_* and β_c , in which resonant interactions provide a constant (independent of vertical wavenumber) downscale energy flux F from the generation to the dissipation region. At high frequencies the flux is provided by an induced diffusion mechanism, at low frequencies by a parametric subharmonic instability mechanism. The inertial range has a vertical wavenumber spectrum

$$E(\beta) \sim \beta^{-2} \quad (8.4)$$

as observed. The downscale energy flux is given by

$$F = \left[1 + \frac{27}{32\sqrt{10}} \right] \frac{\pi f}{N^2} E^2 \beta_*^2, \quad (8.5)$$

where E is the total energy, and f and N are the Coriolis and Brunt Väisälä frequencies, respectively. If the internal wave quantities scale like the Garrett and Munk model (Cairns and Williams, 1976) then

$$F = 2 \cdot 10^{-9} \frac{N^2}{N_0^2} \frac{E^2}{E_{GM}^2} \text{ W kg}^{-1}, \quad (8.6)$$

which has the same functional form as the estimate (6.1) from microstructure data and is a factor 3 larger (if $S^2 \sim E$ which follows if one assumes $\beta_c = \text{constant}$ in the Garrett and Munk model [Gargett, 1990]). Energy flux calculations thus seem to be consistent with dissipation measurements.

A similar result is obtained by Henyey et al. (1986), who integrate the eikonal equations for small-scale waves propagating in a background of large-scale waves. In the geometric optics or WKB-approximation the frequency of a small-scale wave of wavenumber \mathbf{k} propagating in a large-scale background flow $\bar{\mathbf{u}}$ is given by

$$\omega = \omega_0(\mathbf{k}) + \mathbf{k} \cdot \bar{\mathbf{u}}, \quad (8.7)$$

where $\omega_0(\mathbf{k})$ is the intrinsic frequency and $\mathbf{k} \cdot \bar{\mathbf{u}}$ the Doppler shift. The eikonal equations then state that the vertical wavenumber of the small-scale wave changes according to

$$\dot{k}_3 = \frac{d}{dt} k_3 = - \frac{\partial \omega}{\partial z} = - \frac{\partial \bar{u}}{\partial z} \cdot \mathbf{k}. \quad (8.8)$$

The energy flux past a certain wavenumber is given by

$$F = \dot{k}_3 E(k). \quad (8.9)$$

If it is assumed that waves whose vertical wavenumber exceeds $\beta_c = \frac{2\pi}{5m}$ break and are annihilated then the flux past β_c is only made up of waves whose vertical wavenumber increases. This flux was evaluated by Henyey et al. (1986) using a Monte Carlo simulation of wave trajectories in a current field \bar{u} selected randomly from an ensemble with a Garrett and Munk spectrum. They find

$$F = 6.4 \cdot 10^{-11} \frac{N^2}{N_0^2} \cosh^{-1}(N/f) \text{ W kg}^{-1} \quad (8.10)$$

from the simulations and a heuristic model. Their result has the same functional dependence, except for the \cosh^{-1} factor, as McComas and Müller's result and is a factor 6 smaller. A more important difference is, perhaps, that Henyey et al. predict a flux to higher frequencies whereas McComas and Müller calculate a flux to lower frequencies (see Fig. 7).

These two dynamical studies assume that wave breaking is due to chance superposition within a random internal wave field. Wave breaking might also occur as the result of internal waves approaching a critical layer in an ambient geostrophic shear. Vertical critical layers result when changes in the geostrophic flow with depth force the intrinsic frequency toward the lower bound of the internal wave band or if this lower bound is increased with depth. Horizontal critical layers occur either when the intrinsic frequency is Doppler shifted toward the buoyancy frequency N by

lateral changes in the geostrophic flow or when N changes laterally. The specific case of vertical critical layers due to geostrophic shear was considered by Kunze and Müller (1989).

The intrinsic frequency following the mean flow is $\omega_0 = \omega - \mathbf{k} \cdot \bar{\mathbf{u}}$, where the Eulerian frequency ω is invariant in a time-independent mean flow. As a wave propagates down from the surface, the change in geostrophic velocity $\Delta\bar{\mathbf{u}}$ will result in a corresponding change of $k_x \Delta\bar{\mathbf{u}}$ to its intrinsic frequency. A critical layer is reached at a depth where the intrinsic frequency becomes $f = \omega - k_x \Delta\bar{\mathbf{u}}$. As the wave approaches its critical layer it slows down, steepens, breaks, and may convert part of its energy to mixing.

A quantitative estimate of the energy available for mixing was obtained by Kunze and Müller (1989). Following the work of Ruddick (1980) they considered an internal wave field of Garrett and Munk spectral intensity that propagates downward from the surface into a geostrophic flow that is a first baroclinic mode with a surface velocity of 30 cms^{-1} . As the spectrum propagates downward those waves that encounter a critical level are eliminated. The resulting energy flux divergence is shown in Fig. 8 as a function of depth. A maximum value of about $5 \cdot 10^{-9} \text{ Wkg}^{-1}$ is reached at 700 m depths comparable to the estimate (8.6) of the energy flux to high wavenumbers by wave-wave interactions.

9. Wave Breaking

At the heart of our understanding of diapycnal mixing is the concept that mixing is caused by the turbulence resulting from wave breaking either by random chance or in critical layers. Quantitative estimates assume that wave-wave interactions (weak or strong) cascade kinetic energy to small scales; a small fraction

R_f of this energy is converted to potential energy in mixing events and then dissipated. The other part ($1 - R_f$) is dissipated directly. Much of our intuition about the wave breaking process itself has come from the analysis of simple situations where single waves break by shear or gravitational instability. What happens in a more complex environment consisting of many waves is by no means clear. At one extreme are the phenomenological theories of buoyant turbulence. The classical concepts based on the dominance of the buoyancy term in the turbulent kinetic energy equation lead to a kinetic energy spectrum (Lumley, 1964)

$$E(k) = A \epsilon_0^{2/3} [(1 + k_b/k)^{4/3}] k^{-5/3}, \quad (9.1)$$

where A is the empirical Kolmogorov constant, ϵ_0 the kinetic energy dissipation rate and $k_b = (N^3/\epsilon_0)^{1/2}$ the buoyancy wavenumber. Weinstock (1985) calculates the same form for the temperature variance spectrum. The predicted spectral forms are roughly consistent with observations of shear spectra (Gargett et al., 1981) and of temperature gradient spectra (Gregg, 1977). However, the buoyancy flux co-spectrum is calculated by (Lumley, 1964)

$$B(k) \sim N^2 \epsilon_0 [1 + (k_b/k)^{4/3}]^{1/2} k^{-7/3}, \quad (9.2)$$

and decreases with increasing wavenumbers. Also, Weinstock's analysis implies a transfer of temperature variance towards lower wavenumbers for $k < k_b$. These features are certainly contrary to the conventional wisdom of wave breaking.

Starting from wave-wave interaction theory Holloway (1983) is also able to derive the expression (9.1) for the temperature and velocity variance spectra, but under the assumption that there is little buoyancy flux and that nonlinearities cascade

kinetic and potential energy independently to high wavenumbers. As pointed out by Holloway (1989, 1990), dynamical theories exist which are consistent with observed velocity and temperature spectra but which allow for quite different pathways of energy.

Direct numerical simulations in three dimensions have so far dealt only with freely decaying buoyant turbulence (Riley et al., 1981; Metais and Herring, 1989; Siegel and Domaradzki, 1990). Siegel and Domaradzki's study is a large-eddy simulation which achieves Reynolds numbers characteristic of the ocean in a box of about $(10 \text{ m})^3$.

Forced-dissipative experiments have been carried out in two dimensions by Shen and Holloway (1986) with the following surprising energy balance: If external forcing of kinetic energy (and in some runs, potential energy) is applied at low wavenumbers then kinetic energy is converted to potential energy at low wavenumbers. The potential energy then cascades to high wavenumbers where some of it is converted back to kinetic energy which is then scattered to low and high wavenumbers (Fig. 9). The buoyancy flux at the actual overturning events is upwards; gravitational energy is released! It seems that this result is not an artifact of the two-dimensional geometry (Holloway, 1990).

High resolution two-dimensional calculations by Winters and D'Asaro (1979) show the breakdown of an incoming finite-amplitude internal wave in a critical layer. The breakdown is shear-driven although unstable density gradients persist for many buoyancy periods. However, as shown by Winters and Riley (1990), modes driven by shear instability are oriented in the vertical plane of the background shear, whereas convectively unstable modes are oriented in the transverse plane and are hence eliminated from two-dimensional calculations.

All these results certainly demonstrate that our basic notion about the buoyancy flux in wave breaking events is not as solidly founded as we sometimes presume.

10. Horizontal Versus Isopycnal Mixing

A second major issue is that of horizontal versus isopycnal mixing. So far we have not stressed this issue and have used the terms "vertical" and "diapycnal" as synonyms. Diffusion in physical space requires specification of a diffusion tensor. The orientation of this tensor is not known. The principal axes may lie in and orthogonal to the geopotential, isopycnal, neutral or any other surface. The orientation is important. Horizontal diffusion across sloping isopycnal surfaces becomes cross-isopycnal diffusion:

$$K_d = K_v + K_h s^2, \quad (10.1)$$

where s is the slope of the isopycnal and the subscripts d, v, and h indicate diapycnal, vertical and horizontal, respectively (Redi, 1982). Most numerical models use a diffusivity tensor that is diagonal in the horizontal/vertical coordinate system, with the vertical diffusivity (representing internal-wave breaking) much smaller than the horizontal coefficient (representing the stirring by mesoscale eddies). Since mesoscale eddies mix or stir along isopycnal surfaces some researchers argue that the mixing tensor should be diagonal in the isopycnal/diapycnal system.

Additional support for this representation seems to come from the argument that the exchange of water particles on isopycnals does not require any work against gravity. However, neither of these arguments is fully convincing. Mesoscale eddies can mix properties across mean isopycnals as resolved in general circulation models

(discussion below), and exchange of water parcels on horizontal, i.e., geopotential, surfaces also requires no work. Furthermore, potential energy is released when parcels are exchanged within the wedge between the horizontal and isopycnal surfaces, the wedge of baroclinic instability. Indeed, the Archimedean work that is done on a parcel displaced by an infinitesimal amount is given by (Olbers and Wenzel, 1990)

$$dA = \rho [(\alpha \nabla \Theta - \beta \nabla S) \cdot dx] [\nabla \phi \cdot dx], \quad (10.2)$$

where ϕ is the geopotential, Θ the potential temperature, S the salinity, α the thermal expansion coefficient and β the haline contraction coefficient. This form led Olbers and Wenzel to suggest a diffusion tensor (Fig. 10) with three principal components: a large value along the axis half way between the isopycnal and geopotential surfaces where mixing would release the maximum amount of energy, a medium value along the intersection of the isopycnal and geopotential surfaces where mixing results in no release of potential energy, and a small value along the axis perpendicular to these two where mixing requires the maximum amount of work.

11. Baroclinic Instability

Another part of the conventional wisdom is that the small-scale turbulence does the diapycnal mixing and that mesoscale eddies and internal waves cannot support any diapycnal mixing. Ultimately, all diapycnal mixing is done by molecular diffusion. Only molecular diffusion can transport buoyancy across instantaneous, actual density surfaces; mesoscale eddies, internal waves and turbulence cannot. However, all these motions can transport tracers across mean isopycnals and it is the flux across such mean isopycnals which is relevant in general circulation models. An example is the

diapycnal flux across the mean position of the Gulf Stream (Fig. 11) which is clearly supported by rings and meanders. The question is, what controls the flux or rate of diffusion? It may well be (Garrett, 1989) that this flux is determined by the mesoscale eddies and that the smaller scale motions just do what needs to be done, similar to the classical example of three-dimensional turbulence in a homogeneous, non-rotating fluid where energy is cascaded down to the dissipation scales without any back-effect on the larger scales.

If this is indeed true parameterization schemes should be based on the theory of baroclinic instability. Take, e.g., Eady's (1949) classical problem of baroclinic instability in a uniform vertical shear $\partial\bar{u}/\partial z$ over depth H . The stream function of the fastest growing wave is given by

$$\varphi' = \phi(z) \cos(kx + a(z)) \exp\{\omega_it\}, \quad (11.1)$$

where the depth dependence of the amplitude $\phi(z)$ and phase $a(z)$ are sketched in Fig. 12. Since the transverse velocity is $v' \sim \partial_y\varphi'$ and the temperature $T' \sim \partial_z\varphi'$, the transverse heat flux becomes

$$\begin{aligned} \overline{v'T'} &= \frac{1}{2} \phi^2 u' k \partial a / \partial z \exp\{2\omega_it\} \\ &= O(H^2 \frac{N}{f} \frac{\partial\bar{u}}{\partial z} \frac{\partial\bar{T}}{\partial y}) \end{aligned} \quad (11.2)$$

if the transverse velocity is assumed to be limited by $v' = O(\bar{u})$ (Stone, 1974; Bryden, 1979). This transverse heat flux leads to a flux across the sloping isopycnal surface with a diapycnal diffusivity (Garrett, 1989)

$$K_d \sim H^2 f \text{ Ri}^{-3/2}. \quad (11.3)$$

To understand what determines the fluxes, eddy-resolving models need to be run with different "internal-wave" diffusivities. One could then see to what extent the fluxes across mean isopycnals depend on these "internal-wave" diffusivities or whether parameterization like (11.3) are appropriate. It may be that the large diapycnal mixing coefficients seen in Olbers and Wenzel's (1990) inverse calculation is due to baroclinic instability and not to breaking internal waves.

12. Boundary Mixing

The final point is the idea of boundary mixing. Diapycnal mixing coefficients in the main pycnocline have been inferred from dissipation measurements and calculations of the internal-wave energy flux to high wavenumbers. All these estimates are on the order of $5 \cdot 10^{-6}$ to $5 \cdot 10^{-5} \text{ m}^2\text{s}^{-1}$, an order of magnitude smaller than Munk's (1966) "abyssal recipes" value and the values required to satisfy abyssal mass and heat balances by a vertical advective-diffusive balance. One possible resolution of this discrepancy is that vigorous diapycnal mixing at the side wall boundaries of the ocean, in combination with along isopycnal mixing or stirring, gives rise to an effective diapycnal diffusivity of the required magnitude of $10^{-4} \text{ m}^2\text{s}^{-1}$. This idea had already been suggested by Munk (1966) and received observational support from Armi (1978). The questions are, what is the energy source for vigorous boundary mixing and how often does a water parcel encounter a boundary? Armi (1978) suggested that the energy source is the turbulent energy production in the boundary layer caused by mean flows. This hypothesis has been disputed by Garrett (1979a). A more likely source is perhaps the internal-wave field reflecting off a

sloping bottom. As shown by Eriksen (1982, 1985) reflection at a sloping bottom leads to a significant redistribution of the incoming internal energy flux. If it is assumed that reflected waves of high wavenumber break and produce mixing, an energy flux is calculated that may sustain an abyssal equivalent diffusivity of the required magnitude (Garrett and Gilbert, 1988). This mechanism favors low latitudes and steep slopes.

Similarly, Xu (1990) shows that the scattering of internal waves at random bottom topography leads to a transfer of the incoming flux to higher wavenumbers. Although redistribution is smaller than for the reflection problem it is to much higher wavenumbers so that both processes might be of equal efficiency.

Though interior mixing and boundary mixing may have similar effects on the distribution of passive tracers, the dynamics of the flow are profoundly altered. If all mixing happened near the boundaries all bottom water would be upwelled in boundary layers. The interior of the ocean would be quiescent except for the need to transfer fluid along isopycnals from one boundary layer to another (McDougall, 1989).

13. Summary and Conclusion

Diapycnal mixing coefficients are used in oceanic general circulation models to parameterize the effect of the subgrid-scale cross-isopycnal buoyancy fluxes. Important features of the circulation are sensitive to the value and functional dependence of the mixing coefficient. We have briefly reviewed the conventional wisdom that diapycnal mixing is induced by breaking internal gravity waves. All the inferences about the mixing process and mixing rates are indirect. Diapycnal mixing can neither be measured in the ocean nor calculated for realistic ocean conditions. Major issues are unresolved. The basic physical issue is that we do not know what

constitutes a typical breaking and what the energy conversions are in such a typical event. The other issues are ones of relevance. Is internal-wave-induced mixing relevant for coarse-resolution oceanic general circulation models or must the mixing in these models be ascribed to other processes, such as baroclinic instability? Is mixing in the ocean interior of importance or is most of the mixing done near the boundaries of the ocean?

Our knowledge of ocean mixing is not as solid as often presumed; thus considerable research still needs to be done. The many surprises ahead make this a truly exciting field to be in.

ACKNOWLEDGMENTS

I am grateful to all my colleagues on whose research efforts I have drawn in this review and who have generously shared their ideas about mixing with me. It is a pleasure to thank Crystal Miles and Naomi Yanagishita for their help in preparing the manuscript. The author's research reported here was supported by the Office of Naval Research.

REFERENCES

- Armi, L., 1978. Some evidence for boundary mixing in the deep ocean. *J. Geophys. Res.*, 83, 1971–1979.
- Benney, D. J. and P. G. Saffman, 1966: Nonlinear interactions of random waves in a dispersive medium. *Proc. Roy. Soc. London*, A289, 301–320.
- Bretherton, F. P., 1969. Waves and turbulence in stably stratified fluids. *Radio Sci.*, 4, 1279–1287.
- Bryan, F., 1987: Parameter sensitivity of primitive equation ocean general circulation models. *J. Phys. Oceanogr.*, 17, 970–985.
- Bryden, H. L., 1979: Poleward heat flux and conversion of available potential energy in Drake Passage. *J. Mar. Res.*, 37, 1–22.
- Cains, J. L. and G. O. Williams, 1976: Internal wave observations from a midwater float, Part II. *J. Geophys. Res.*, 81, 1943–1950.
- Cummins, P. F., G. Holloway, and A. E. Gargett, 1990: Sensitivity of the GFDL ocean general circulation model to a parameterization of vertical diffusion, *J. Phys. Oceanogr.*, 20, 817–830.
- Desaubies, Y. J. F. and W. K. Smith, 1982: Statistics of Richardson number and instability in oceanic internal waves. *J. Phys. Oceanogr.*, 12, 1245–1259.
- Eady, E. T., 1949: Long waves and cyclone waves. *Tellus*, 1 (3), 33–52.
- Eriksen, C. C., 1982: Observations of internal wave reflection off sloping bottoms. *J. Geophys. Res.*, 87, 525–538.
- Eriksen, C. C., 1985: Implications of ocean bottom reflection for internal wave spectra and mixing. *J. Phys. Oceanogr.*, 15, 1145–1156.
- Evans, D. L., 1982: Observations of small-scale shear and density structure in the ocean. *Deep Sea Res.*, 29, 581–595.
- Gargett, A. E., 1984: Vertical eddy diffusivity in the ocean interior. *J. Mar. Res.*, 42, 359–393.
- Gargett, A. E., 1990: Do we really know how to scale the turbulent kinetic energy dissipation rate ϵ due to breaking of oceanic internal waves? *J. Geophys. Res.*, 95, 15,971–15,974.
- Gargett, A. E., P. J. Hendricks, T. B. Sanford, T. R. Osborne and A. J. Williams, III, 1981: A composite spectrum of vertical shear in the upper ocean. *J. Phys. Oceanogr.*, 11, 1258–1271.
- Garrett, C. J. R., 1979a: Comment on "Some evidence for boundary mixing in the deep ocean" by Laurence Armi. *J. Geophys. Res.*, 84, 5095.

- Garrett, C. J. R. 1979b: Mixing in the ocean interior. *Dyn. Atmos. Oceans*, 3, 239–265.
- Garrett, C., 1989: Are diapycnal fluxes linked to lateral stirring rates? In: *Parameterization of small-scale processes. Proceedings, 'Aha Huliko'a Hawaiian Winter Workshop*. P. Müller and D. Henderson, eds., Hawaii Institute of Geophysics, Special Publication, 317–327.
- Garrett, C. J. R. and W. H. Munk, 1972: Oceanic mixing by breaking internal waves. *Deep Sea Res.*, 19, 823–832.
- Garrett, C. and D. Gilbert, 1988: Estimates of vertical mixing by internal waves reflected off a sloping bottom. In: *Small-scale turbulence and mixing in the ocean*, J. C. J. Nihoul and B. M Jamart, eds., Elsevier, pp. 405–423.
- Gordon, A. L., Molinelli, E. and T. Baker, 1982: *Southern Ocean Atlas*, Columbia University Press.
- Gregg, M. C., 1977: A comparison of finestructure spectra from the main thermocline. *J. Phys. Oceanogr.*, 7, 33–40.
- Gregg, M. C., 1987: Diapycnal mixing in the thermocline: A review. *J. Geophys. Res.* 92, 5249–5286.
- Gregg, M. C., 1989: Scaling turbulent dissipation in the thermocline. *J. Geophys. Res.*, 94, 9686–9698.
- Hasselmann, K. F., 1966: Feynman diagrams and interaction rules of wave-wave scattering processes. *Rev. Geophys. Space Phys.*, 4, 1–32.
- Hasselmann, K. F., 1967: Nonlinear interactions treated by methods of theoretical physics (with applications to the generation of waves by wind). *Proc. Roy. Soc. London*, 299, 77–100.
- Henyey, F. S., D. B. Creamer, K. B. Dysthe, R. L. Schult and J. A. Wright, 1986: The energy and action of small waves riding on large waves. *J. Fluid. Mech.*, 189, 443–462.
- Hogg, N. G., P. Biscaye, W. Gardner and W. J. Schmitz, Jr., 1982: On the transport and modification of Antarctic bottom water in the Vema Channel. *J. Mar. Res.*, 40, 231–263.
- Holloway, G., 1983: A conjecture relating oceanic internal waves and small-scale processes. *Atmosphere; Atmos. Ocean*, 21, 107–122.
- Holloway, G., 1989: Relating turbulence dissipation measurements to ocean mixing. In: *Parameterization of small-scale processes. Proceedings, 'Aha Huliko'a Hawaiian Winter Workshop*. P. Müller and D. Henderson, eds., Hawaii Institute of Geophysics, Special Publication, 329–339.
- Holloway, G. 1990: Subgrid-scale representation. In: *Oceanic Circulation Models*, D. Anderson, ed., Kluwer.

- Kunze, E. and P. Müller, 1989: The effect of internal waves on vertical geostrophic shear. In: *Parameterization of small-scale processes. Proceedings, 'Aha Huliko'a Hawaiian Winter Workshop.* P. Müller and D. Henderson, eds., Hawaii Institute of Geophysics, Special Publication, 271-285.
- Ledwell, J. R., 1989: A strategy for open ocean mixing experiments. In: *Parameterization of small-scale processes. Proceedings, 'Aha Huliko'a Hawaiian Winter Workshop.* P. Müller and D. Henderson, eds., Hawaii Institute of Geophysics, Special Publication, 157-163.
- Ledwell, J. R., A. J. Watson, and W. S. Broecker, 1986: A deliberate tracer experiment in Santa Monica Basin. *Nature*, 323, 322-342.
- Levitus, S., 1982: *Climatological atlas of the world ocean.* NOAA Res. Rep. No. 13, 173 pp.
- Lilly, D. K., D. E. Waco, and S. I. Adelfang, 1974: Stratospheric mixing estimated from high-altitude turbulence measurements. *J. Appl. Meteor.*, 13, 488-493.
- Lumley, J. L., 1964: The spectrum of nearly inertial turbulence in a stably stratified fluid. *J. Atmos. Sci.*, 21, 99-102.
- McComas, C. H. and P. Müller, 1981: The dynamic balance of internal waves. *J. Phys. Oceanogr.*, 11, 970-986.
- McDougall, T. J., 1989: Dianutral Advection. In: *Parameterization of small-scale processes. Proceedings, 'Aha Huliko'a Hawaiian Winter Workshop.* P. Müller and D. Henderson, eds., Hawaii Institute of Geophysics, Special Publication, 289-315.
- Métais, O. and J. R. Herring, 1989: Numerical simulations of freely evolving turbulence in stably stratified fluids. *J. Fluid Mech.*, 202, 117-148.
- Müller, P. and D. Henderson, 1989: *Parameterization of small-scale processes. Proceedings, 'Aha Huliko'a Hawaiian Winter Workshop.* Hawaii Institute of Geophysics, Special Publication, 365 pp.
- Müller, P. and G. Holloway, 1989: Parameterization of small-scale processes. *Trans. Amer. Geophys. Union*, 70 (36), 818-820, 830.
- Müller, P., G. Holloway, F. Henyey and N. Pomphrey, 1986: Nonlinear interactions among internal gravity waves. *Rev. Geophys.*, 24, 493-536.
- Müller, P. and D. J. Olbers, 1975: On the dynamics of internal waves in the deep ocean. *J. Geophys. Res.*, 80, 3848-3860.
- Munk, W. H., 1966: Abyssal Recipes. *Deep Sea Res.*, 13, 707-730.
- Munk, W. H., 1981. Internal waves and small-scale processes. In: *Evolution of Physical Oceanography.* B. A. Warren and C. Wunsch, eds., The MIT Press, 264-291.
- Munk, W. H. and E. R. Anderson, 1948: Notes on a theory of the thermocline. *J. Mar. Res.*, 7, 276-295.

- Oakey, N. S., 1982: Determination of the rate of dissipation of turbulent energy from simultaneous temperature and velocity shear microstructure measurements. *J. Phys. Oceanogr.*, 12, 256-271.
- Olbers, D. J., 1976: Nonlinear energy transfer and the energy balance of the internal wave field in the deep ocean. *J. Fluid Mech.*, 74, 375-399.
- Olbers, D. J., M. Wenzel and J. Willebrand, 1985: The inference of North Atlantic circulation parameters from climatological hydrographic data. *Rev. Geophys.*, 23, 313-356.
- Olbers, D. J., and M. Wenzel, 1990: Determining diffusivities from hydrodynamic data by inverse methods with applications to the Circumpolar Current. In: *Oceanic Circulation Models*, D. Anderson, Ed., Kluwer.
- Osborn, T. R., 1980: Estimates of the local rate of vertical diffusion from dissipation measurements. *J. Phys. Oceanogr.*, 10, 83-89.
- Osborn, T. R. and C. S. Cox, 1972: Oceanic fine structure. *Geophys. Fluid Dyn.*, 3, 321-345.
- Pacanowski, R. C. and S. G. H. Philander, 1981: Parameterization of vertical mixing in numerical models of tropical oceans. *J. Phys. Oceanogr.*, 11, 1443-1451.
- Pedlosky, J., 1979: *Geophysical fluid dynamics*, 2nd ed., Springer-Verlag, 710 pp.
- Redi, M. H., 1982: Oceanic isopycnal mixing by coordinate rotation. *J. Phys. Oceanogr.*, 12, 1154-1158.
- Richardson, P. L., Cheney, R. E. and Worthington, L. V., 1978: A census of Gulf Stream rings, Spring 1975. *J. Geophys. Res.*, 83 (C12), 6136-6143.
- Riley, J. J., R. W. Metcalfe and M. A. Weissman, 1981: Direct numerical simulations of homogeneous turbulence in density-stratified fluids. In: *Nonlinear properties of internal waves*, B. J. West, ed., American Institute of Physics, Vol. 76, 79-112.
- Ruddick, B., 1980: Critical layers and the Garrett-Munk spectrum. *J. Mar. Res.*, 38, 135-145.
- Saunders, P. M., 1987. Flow through discovery gap. *J. Phys. Oceanogr.*, 17, 631-643.
- Shen, C. Y. and G. Holloway, 1986: A numerical study of the frequency and the energetics of nonlinear internal gravity waves. *J. Geophys. Res.*, 91 (C1), 953-973.
- Siegel, D. A., and J. A. Domaradzki, 1990: Large-eddy simulation of the decay of small-scale internal gravity wave field. (Preprint).
- Stommel, H. and F. Schott, 1977: The beta spiral and the determination of the absolute velocity field from hydrographic station data. *Deep Sea Res.*, 24, 325-329.

- Stone, P. H., 1974: The meridional variation of the eddy heat fluxes and their parameterization. *J. Atmos. Sci.*, 31, 444-456.
- Thorpe, S. A., 1973: Turbulence in stably stratified fluids: A review of laboratory experiments. *Bound.-Layer Meteor.*, 5, 95-119.
- Weinstock, J., 1985: On the theory of temperature spectra in a stably stratified fluid. *J. Phys. Oceanogr.*, 15, 475-477.
- Winters, K. B., and E. A. D'Asaro, 1989: Two-dimensional instability of finite amplitude internal gravity wave packets near a critical level. *J. Geophys. Res.*, 94, 12,709-12,719.
- Winters, K. B. and J. J. Riley, 1990: Three-dimensional instability of wavelike flows. 36 pp. (Preprint).
- Xu, N., 1990: *Interactions of internal gravity waves with random bottom topography and a straight slope*. M. S. Thesis, University of Hawaii.

FIGURE CAPTIONS

Fig. 1. Poleward heat transport in a coarse resolution oceanic general circulation model as a function of latitude for various values of the vertical diffusivity ranging from 0.1 to $2.5 \cdot 10^{-1} \text{ m}^2\text{s}^{-1}$. From Bryan (1987).

Fig. 2. Map of the diapycnal diffusion coefficient in the North Atlantic for two depth ranges, as inferred from beta-spiral calculations. Units are $10^{-4} \text{ m}^2\text{s}^{-1}$. Contours are logarithmically spaced with interval 0.5. Areas with values larger than $10^{-5} \text{ m}^2\text{s}^{-1}$ are shaded. From Olbers et al. (1985).

Fig. 3. Diapycnal diffusivity in the Antarctic Circumpolar Current for the depth range from 100 to 800 m, as inferred from beta-spiral calculations. Contours are logarithmically spaced with interval 0.5. Contours which are larger than $10^{-4} \text{ m}^2\text{s}^{-1}$ are full. Areas with values larger than $10^{-3} \text{ m}^2\text{s}^{-1}$ are shaded. From Olbers and Wenzel (1990).

Fig. 4. Vertical spreading of the tracer during the Santa Monica Basin Experiment. Each profile is an average of ten or so individual profiles, with the error bars indicating the variance in shape of the individual profiles. The target surface of the injection was the 5.085°C potential temperature surface. The height is really a transformed coordinate based on the potential temperature profiles and the mean height versus temperature profile for the middle (51 d) survey. The concentration shown is normalized so that the area under each curve is unity. The days after injection given in the key are nominal; in reality each survey cruise was about 10 days long. The diapycnal diffusivity inferred from the spreading is about $0.3 \text{ cm}^2\text{s}^{-1}$. From Ledwell (1989).

Fig. 5. Comparison of three different mid-latitude sites: PATCHEX, PATCHEXn, RING82I. The three panels show, as a function of pressure, the dissipation rate ϵ normalized by the buoyancy frequency N , the 10 m vertical shear S normalized by the 10 m shear of the Garrett and Munk model, and the dissipation rate normalized by buoyancy frequency and shear. Note that the shear scaling greatly reduces the large differences when ϵ is scaled only by N . From Gregg (1989).

Fig. 6 Coraparison of calculated probability density function of Richardson number with measured frequency function for two data sets obtained by Evans (1982). From Desaubies and Smith (1982).

Fig. 7. Schematic representation of the dynamical balance of McComas and Muller (1981). Energy is generated at low vertical wave number $|k_z| < \beta_*$. Between β_* and β_c there is an inertial range where the ID mechanism at high frequencies and the PSI mechanism at low frequencies provide a constant energy flux to high wave numbers $|k_z| > \beta_c$, where energy is dissipated. The wave number β_c is determined

as the wave number where the spectrum must roll off because the nonlinear transfer can no longer keep up with dissipation. From McComas and Müller (1981).

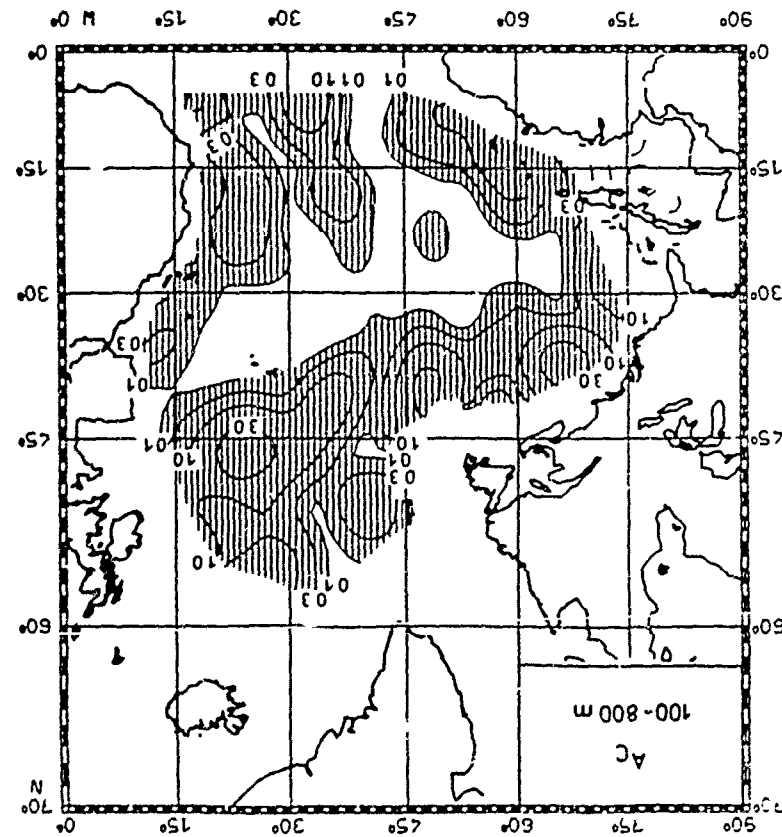
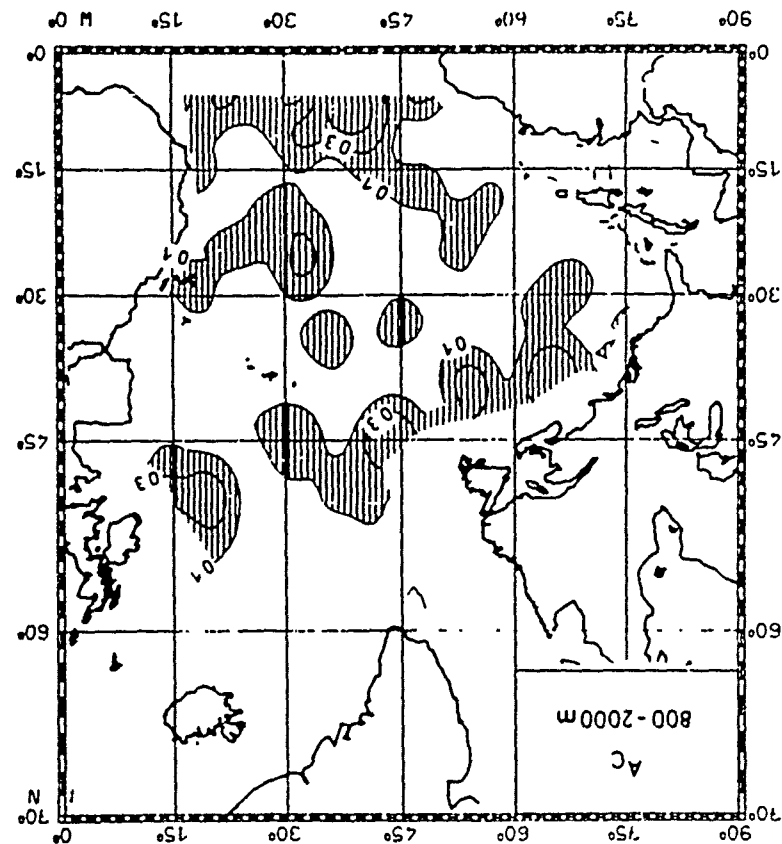
Fig. 8. (a) Energy-flux divergence and (b) momentum-flux divergence due to critical layer absorption of internal waves in an ambient geostrophic shear with a 30-cm/s surface velocity. The energy-flux divergence has maximum values of $\sim 5 \times 10^{-9}$ W/kg, which is comparable to the estimate of the energy flux through the internal wave field to high wavenumbers. The momentum-flux divergence drives an "Ekman" mean flow $\tilde{v} = (1/f)\partial\langle u'w' \rangle / \partial z$ of up to 0.01 cm/s (10 m/day), which is insignificant. From Kunze and Müller (1989).

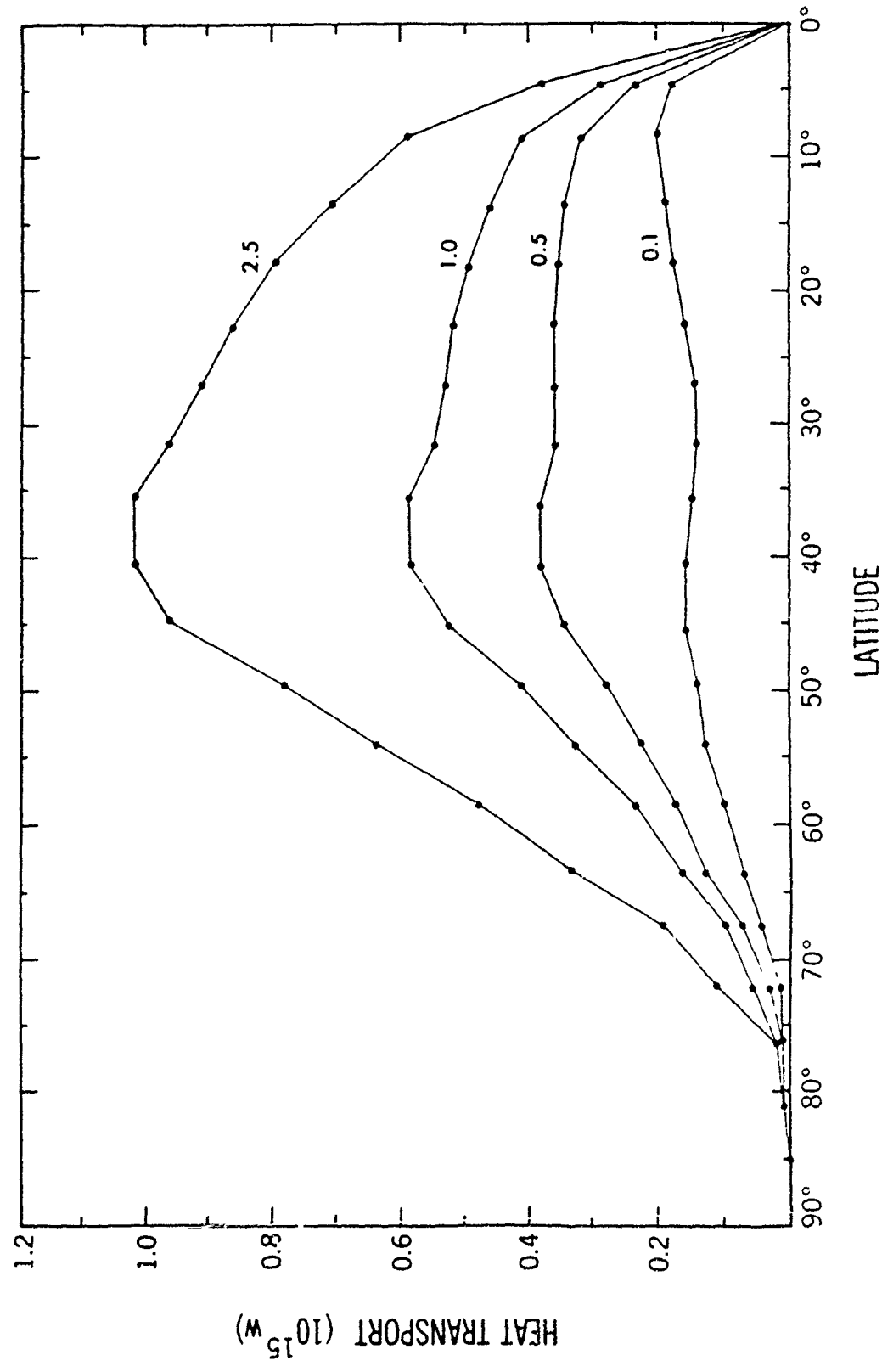
Fig. 9. Time-averaged transfer of kinetic energy and potential energy and conversion rate from kinetic to potential energy as a function of k_x , k_z and total k (from Shen and Holloway, 1986). Note that potential energy is converted to kinetic energy at the higher (overturning) wavenumbers.

Fig. 10. Amount of work done by the Archimedean force. The work done on a particle infinitesimally displaced in a certain direction is proportional to the distance between the origin and the curve in that direction. Work is done on the particle where the curve is solid. The particle must do work where the curve is dashed.

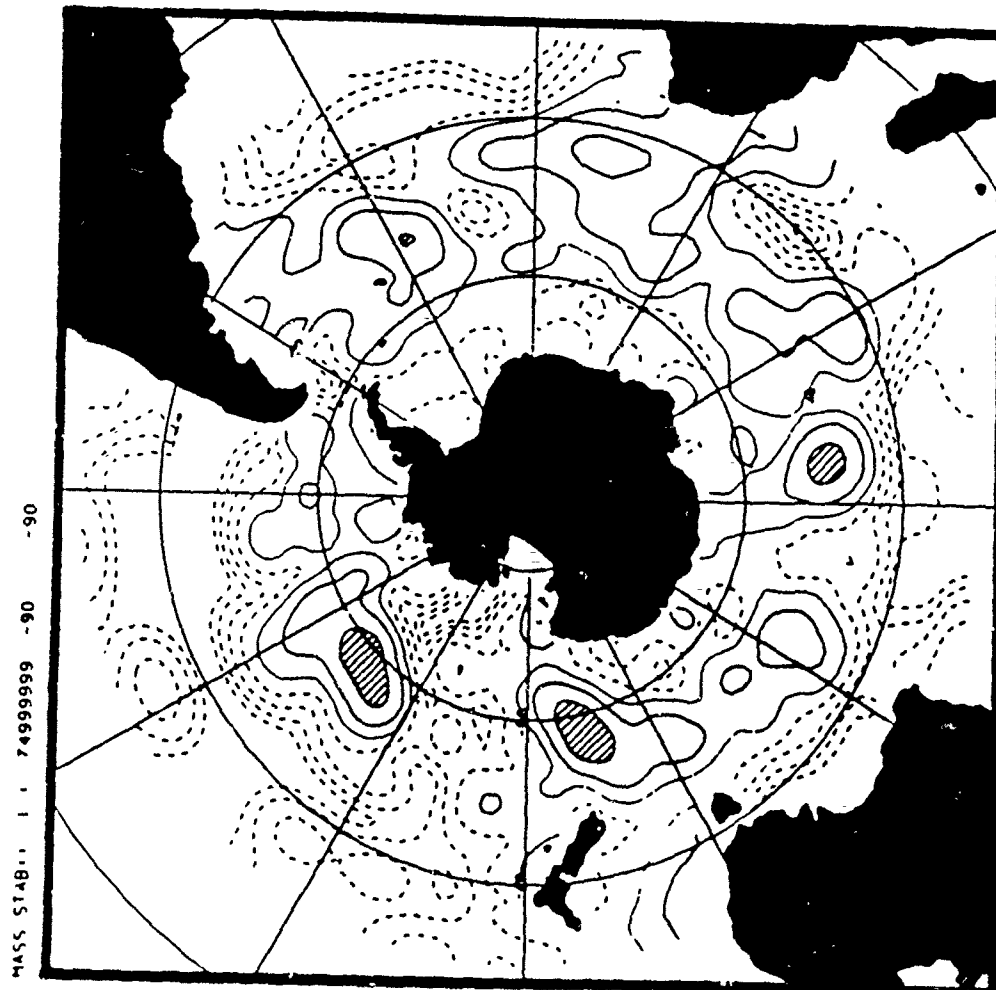
Fig. 11. Chart of the topography (hectometers) of the 15° isothermal surface showing the Gulf Stream, nine cold-core and three warm-core rings. Contours are based on XBT, CTD, hydrographic and satellite infrared data from the period March 16 to July 9, 1975. From Richardson et al. (1978).

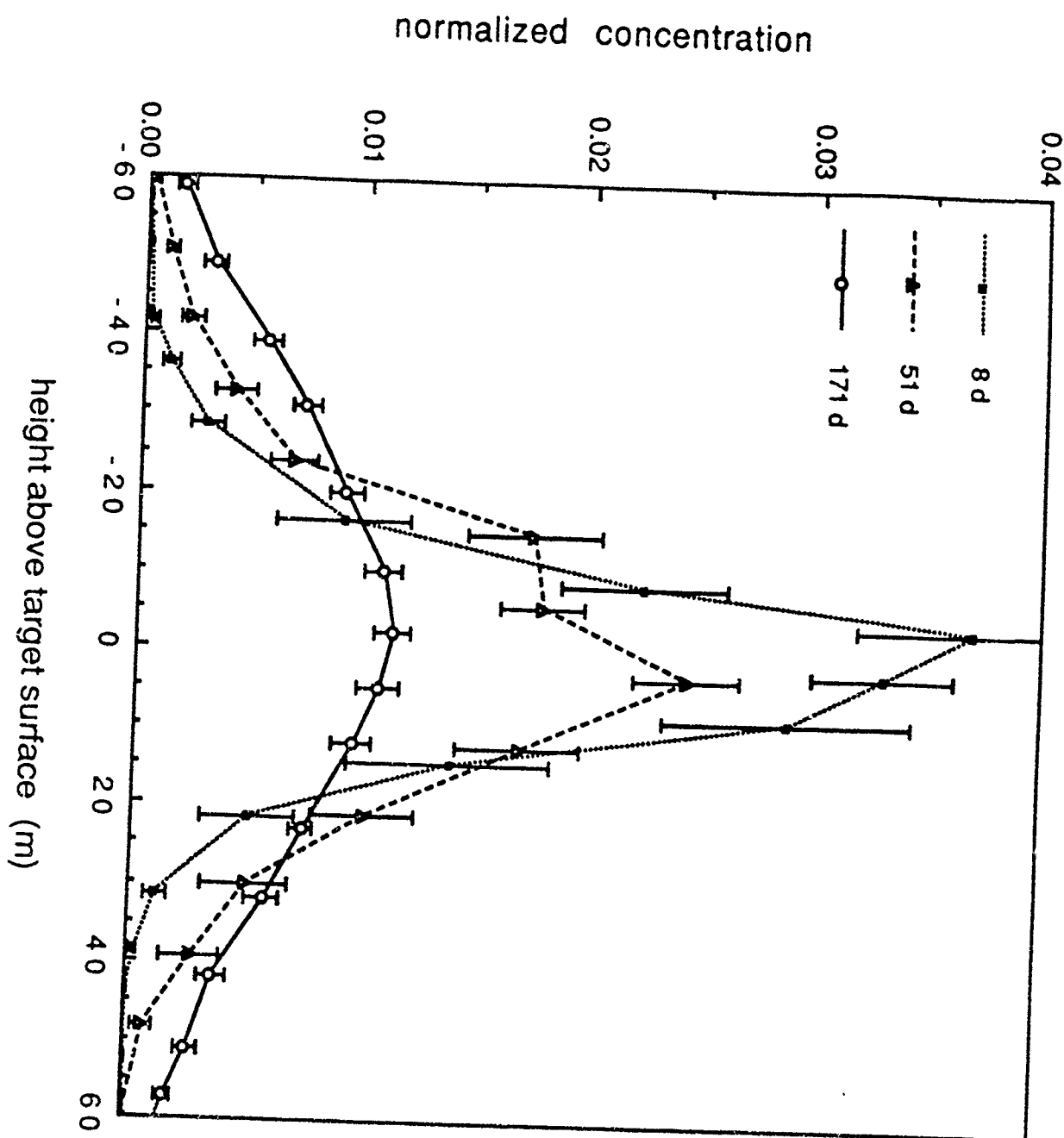
Fig. 12. The amplitude $|\phi(z)|$ and the phase $a(z)$ as a function of normalized height z for the most unstable wave in the Eady (1949) model of baroclinic instability. Note that the increase of a with height implies a transverse heat flux. From Pedlosky (1979).

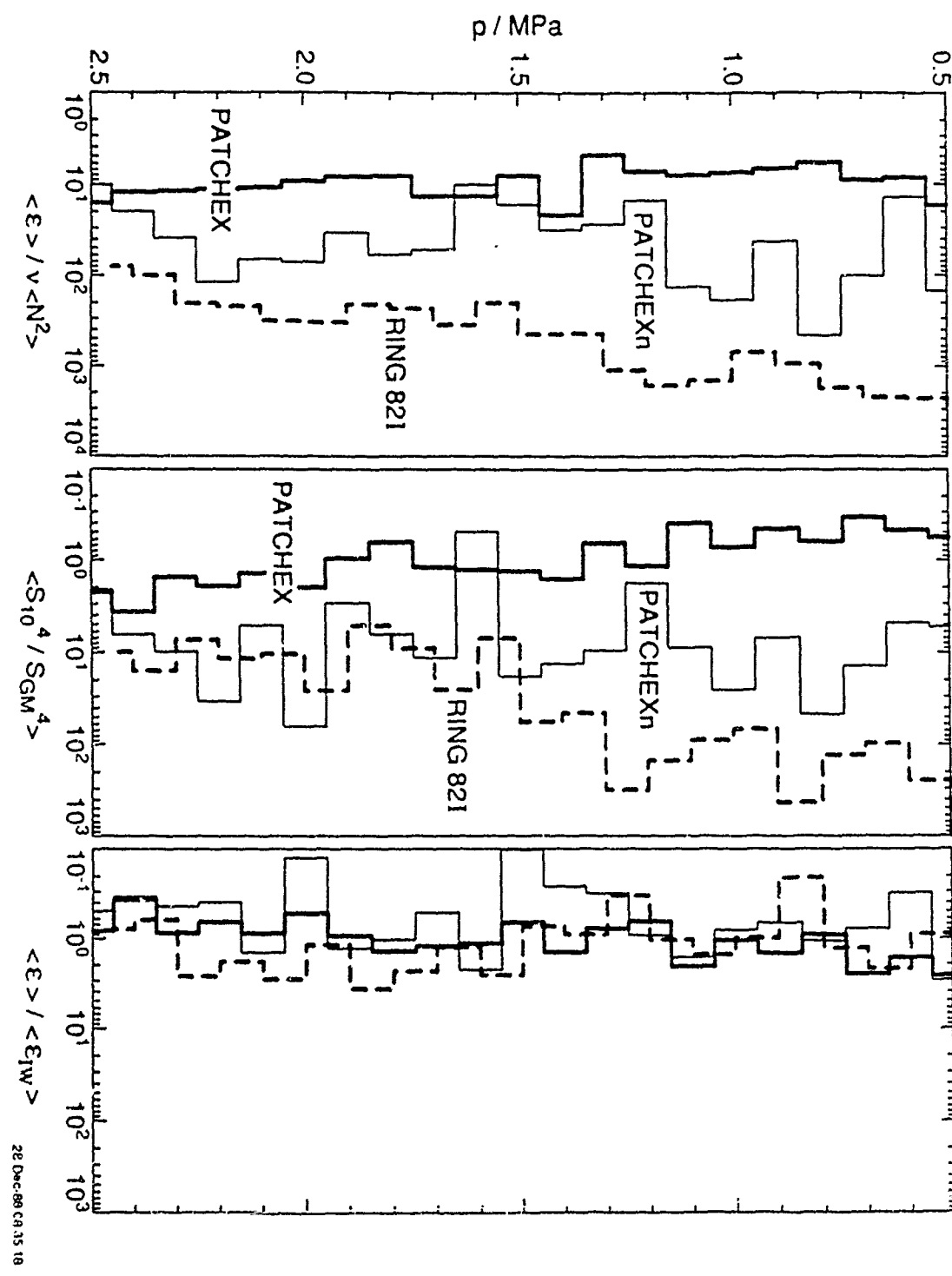


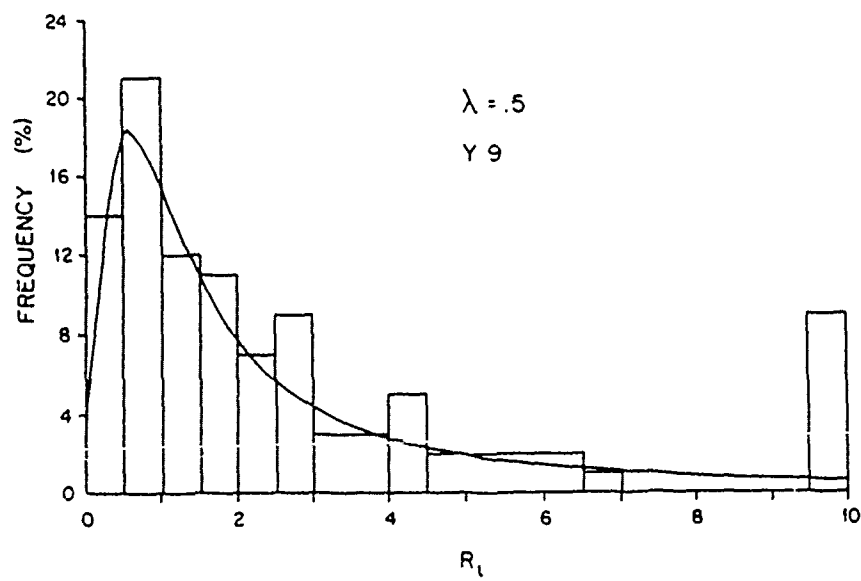
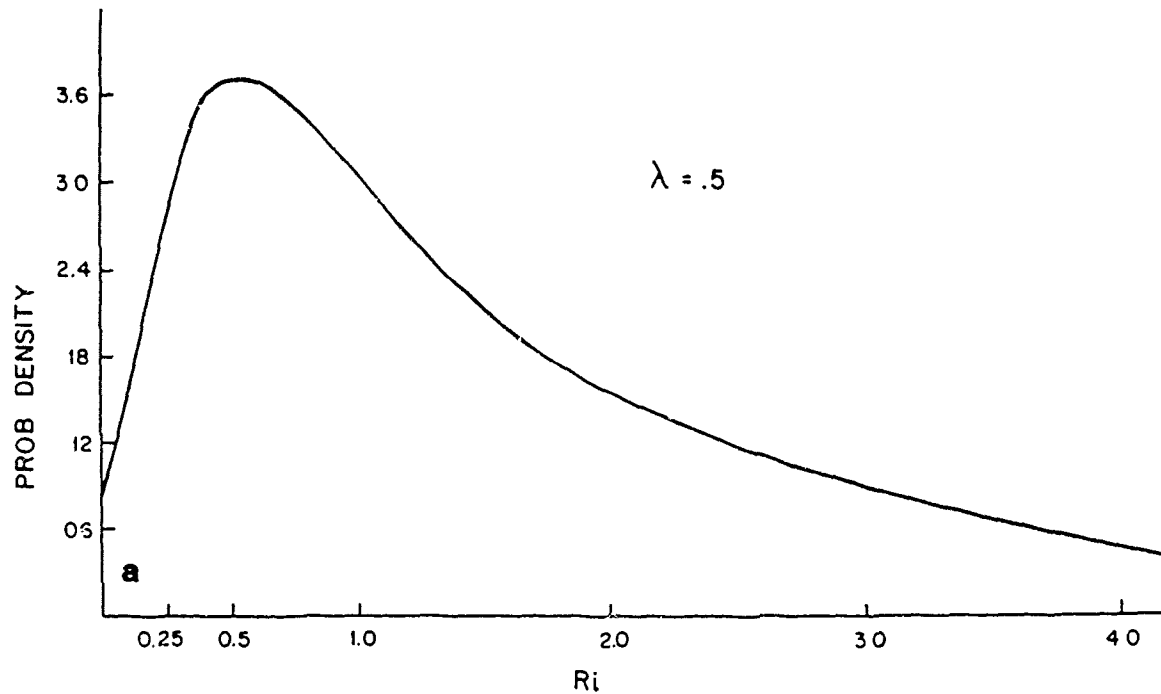


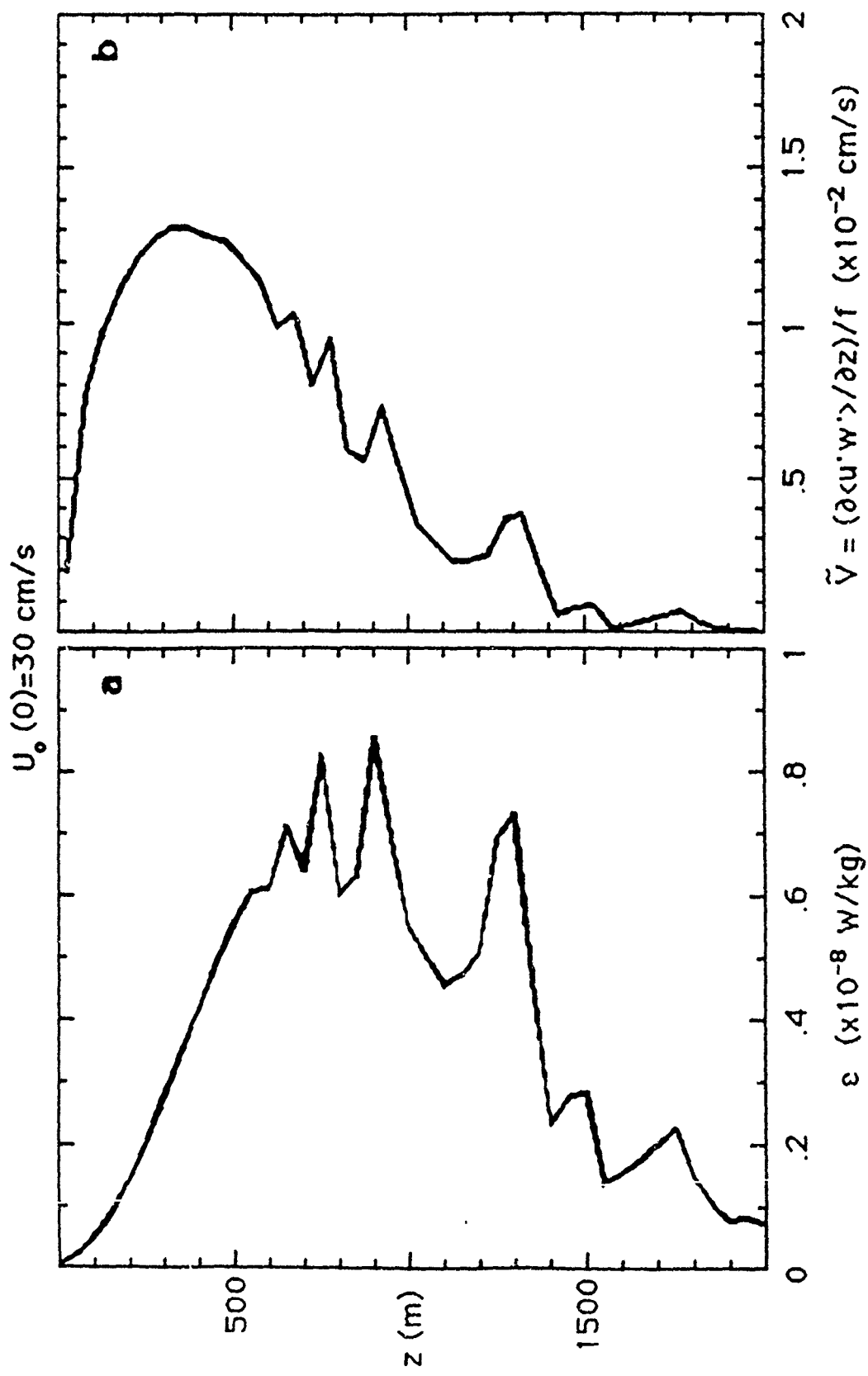
UVW: UVW2BON.C3 / ERH: S-POT(0) / ANP: 100- 800M

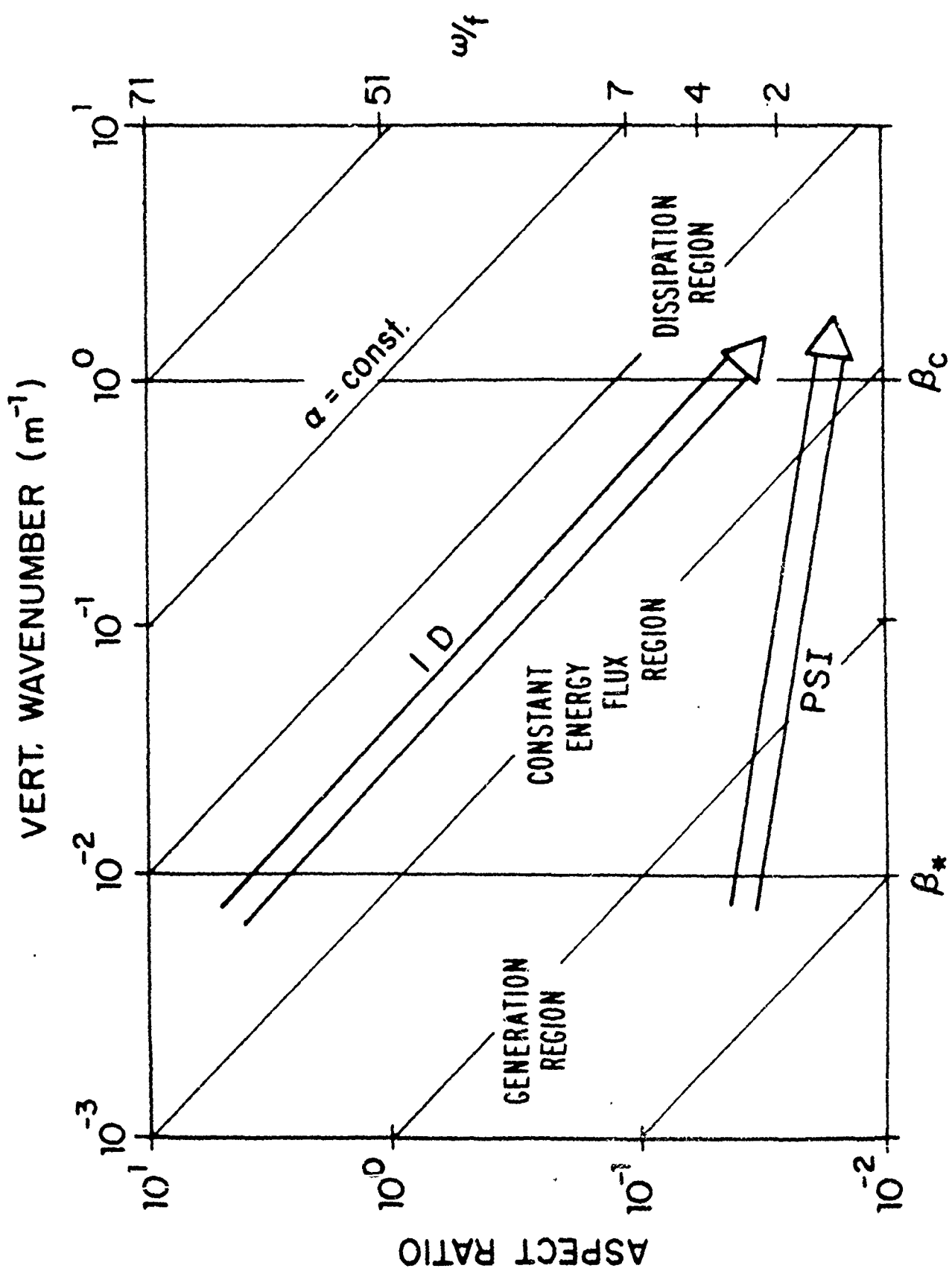






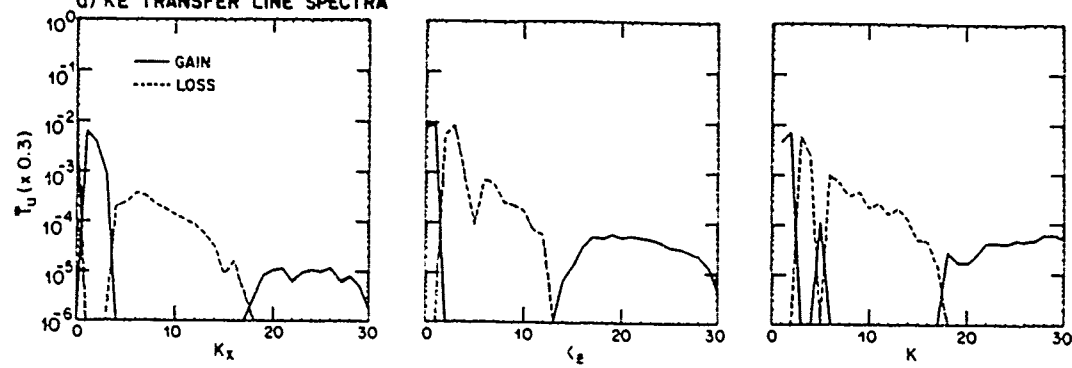




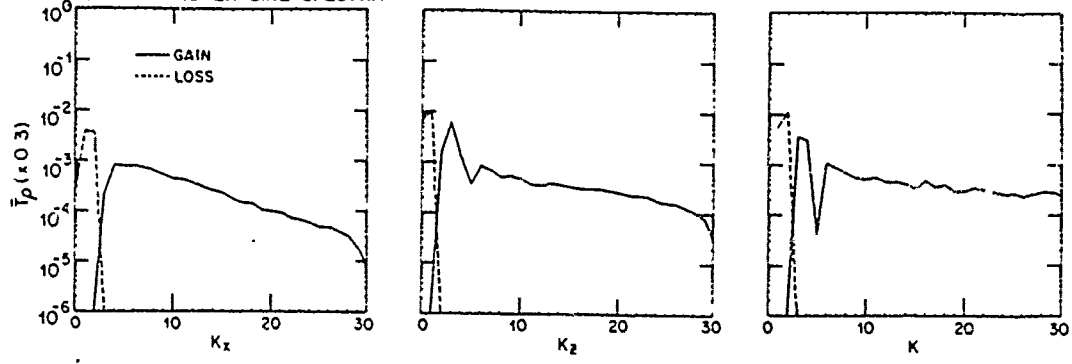


CASE 3

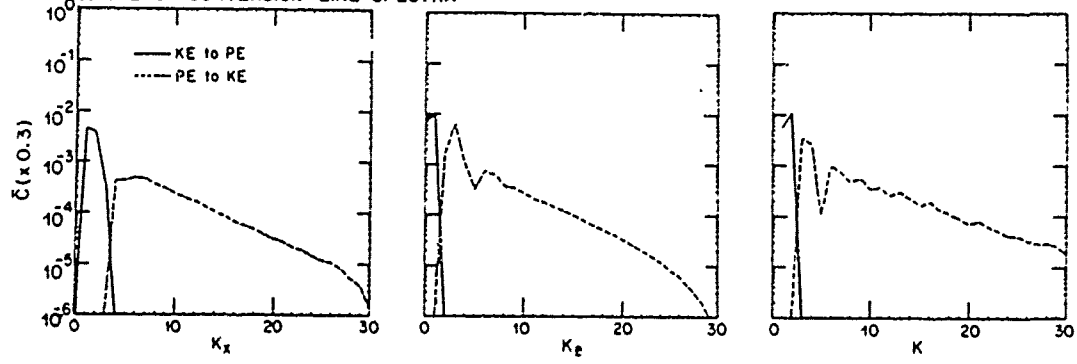
a) KE TRANSFER LINE SPECTRA



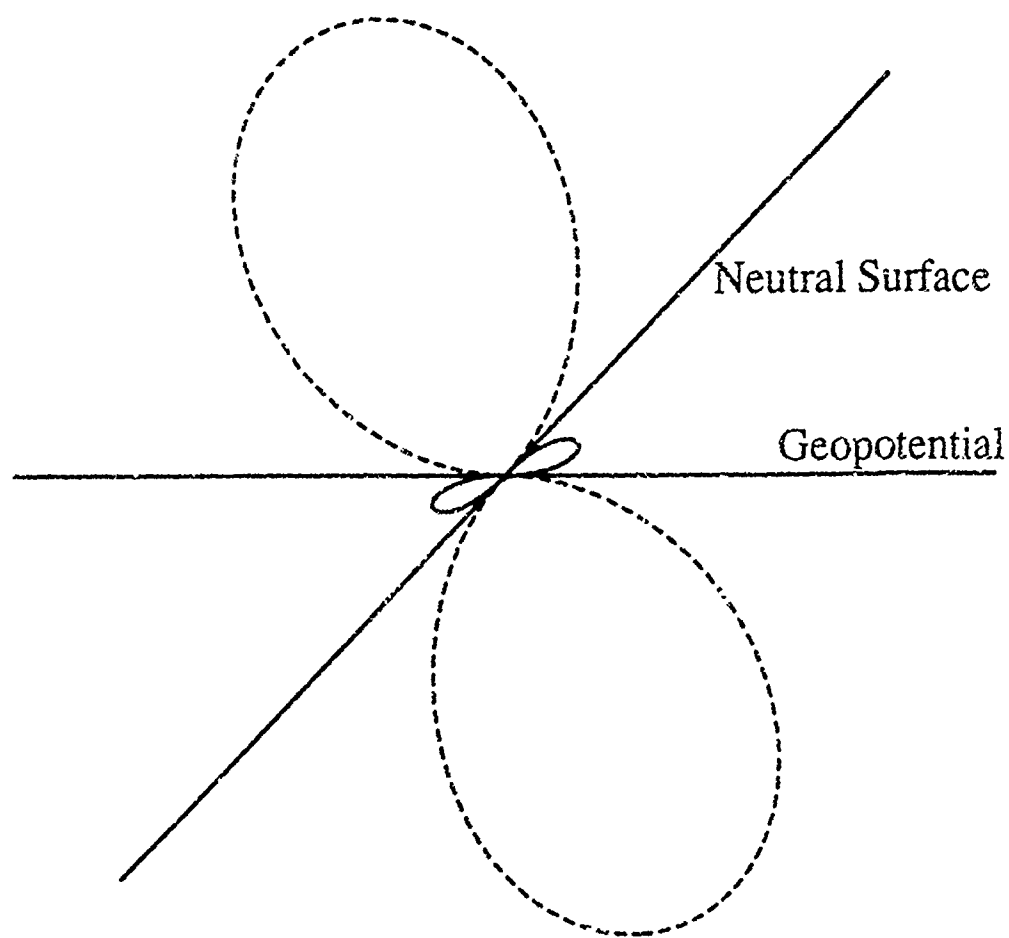
b) PE TRANSFER LINE SPECTRA



c) ENERGY CONVERSION LINE SPECTRA



Orientation of Diffusion Tensor
(Olbers and Wenzel, 1989)



$$dA = \rho [(\alpha \nabla \theta - \beta \nabla S) \cdot d\mathbf{x}] [\nabla \Phi \cdot d\mathbf{x}]$$

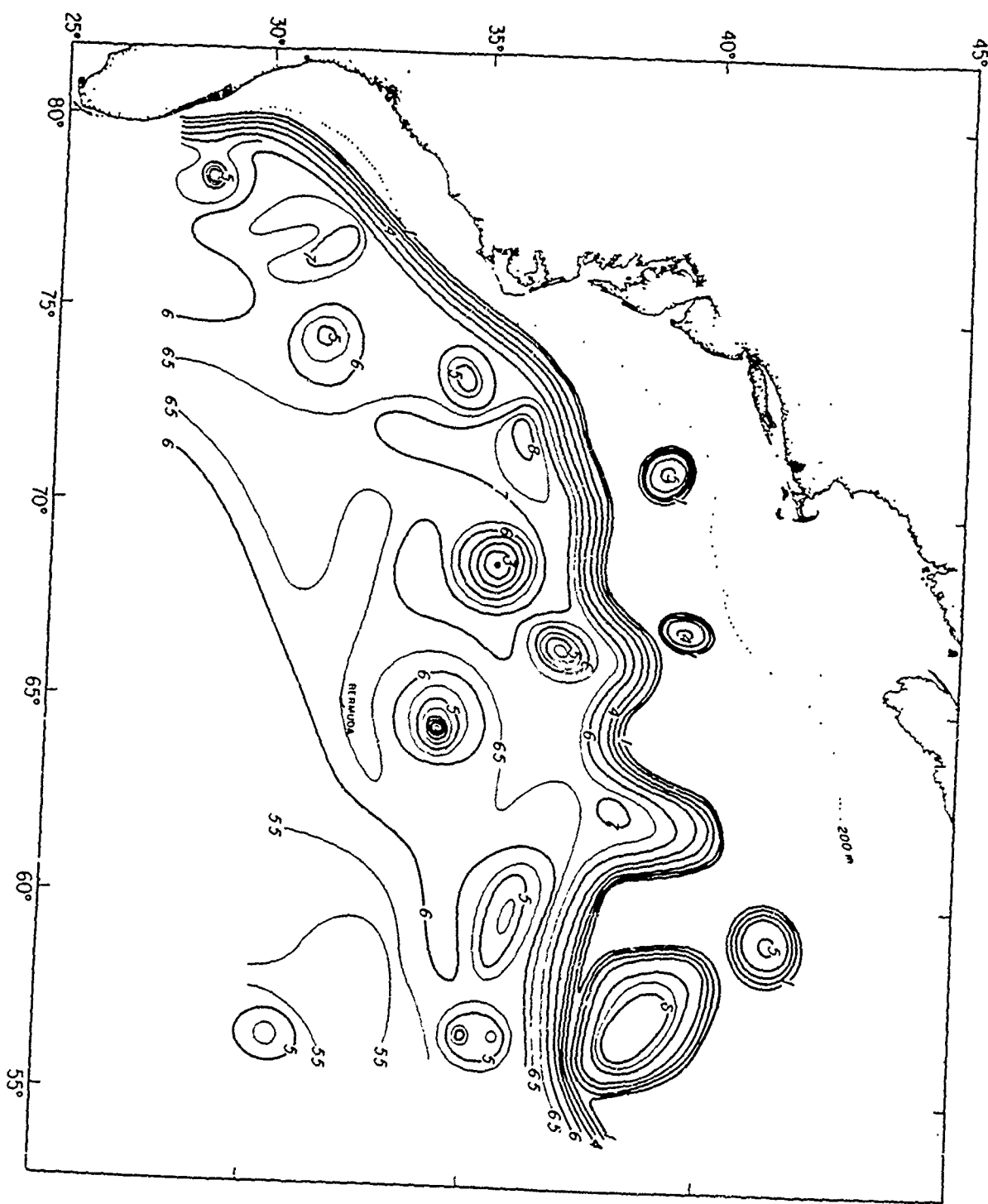
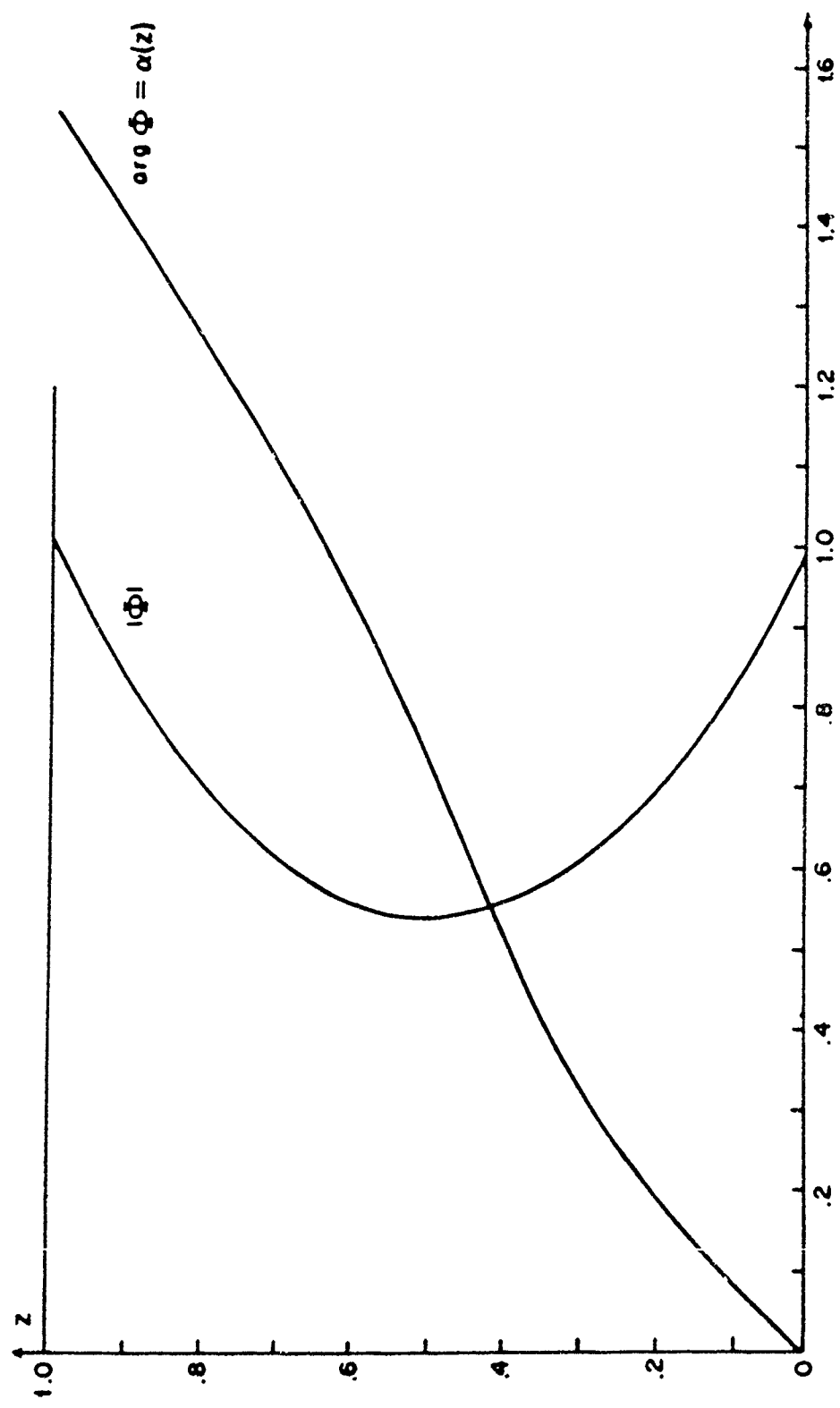


Fig. 1



LARGE-EDDY SIMULATIONS OF OCEANIC BOUNDARY LAYERS

James C. McWilliams, Patrick C. Gallacher, Chin-Hoh Moeng,
and John Wyngaard
National Center for Atmospheric Research

Planetary boundary layers in the ocean occur because of boundary fluxes of momentum and buoyancy, either through exchanges with the atmosphere above or the solid earth below. They almost always occur with very large Reynolds number and thus are appropriate targets for Large-Eddy Simulations (LES). There are many similarities with the atmospheric planetary boundary layer, of course, but there are also substantial differences: the replacement of water vapor and clouds by salinity as the companion of temperature in controlling buoyancy, the differing patterns of radiative forcing of buoyancy, the different surface momentum boundary condition (fixed flux rather than zero velocity), and the presence of strong surface gravity and inertial wave velocities in the turbulent layer. The history of LES for the atmosphere is lengthy, but its applications for the ocean are preliminary and relatively recent. Attention is focused on two particular solutions we have obtained for the surface layer: either strong, negative buoyancy flux or strong wind stress over a stably stratified upper ocean in the middle latitudes where the rotational frequency is large. We compare these with atmospheric convective solutions and with recent stable, stress-driven solutions by Mason and Derbyshire (1990) and Coleman et al. (1990)

Near Surface Mixing and the Oceans' Role in Climate

Mark A. Cane
Lamont-Doherty Geological Observatory
Palisades, NY 10964

The component of the climate system of greatest concern to us is the atmosphere. The direct influence of the ocean on the atmosphere is almost entirely through sea surface temperature (SST), which exerts a strong control on the surface heat exchange and hence on atmospheric circulation features. A secondary influence is via gas exchange, which also is strongly temperature dependent.

In only a few regions (eg the Gulf Stream, the equator, eastern boundary upwelling zones) is large scale ocean dynamics the primary determinant of SST. Over most of the ocean the important terms are surface heat exchange with the atmosphere and small scale processes inducing near surface mixing in the presence of stratification. The surface heat flux is very poorly known: parameterizations are uncertain and the data needed to compute it is sparse and often inaccurate. The radiative effects of clouds are a particularly severe problem.

To some extent, it is possible to improve on standard formulas by an inverse calculation with an ocean model. A byproduct of such a calculation is the conclusion that it is very difficult to test mixing parameterizations against data because of the large uncertainties in the surface heat flux.

A very long list of mechanisms has been suggested as contributors to near-surface mixing in the ocean, including free convection, surface waves, Langmuir circulations, shear instabilities associated with mean flows or internal inertial-gravity waves, and fish. Looking at the issue from the perspective of climate, we take the point of view that we need not be concerned with the precise timing of mixing events, only their long term effects. We hypothesize that these effects can be accounted for by a formulation in which mixing depends solely on gradient Richardson number, Ri . We assume very strong mixing for $Ri < Ri_c$ and little mixing otherwise.

Our mixing model is compared with some of the standard mixed layer models, including bulk models (Price, Mellor-Yamada). The essential result is that the behavior of these models can be reproduced. The effect of only having variables available at the coarse resolutions characteristic of contemporary ocean circulation models is also considered.

CONJUNCTIVE FILTERING PROCEDURES IN SURFACE WATER FLOW AND TRANSPORT

Keith W. Bedford *

October 30, 1990

INTRODUCTION

The modeling and prediction of turbulent flow and transport in surface waters is a particularly challenging problem for a number reasons. First, the flows are highly time varying in both the mean and fluctuating components and are the result of a variety of interacting fluid phenomena. Second, these interacting nonlinear fluid mechanisms often do not separate into well defined spectral regions i.e. they overlap. Third, stratification affects the macroscale level through internal waves, blocking etc.. Fourth, the planform geometry and bottom bathymetry are irregular with both large scale and small scale variability which, in the case of lakes, reservoirs and estuaries is of the same scale as the flow physics. Finally and of significance is that the depth scale is two to three orders of magnitude smaller than the horizontal length scale.

No better example of the type of water body being considered with this class of models exists than the Great Lakes. Certainly any estuary or other large lakes or reservoirs are equally complex. Figure 1 (Bedford 1990, Bedford and Abdelrhman 1987 and Boyee 1974) presents a schematic of the basic coherent fluid mechanisms and their typical length and time scale. The dynamic response of the Lakes is particularly complex as resonant or near resonant interactions result in strong storm

*Professor of Civil Engineering and Atmospheric Sciences, Director Great Lakes Forecasting Program, Ohio State University, 2070 Neil Avenue, Columbus, Ohio 43210.

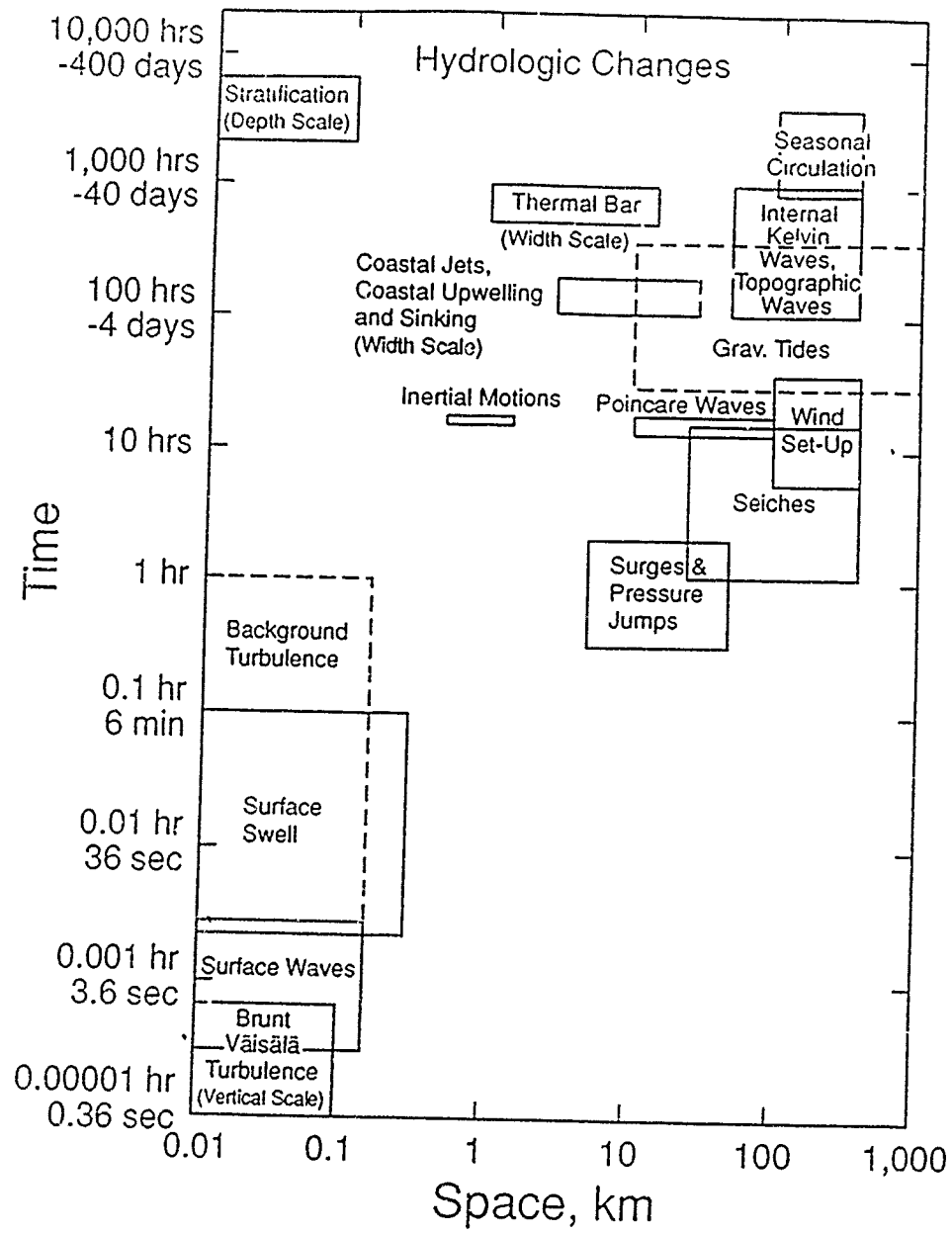


Figure 1: Space-time process schematic

surges (Libicki and Bedford 1990, Dingman and Bedford 1984) which develop in a matter of hours ($\sim 6\text{-}7$) and result in internal waves, nearshore Kelvin waves

and jets, and upwelling and downwelling events lasting a matter of days. Persistent wind driven currents continue against a backdrop of turbulence. Traditional model formulations of these processes depend upon average equations prepared with Reynold's definition of the average. Field data collected in a number of surface water sites at time and space intervals which resolve turbulence (Gross and Nowell 1983, Gross and Nowell 1985, Bedford et al. 1987 for example) clearly indicate that the stationarity requirement is met at the 90% confidence interval for averaging periods of approximately 10-15 minutes. Occasionally these periods might extend to an hour during quiescent periods with no tide or seiche activity. Consequently there is no steady Reynold's mean at periods greater than 10-15 minutes.

In 1978 our research group began undertaking an examination of the structural aspects of the three dimensional models used for these calculations. Attention was first drawn to examining the effect of the compressed vertical scale by analysis of time and space requirements imposed by the traditionally used coarse horizontal grid on the interpretation of data calculated at scales below the "horizontal scale" and its associated time scale. In Babajimopoulos and Bedford (1980) and Bedford and Babajimopoulos (1980) a rigid lid rectangular lake was examined by means of a model prepared via Leonard's (1974) higher order averaging procedure. The length was assumed to be three orders of magnitude larger than the depth and a constant (in the mean) spectrally correct wind shear was imposed at the surface. Sampling at the basin center at mid depth was used for the reported results. A free surface version of this model was also developed and tested.

In examining the results (Bedford 1981) a number of differences between the rigid and free surface model were explored but two items continue to be relevant here. First there was a two sloped spectra during all stationary portions of the simulation. At wave numbers, k_d , corresponding to the local water depth and higher

the spectra were $-5/3$ sloped, while at k_d and lower the slopes were proportional to k^{-3} . Essentially the models propagated energy inputs according to two dimensional turbulence theory and along with additional arguments presented in the references concluded that the use of the term "3D" for these models was a misnomer.

The resolution of the $-5/3$ region in the spectra, while on first thought an indication of possible 3D turbulence activity, occurred in a wave number and frequency region which was well below the minimal horizontal grid scale. Therefore a second result of this work spoke to the very anisotropic grid structure and quite small time steps required for stability (free surface) purposes. In essence there are two fixed spatial scales in these models below which model resolved results should either be interpreted with great care or eliminated with proper averaging. These are the scale of the horizontal grid Δx and its associated time of travel, $\Delta x/u = t_l$; and the depth, d , and its associated time scale t_d . In most model grids $\Delta x \gg h$ as say for instance in Lake Erie where the horizontal grid = $500m$ and the average depth is $20m$. The corresponding time scales based upon the vertical depth, t_d , and time step for the model, Δt , are quite small in contrast to the grid based horizontal time scale, t_l . Therefore in using Δx and t_l as the minimum resolution scales it was argued that very small time steps resolved portions of the spectra that were not fully supported by 3D physics. That is Δt inadvertently would resolve improper physics. It was argued that time resolution on the order of t_l was the minimally justified temporal resolution of the model.

To address this consistency issue combined space-time filtering was suggested (Bedford and Dakhoul 1982) and tested (Dakhoul and Bedford 1986a, b) and a consistency requirement between space-time averaging scales was examined. The methodology was initially tested on a Burger's equation solution and compared to results calculated with a variety of other averaging methods of recent (LES) and

historical (Reynold's) relevance. The theory and tests were limited to isotropic filters. The acute problem of anisotropic grids and filters generated by shallow flows was not addressed.

Recognizing that the use of moving averages gives rise to a different and reduced set of averaging operations, Bedford et al.(1987) and Dingman (1986) explored the requirement of consistent higher order analog averaging (suggested by LES) on the linear differential terms in the governing equations. In so doing it became possible to unify a wide variety of seemingly disparate numerical methods and view them as digital versions of either a Gaussian or uniform weight function analog filters with each digital method distinguished only by what integer coefficient was used in the analog representation. The key operation permitting this unification was at the time interpreted as a necessity for double or cascade averaging the linear terms to be consistent with the perception that the nonlinear terms were also "double averaged". The requirement for analyzing the linear terms consistently with the nonlinear terms is not often (if at all) discussed in the literature.

In a thorough treatment, by Aldama (1990, see also Dissertation Aldama, 1985), the space-time filter was invoked as part of a three-scale approach to the LES method. Space-time consistency was placed upon a sound analytical footing and Burger's flow calculations further validated the space-time filter approach. Of significance was the extremely thorough asymptotic expansion analysis of the inertia and cross terms resulting from space-time filtering. The analysis of convergence and scale effects led to the conclusion that the subgrid-scale terms were so unimportant that they could almost be ignored. This essential result, exploited by Rossman (1987), led to a turbulent flow model that was essentially closure-free; a conclusion rather at odds with most published turbulence modeling techniques. In testing this formulation, Rossman applied it to the calculation of flow over a backward step and

perform detailed comparisons to laboratory data. Unsettling though was that a small amount of dissipation via a Smagorinsky-like term was required.

While the above "closure-free" approximation was argued primarily from the effects of scale, Yeo (1987) and Yeo and Bedford (1988, 1990a, b) provided a full theoretical derivation of these results via a conjunctive filtering operation based upon the combined use of a low pass and a high pass filter. Based upon this filter an analysis of the resulting terms revealed the presence of mean flow representations for shear, velocity and vortex stretching based energy transfer mechanisms.

When coupled with the requirement for "double or cascade averaging" the presence of these formulations raises a number of questions not the least of which is what happened to the sub-grid scale terms.

The purpose of this paper is to review this conjunctive averaging technique and to demonstrate that, by reformulating the derivation of the governing equation, the role of double averaging is now seen as an act of separation followed by averaging. The conjunctive averaging is also seen to provide resolution sufficient to fully and robustly achieve the low pass average equations. Finally with the subgrid terms being so unimportant in the average equations the issue is raised as to whether we are really using the average equations or whether in fact we are using equations that are merely separated. The current practice of analyzing only the nonlinear portion of the equations is seen as an incomplete implementation of either the averaging or the separation approach and thereby continues to require empirical augmentation.

FILTERING PROCEDURES

Low Pass Filtering/Averaging

Following the seminal work of Leonard (1974) a total field variable (f) is decomposed into its low pass averaged component (\bar{f}) and its deviation (f') with the low

pass filtered variable defined as

$$\bar{f}(\underline{x}, t) = \int_{-\infty}^{+\infty} \int \int \int G(\underline{x} - \underline{x}', t - t') f(\underline{x}', t') d\underline{x}' dt \quad (1)$$

Here $G(\underline{x}, t)$ is the weight function constrained such that

$$\int_{-\infty}^{+\infty} \int \int \int G(\underline{x}, t) d\underline{x} dt = 1.0 \quad (2)$$

The uniform or Gaussian filters (Leonard 1974, Kwak 1975, Clark et al. 1979) are the most widely used weight functions with the space-time filter (Dakhoul and Bedford 1986a,b) being composed as,

$$G(\underline{x}, t) = \left(\frac{\gamma_t}{\pi} \right)^{\frac{1}{2}} \frac{1}{\Delta_t} \exp\left(-\frac{\gamma_t t^2}{\Delta_t^2}\right) \prod_{i=1}^3 \left(\frac{\gamma_i}{\pi} \right)^{\frac{1}{2}} \frac{1}{\Delta_i} \exp\left(-\frac{\gamma_i x_i^2}{\Delta_i^2}\right) \quad (3)$$

In Eqn. (3) γ_t and γ_i are the standard filter coefficients and Δ_t and Δ_i are related to the second moments as,

$$\frac{\Delta_t}{2\gamma_t} = \int_{-\infty}^{+\infty} t^2 G(\underline{x}, t) dt \quad (4)$$

$$\frac{\Delta_i}{2\gamma_i} = \int_{-\infty}^{+\infty} \int \int |x_i| G(\underline{x}, t) d\underline{x} \quad (5)$$

The response function for the low pass filter is found from taking the Fourier transform, $F[]$, of the filtering operation such that

$$R(\underline{k}, \omega) = \frac{F[\bar{f}]}{F[f]} = F[G] = L(\underline{k}, \omega) \quad (6)$$

In Eqn. (6) \underline{k} is the wavenumber vector and ω is the radian frequency.

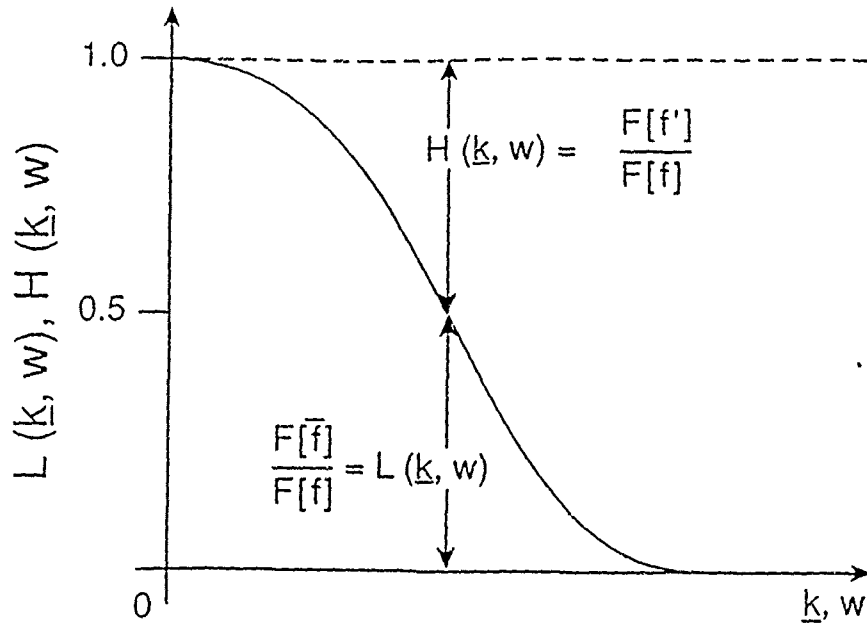


Figure 2: Schematic of high pass and low pass filter response function

High Pass Filter

From Yeo (1987), Yeo and Bedford (1988, 1990a,b) the complementarity principle form the signal processing literature is adopted to derive a high pass filter response function to resolve the high frequency portions of the signal. With regard to Figure 2 the response functions, summing to 1.0, give,

$$1 = \frac{F[\bar{f}]}{F[f]} + \frac{F[f']}{F[f]} \quad (7)$$

The first term on the right hand side of Eqn. (7) is the response function of the low pass filter, $L(\underline{k}, \omega)$, and the second term is the response function of the high pass filter, $H(\underline{k}, \omega)$, i.e.

$$1 = L(\underline{k}, \omega) + H(\underline{k}, \omega) \quad (8)$$

Therefore the high pass response function for uniform and Gaussian space filters

become,

$$H(\underline{k}) = 1 - \frac{\sin(\underline{k} \frac{\Delta_i}{2})}{\underline{k} \frac{\Delta_i}{2}}; H(\underline{k}) = 1 - \exp\left(-\frac{\Delta_i^2 \underline{k}^2}{4\gamma_i}\right) \quad (9)$$

The inverse Fourier transform gives,

$$H(\underline{x}) = F^{-1}[H(\underline{k})] = \delta(\underline{x}) - G(\underline{x}), \quad (10)$$

where $\delta(\underline{x})$ is the Dirac delta function. Therefore an equation for the fluctuating components can be found by applying the high pass filter to the governing equations

$$\begin{aligned} f'(\underline{x}, t) &= \int_{-\infty}^{+\infty} \int \int [\delta(\underline{x} - \underline{x}') - G(\underline{x} - \underline{x}')] f(\underline{x}') d\underline{x}' \\ &= c \Delta_i^2 \frac{\partial^2 f}{\partial \underline{x}^2} + O(\Delta_i^4) \end{aligned} \quad (11)$$

where c is a coefficient determined by the second moment of the filter. Note that this is essentially the same result but in generalized form as derived by Kwak et al (1975).

Implementation of Filters

If for example the Gaussian space filter is used then the response function $L(\underline{k})$ is written as,

$$\begin{aligned} L(\underline{k}) &= \exp\left(-\sum_{i=1}^3 a_i k_i^2\right) \\ &= 1 - (a_1 k_1^2 + a_2 k_2^2 + a_3 k_3^2) + \frac{1}{2!} (a_1 k_1^2 + a_2 k_2^2 + a_3 k_3^2)^2 - \dots \end{aligned} \quad (12)$$

where $a_i = \frac{\Delta_i^2}{4\gamma_i}$. Using a general formula from Fourier analysis (eg. Hildebrand 1976, Blinchikoff and Zverev 1976),

$$F[f'] = F[f] - F[\bar{f}]$$

$$\begin{aligned}
&= H(\underline{k})F[f] \\
&= [(a_1 k_1^2 + a_2 k_2^2 + a_3 k_3^2) \\
&\quad - \frac{1}{2!}(a_1 k_1^2 + a_2 k_2^2 + a_3 k_3^2)^2 + \dots]F[f] \\
&= -F[(a_1 \frac{\partial^2}{\partial x^2} + a_2 \frac{\partial^2}{\partial y^2} + a_3 \frac{\partial^2}{\partial z^2})f \\
&\quad + \frac{1}{2!}(a_1^2 \frac{\partial^4}{\partial x^4} + a_2^2 \frac{\partial^4}{\partial y^4} + a_3^2 \frac{\partial^4}{\partial z^4} + 2a_1 a_2 \frac{\partial^4}{\partial x^2 \partial y^2} \\
&\quad + 2a_2 a_3 \frac{\partial^4}{\partial y^2 \partial z^2} + 2a_3 a_1 \frac{\partial^4}{\partial z^2 \partial x^2})f + \frac{1}{3!}(\dots)f + \dots] \\
&= -F[\Phi(f) + \frac{1}{2!}\Phi^2(f) + \frac{1}{3!}\Phi^3(f) + \dots] \tag{13}
\end{aligned}$$

With the assumption of a symmetric filter then $\Delta = \Delta_1 = \Delta_2 = \Delta_3$ and $\gamma = \gamma_1 = \gamma_2 = \gamma_3$, and

$$f'(\underline{x}, t) = f - \bar{f} = -\alpha \nabla^2 f - \frac{1}{2!} \alpha^2 \nabla^4 f - \frac{1}{3!} \alpha^3 \nabla^6 f + \dots \tag{14}$$

where $\alpha = \frac{\Delta^2}{4\gamma}$. This series to the second term is identical to the Leonard/Clark formulation (Leonard 1974, Clark et al. 1979). While a more generalized form of the Leonard/Clark relationship the fact remains that the fluctuating quantity is related to the total field variable. It is desirable to relate $f'(\underline{x}, t)$ to the low pass average variable $\bar{f}(\underline{x}, t)$.

Using the complementarity principle the Fourier transform, $F[f']$, can be written as

$$\begin{aligned}
F[f'] &= H(\underline{k})F[f] = \frac{H(\underline{k})}{L(\underline{k})}F[\bar{f}] \\
&= F[-\Phi(\bar{f}) + \frac{1}{2!}\Phi^2(\bar{f}) - \frac{1}{3!}\Phi^3(\bar{f}) + \dots] \tag{15}
\end{aligned}$$

The final form for Eqn. (15) becomes,

$$f'(\underline{x}, t) = -\Phi(\bar{f}) + \frac{1}{2!}\Phi^2(\bar{f}) - \frac{1}{3!}\Phi^3(\bar{f}) + \dots \quad (16)$$

and is a series expansion for the fluctuating component which is based on the low pass averaged variable. For convenience the series expansion for f' as a function of the total field variable f will be called the YB-I series and the series for f' in terms of \bar{f} will be called the YB-II series (Yeo and Bedford 1988).

The Nonlinear Terms

The inertia, $u_i u_j$, or advection terms, $u_i \phi$, can be analyzed with the YB-II series in the following manner. Two functions f and g are written with the YB-II series as

$$\begin{aligned} f &= \bar{f} - \Phi(\bar{f}) + \frac{1}{2!}\Phi^2(\bar{f}) - \frac{1}{3!}\Phi^3(\bar{f}) \dots \\ g &= \bar{g} - \Phi(\bar{g}) + \frac{1}{2!}\Phi^2(\bar{g}) - \frac{1}{3!}\Phi^3(\bar{g}) \dots \end{aligned} \quad (17)$$

The product of f and g in Eqn. (17) becomes,

$$\begin{aligned} fg &= \bar{f}\bar{g} - \bar{f}\Phi(\bar{g}) - \bar{g}\Phi(\bar{f}) + \frac{1}{2!}\bar{f}\Phi^2(\bar{g}) \\ &\quad + \Phi(\bar{f})\Phi(\bar{g}) + \frac{1}{2!}\bar{g}\Phi^2(\bar{f}) \dots \end{aligned} \quad (18)$$

Now the average \bar{fg} in terms of the product of average variables is required therefore from the YB-I series,

$$\bar{fg} = fg + \Phi(fg) + \frac{1}{2!}\Phi^2(fg) + \frac{1}{3!}\Phi^3(fg) + \dots \quad (19)$$

After substitution of Eqn. (18) into Eqn. (19) and considerable algebra (Yeo 1987) there results the following power series for \bar{fg} ;

$$\overline{fg} = \overline{f}\overline{g} + 2\alpha\overline{f}_{,k}\overline{g}_{,k} + \frac{1}{2!}(2\alpha)^2\overline{f}_{,kl}\overline{g}_{,kl} + \frac{1}{3!}(2\alpha)^3\overline{f}_{,klm}\overline{g}_{,klm} + \dots \quad (20)$$

Here a symmetric filter has again been assumed for clarity's sake; i.e. $\alpha = \frac{\Delta^2}{4\gamma}$.

This series is called the YB-III series.

Via application to the inertia and advection terms in the governing equations the YB-III series gives

$$R_{ij}^l = \overline{u_i u_j} - \overline{u}_i \overline{u}_j = 2\alpha \overline{u}_{i,k} \overline{u}_{j,k} + \frac{1}{2!}(2\alpha)^2 \overline{u}_{i,kl} \overline{u}_{j,kl} + \text{HOT} \dots \quad (21)$$

and

$$Q_j^l = \overline{u_j \phi} - \overline{u}_j \overline{\phi} = 2\alpha \overline{u}_{j,k} \overline{\phi}_{,k} + \frac{1}{2!}(2\alpha)^2 \overline{u}_{j,kl} \overline{\phi}_{,kl} + \text{HOT} \dots \quad (22)$$

EQUATION PREPARATION

It is customary even in the LES method to simply start with the average equations and then apply the filtering operations only to the inertial or advection terms. This analysis is carried forward via a decomposition of the nonlinear terms and subsequent analysis of the product of the mean field variables and the cross terms via the low pass filter operations. The subgrid scale terms are then empirically represented by mean field variables. One of the issues this paper would like to raise is that by focusing attention on just the nonlinear terms several conceptual issues are ignored which, if properly addressed, might provide a more consistent approach to the question of averaging. Therefore this section reviews the governing equation

and the various possible forms from separation and averaging.

Total Field Equations

The starting point is the total field equations for velocity, u_i , and scalar ϕ .

$$\frac{\partial u_i}{\partial t} + (u_i u_j)_{,j} + \frac{1}{\rho} P_{,i} - \nu u_{i,jj} = L(\underline{x}, t) = 0 \quad (23)$$

$$\frac{\partial \phi}{\partial t} + (u_j \phi)_{,j} - \lambda \phi_{,jj} = M(\underline{x}, t) = 0 \quad (24)$$

In Eqns. (23,24) ν and λ are the kinematic viscosity and molecular diffusivity respectively.

Separated Total Field Equations

Before proceeding to the average equation lets reverse the order of the operations usually applied and separate the total field variable f into an average or slowly evolving term \bar{f} and the rapidly evolving or fluctuating component f' and reformulate Eqns. (23,24) without any loss of information. Eqns.(23) and (24) becomes,

$$\begin{aligned} \frac{\partial \bar{u}_i}{\partial t} + (\bar{u}_i \bar{u}_j)_{,j} + \frac{1}{\rho} \bar{P}_{,i} - \nu \bar{u}_{i,jj} &= A_i \\ &= -\left\{ \frac{\partial u'_i}{\partial t} + (u'_i u'_j + u'_i \bar{u}_j + \bar{u}_i u'_j)_{,j} + \frac{1}{\rho} P'_{,j} - \nu u'_{i,jj} \right\} \end{aligned} \quad (25)$$

$$\begin{aligned} \frac{\partial \bar{\phi}}{\partial t} + (\bar{u}_j \bar{\phi})_{,j} - \lambda \bar{\phi}_{,jj} &= B \\ &= -\left\{ \frac{\partial \phi'}{\partial t} + (u'_j \phi'_j + \bar{u}_j \phi' + u'_j \bar{\phi})_{,j} - \lambda \phi'_{,jj} \right\} \end{aligned} \quad (26)$$

At first glance these are equations that are expressed in terms of averaged variables and do not contain the problems with the nonlinear terms that are so often encountered. It is, of course, recognized that no variability has been eliminated

from the these equations either. Finally the scale of the separation is set by the filter coefficient which, for the equation preparation phase, doesn't necessarily have to be connected to the grid size at all.

Averaged Field Equations

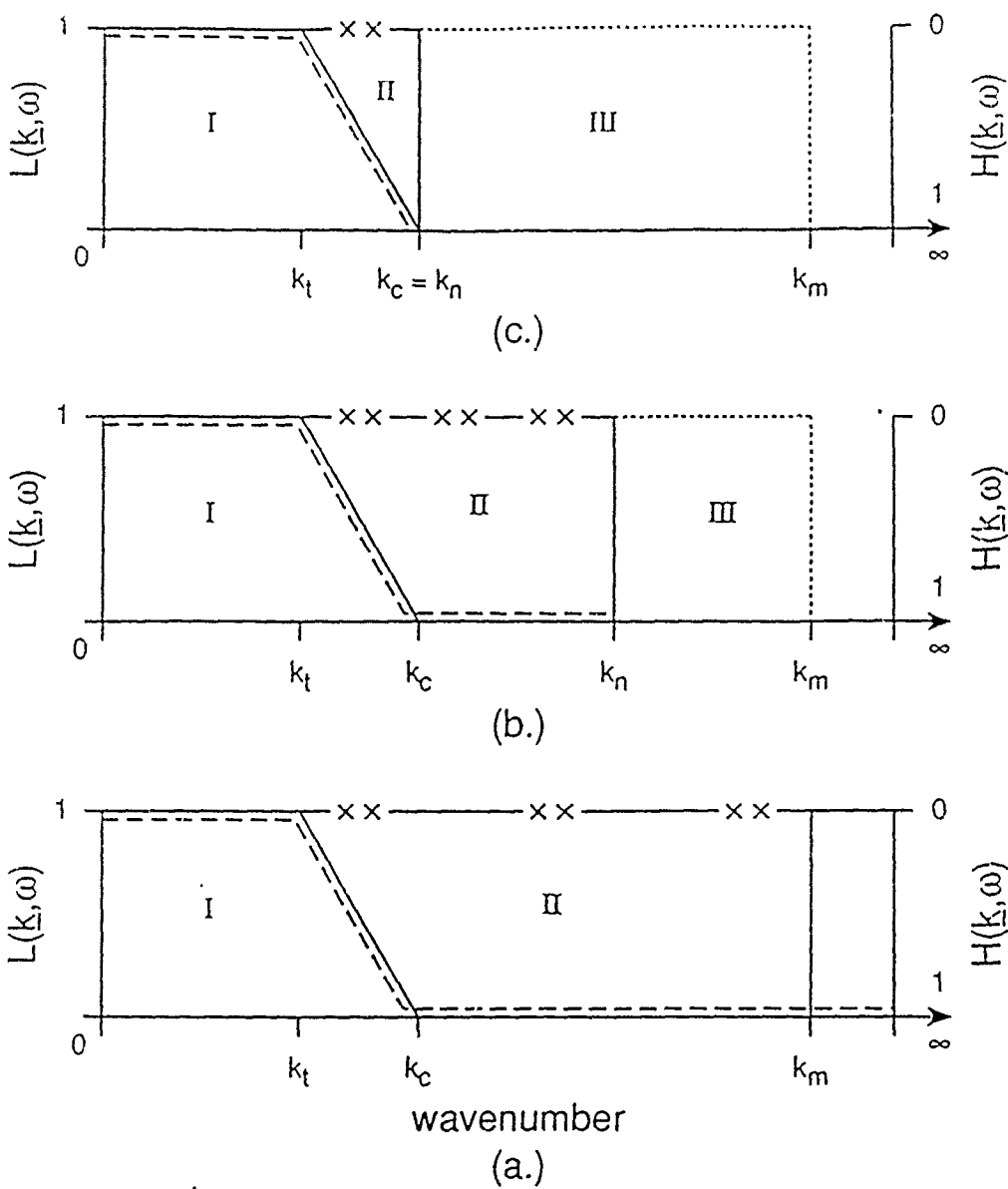
To derive the averaged equations, Eqns.(23) and (24) are filtered via Eqn. (1). The operation is straightforward and results in the following equations

$$\frac{\partial \bar{u}_i}{\partial t} + (\bar{u}_i \bar{u}_j)_{,j} + \frac{1}{\rho} \bar{P}_{,i} - \nu \bar{u}_{i,jj} = \bar{L}(\underline{x}, t) = 0 \quad (27)$$

$$\frac{\partial \bar{\phi}}{\partial t} + (\bar{u}_j \bar{\phi})_{,j} - \lambda \bar{\phi}_{,jj} = \bar{M}(\underline{x}, t) = 0 \quad (28)$$

The resolution of these equations is defined by the response function of the filter which implies (Figure 3a) that no variability is resolved past k_c the cutoff wavenumber nor above the response function in the region with wavelengths less than k_c . With the average defined as in Eqn. (1) the resolution of the filter functions is defined for the continuum equations all the way to $k = \infty$ (Fig. 3a) even though $L(k, \omega)$ might equal zero at k_c well below $k = \infty$. With this definition of the analog filter, zone II in Figure (3a) defines the fluctuations theoretically resolved by the analog high pass filter. Zone I represents the low pass filtered portion of the response function.

The implementation of the analog filter while straightforward requires examination. The traditional analysis step has been to decompose or separate the nonlinear term and proceed ahead with averaging. However, as suggested in Eqns. (25,26) the act of separation if applied to one portion of the equation, should for consistency be applied to all the terms in the equation. Since Eqns. (25,26) are the total field equations it is natural to require that the average of the separated total field



KEY

— dashed line domain definition for high pass $\{H(\bar{k}, \omega)\}$ /low pass $\{L(\bar{k}, \omega)\}$ response functions

Zone I filtered variable
 Zone II resolved fluctuations
 Zone III unresolved, subgrid fluctuations

k_c, k_n, k_m, k_t = cutoff, Nyquist, microscale and transition wavenumber respectively

Figure 3: Highpass/lowpass response function domain for a.) analog, b.) digital ($k_c < k_n$), and c.) digital ($k_c = k_n$) filters.

equations result in Eqns. (27,28); the next section deals with that issue.

Averaged/Separated Equations

If the average (Eqn. 1) of Eqns. (25,26) is taken and the averaging operation applied consistently to each term, the following equation results,

$$\begin{aligned} \frac{\partial \bar{u}_i}{\partial t} + \underbrace{(\bar{u}_i \bar{u}_j)_{,j}}_1 + \frac{1}{\rho} \bar{P}_{,i} - \nu \bar{u}_{i,j,j} &= \bar{A}_i \\ = -\left\{ \frac{\partial \bar{u}'_i}{\partial t} + \underbrace{(\bar{u}_i u'_j + u'_i \bar{u}_j + \bar{u}'_i u'_j)_{,j}}_2 + \frac{1}{\rho} \bar{P}'_{,i} - \nu \bar{u}'_{i,j,j} \right\} \end{aligned} \quad (29)$$

and

$$\begin{aligned} \frac{\partial \bar{\phi}}{\partial t} + \underbrace{(\bar{u}_j \bar{\phi})_{,j}}_3 - \lambda \bar{\phi}_{i,j,j} &= \bar{B} \\ = -\left\{ \frac{\partial \bar{\phi}'}{\partial t} + \underbrace{(\bar{u}_j \phi' + u'_j \bar{\phi} + \bar{u}'_j \phi')_{,j}}_4 - \lambda \bar{\phi}'_{i,j,j} \right\} \end{aligned} \quad (30)$$

While not in a final form for comparison to Eqns. (27,28), two comments are necessary at this point. First, the sum of the terms 1 and 2 are the terms resulting from the decomposition of the nonlinear term. These terms are universally said to equal $\bar{u}_i u'_j$. The same is said of the sum of the terms 3 and 4. Secondly, the analysis of the equations (29,30), even in LES, stops at this point as the linear term decomposition is never performed and therefore the issue of "double averaging" of them never arises. Certainly on first inspection, generalized consistent separation provides a more complex equation system when averaged than traditional treatments suggest. While seemingly not an improvement as measured by apparent equation simplification the terms in the fully prepared equations (29,30) will provide the heretofore missing terms necessary to explain several of the questions raised earlier.

EQUATION ANALYSIS

It is desireable to compare the averaged equations in (27) and (28) to the filtered separated equations in (29) and (30) as they should be equal. To do this comparison Eqns. (27,28) are first analyzed.

Analysis of the Average Field Equations

By use of the YB-III series expansion in Eqns. (21) and (22) Eqns. (27,28) become,

$$\frac{\partial \bar{u}_i}{\partial t} + (\bar{u}_i \bar{u}_j)_{,j} + \frac{1}{\rho} \bar{P}_{,i} - \nu \bar{u}_{i,j,j} + R_{i,j,j}^l = \bar{L}(\underline{x}, t) = 0 \quad (31)$$

$$\frac{\partial \bar{\phi}}{\partial t} + (\bar{u}_j \bar{\phi})_{,j} - \lambda \bar{\phi} + Q_{j,j}^l = \bar{M}(\underline{x}, t) = 0 \quad (32)$$

It is remarked that these are the essential equations resulting from the "closure free" formulation referred to in the introduction. The closure free label results from the fact that no turbulent correlations are present which must be empirically specified.

A further comparison points to yet another matter requiring explanation. As noted, the YB-III expansion for symmetric filters results in Eqn. (21) which is rewritten as

$$\bar{u}_i \bar{u}_j = \bar{u}_i \bar{u}_j + R_{ij} = \bar{u}_i \bar{u}_j + 2\alpha(\bar{u}_{i,k} \bar{u}_{j,k}) + \dots \quad (33)$$

Eqn. (33) may be compared to the Leonard/Clark reduction for $\bar{u}_i \bar{u}_j$ as follows,

$$\begin{aligned} \bar{u}_i \bar{u}_j &= \bar{u}_i \bar{u}_j + \bar{u}_i u'_j + u'_i \bar{u}_j + u'_i u'_j \\ &= \bar{u}_i \bar{u}_j + [2\alpha(\bar{u}_{i,k} \bar{u}_{j,k}) + \dots] + \bar{u}'_i u'_j \end{aligned} \quad (34)$$

It is clearly seen that at least through the second order filter length terms, these expansions are identical except for the presence of the "closure" terms in the Leonard/Clark approximation. An explanation of this difference will follow, but first the comparison of the average equations in (31) and (32) to Eqns. (29, 30) will be finished.

Analysis of the Generalized Averaged/Separated Equation

It is necessary to look a bit more at the linear terms. From Dingman (1986) or Bedford et al. (1987) it is a very simple matter to show that two important averaging rules used in Reynold's averaged equations do not adapt to the case of the moving average definitions in use for the LES procedure. For any function $f(\underline{x}, t)$ where $f(\underline{x}, t) = \bar{f}(\underline{x}, t) + f'(\underline{x}, t)$ then

$$\bar{f}'(\underline{x}, t) \neq 0 \quad (35)$$

$$\text{and } \bar{\bar{f}}(\underline{x}, t) \neq \bar{f}(\underline{x}, t) \quad (36)$$

Concentrating on the impact of Eqn. (36) the linear terms in Eqns. (29,30) are double averaged and can be further simplified by applying the higher order averaging definition from Leonard (1974). Therefore for symmetric filters

$$\bar{\bar{f}} = \bar{f} + \alpha \bar{f}_{,kk} + (\text{HOT}). \quad (37)$$

and Eqns. (29,30) become,

$$\begin{aligned} \frac{\partial \bar{\bar{u}}_i}{\partial t} + [\bar{u}_i \bar{u}_j + \bar{u}_i u'_j + \bar{u}'_i \bar{u}_j + \bar{u}'_i u'_j]_{,j} + \frac{1}{\rho} \bar{P}_{,i} - \nu \bar{u}_{i,jj} &= C_i \\ = -\alpha \underbrace{\left[\frac{\partial}{\partial t} (\bar{u}_{i,kk}) \right]}_a + \underbrace{\frac{1}{\rho} \bar{P}_{,ikk}}_b - \underbrace{\nu \bar{u}_{i,jjkk}}_c \end{aligned}$$

$$- \left[\overbrace{\frac{\partial}{\partial t}(\bar{u}'_i)}^a + \overbrace{\frac{1}{\rho} \bar{P}'_{,i}}^b - \overbrace{\nu \bar{w}'_{i,jj}}^c \right] \quad (38)$$

and

$$\begin{aligned} \frac{\partial \bar{\phi}}{\partial t} &+ [\bar{u}_j \bar{\phi} + \bar{u}_j \bar{\phi}' + \bar{u}'_j \bar{\phi} + \bar{u}'_j \bar{\phi}']_{,j} - \lambda \bar{\phi}_{,jj} = D_i \\ &= -\alpha \left[\underbrace{\frac{\partial}{\partial t}(\bar{\phi}_{,kk})}_d - \underbrace{\lambda \bar{\phi}_{,jjkk}}_e \right] \\ &\quad - \left[\underbrace{\frac{\partial}{\partial t}(\bar{\phi}')}_d - \underbrace{\lambda \bar{\phi}'_{,jj}}_e \right] \end{aligned} \quad (39)$$

The relationship of the conjunctive and high pass filter is seen as follows. If Eqn. (16) is used for fluctuating term then the terms (a) - (e) cancel out respectively. The remaining portion of Eqns. (38,39) are equal to Eqns. (27,28) and (31, 32) under the following condition,

$$\bar{u}_i \bar{u}_j = \bar{u}_i \bar{u}_j + R'_{ij} = \bar{u}_i \bar{u}_j + \bar{u}_i \bar{u}'_j + \bar{u}'_i \bar{u}_j + \bar{u}'_i \bar{u}'_j \quad (40)$$

$$\bar{u}_j \bar{\phi} = \bar{u}_j \bar{\phi} + Q'_j = \bar{u}_j \bar{\phi} + \bar{u}_i \bar{\phi}' + \bar{u}'_i \bar{\phi} + \bar{u}'_i \bar{\phi}' \quad (41)$$

If the equivalence of the first term of R_{ij} (R'_{ij}) and the Leonard/Clark reduction for $\bar{u}_i \bar{u}_j + \bar{u}_i \bar{u}'_j + \bar{u}'_i \bar{u}_j$ is invoked then equivalence for Eqns. (31,31) is achieved when,

$$\bar{u}'_i \bar{u}'_j = R''_{ij} = \frac{1}{2!} (2\alpha)^2 \bar{u}_{i,kl} \bar{u}_{j,kl} + \text{HOT} \quad (42)$$

The order of these terms is consistent with the asymptotic analyses of Aldama (1990). This is yet another way of interpreting the correlation term $\bar{u}'_i \bar{u}'_j$ as again being relatively unimportant if not negligible. The corresponding terms for equivalence in the scalar flux equation are,

$$\bar{u}'_j \bar{\phi} = Q''_j = \frac{1}{2!} (2\alpha)^2 \bar{u}_{j,kl} \bar{\phi}_{,kl} + \text{HOT} \quad (43)$$

Before leaving this section it is important to point out that the act of separation followed by averaging is not and should not be confined to just the nonlinear terms. The linear terms resulting from separation also require "closure" and one measure of a satisfactory representation for the low pass and high pass components is whether the terms (a)-(e) (Eqns. 38,39) cancel. Only a comprehensively derived equation for $\bar{\alpha}$ and α' will allow this to occur. Therefore, these cancellations become a constraint that must be adhered to in the derivation of a closure for α' .

Digitization / Discretization - Interpretive Constraints

The act of discretization of a continuous domain is a digitization and the signal processing literature (e.g. Hamming 1990) provides considerable material on the constraints in adapting and interpreting analog and digital filters. One of the most elementary is the Nyquist wavenumber, k_n (or frequency). If for the time being we assume that $\underline{k}_c = k_n$ and $\omega_c = \omega_n$ (Fig 3c) then from the signal processing literature it is well known that all variability is removed via the low pass filter at $\underline{k}_c = k_n$ and that any information from the spectrum for $\underline{k}_c > k_n$ is not useable as it is aliased data. Therefore the low pass filter domain does not extend beyond \underline{k}_c . If we are again faithful to the signal processing literature the high pass filter defined from $L(\underline{k},\omega)$ is also subject to the same constraint (Hamming 1990). Therefore the fluctuations are also only defined in a domain from $0 \rightarrow \underline{k}_n = \underline{k}_c$ and not beyond as in zone III (Figs. 3b-c). The implication then is that the turbulence (f') being defined and parameterized in the averaged equations is defined only at the resolved grid scales and lower (in wavenumber). Therefore fluctuations at the grid scale or higher (zone III, Figs 3b-3c) are not defined nor included in the averaged turbulent flow equations. This is intuitive. In light of this constraint and its implication, the use of the term subgrid scale to refer to the term $\overline{u'_i u'_j}$ is misleading as this term

does not include zone III fluctuations from the grid wavenumber and higher which are thought to require parameterization. Rather only the portion of the domain in zone II is parameterized. It is possible (Fig. 3b) to have $k_c < k_n$ and a much larger region of fluctuation response function domain (zone II) obtains. However, with the perfectly flat low pass response between k_c and k_n , $\overline{u'_i u'_j}$ in zone II could still average to zero. Should the response function fluctuate about $R = 0$ in zone II ($k_c \rightarrow k_n$) such as with the uniform filter response function, then the contribution to $\overline{u'_i u'_j}$ will be finite. In numerical models therefore, schematic 3c represents the response function with quite small $\overline{u'_i u'_j}$ contributions (if any).

The region between k_t and k_c is the transition region and it is this region where the cross product terms $\overline{u'_i \bar{u}_j}$ and $\overline{\bar{u}_i u'_j}$ are important.

What the YB-III expansion on the nonlinear term $\overline{u_i u_j}$ and $\overline{u_j \phi}$ does is to fully and completely specify the actual average equations resolved to the permissible limit k_n or its numerical model form where $k_c = k_n$. It has also been argued that at the limit of the filter imposed by the model grid is $k_c = k_n$, and that the $\overline{u'_i u'_j}$ (or $\overline{u'_i \phi'}$) terms are quite small and therefore do not represent contributions from the "subgrid scale" (zone III, Figs 3b,3c) as they are beyond the Nyquist limit of the filter domain.

Behavior of R_{ij} Approaching the Cutoff Wavenumber

It is instinctive to analyse the behavior of R_{ij} (and by implication Q_j) in the limit of high wavenumber. While the asymptotic analyses of Aldama (1990) provides one approach, a more simplistic derivation illustrates the point. After Blinchikoff and Zverev (1976) a very simple one dimensional test is initiated by defining,

$$u_i = a e^{I k_i x}; u_j = b e^{I k_j x} \quad (44)$$

with $I = \sqrt{-1}$. Assuming isotropic filter widths the average values are defined as,

$$\begin{aligned}\bar{u}_i &= a e^{-\alpha k_i^2} e^{Ik_i x} \text{ and} \\ \bar{u}_j &= b e^{-\alpha k_j^2} e^{Ik_j x}\end{aligned}\quad (45)$$

The average of the product $u_i u_j$ is defined from Eqn. (44) as,

$$\bar{u}_i \bar{u}_j = ab e^{-\alpha(k_i + k_j)^2} e^{I(k_i + k_j)x} \quad (46)$$

Using the YB-III series and some algebra yields

$$e^{-2\alpha k_i k_j} = 1 - (2\alpha)k_i k_j + \frac{1}{2!}(2\alpha)^2 k_i^2 k_j^2 + \text{HOT} \quad (47)$$

In numerical models the Nyquist sampling limit is set by the grid scale and in traditional LES models it is also the case that k_c and ω_c are equal to the Nyquist limits. The relative contribution of the terms in the power series for R_{ij} is therefore defined (Hamming 1990) up to k_c (ω_c) and can be evaluated by integrating Eqn (47) from 0 to k_c . If the wavenumbers are nondimensionalized by k_c and denoted by an asterisk then

$$\begin{aligned}&\int_0^1 \int \exp\left(\frac{\pi^2}{12} k_i^* k_j^*\right) dk_i^* dk_j^* \\ &= \int_0^1 \int [1 - \frac{\pi^2}{12} k_i^* k_j^* + \frac{\pi^4}{288} k_i^* k_j^* + \text{HOT}] dk_i^* dk_j^* \quad (48)\end{aligned}$$

Table 1 contains a summary of the ratio of the approximate to exact and the percentage relative error for the first three terms.

A Final Note on R_{ij}

The representation of turbulence in Zone II in terms of the mean flow by R_{ij} (Q_j) is generalized and contains several interesting features. It is a simple matter to show the structure of R_{ij} in terms of vorticity, Ω_{ij} , and strain rate S_{ij} . In terms

Table 1: Convergence Rate vs. Number of Terms in R_{ij}

	No Term $\bar{u}_i \bar{u}_j = \bar{u}_i \bar{u}_j$	To First Term $\bar{u}_i \bar{u}_j = \bar{u}_i \bar{u}_j + R_{ij}^1$	To Second Term $\bar{u}_i \bar{u}_j = \bar{u}_i \bar{u}_j + R_{ij}^1 + R_{ij}^2$
Ratio = Approximate	1.2104	0.9615	1.0070
Exact			
Relative Error	21%	3.85%	0.7%

of the averaged field variables,

$$S_{ij} = \frac{1}{2}(\bar{u}_{i,j} + \bar{u}_{j,i}) \text{ and} \quad (49)$$

$$\Omega_{ij} = \frac{1}{2}(\bar{u}_{i,j} - \bar{u}_{j,i}). \quad (50)$$

The first term in R_{ij}^1 , can then be written as

$$R_{ij}^1 = (2\alpha) [\underbrace{S_{ik} S_{jk}}_a + \underbrace{S_{ik} \Omega_{jk} + \Omega_{ik} S_{jk}}_b + \underbrace{\Omega_{ik} \Omega_{jk}}_c] \quad (51)$$

Term (a) is the deformation tensor which is a basis for the Smagorinsky model. Term (c) is the rotation tensor which has also been used as the basis for empirical functions describing flows with high velocity. The terms in (b) are essentially vortex stretching terms.

It is interesting that all three of these terms result from full resolution of low pass average equations including the cross term contribution. These terms represent activity between k_i and k_c (i.e. zone I and zone II) and do not represent subgrid scale activity. Yet the fact remains that these terms in more simplified form have formed the basis for a variety of " closures " for the subgrid scale activity. With these average equations containing so little a contribution from the $\bar{u}'_i \bar{u}'_j$ ($\bar{u}'_i \phi$) terms and no subgrid scale contribution how might equations be formulated which include

the effects of turbulence from all wavenumbers up to the microscale wavenumber (zone III). The next section explores this requirement.

THE SEPARATED EQUATIONS

Analog Considerations - A Two Scale Separation

The total field or continuous analog equations listed in Eqns. (23,24) are valid for all wavenumbers up to the microscale, k_m , as are the separated equations in Eqns. (25,26). The separated and total field equations are quite appealing as the decomposition of the nonlinear term is not a problem. Furthermore comparison of total equations (25, 26) with the averaged equations (31,32) reveals considerable equivalence in the terms which are functions of the averaged variables. However, the essential difference between the two equations is that the full effect of the fluctuating physics is retained in Eqns. (25,26), and not so in Eqns. (31,32). It is quite simple to derive an equation for the fluctuating components. Subtracting Eqns. (31,32) from Eqns. (25,26) gives that

$$\begin{aligned} \frac{\partial u'_i}{\partial t} + (u'_i \bar{u}_j + \bar{u}_i u'_j + u'_i u'_j)_{,j} &= R_{i,j,j} \\ &= -\frac{1}{\rho} P'_{,i} + \nu u'_{i,j,j} \end{aligned} \quad (52)$$

$$\begin{aligned} \frac{\partial \phi}{\partial t} + (u'_i \bar{\phi} + \bar{u}_i \phi' + u'_i \phi')_{,i} &= Q_{i,i} \\ &= \lambda \phi'_{,jj} \end{aligned} \quad (53)$$

It is noticed that there is an explicit turbulence and mean flow interaction as contrasted with the mean flow equations. The two scale separation employed here is permitted because of the analog nature of the filter wherein the filter function is essentially continuously defined to the mesoscale limit. Therefore the turbulence represents all the domain in zone II, Figure 3a. The model/digital form is different however.

The Digital Formulation - A Three Scale Approach

As noted in the previous section the introduction of the grid essentially digitizes the continuum and for all intents and purposes moves the Nyquist wavenumber from ∞ back to k_c the cutoff wavenumber (Fig. 3c). This reorganization results in the low pass/high pass filter domain extending only to k_c , k_n and results in a total field equation separated into the low frequency terms (zone I in Fig. 3c), the resolved turbulent fluctuations (α' , zone II in Fig. 3c) and the subgrid scale turbulent fluctuations (α^* , zone III, Fig. 3c). With this three scale definition a total field variable is separated into three components such that,

$$\alpha(\underline{x}, t) = \bar{\alpha}(\underline{x}, t) + \alpha'(\underline{x}, t) + \alpha^*(\underline{x}, t) \quad (54)$$

This separation can be directly inserted into the total field equations, however, it is more convenient to recognize that the resolved scale turbulence can be "closed" via the YB-II series valid to $k_c = k_n$ i.e.

$$\alpha(\underline{x}, t) = \bar{\alpha}(\underline{x}, t) + (-\alpha \bar{f}_{,ii} + \text{HOT}) + \alpha^*(\underline{x}, t) \quad (55)$$

Using only the first term of the α' expansion, substitution of Eqn.(55) into Eqns. (23,24) gives for isotropic filters,

$$\begin{aligned} \frac{\partial \bar{u}_i}{\partial t} + (\bar{u}_i \bar{u}_j)_{,j} + \frac{1}{\rho} \bar{P}_{,i} + \nu \bar{u}_{i,jj} - \\ \alpha \left\{ \frac{\partial}{\partial t} (\bar{u}_{i,kk}) + (\bar{u}_i \bar{u}_{j,kk} + \bar{u}_{i,k} \bar{u}_j + \bar{u}_{i,kk} \bar{u}_{j,kl})_{,j} \right. \\ \left. + \frac{1}{\rho} \bar{P}_{,ijj} + \nu \bar{u}_{i,jj,kk} \right\} \\ = \frac{\partial u_i^*}{\partial t} + (u_i^* u_j^*)_{,j} + \frac{1}{\rho} P_{,i}^* + \nu u_{i,jj}^* \\ + \underbrace{\{(\bar{u}_i - \alpha \bar{u}_{i,kk})(u_j^*) + (u_i^*)(\bar{u}_j - \alpha \bar{u}_{j,kk})\}}_a \end{aligned} \quad (56)$$

$$\begin{aligned}
\frac{\partial \bar{\phi}}{\partial t} + (\bar{u}_i \bar{\phi})_{,i} - \lambda \bar{\phi}_{,jj} \\
- \alpha \left\{ \frac{\partial}{\partial t} \bar{\phi}_{,jj} + (\bar{u}_{i,jj} \bar{\phi} + \bar{u}_{i,j} \bar{\phi}_{,jj} + \bar{u}_{i,jj} \bar{\phi}_{,kk})_{,i} - \lambda \bar{\phi}_{,j,jk} \right\} \\
= \frac{\partial \phi_i^*}{\partial t} + (u_i^* \phi^*)_{,i} - \lambda \phi_{,jj}^* \\
+ \underbrace{\{(\bar{u}_i - \alpha \bar{u}_{i,kk})(\phi_j^*) + (u_i^*)(\bar{\phi} - \alpha \bar{\phi}_{,kk})\}}_b
\end{aligned} \tag{57}$$

The terms on the left hand side of Eqns. (56,57) represent activity valid in the region $k < k_c = k_n$ expressed in terms of the filtered quantity, while the right hand side represents the actual subgrid scale activity and its interaction with the resolved (not mean) flow through terms (a) and (b). It is noted that the first four terms in the Eqn. (56) and the first three terms of Eqn. (57) are identical to the first four terms in the average momentum equation (31) and the first three terms in the transport equation (32) respectively. Yet Eqns.(56,57) are wholly different in that unlike Eqns. (31,32) these equations include all the resolved and subgrid scale activity. That the filtered lower order differential terms in the average and total equations are identical is a major source of misconception about whether the average equations are being used in turbulence models or whether in fact it is the total field equations separated into the three basic components that should be used.

CONCLUDING REMARKS

An attempt has been made in this paper to clarify some misinterpretations of the role and use of the averaged equations for turbulent flow and transport modeling. The intended result of these clarifications is to divert modeler's attention to the fact that many if not most modelers who employ the concept of subgrid scale parameterization are not using (nor should they use) the averaged equations as the concept

of subgrid scale contributions to properly low pass filtered or averaged equations is inapplicable. If one wishes to robustly include the subgrid effects then the total field equations must be used. The process of separation into filtered (averaged) and turbulent components yields a two-scale separation which can be formally applied to the continuous or analog equation. However, the digitization of the total equations via the numerical grid introduces a third separation resulting from the introduction of the Nyquist wavenumber and its equivalence to the cutoff wavenumber. In so doing a three-scale separation is achieved, i.e. averaged variables, grid resolved turbulent fluctuations which can be formally related to the averaged variables, and the subgrid scale turbulence. By contrasting the average and the total/separated equations it is noticed that one of the possible sources of conceptual confusion exists because the fundamental terms in both sets of equations are identical, i.e. the filtered first order differential terms and the molecular terms. Several more specific comments apply.

First by use of high pass averaging techniques from the signal processing literature the function components can, for Gaussian (and uniform) filters, be expanded in a power series as a function of not only the unfiltered or total variable but more importantly the filtered variable. This series can be used to create a direct power series expansion for the average nonlinear advection and inertia terms.

Second, the use of this generalized series expansion results in a set of averaged governing differential equations which do not contain any formal turbulent correlation closure terms as they were not derived by a separation methodology applied to the nonlinear terms.

Third, the traditional preparation of the average equations by separation of the nonlinear portions of the equation followed by averaging is seen to be incomplete in that the entire equation must be formally separated and then averaged. These

separated then filtered equations formally reduce to the directly averaged equations and in so doing it is shown that the Leonard/Clark terms are formally equal to the first term of the conjunctive filter derived power series expansion of the nonlinear terms.

Finally, the terms $\overline{u'_i u'_j}$ and $\overline{u'_i \phi'_j}$ are shown to be quite small in the averaged equations. This is intuitive because the domain of the filter only extends to the Nyquist limit when considering a discretization (digitization) of the continuous equations. Thus the concept of subgrid scale contributions is not applicable to the correctly averaged equations.

ACKNOWLEDGEMENTS

This paper is a contribution from the Great Lakes Forecasting Program and support from CRAY Research Inc., NOAA-Ohio Sea Grant, Ohio State University, and the U.S. Geological Survey Water Resources Center is gratefully acknowledged. Earlier support for this work came from National Science Foundation Grant No. CEE 8410552 and is also appreciated. The author benefitted considerably from conversations with C.F. Kuan, D. Podber, G. Baker, T. Herbert and Y. Guzennac and their suggestions are appreciated.

REFERENCES

- [1] Aldama, A. 1985. "Theory and Applications of Two and Three Scale Filtering Approaches for Turbulent Flow Simulations," Ph.D. Thesis Dept. Civil Engineering, Massachusetts Institute of Technology, Cambridge, Mass.

- [2] Aldama, A. 1990. Filtering Techniques for Turbulent Flow Simulations, Lecture Notes in Engrg, Springer Verlag, Berlin.
- [3] Babajimopoulos, C. and K. Bedford, 1980. "Formulating Lake Models which Preserve Spectral Statistics," J. Hydraulic Engrg., 106, pgs 1-19.
- [4] Bedford, K. 1981, "Spectra Preservation Capabilities of Great Lakes Transport Models," in : Transport Models for Island and Coastal Waters, ed. H. Fisher, Academic Press, pgs 172-221.
- [5] Bedford, K. 1990, "Diffusion, Dispersion and Subgrid Scale Parameterization," in : Coastal, Estuarial and Harbour Engineers Reference Book, ed. M. Abbott and W. Price, Chapman and Hall Ltd., London; (to appear).
- [6] Bedford, K. and M. Abdelrhman, 1987. "Analytical and Experimental Studies of the Benthic Boundary Layer and Their Applicability to Near Bottom Transport in Lake Erie," J. Great Lakes Research, 13, pgs 628-648.
- [7] Bedford, K. and C. Babajimopoulos, 1980. "Verifying Lake Transport Models with Spectral Statistics," J. Hydraulic Engrg., 106, pgs 21-38.
- [8] Bedford, K. and Y. Dakhoul 1982. "Applying LES Turbulence Modeling to Open Channel Flow," in : Applying Research to Hydraulic Practice, ed. P. Smith, Amer. Soc. Civil Engrs, NY; pgs 32-43.
- [9] Bedford, K., S. Dingman and W. Yeo, 1987. "Preparation of Estuary and Marine Model Equations by Generalized Filtering Methods," in : Three-Dimensional Models of Marine and Estuary Dynamics, ed. J. Nihoul and B. Jamart, Elsevier Pub., Amsterdam, pgs 113-125.
- [10] Bedford, K., O. Wai, C. Libicki and R. Van Evra III 1987. "Sediment Entrainment and Deposition Measurements in Long Island Sound," J. Hydraulic Engrg.,

113, pgs 1325-1342.

- [11] Blinchikoff, H. and A. Zverev, 1976. Filtering in the Time and Frequency Domain, John Wiley Co. NY.
- [12] Boyce, F. 1974. "Some Aspects of Great Lakes Physics of Importance to Biological and Chemical Processes," J. Fisheries Res. Board of Canada, 31, pgs 689-730.
- [13] Clark, R., J. Ferziger and W. Reynolds, 1979. "Evaluation of Sub-grid Scale Models Using an Accurately Simulated Turbulent Flow," J. Fluid Mech., 91, pgs 1-16.
- [14] Dakhoul, Y. and K. Bedford, 1986a. "Improved Averaging Method for Turbulent Flow Simulation. Part I : Theoretical Development and Application to Burger's Transport Equation," Int. J. Numerical Methods in Fluids, 6, pgs 49-64.
- [15] Dakhoul, Y. and K. Bedford, 1986b. "Improved Averaging Method for Turbulent Flow Simulation. Part II : Calculations and Verifications," Int. J. Numerical Methods in Fluids, 6, pgs 65-82.
- [16] Dingman, J. 1986. "The Development and Application of Generalized Higher Order Filtering Techniques to the Continuum Wave Equations," Ph.D. Dissertation, Dept. of Civil Engineering, Ohio State University, Columbus, Ohio.
- [17] Dingman, J. and K. Bedford, 1984. "The Lake Erie Response to the January 1978 Cyclone," J. Geophysical Research, 89, 6427-6445.
- [18] Gross, T. and A Nowell, 1983. "Mean Flow and Turbulence Scaling in a Tidal Boundary Layer," Cont. Shelf Research, 2, pgs 109-126.

- [19] Gross, T. and A Nowell, 1985. "Spectral Scaling in a Tidal Boundary Layer," J. Physical Oceanography, 15, pgs 496-508.
- [20] Hamming, R. 1989. Digital Filters, 3rd ed., Prentice Hall, N.J.
- [21] Hildebrand, F. 1976. Advanced Calculus for Applications, 2nd ed., Prentice Hall, N.J.
- [22] Kwak, D., W. Reynolds and J. Ferziger, 1975. "Three-Dimensional Time Dependent Computation of Turbulent Flow," Dept. TF-5, Dept. Mech. Engrg, Stanford University, Stanford, California.
- [23] Leonard, A. 1974. "Energy Cascade in Large Eddy Simulations of Turbulent Fluid Flows," Adv. in Geophysics, 18A, pgs 237-248.
- [24] Libicki, C. and K. Bedford, 1990. "Sudden, Extreme Lake Erie Storm Surges and the Interaction of Wind-Stress, Resonance and Geometry," J. Great Lakes Research, 16, pgs 380-395.
- [25] Rosman, P. 1987. "Modeling Shallow Water Bodies Via Filtering Techniques," Ph.D. Thesis, Dept. of Civil Engineering, Massachusetts Institute of Technology, Cambridge Mass.
- [26] Yeo, W. 1987. "A Generalized High Pass/Low Pass Filtering Procedure for Deriving and Solving Turbulent Flow Equations," Ph.D. Dissertation, Dept. of Civil Engineering, Ohio State University, Columbus, Ohio.
- [27] Yeo, W. and K. Bedford, 1988. "Closure-Free Turbulence Modeling Based Upon a Conjunctive Higher Order Averaging Procedure," in : Computational Methods in Flow Analysis, ed. H. Niki and M. Kawahara, Okayama University of Science, pgs 844-851.

- [28] Yeo, W. and K. Bedford, 1990a. "A Generalized High Pass/Low Pass Averaging Procedure for Deriving Turbulent Flow and Transport Model Equations,"(Submitted).
- [29] Yeo, W. and K. Bedford, 1990b. "A First Analysis of the Generalized High Pass/Low Pass Averaging Procedure and Resulting Turbulent Flow and Transport Model Equations,"(Submitted).

UNCLASSIFIED
SECURITY CLASSIFICATION OF THIS PAGE

REPORT DOCUMENTATION PAGE							
1a. REPORT SECURITY CLASSIFICATION Unclassified			1b. RESTRICTIVE MARKINGS				
2a. SECURITY CLASSIFICATION AUTHORITY			3. DISTRIBUTION/AVAILABILITY OF REPORT Approved for public release; distribution unlimited				
2b. DECLASSIFICATION/DOWNGRADING SCHEDULE			5. MONITORING ORGANIZATION REPORT NUMBER(S)				
4. PERFORMING ORGANIZATION REPORT NUMBER(S)			7a. NAME OF MONITORING ORGANIZATION Office of Naval Research				
6a. NAME OF PERFORMING ORGANIZATION University of South Florida		6b. OFFICE SYMBOL (If applicable)	7b. ADDRESS (City, State, and ZIP Code) Department of the Navy 800 North Quincy Street Arlington, Virginia 22217				
6c. ADDRESS (City, State, and ZIP Code) 140 - 7th Avenue South St. Petersburg, Florida 33701		8a. NAME OF FUNDING/SPONSORING ORGANIZATION			8b. OFFICE SYMBOL (If applicable)		
8c. ADDRESS (City, State, and ZIP Code)			9. PROCUREMENT INSTRUMENT IDENTIFICATION NUMBER N00014-90-J-4120				
			10. SOURCE OF FUNDING NUMBERS	PROGRAM ELEMENT NO.	PROJECT NO. 4229078-01	TASK NO.	WORK UNIT ACCESSION NO.
11. TITLE (Include Security Classification) Large Eddy Simulation...Where Do We Stand?							
12. PERSONAL AUTHOR(S) Boris Galperin (ed.)							
13a. TYPE OF REPORT Workshop Proceedings		13b. TIME COVERED FROM 9/1/90 TO 9/30/91		14. DATE OF REPORT (Year, Month, Day) December 1990		15. PAGE COUNT 253	
16. SUPPLEMENTARY NOTATION							
17. COSATI CODES			18. SUBJECT TERMS (Continue on reverse if necessary and identify by block number) Turbulence Theories; Large Eddy Simulation; Computational Fluid Dynamics; Compressible Flows; Reacting Flows; Incompressible Flows; (CONTINUE ON REVERSE SIDE)				
19. ABSTRACT (Continue on reverse if necessary and identify by block number) These proceedings contain abstracts, extended abstracts and lectures presented at the International Workshop on Large Eddy Simulation, held at St. Petersburg Beach, Florida, December 19-21, 1990. The presentations cover the major aspects of the theory of large eddy simulation and application of this technique to various complex engineering and geophysical flows. Several topics included;							
20. DISTRIBUTION/AVAILABILITY OF ABSTRACT <input checked="" type="checkbox"/> UNCLASSIFIED/UNLIMITED <input type="checkbox"/> SAME AS RPT. <input type="checkbox"/> DTIC USERS				21. ABSTRACT SECURITY CLASSIFICATION Unclassified			
22a. NAME OF RESPONSIBLE INDIVIDUAL				22b. TELEPHONE (Include Area Code)		22c. OFFICE SYMBOL	

DD FORM 1473, 84 MAR

66E93
1980

83 APR edition may be used until exhausted.
All other editions are obsolete.

SECURITY CLASSIFICATION OF THIS PAGE

UNCLASSIFIED

BLOCK #18 CONTINUED

Atmospheric Boundary Layers; Oceanic Circulation; Subgrid scale Parameterization.

including atmospheric physics, and physical oceanography

Unclassified

SECURITY CLASSIFICATION OF THIS PAGE